Model order reduction and substructuring methods for nonlinear structural dynamics

Wu, Long

DOI
10.4233/uuid:f9736e8b-d00f-4e25-b456-48bd65b43788

Publication date
2018

Document Version
Final published version

Citation (APA)
Wu, L. (2018). *Model order reduction and substructuring methods for nonlinear structural dynamics*. [Dissertation (TU Delft), Delft University of Technology]. https://doi.org/10.4233/uuid:f9736e8b-d00f-4e25-b456-48bd65b43788

MODEL ORDER REDUCTION
and
SUBSTRUCTURING METHODS
for
NONLINEAR STRUCTURAL DYNAMICS

Long WU

MODEL ORDER REDUCTION
and
SUBSTRUCTURING METHODS
for
NONLINEAR STRUCTURAL DYNAMICS

Proefschrift

ter verkrijging van de graad van doctor
aan de Technische Universiteit Delft,
op gezag van de Rector Magnificus prof. ir. T. H. J. J. van der Hagen,
voorzitter van het College voor Promoties,
in het openbaar te verdedigen op maandag 3rd juli 2018 om 10:00 uur

door

Long WU

Master of Engineering in Power Engineering and Engineering Thermophysics,
Xi’an Jiaotong University, Xi’an, China,
geboren te Shaanxi, China.

Dit proefschrift is goedgekeurd door de

promotor: Prof. dr. ir. A. van Keulen
copromotor: Dr. ir. P. Tiso

Samenstelling promotiecommissie:

Rector Magnificus	voorzitter
Prof. dr. ir. A. van Keulen	Technische Universiteit Delft
Dr. ir. P. Tiso	Eidgenössische Technische Hochschule Zürich
Onafhankelijke leden:	
Prof. dr. ir. D. J. Rixen	Technische Universität München
Prof. dr. E. Chatzi	Eidgenössische Technische Hochschule Zürich
Prof. dr. P. G. Steeneken	Technische Universiteit Delft
Prof. dr. ir. J. W. van Wingerden	Technische Universiteit Delft
Prof. dr. H. Nijmeijer	Technische Universiteit Eindhoven

This project was financially sponsored by China Scholarship Council from Sep. 2013 to Sep. 2017. The final stage of this project was co-financed by ETH Zürich from Oct. 2017 to Dec. 2017.

Keywords: model order reduction, geometrical nonlinearities, component mode synthesis, multibody system dynamics, modal derivatives

Printed by: Ipskamp Printing, The Netherlands.

Author email: wulongxjtu@gmail.com

ISBN 978-94-6186-935-7

An electronic version of this dissertation is available at
`http://repository.tudelft.nl/`.

to my parents
献给我的父母

SUMMARY

Dynamic analysis of large-size finite element models has been commonly applied by mechanical engineers to simulate the dynamic behavior of complex structures. The ever-increasing demand for both detailed and accurate simulation of complex structures forces mechanical engineers to pursue a balance between two conflicting goals during the simulations: low computational cost and high accuracy. These goals become extremely difficult for geometric nonlinear structural dynamical problems. When geometrical nonlinearities are introduced, the internal force vector and Jacobians are configuration dependent, and the corresponding updates are computationally expensive. This thesis presents nonlinear model order reduction techniques that aim to perform detailed dynamic analysis of multi-component structures with reduced computational cost, without degrading the accuracy too much. Special attention is given to flexible multibody system dynamics.

For multi-component structures featuring many interface degrees of freedom, standard substructuring dynamics can be combined with interface reduction techniques to obtain compact reduced order models. Chapter 2 summarized a variety of interface reduction techniques for the well-known Craig-Bampton substructuring method. These approaches are reviewed and compared in terms of both computational cost and accuracy. A multilevel interface reduction method is presented as a more generalized approach, where a secondary Craig-Bampton reduction is performed when the subsystems are assembled within localized subsets. The multilevel interface reduction method provides an accurate representation of the full linear model with significantly lower computational cost.

In Chapter 3, we extend the Craig-Bampton method to geometric nonlinear problems by augmenting the system-level interface modes and internal vibration modes of each substructure with their corresponding modal derivatives. The modal derivatives are capable of describing the bending-stretching coupling effects exhibited by geometric nonlinear structures. Once the reduced order model is constructed by Galerkin projection, the upcoming challenge is the computation of the reduced nonlinear internal force vectors and tangent matrices during the time integration. The evaluation of these objects scales with the size of the full order model, and it is therefore expensive, as it needs to be repeated multiple time within every time step of the time integration. To address this problem, we directly express the reduced nonlinear vectors and matrices as a polynomial function of the modal coordinates, using substructure-level higher-order tensors with much smaller size. This enhanced Craig-Bampton method offers flexibility for reduced modal basis construction, as modal derivatives need to be computed only for substructures actually featuring geometrical nonlinearities, and do not need the prior knowledge of the nonlinear response of the full system with training load cases.

For flexible multibody systems, each body undergoes both overall rigid body motion and flexible behavior. To describe the dynamic behavior of each body accurately, the floating frame of reference is commonly applied. In Chapter 4, the enhanced Craig-Bampton method, as proposed in Chapter 3, is embedded in the floating frame of reference. We consider here structures modeled with von-Karman beam elements. Interface reduction methods are in this context unnecessary since the adjacent bodies are connected through a single node. The proposed reduction method constitutes a natural and effective extension of the classical linear modal reduction in the floating frame.

For more complex geometries, like wind turbine blades, extremely simplified beam models can not capture the complexity of the real three-dimensional structure, and therefore the dynamic behavior might not be accurately modeled. In Chapter 5, we present an enhanced Rubin substructuring method for three-dimensional nonlinear multibody systems. The standard Rubin reduction basis is augmented with the modal derivatives of both the free-interface vibration modes and the attachment modes to include bending-stretching coupling effects triggered by the nonlinear vibrations. When compared to the enhanced Craig-Bampton method proposed in Chapter 4, the enhanced Rubin method better reproduces the geometrical nonlinearities occurring at the interface, and, as a consequence, higher accuracy can be achieved.

In Chapter 6, the overall conclusions are drawn and recommendations for further study are provided.

SAMENVATTING

Dynamische analyse van grote eindige elementen modellen is een wijdverbreide methode onder werktuigbouwkundigen om het dynamisch gedrag van complexe structuren te simuleren. De steeds stijgende noodzaak voor nauwkeurige en gedetailleerde simulatie van complexe structuren dwingt werktuigbouwkundigen tot het vinden van een balans tussen twee eisen: lage rekentijd en hoge nauwkeurigheid. Het is extreem lastig om aan deze eisen te voldoen wanneer de structurele dynamica geometrisch niet-lineair is. Zodra geometrische niet-lineairiteiten worden geïntroduceerd worden de interne krachtvector en de Jacobiaan afhankelijk van de configuratie, en de bijbehorende updates zijn rekenkundig duur. In deze thesis worden niet-lineaire reductietechnieken gepresenteerd, die streven naar een gedetailleerde analyse van systemen met meerdere componenten met gereduceerde rekenkosten, zonder de nauwkeurigheid te veel te degraderen. Speciale aandacht wordt geschonken aan de dynamica van flexibele meerderelichaamsystemen.

Voor structuren met meerdere componenten en vele vrijheidsgraden op de raakvlakken kunnen standaard dynamische substructuur-technieken worden gecombineerd met interface reductietechnieken om compacte gereduceerde modellen te verkrijgen. In hoofdstuk 2 worden een aantal interface reductietechnieken voor de bekende Craig-Bampton substructuurmethode samengevat. Deze technieken worden beoordeeld en vergeleken op het gebied van rekentijd en nauwkeurigheid. Als een algemenere methode wordt een interface reductietechniek gegeven met meerdere niveaus, waarbij een tweede Craig-Bampton reductie wordt uitgevoerd wanneer de subsystemen zijn geassembleerd in gelokaliseerde subsets. Deze interface reductietechniek met meerdere niveaus geeft een nauwkeurige representatie van het volledige lineaire model, met een significant lagere rekentijd.

In hoofdstuk 3 breiden we de Craig-Bampton methode uit naar geometrisch nietlineaire problemen door de interface trilvormen op systeemniveau en de interne trilvormen op het niveau van iedere substructuur uit te breiden met hun bijbehorende afgeleiden. De modale afgeleiden kunnen de koppelingseffecten tussen buiging en uitrekking beschrijven, die geometrisch niet-lineaire structuren vertonen. Zodra het reductiemodel is opgesteld met behulp van Galerkin projectie, is de volgende uitdaging het berekenen van de gereduceerde niet-lineaire interne krachtenvector en de tangentmatrices gedurende de tijdsintegratie. Het evalueren van deze objecten schaalt met het formaat van het volledige model, en moet meerdere keren herhaald worden in iedere tijdstap van de tijdsintegratie, en kost zodoende veel rekentijd. Om dit probleem te adresseren, drukken we gereduceerde niet-lineaire vectoren en matrices direct uit als een polynoomfunctie van de modale coördinaten, gebruikmakend van hogere-orde tensoren op substructuurniveu met een veel kleiner formaat. Deze verbeterde Craig-Bampton methode biedt flexibiliteit voor het construeren van een reduceerde basis, omdat modaalafgeleiden alleen berekend hoeven te worden voor die substructuren die daadwerkelijk geometrisch

niet-lineair gedrag vertonen, en omdat de methode geen voorkennis vereist van het niet-lineaire gedrag van de volledige structuur.

In flexibele meerderelichaamssystemen ondergaat ieder lichaam zowel starrelichaamsbewegingen en flexibel gedrag. Om het dynamisch gedrag van iedere component accuraat te beschrijven, wordt gewoonlijk een zwevend referentiekader toegepast. In hoofdstuk 4 passen we het verbeterde Craig-Bampton model, zoals geïntroduceerd in hoofdstuk 3, toe in een zwevend referentiekader. Hier beschouwen we structuren gemodelleerd met von Karman balkelementen. Interface reductietechnieken zijn in deze context onnodig, omdat aangrenzende elementen verbonden zijn met een enkel knooppunt. De voorgestelde reductietechniek bestaat uit een effectieve, natuurlijk volgende, extensie van het klassieke lineaire reductietechnieken in een zwevend referentiekader.

Voor complexere structuren, zoals rotorbladen van windturbines, kunnen de extreem versimpelde balkmodellen de complexiteit van de echte driedimensionale structuur niet omschrijven, en komt de nauwkeurigheid van de dynamische analyse dus in het geding. In hoofdstuk 5 presenteren we een verbeterde Rubin substructuurtechniek voor driedimensionale niet-lineaire systemen met meerdere lichamen. De standaard Rubin reductiebasis wordt uitgebreid met de modaalafgeleiden van zowel de vrije-interface vibratie vormen als de hechttrilvormen, om zo de effecten van koppeling tussen buiging en uitrekking, die wordt veroorzaakt door niet-lineaire vibraties, te introduceren. In vergelijking met de verbeterde Craig-Bampton methode uit hoofdstuk 4 reproduceert de verbeterde Rubin methode de geometrische niet-lineariteiten op de interfaces beter, en, als gevolg wordt er een hogere nauwkeurigheid bereikt.

In hoofdstuk 6 worden algemene conclusies getrokken, en worden aanbevelingen voor vervolgstudies gegeven.

CONTENTS

NOMENCLATURE

ABBREVIATIONS

AMs	attachment modes
CB	Craig-Bampton
CB-ROM	reduced-order model featuring Craig-Bampton substructuring method
CFR	corotational frame of reference
CMs	constraint modes
CMS	component mode synthesis
DoFs	degrees of freedom
ECB	enhanced Craig-Bampton
ECSW	energy conserving sampling and weighting
EoMs	equations of motion
FE	finite element
FFR	floating frame of reference
FMBS	flexible multibody system
FVMs	free-interface vibration modes
GRE	global relative errors
HFM	high fidelity model
ILCMs	interface-level constraint modes
ILIVMs	interface-level internal vibration modes
IVMs	internal vibration modes
LCC	local-level characteristic constraint
LL-ROM	reduced-order model featuring local-level interface reduction
MDs	modal derivatives
MIVMs	merged internal vibration modes
ML-ROM	reduced-order model featuring multilevel interface reduction
MMI	maximum modal interaction
MOR	model order reduction
POD	proper orthogonal decomposition
RMS error	root mean square error
ROB	reduced-order basis
ROM	reduced-order model
SCC	system-level characteristic constraint
SL-ROM	reduced-order model featuring system-level interface reduction
SVD	singular value decomposition
VMs	vibration modes

SYMBOLS

Meanings of global symbols, unless noted otherwise in the context:

SCALARS

$\mathcal{C}$	weight factors
E	Young modulus
I	moment of inertia
t	time
t_h	thickness
$\mathcal{T}$	kinetic energy
$\mathcal{U}$	strain energy
$\mathcal{S}$	speed up factor
ρ	density
θ	rotation angle
ν	Poisson's ratio

VECTORS

$\mathbf{f}$	nonlinear internal force vector
$\mathbf{g}$	external load vector
$\mathbf{p}$	connecting load vector
$\mathbf{q}$	nodal DoFs vector o the finite element model
$\mathbf{Q}_v$	quadratic velocity vector
$\mathbf{r}$	global position vector
$\mathbf{R}$	position vector of the origin of the floating frame
$\mathbf{Re}$	residual vector
$\boldsymbol{\lambda}$	vector of Lagrange multipliers
$\boldsymbol{\phi}$	vector of a single vibration mode
$\boldsymbol{\theta}$	vector of Euler parameters
$\boldsymbol{\vartheta}$	vector of a single modal derivative
$\boldsymbol{\eta}$	modal DoFs vector of linear vibration modes

MATRICES

$\mathbf{A}$	transformation matrix
$\mathbf{B}$	Boolean matrix
$\mathbf{I}$	identity matrix
$\mathbf{K}$	stiffness matrix
$\mathbf{M}$	mass matrix
$\mathbf{N}$	matrix of shape functions for finite element model
$\mathbf{X}$	matrix of classic CB/Rubin reduction basis
$\mathbf{V}$	matrix of enhanced CB/Rubin reduction basis with modal derivatives
$\boldsymbol{\Phi}$	matrix of vibration modes
$\boldsymbol{\Psi}$	matrix of constraint modes or attachment modes
$\boldsymbol{\Theta}$	matrix of modal derivatives

1

INTRODUCTION

1.1. MOTIVATION

For ages, mechanical engineers have been devoted to analyzing the dynamic behavior of structures (airplanes, wind turbines, vehicles, etc.). The analysis involves predicting displacements, deformations, and stresses of the structure at hand over a time span, under a given dynamic load. Reliable dynamic analysis tools are therefore of primary importance during the design process. For example, the Tacoma Narrows Bridge collapsed in 1940 under 64km/h wind conditions (Billah & Scanlan, 1991), after the bridge had come into service for only five months. The collapse was due to a design that did not thoroughly consider dynamic instability caused by the coupling between structural deformation and wind load. As a consequence, this wind-induced collapse boosted the research field of aerodynamic analysis (a branch of dynamic analysis).

For simple structures subjected to simple loads, the dynamic analysis can be conducted analytically. For more complex structures and more involved loading conditions, we need to rely on more advanced computational methods. In particular, the introduction of the finite element (FE) method (Clough, 1960) around 1960 marked a critical milestone in the history of computational dynamic analysis. The basic idea of FE modeling is to divide a complex domain into a finite number of smaller and simpler units, called elements, and thus generate a discretized, finite dimension model which can be analyzed by computer. As such, the FE method offers an approximate but accurate solution for the structural behaviors, provided that the discretization is fine enough. Today, it is a routine task to build large FE models of structures featuring complex geometry, material distribution and applied loads. For illustration, a simplified FE model of a 61.5m blade of the NREL 5MW reference wind turbine, which is originally designed by Sandia National Laboratories (Resor, 2013), is depicted in Fig. 1.1.

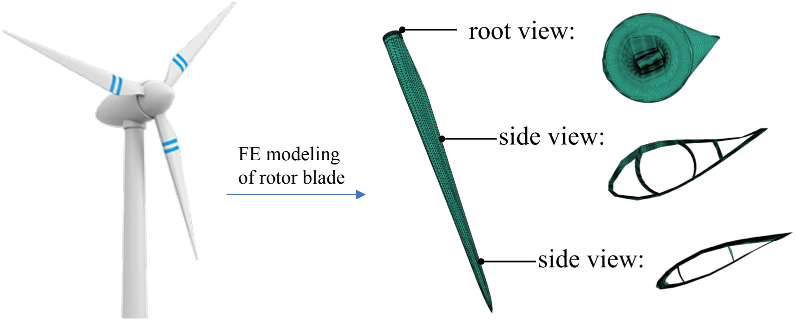

Figure 1.1: FE modelling of a 61.5m blade of the NREL 5MW wind turbine (Resor, 2013).

Unfortunately, FE models often feature thousands or even millions of degrees of freedom (DoFs). This makes the computation of the dynamic response infeasible, due to the time and memory resources involved. If different designs and load cases need to be performed, the dynamic assessment of the system cannot be completed in reasonable time. In the context of wind turbines, a considerable number of loading conditions is prescribed by the design standard International Electro-technical Commission (IEC) 61400-1 wind turbines (TC88-MT, 2005), resulting in a minimum acceptable number of simulations in the order of 1880 (Hansen *et al.*, 2015). This number grows rapidly when one or more of the parameters associated with the site environmental conditions lies outside the range of the IEC reference conditions and may quickly result in up to 3,200,000 simulations (Graf *et al.*, 2016). Therefore, the large computational costs become a bottleneck during the design process.

This problem is even more exacerbated in the case of nonlinear analysis. Nonlinearities arrive in many aspects of the structural behavior. Among others, an essential type of nonlinearity is the geometrical nonlinearity (the main focus of this work), which arises from nonlinear strain-displacement relations due to non-infinitesimal displacements and rotations. This effect is ubiquitous in thin-walled structures in automotive, biomedical, and aerospace applications. Nonlinear models typically result in computational requirements which are orders of magnitude larger than their linear counterparts. For this reason, efficient techniques - known as Model Order Reduction (MOR) - need to be developed to enable accurate dynamic analysis at an affordable computational cost.

1.2. MODEL-ORDER REDUCTION

MOR techniques aim to establish an approximation of the original model with much smaller size, i.e., a reduced-order model (ROM), to simulate the behavior of large-scale dynamical systems. MOR techniques can be divided into two branches: *the model-based reduction techniques* and *the data-based reduction methods*. The detailed review of the model-based reduction techniques has been given in (Besselink *et al.*, 2013).

Model-based reduction techniques are well developed for linear systems. The basic idea is to project the high fidelity model onto a much smaller subspace. The challenging point is how to construct an efficient reduction basis and then project the original model onto this low-dimension subspace. As reviewed in (Besselink *et al.*, 2013), the model-based reduction techniques for the linear system can be divided into three categories: 1. Krylov subspace based MOR (Pillage & Rohrer, 1990); 2. Balanced truncation based MOR (Mullis & Roberts, 1976); 3. Mode displacement methods (Rayleigh, 1945). While the first two MOR techniques are more useful in the fields of mathematics and system control, respectively, the third MOR method is commonly applied for dynamic structural analysis. The modal truncation based MOR technique uses a selected set of vibration modes, obtained from eigenvalue analysis, to establish the low-dimensional subspace. To compensate for the omitted vibration modes, the mode acceleration (Cornwell *et al.*, 1983) and modal truncation augmentation (Dickens *et al.*, 1997) have been proposed as static correction methods for the classic modal truncation.

The data-based reduction methods, on the other hand, are commonly applied to nonlinear systems. One well-established approach is Proper Orthogonal Decomposition (POD) (Berkooz *et al.*, 1993). To construct the reduction basis, we need to extract representative data, i.e. snapshots, from the original model at first, and then calculate the principal components using the singular value decomposition (SVD) (Golub & Reinsch, 1970). Therefore, the data-based reduction methods require data from the original model, and consequently, may be computationally expensive if the required data from a high fidelity model needs to be frequently updated.

Nowadays, an active research topic is to extend the linear modal truncation method to the nonlinear regime. *Modal derivatives* are one of the most efficient approaches to enrich the linear modal basis and to represent the effects of nonlinearity. The definition of modal derivatives was first proposed in 1985 (Idelsohn & Cardona, 1985*a*) and then was simplified by Slaats (Slaats *et al.*, 1995). The modal derivatives are calculated by differentiating the nonlinear static problems with respect to the modal amplitudes when the structures are slightly perturbed from the equilibrium position along the direction of vibration modes. Recently, the modal derivatives based MOR method has been widely applied in the nonlinear dynamic analysis (Weeger *et al.*, 2016, Jain *et al.*, 2017, Rutzmoser *et al.*, 2017).

At the early stage, researchers applied MOR techniques to establish a ROM for the entire system at once, featuring only relatively small to moderate displacements and rotations. The classic MOR techniques can be further extended to the following cases:

- For large industrial applications, such as car bodies and multi-bay panels of airframe structures, engineers may want to divide the structure into several substructures, usually corresponding to parts independently designed and analyzed. This procedure is often referred to as *substructured systems*.

- When the entire structure can be divided into several rigid or flexible bodies, where each body may undergo large rigid translations or rotations, for example, wind turbine blades, the analysis of such models is usually referred to *flexible multibody system dynamics*.

In this dissertation, we extend the application of modal-derivatives based nonlinear MOR method to both *substructured systems* and *flexible multibody system*. The following two sections give a brief introduction to the MOR aspects related to substructured and flexible multibody systems.

1.3. DYNAMIC SUBSTRUCTURING

Dynamic substructuring is an efficient engineer tool to simulate the dynamics of multi-component systems. When the dynamic analysis of a large and complicated structure is almost prohibitive, it is easier to decompose the entire structure into smaller and simpler *substructures* (or subsystems). The dynamic behavior of each substructure is much easier to investigate. Using parallel computation, the evaluation of each subsystem can be performed in parallel with much lower cost. Thereafter all substructures are assembled to obtain the dynamic model of the total system.

Dynamic substructuring, also called the component mode synthesis technique, was first proposed by Hurty (Hurty, 1960, 1965). Craig and Bampton then extended this idea as a fixed-interface method, by extending the constraint modes with a truncated subset of the internal vibration modes. These modes are determined by fixing each individual substructure at its interfaces (Bampton & Craig, 1968). Later, Rubin (Rubin, 1975) and McNeal (MacNeal, 1971) proposed a free-interface method, where the interfaces of each subsystem are set free when calculating the vibration modes. A more recent component mode synthesis technique, called Dual Craig-Bampton method (Rixen, 2004), was inspired by both Craig-Bampton method and the Rubin method and explicitly set the interface force vector as part of the degrees of freedom.

Compared to the dynamic analysis of the entire system at once, evaluating the system's dynamic properties in a component-wise fashion (i.e., substructuring system) features the following advantages (Voormeeren, 2012):

- *Computational size reduction.* By analyzing each subsystem with a much smaller size, we are able to investigate the structural behavior of complex systems, which are too large to be analyzed as an entire system.
- *Computational time savings.* We can investigate the reduced order model of each substructure in parallel before all the subsystems are assembled.
- *Local modification.* During the design process, the relevant subcomponents can be modified and reanalyzed at a local level, whereas the entire system is then investigated at a relatively low additional cost.
- *Flexible distribution of subsystem size.* Different levels of mesh density (i.e. the local fineness of the FE model) can be flexibly allocated to the different subsystems, depend on the customer demand.

Although the substructuring techniques are efficient and commonly used in the dynamic analysis, the computational efficiency may still be limited by the number of interface DoFs. This particularly holds true when the subsystems are connected through relatively large and complex interfaces. To overcome this problem, mechanical engineers commonly apply a technique named *interface reduction*. Interface reduction is often necessary for FE models featuring shell and solid elements, where the interface usually consists of a nodal-based line or surface, see Fig. 1.2 as an example.

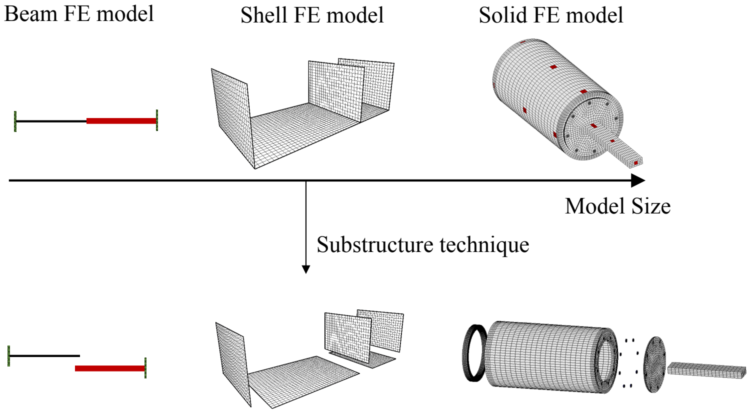

Figure 1.2: Illustration of substructuring for beam (left), shell (middle) and solid (right) FE models.

Based on the different demands for computational savings and overall accuracy, engineers can use different interface reduction methods. Three of the most commonly used interface reduction methods are summarized here:

- *System-level interface reduction* (Tran, 2001). It is applied after all subsystems have been assembled. An eigenvalue analysis is performed for the assembled system whereas all DoFs are statically condensed to the interface DoFs, and a further modal truncation is done to reduce the interface DoFs. Moreover, the system-level interface modes have to be recomputed for all interface DoFs even if a local modification occurs at one substructure during the design process. This technique can properly model the interaction between all substructures. The eigenvalue analysis for all interface DoFs, however, can still be relatively expensive for a large-scale system featuring many interface DoFs.

- *Local-level interface reduction* (Hong *et al.*, 2013). It is applied before each subsystem is assembled, i.e., an eigenvalue analysis is performed for each subsystem when the DoFs of the individual subsystem are statically condensed to its corresponding interface DoFs. The local-level interface reduction reduces the computational effort by localizing the eigenvalue problem at the interface of each substructure with a much smaller size. However, this method totally neglects the coupling between different substructures. Moreover, the accuracy will be compromised if the independent reduction bases for the individual subsystem is inadequate.

- *Undeformed interface reduction* (Lindberg *et al.*, 2013). An undeformed interface reduction can also be applied by assuming that the interface undergoes only rigid body motions. This method, however, is suitable only when rigid joint connections are imposed between adjacent substructures.

While the standard substructuring techniques can dramatically reduce the internal DoFs of the individual subsystems, the mentioned interface reduction methods can further reduce the interface DoFs of the assembled systems. Therefore, the standard substructuring dynamics, combined with interface reduction, can be utilized to obtain a truly compact model.

1.4. FLEXIBLE MULTIBODY SYSTEM

A flexible multibody system (FMBS) is an integration of several flexible bodies, where each of them may undergo large translations and rotations, as well as elastic behavior. For flexible multibody dynamic analysis, it is crucial to select the appropriate reference frame (Wasfy & Noor, 2003) to describe the motion of each body. Three types of frames to describe the overall motion of the FMBS are summarized here:

- *Inertial Frame*. The inertial frame is utilized as a global reference to describe the structures undergoing large rotations and large deformations(Bathe *et al.*, 1975). By doing so, we only build one frame for all the rigid and flexible bodies, without distinguishing between the rigid body motion and elastic behavior.

- *Floating Frame*. In the floating frame technique, a reference frame (Shabana, 2005) is defined for each flexible body separately. The reference frame follows the overall rigid body motion of the corresponding body. Therefore, the relative displacements with respect to such frame are measured, excluding the rigid body motion of the reference frame.

- *Corotational Frame*. The corotational frame (Belytschko & Hsieh, 1973) is similar to the floating frame. Instead of introducing one frame for each body, a frame is defined for each finite element. Compared to floating frame, the corotational frame is suitable for systems undergoing large high-speed rigid body motions. However, the computational cost of the corotational frame is far more expensive than its counterpart for the floating frame approach.

As compared to the corotational frame approach, a major advantage of the floating frame concept is the option to adopt model order reduction techniques inherited from the substructuring realm. This is of great significance when geometric nonlinearities have to be considered. Therefore, the floating frame will be adopted in this thesis, for the nonlinear MOR of FMBS.

1.5. THESIS AIM AND OUTLINE

The principal aim of this dissertation is to answer the following research question:

“How can the computational cost for the dynamic analysis of a complex structure, which features both nonlinear effects and large rigid body motions, be reduced efficiently?”

Following the spirit of component-wise analysis, this major objective can be split into three key questions. By doing so, we can approach the final target step-by-step. The first challenge, before we enter the nonlinear domain, can be stated as:

“What is the proper substructuring and interface reduction technique to reduce the computational cost when geometric nonlinear effects and rigid body motions are not yet included?”

The interface reduction techniques for the linear Craig-Bampton substructuring are commonly used by engineers working in structural dynamics issues, **Chapter 2** gives a good review of interface reduction techniques. This chapter is essential for choosing the proper interface reduction technique when we consider the geometric nonlinearities, especially when the modal derivatives, which grow quadratically with respect to the number of interface modes, are applied.

When the proper substructuring methods and interface reduction in Chapter 2 are applied to a linear structure, we are ready to address the second subproblem:

“How can we extend the well-established linear substructuring methods and interface reduction techniques to the geometric nonlinear regime?”

To solve this problem, in **Chapter 3**, a model order reduction method is proposed for the dynamic analysis of complex systems featuring multiple components and geometrical nonlinearities. The proposed approach is a nonlinear extension to the classical Craig-Bampton model with system-level interface reduction.

A major characteristic of FMBS is that the subsystems may undergo large rigid body motions. Therefore, when the structural dynamic analysis of FMBS is concerned, the following problem has to be addressed:

"How can we further augment the nonlinear MOR techniques for the flexible multibody system, when large rigid body motions have to be considered?"

To answer this question, in **Chapter 4**, the modal derivatives enhanced Craig-Bampton method is proposed for the dynamic analysis of flexible multibody systems featuring large overall motions and geometric nonlinear behavior. The analysis in Chapter 4 is limited to two-dimensional beam structures using the nodal-fixed floating frame. This approach is further extended to three-dimensional shell structures in **Chapter 5** using a mean-axis floating frame. The enhanced Rubin substructuring method is proposed in Chapter 5.

The conclusions of this dissertation are finally presented in **Chapter 6**. Recommendations for future work are also provided at the end of this dissertation.

The structure of this dissertation is visualized in Fig. 1.3. Based on the "yes or no" questions in the flow chart, the visual outline quickly locates the relevant chapters for different readers.

This dissertation is a collection of published or submitted papers. The main chapters are all self-contained. All abbreviations and global variables are listed in the Nomenclature, while all other local variables are defined in each chapter independently. Inevitably, there is overlap between chapters. To offer a clear view, the overlap is visualized in Fig. 1.3, by connecting the key techniques in the highlighted blocks with their relevant chapters.

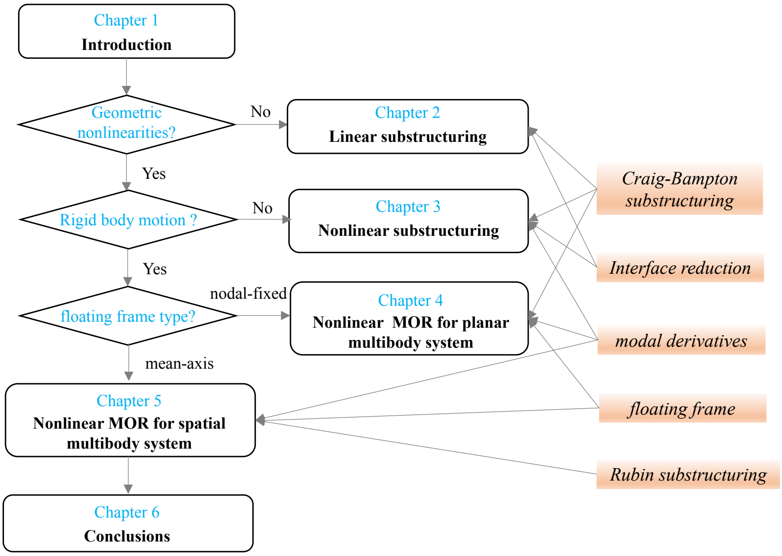

Figure 1.3: Visual outline of this dissertation in a flowchart.

2

INTERFACE REDUCTION WITH LINEAR CRAIG-BAMPTON SUBSTRUCTURING FOR COMPONENT MODE SYNTHESIS

Component mode synthesis is commonly used to simulate the structural behavior of complex systems. Among other component mode synthesis techniques, the Craig-Bampton method stands out for its popularity. However, for finely meshed systems featuring many components, the size of the resulting assembled system is dominated by the interface degrees of freedom. The system-level interface reduction technique aims at reducing the size of the assembled reduced model by extracting few dominant interface modes. If the size of the interface degrees of freedom is large, the resulting problem is almost as computationally expensive as the one associated to the full model. Conversely, the local-level interface reduction technique reduces the interface of each substructure before *assembly. In this case, the computational effort associated to the local eigenvalue problem is moderate, but issues arise when enforcing compatibility between interfaces. In this chapter, we assess the different interface reduction techniques on large size realistic examples.*

This chapter is based on the paper "Wu, L., Tiso, P., van Keulen, F., Interface Reduction with Multilevel Craig-Bampton Substructuring for Component Mode Synthesis. AIAA journal. Vol. 56, No. 5 (2018), pp. 2030-2044."

2.1. INTRODUCTION

A system consisting of multiple components can be modeled efficiently with proper component mode synthesis (CMS) techniques. In CMS, the dynamics of a substructure is described by a truncated set of vibration modes of each subsystem, combined with a set of static modes accounting for the coupling with neighboring subcomponents (Klerk *et al.*, 2008). The classic Craig-Bampton (CB) method was first proposed in (Hurty, 1960, 1965) and then simplified in (Bampton & Craig, 1968, Craig, 2000). It combines the concepts of component-wise analysis and modal reduction techniques, and is one of the well known CMS technologies. In the CB method, the coupling at an interface is realized by using a set of constraint modes (CMs) and retaining all degrees of freedom (DoFs) at the interface. However, the size of the CB basis may be dominated by the CMs DoFs if the finite element (FE) mesh is sufficiently fine. Obviously, this limits the achievable reduction and hence decreases the efficiency of the substructuring approach. In this context, a proper interface reduction technique is a must to bring the reduction basis to a manageable size.

In 1977, Craig and Chang (Craig Jr & Chang, 1977) proposed three interface reduction methods by applying either Guyan, Ritz, or modal reduction at the interface. Castanier (Castanier *et al.*, 2001) rediscovered the modal reduction techniques by using a secondary eigenvalue analysis to the interface partition of the CB system and proposing the commonly used system-level characteristic constraint (SCC) modes. This technique is applied after the system-level matrices are constructed. Consequently, it does not offer flexibility for design runs as the SCC modes must be recomputed for all the interface DoFs even if a design change occurs at a single substructure. In order to bring the interface reduction to substructure level, Hong (Hong *et al.*, 2013) recently formulated the interface reduction by generating the local-level characteristic constraint (LCC) modes from mass and stiffness matrices associated to the interface DoFs before assembly. The local-level interface reduction simplified the eigenvalue problem by neglecting the coupling between neighboring subcomponents. For specific systems where the stiffness of adjacent substructures is significantly different, an undeformed interface reduction (Lindberg *et al.*, 2013) can also be applied by assuming that the interface undergoes only rigid body motions.

Most of the interface reduction techniques mentioned here are developed for the CB method, owing to its wide application in CMS problems. Tran (Tran, 2001, 2009) indicated that the interface reduction techniques can be implemented with the CB method, as well as various free or hybrid interface mode based substructuring techniques, like the CMS method proposed by MacNeal (MacNeal, 1971) and later by Rubin (Rubin, 1975). The interface reduction idea can also be applied to the dual CB method proposed by Rixen (Rixen, 2002, 2004). For large-scale structures with multiple interfaces, Aoyama (Aoyama & Yagawa, 2001) introduced an optional reduction method by analyzing the eigenmodes from adjacent subcomponents to reduce the computational cost. Interface reduction has also been efficiently extended to the CB approach for acoustic-structure coupled, fluid-filled piping systems (Herrmann *et al.*, 2010). Balmès applied the generalized constraint modes, which are linear combinations of the constraint modes, to provide a compatible model with an optimal selection of the generalized constraint modes (Balmès, 1996). This idea can be further extended to system design process as shown in (des Roches *et al.*, 2011). Bennighof (Bennighof & Lehoucq, 2004) proposed the automatic multilevel substructuring (AMLS) method, which is a multilevel extension of the CMS substructuring based on the sparsity of the system matrices. The AMLS method was widely applied in the field of applied mathematics, by recursively applying the Gaussian block elimination and modal condensation of the system matrices (Lee *et al.*, 2011, Kim, 2006, Zhao & Yu, 2015). Besides all the reduction methods using "interface modes", an alternative method called double modal synthesis (Jezequel & Seito, 1994, Besset & Jézéquel, 2007) can also be applied to compensate the modal truncation. The double modal synthesis is further used to analyze brake squeal in (Monteil *et al.*, 2016). The extension of the current interface reduction techniques to geometrical nonlinear domain remains a relevant topic. Recently, Sinou (Sinou & Besset, 2017) extended the double modal synthesis to study the self-excited vibrations and time analysis of brake squeal in a nonlinear region. Kuether (Kuether *et al.*, 2016, 2017) recently proposed a non-intrusive model order reduction technique by applying the system-level interface reduction. The authors' current efforts are directed to extend classic CB methods with both system-level interface reduction and modal derivatives (first proposed in (Idelsohn & Cardona, 1985*a*)), for problems characterized by distributed geometric nonlinearities.

For linear systems, the system-level (Castanier *et al.*, 2001) and local-level (Hong *et al.*, 2013) interface reduction methods are two of the most commonly used techniques for the CMS problem due to their easy implementation and applicability. The system-level interface reduction can be computationally expensive when the number of interface DoFs is large. On the other hand, the local-level counterpart reduces the computational effort by localizing the interface reduction at each substructure. However, the interface compatibility will be compromised if the independent reduction basis for each subsystem is inadequate. In this chapter, we discuss two variants of the multilevel interface reduction method. We assemble the substructures into localized subsets. A secondary CB substructuring procedure is then applied in each subset. In the first variant, a secondary CB reduction is applied to the interface DoFs of the subset only, while, in the second variant, the CB reduction is performed on all the DoFs of the subset. As opposed to the local-level method, the multilevel idea does not simplify the interface coupling. Therefore, it is able to get accurate approximation compared to system-level interface reduction methods, while enabling computational savings by setting smaller subsets and the possibility for parallelization for interface reduction.

This chapter is organized as follows: In Section 2.2, the classic CB method is briefly introduced. The subcomponents are assembled in a primal manner, i.e., a unique set of interface DoFs is defined. In Section 2.3, the existing system-level and local-level interface reduction techniques proposed in (Castanier *et al.*, 2001, Hong *et al.*, 2013) are summarized and evaluated. Section 2.4 discusses two multilevel interface reduction variants discussed above. A computational complexity analysis is presented in Section 2.5, and the advantages of the multilevel interface reduction methods are discussed, compared to the SCC and LCC modes based methods. In Section 2.6, representative numerical examples are investigated. Discussions and conclusions are provided in Section 2.7.

2.2. CRAIG-BAMPTON METHOD AND PRIMAL ASSEMBLY

In this section, we first briefly outline the CB method (Bampton & Craig, 1968) for subcomponents. Then, the subcomponents are assembled in a primal manner (Voormeeren, 2012) by choosing a unique set of interface DoFs. For a linear undamped system composed of H subsystems, the equations of motion (EoMs) for the subcomponents can be written as

$$\mathbf{M}_{(s)}\ddot{\mathbf{q}}_{(s)}\{t\} + \mathbf{K}_{(s)}\mathbf{q}_{(s)}\{t\} = \mathbf{g}_{(s)}\{t\} + \mathbf{p}_{(s)}\{t\}, \quad s = 1,\dots,H, \tag{2.1}$$

where $\mathbf{M}_{(s)}$ and $\mathbf{K}_{(s)}$ are the constant mass and stiffness matrices, $\mathbf{g}_{(s)}$, $\mathbf{p}_{(s)}$ and $\mathbf{q}_{(s)}$ are the external load vector, the connecting load vector imposed by neighboring subsystems and the generalized nodal DoFs vector of the s^{th} decoupled subcomponent, respectively. The argument of functional dependency on time is enclosed in curly brackets.The number of substructures is indicated by H. The EoMs of the global system with substructures can be expressed in a block-diagonal format as

$$\mathbf{M}_{\mathcal{G}}\ddot{\mathbf{q}}_{\mathcal{G}} + \mathbf{K}_{\mathcal{G}}\mathbf{q}_{\mathcal{G}} = \mathbf{g}_{\mathcal{G}} + \mathbf{p}_{\mathcal{G}}, \tag{2.2}$$

with

$$\mathbf{M}_{\mathcal{G}} = \begin{bmatrix} \mathbf{M}_{(1)} & & \\ & \ddots & \\ & & \mathbf{M}_{(H)} \end{bmatrix} \triangleq \operatorname{diag}(\mathbf{M}_{(1)},\dots,\mathbf{M}_{(H)}), \quad \mathbf{q}_{\mathcal{G}} = \begin{bmatrix} \mathbf{q}_{(1)} \\ \vdots \\ \mathbf{q}_{(H)} \end{bmatrix} \triangleq \operatorname{col}(\mathbf{q}_{(1)},\dots,\mathbf{q}_{(H)}),$$

$$\mathbf{K}_{\mathcal{G}} = \operatorname{diag}(\mathbf{K}_{(1)},\dots,\mathbf{K}_{(H)}), \quad \mathbf{g}_{\mathcal{G}} = \operatorname{col}(\mathbf{g}_{(1)},\dots,\mathbf{g}_{(H)}), \quad \mathbf{p}_{\mathcal{G}} = \operatorname{col}(\mathbf{p}_{(1)},\dots,\mathbf{p}_{(H)}),$$

where the subscript $\mathcal{G}$ indicates that the vectors and matrices are stacked for the entire system. For the sake of simplicity, the time dependence has been omitted.

2.2.1. CRAIG-BAMPTON METHOD

The CB method is a powerful and popular substructuring technique that allows for independent reduction of subdomains, and it is therefore well-suited when subcomponents are developed independently by different parties, and eventually assembled. Let us focus on the s^{th} subsystem. The linear EoMs can be partitioned into internal DoFs $\mathbf{q}^I_{(s)} \in \mathbb{R}^{n^I_{(s)}}$ and boundary DoFs $\mathbf{q}^B_{(s)} \in \mathbb{R}^{n^B_{(s)}}$ with $n^I_{(s)} + n^B_{(s)} = n_{(s)}$, which gives

$$\mathbf{M}_{(s)}\ddot{\mathbf{q}}_{(s)} + \mathbf{K}_{(s)}\mathbf{q}_{(s)} = \mathbf{p}_{(s)} \Leftrightarrow \begin{bmatrix} \mathbf{M}^{BB}_{(s)} & \mathbf{M}^{BI}_{(s)} \\ \mathbf{M}^{IB}_{(s)} & \mathbf{M}^{II}_{(s)} \end{bmatrix} \begin{bmatrix} \ddot{\mathbf{q}}^B_{(s)} \\ \ddot{\mathbf{q}}^I_{(s)} \end{bmatrix} + \begin{bmatrix} \mathbf{K}^{BB}_{(s)} & \mathbf{K}^{BI}_{(s)} \\ \mathbf{K}^{IB}_{(s)} & \mathbf{K}^{II}_{(s)} \end{bmatrix} \begin{bmatrix} \mathbf{q}^B_{(s)} \\ \mathbf{q}^I_{(s)} \end{bmatrix} = \begin{bmatrix} \mathbf{p}^B_{(s)} \\ \mathbf{0} \end{bmatrix}, \tag{2.3}$$

where we assume that the external forces $\mathbf{g}_{(s)}$ are $\mathbf{0}$ as we are interested in the free vibration of the system. Typically, the number of boundary DoFs is much smaller than the number of internal DoFs ($n^B_{(s)} \ll n^I_{(s)}$).

The CB transformation is a linear combination of constraint modes (CMs) $\mathbf{\Psi}^{IB}_{(s)}$ and internal vibration modes (IVMs) $\mathbf{\Phi}^{II}_{(s)}$ by stating

$$\mathbf{q}_{(s)} = \begin{bmatrix} \mathbf{q}^B_{(s)} \\ \mathbf{q}^I_{(s)} \end{bmatrix} = \begin{bmatrix} \mathbf{I}^{BB}_{(s)} & \mathbf{0} \\ \mathbf{\Psi}^{IB}_{(s)} & \mathbf{\Phi}^{II}_{(s)} \end{bmatrix} \begin{bmatrix} \mathbf{q}^B_{(s)} \\ \boldsymbol{\eta}^I_{(s)} \end{bmatrix} \triangleq \mathbf{X}_{(s)}\boldsymbol{\Upsilon}_{(s)}, \tag{2.4}$$

where $\boldsymbol{\eta}^{I}_{(s)}$ is the vector of modal coordinates with respect to the IVMs, $\mathbf{X}_{(s)}$ and $\boldsymbol{\gamma}_{(s)}$ are the CB reduction matrix and corresponding generalized coordinate vector of the s^{th} subsystem. The matrix $\mathbf{I}^{BB}_{(s)} \in \mathbb{R}^{n^B_{(s)} \times n^B_{(s)}}$ is an identity matrix.

The IVMs $\boldsymbol{\Phi}^{II}_{(s)} \in \mathbb{R}^{n^I_{(s)} \times m^I_{(s)}}$ can be obtained by solving the internal eigenvalue problem with fixed interface, i.e., $\mathbf{q}^{B}_{(s)} = \mathbf{0}$, as

$$\left(\mathbf{K}^{II}_{(s)} - \omega^2_{j,(s)}\mathbf{M}^{II}_{(s)}\right)\boldsymbol{\phi}^{II}_{j,(s)} = \mathbf{0}, \quad j = 1,\ldots,n^I_{(s)}. \tag{2.5}$$

The IVMs are a truncated set of the eigenmodes, and can be written in a matrix format as $\boldsymbol{\Phi}^{II}_{(s)} = [\boldsymbol{\phi}^{II}_{1,(s)},\ldots,\boldsymbol{\phi}^{II}_{m^I_{(s)},(s)}]$, with $m^I_{(s)} \ll n^I_{(s)}$. The eigenvalues could be rewritten in a diagonal matrix as $\boldsymbol{\omega}^2_{(s)} = \mathrm{diag}[\omega^2_{1,(s)},\ldots,\omega^2_{m^I_{(s)},(s)}]$. Mass normalization is applied with

$$\left(\boldsymbol{\Phi}^{II}_{(s)}\right)^T \mathbf{M}^{II}_{(s)}\boldsymbol{\Phi}^{II}_{(s)} = \mathbf{I}^{II}_{(s)}. \tag{2.6}$$

The CMs $\boldsymbol{\Psi}^{IB}_{(s)} \in \mathbb{R}^{n^I_{(s)} \times n^B_{(s)}}$ are the static responses of the internal DoFs that result from a unit displacement applied at an interface DoF while the other interface DoFs are fixed. Thus, they are computed by solving

$$\boldsymbol{\Psi}^{IB}_{(s)} = -(\mathbf{K}^{II}_{(s)})^{-1}\mathbf{K}^{IB}_{(s)}. \tag{2.7}$$

With (2.4) we generate a projection basis for the s^{th} substructure, where the interface DoFs $\mathbf{q}^{B}_{(s)}$ are retained without reduction. The reduced EoMs for the substructure are obtained via a classic Galerkin projection, and expressed by

$$\underbrace{\begin{bmatrix} \widetilde{\mathbf{M}}^{BB}_{(s)} & \widetilde{\mathbf{M}}^{BI}_{(s)} \\ \widetilde{\mathbf{M}}^{IB}_{(s)} & \mathbf{I}^{II}_{(s)} \end{bmatrix}}_{\widetilde{\mathbf{M}}_{(s)}} \begin{bmatrix} \ddot{\mathbf{q}}^{B}_{(s)} \\ \ddot{\boldsymbol{\eta}}^{I}_{(s)} \end{bmatrix} + \underbrace{\begin{bmatrix} \widetilde{\mathbf{K}}^{BB}_{(s)} & \mathbf{0} \\ \mathbf{0} & \boldsymbol{\omega}^2_{(s)} \end{bmatrix}}_{\widetilde{\mathbf{K}}_{(s)}} \begin{bmatrix} \mathbf{q}^{B}_{(s)} \\ \boldsymbol{\eta}^{I}_{(s)} \end{bmatrix} = \underbrace{\begin{bmatrix} \widetilde{\mathbf{g}}^{B}_{(s)} \\ \widetilde{\mathbf{g}}^{I}_{(s)} \end{bmatrix}}_{\widetilde{\mathbf{g}}_{(s)}} + \begin{bmatrix} \mathbf{p}^{B}_{(s)} \\ \mathbf{0} \end{bmatrix}, \tag{2.8}$$

where

$$\widetilde{\mathbf{K}}^{BB}_{(s)} = \mathbf{K}^{BB}_{(s)} + \mathbf{K}^{BI}_{(s)}\boldsymbol{\Psi}^{IB}_{(s)} \quad \text{and} \quad \widetilde{\mathbf{M}}^{BB}_{(s)} = \mathbf{M}^{BB}_{(s)} + \mathbf{M}^{BI}_{(s)}\boldsymbol{\Psi}^{IB}_{(s)} + (\boldsymbol{\Psi}^{IB}_{(s)})^T\mathbf{M}^{IB}_{(s)} + (\boldsymbol{\Psi}^{IB}_{(s)})^T\mathbf{M}^{II}_{(s)}\boldsymbol{\Psi}^{IB}_{(s)} \tag{2.9}$$

are the interface components of the stiffness and mass matrices, respectively, of the s^{th} substructure after the CB transformation.

To illustrate the concept, we consider here a ⊓-shaped model composed of 4 substructures (S_1 to S_4) connected through 3 interfaces (B_1 to B_3), as shown in Fig. 2.1. The model is fixed at the bottom ($z = 0$). The CMs and IVMs for each substructure can be calculated independently. It should be noticed at this stage that the individual CMs, as shown in Fig. 2.1, reflect a more localized deformation pattern around a specified interface DoF, as the interface discretizations in the ⊓-shaped structure are sufficiently fine.

In the next subsection,we shall briefly summarize the primal assembly of the substructures after the CB reduction.

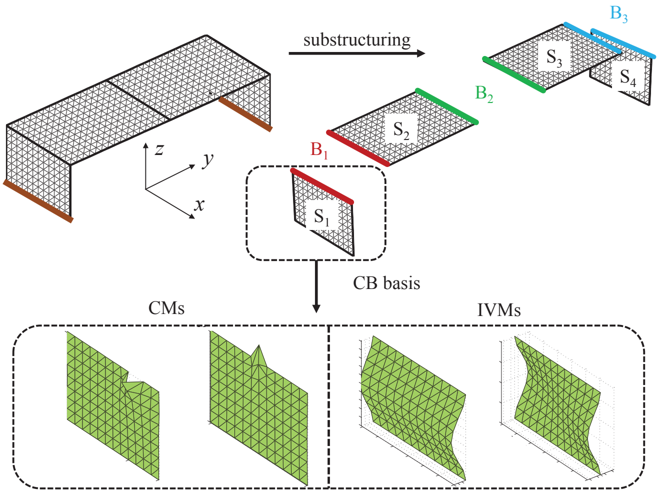

Figure 2.1: Illustration of the CB reduction on a ⊓-shaped FE model composed of 4 substructures and 3 interfaces.

2.2.2. PRIMAL ASSEMBLY OF COMPONENT MODELS

The CB transformations (2.4) for each substructure can be collected for the entire system in a block-diagonal form by stating

$$\mathbf{q}_{\mathcal{G}} = \mathbf{X}_{\mathcal{G}} \boldsymbol{\gamma}_{\mathcal{G}}, \tag{2.10}$$

where $\mathbf{X}_{\mathcal{G}} = \mathrm{diag}(\mathbf{X}_{(1)}, \dots, \mathbf{X}_{(H)})$ is a block-diagonal matrix consisting of all substructure CB reduction matrices, and $\boldsymbol{\gamma}_{\mathcal{G}} = \mathrm{col}(\boldsymbol{\gamma}_{(1)}, \dots, \boldsymbol{\gamma}_{(H)})$ is the assembled set of the generalized coordinates of subsystems for the global system.

By substituting (2.10) in (2.2), the reduced EoMs for the full system are obtained via Galerkin projection

$$\mathbf{X}_{\mathcal{G}}^T \mathbf{M}_{\mathcal{G}} \mathbf{X}_{\mathcal{G}} \ddot{\boldsymbol{\gamma}}_{\mathcal{G}} + \mathbf{X}_{\mathcal{G}}^T \mathbf{K}_{\mathcal{G}} \mathbf{X}_{\mathcal{G}} \boldsymbol{\gamma}_{\mathcal{G}} = \mathbf{X}_{\mathcal{G}}^T \mathbf{g}_{\mathcal{G}} + \mathbf{X}_{\mathcal{G}}^T \mathbf{p}_{\mathcal{G}}. \tag{2.11}$$

At this stage, the interfaces are assembled in a fully compatible way. When all substructures are coupled, the displacement compatibility and force equilibrium at the interface DoFs must be enforced. The compatibility condition states that any pair of matching interface DoFs $\mathbf{q}_{(j)}^B$ and $\mathbf{q}_{(k)}^B$ must have the same displacement, while the force equilibrium requires that the summation of the connection forces should be equal to zero. These conditions are then given in (Klerk *et al.*, 2008) by satisfying

$$\begin{cases} \mathbf{q}_{(j)}^B - \mathbf{q}_{(k)}^B = \mathbf{0} & \Rightarrow \quad \mathbf{B}_{\mathcal{CB}} \boldsymbol{\gamma}_{\mathcal{G}} = \mathbf{0}, \\ \mathbf{p}_{(j)}^B + \mathbf{p}_{(k)}^B = \mathbf{0} & \Rightarrow \quad \mathbf{L}_{\mathcal{CB}}^T \mathbf{X}_{\mathcal{G}}^T \mathbf{p}_{\mathcal{G}} = \mathbf{0}, \end{cases} \tag{2.12}$$

where the compatibility condition is transformed to generalized coordinates $\boldsymbol{\gamma}_{\mathcal{G}}$ by introducing the $\mathbf{B}_{\mathcal{CB}}$ matrix. The matrix $\mathbf{L}_{\mathcal{CB}}$ is the primal assembly operator by localizing the interface DoFs of the substructures in the global set of DoFs $\boldsymbol{\gamma}_{\mathcal{G}}$. The matrices $\mathbf{B}_{\mathcal{CB}}$ and $\mathbf{L}_{\mathcal{CB}}$ are Boolean matrices here.

Classically, the subcomponents can be assembled in a primal manner (Voormeeren, 2012), i.e., a new reduced set of generalized coordinates of the assembled system $\boldsymbol{\xi}_{\mathcal{CB}}$ for the CB model is defined here as

$$\boldsymbol{\xi}_{\mathcal{CB}} = \mathrm{col}\left(\mathbf{q}^{B}_{\mathcal{CB}}, \boldsymbol{\eta}^{I}_{\mathcal{CB}}\right), \quad \text{with} \quad \boldsymbol{\eta}^{I}_{\mathcal{CB}} = \mathrm{col}\left(\boldsymbol{\eta}^{I}_{(1)}, \dots, \boldsymbol{\eta}^{I}_{(H)}\right), \tag{2.13}$$

where $\mathbf{q}^{B}_{\mathcal{CB}} \in \mathbb{R}^{n^{B}_{\mathcal{CB}}}$ consists of the unique choice of all interface DoFs $\mathrm{col}(\mathbf{q}^{B}_{(1)}, \dots, \mathbf{q}^{B}_{(H)})$ and $\boldsymbol{\eta}^{I}_{\mathcal{CB}} \in \mathbb{R}^{m^{I}_{\mathcal{CB}}}$ contains the internal generalized coordinates of all the substructures. For internal vibration modes, it holds that $m^{I}_{\mathcal{CB}} = \sum_{s=1}^{s=H} m^{I}_{(s)}$ since the internal DoFs of each substructure are independent, where $m^{I}_{(s)}$ is the number of internal modal coordinates for the s^{th} substructure. The compatibility condition ensures no relative motion between the boundaries of connected substructures. Mathematically, this is obtained by stating

$$\boldsymbol{\gamma}_{\mathcal{G}} = \mathbf{L}_{\mathcal{CB}} \boldsymbol{\xi}_{\mathcal{CB}}. \tag{2.14}$$

The primal assembly operator $\mathbf{L}_{\mathcal{CB}}$ must span the null space of $\mathbf{B}_{\mathcal{CB}}$ if a fully compatible interface assembly is applied as in (Klerk *et al.*, 2008), i.e.,

$$\mathbf{L}_{\mathcal{CB}} = \mathrm{null}(\mathbf{B}_{\mathcal{CB}}). \tag{2.15}$$

Substitution of (2.14) into (2.11) and (2.12) yields

$$\begin{cases} \mathbf{X}^{T}_{\mathcal{G}} \mathbf{M}_{\mathcal{G}} \mathbf{X}_{\mathcal{G}} \mathbf{L}_{\mathcal{CB}} \ddot{\boldsymbol{\xi}}_{\mathcal{CB}} + \mathbf{X}^{T}_{\mathcal{G}} \mathbf{K}_{\mathcal{G}} \mathbf{X}_{\mathcal{G}} \mathbf{L}_{\mathcal{CB}} \boldsymbol{\xi}_{\mathcal{CB}} = \mathbf{X}^{T}_{\mathcal{G}} \mathbf{g}_{\mathcal{G}} + \mathbf{X}^{T}_{\mathcal{G}} \mathbf{p}_{\mathcal{G}}, \\ \mathbf{B}_{\mathcal{CB}} \mathbf{L}_{\mathcal{CB}} \boldsymbol{\xi}_{\mathcal{CB}} = \mathbf{0}, \\ \mathbf{L}^{T}_{\mathcal{CB}} \mathbf{X}^{T}_{\mathcal{G}} \mathbf{p}_{\mathcal{G}} = \mathbf{0}, \end{cases} \tag{2.16}$$

where the second equation in (2.16) is naturally satisfied, as $\mathbf{L}_{\mathcal{CB}} = \mathrm{null}(\mathbf{B}_{\mathcal{CB}})$. By premultiplication of the remaining equations with $\mathbf{L}^{T}_{\mathcal{CB}}$ and noting that $\mathbf{L}^{T}_{\mathcal{CB}} \mathbf{X}^{T}_{\mathcal{G}} \mathbf{p}_{\mathcal{G}} = \mathbf{0}$, the primal EoMs for the coupled system give

$$\underbrace{\mathbf{L}^{T}_{\mathcal{CB}} \mathbf{X}^{T}_{\mathcal{G}} \mathbf{M}_{\mathcal{G}} \mathbf{X}_{\mathcal{G}} \mathbf{L}_{\mathcal{CB}}}_{\widetilde{\mathbf{M}}_{\mathcal{CB}}} \ddot{\boldsymbol{\xi}}_{\mathcal{CB}} + \underbrace{\mathbf{L}^{T}_{\mathcal{CB}} \mathbf{X}^{T}_{\mathcal{G}} \mathbf{K}_{\mathcal{G}} \mathbf{X}_{\mathcal{G}} \mathbf{L}_{\mathcal{CB}}}_{\widetilde{\mathbf{K}}_{\mathcal{CB}}} \boldsymbol{\xi}_{\mathcal{CB}} = \underbrace{\mathbf{L}^{T}_{\mathcal{CB}} \mathbf{X}^{T}_{\mathcal{G}} \mathbf{g}_{\mathcal{G}}}_{\widetilde{\mathbf{g}}_{\mathcal{CB}}}, \tag{2.17}$$

where the assembled matrices and vectors $\widetilde{\mathbf{M}}_{\mathcal{CB}}$, $\widetilde{\mathbf{K}}_{\mathcal{CB}}$ and $\widetilde{\mathbf{g}}_{\mathcal{CB}}$ can be further partitioned corresponding to the interface coordinates $\mathbf{q}^{B}_{\mathcal{CB}}$ and internal coordinates $\boldsymbol{\eta}^{I}_{\mathcal{CB}}$. The reduced EoMs (2.17) are therefore rewritten in a partitioned style as

$$\begin{bmatrix} \widetilde{\mathbf{M}}^{BB}_{\mathcal{CB}} & \widetilde{\mathbf{M}}^{BI}_{\mathcal{CB}} \\ \widetilde{\mathbf{M}}^{IB}_{\mathcal{CB}} & \mathbf{I}^{II}_{\mathcal{CB}} \end{bmatrix} \begin{bmatrix} \ddot{\mathbf{q}}^{B}_{\mathcal{CB}} \\ \ddot{\boldsymbol{\eta}}^{I}_{\mathcal{CB}} \end{bmatrix} + \begin{bmatrix} \widetilde{\mathbf{K}}^{BB}_{\mathcal{CB}} & \mathbf{0} \\ \mathbf{0} & \boldsymbol{\omega}^{2}_{\mathcal{CB}} \end{bmatrix} \begin{bmatrix} \mathbf{q}^{B}_{\mathcal{CB}} \\ \boldsymbol{\eta}^{I}_{\mathcal{CB}} \end{bmatrix} = \begin{bmatrix} \widetilde{\mathbf{g}}^{B}_{\mathcal{CB}} \\ \widetilde{\mathbf{g}}^{I}_{\mathcal{CB}} \end{bmatrix}, \tag{2.18}$$

where $\boldsymbol{\omega}^{2}_{\mathcal{CB}} = \mathrm{diag}(\boldsymbol{\omega}^{2}_{(1)}, \dots, \boldsymbol{\omega}^{2}_{(H)})$ and $\mathbf{I}^{II}_{\mathcal{CB}} \in \mathbb{R}^{m^{I}_{\mathcal{CB}} \times m^{I}_{\mathcal{CB}}}$ is the identity matrix. The detailed formulation of the partitioned matrices $\widetilde{\mathbf{M}}^{BB}_{CB}$ and $\widetilde{\mathbf{K}}^{BB}_{CB}$ can be found in (Voormeeren, 2012), and will be not discussed here.

If the finite element mesh is sufficiently fine and many subcomponents with distributed interfaces are considered, the size of these reduced system-level matrices is dominated by the interface DoFs. Although the number of DoFs is aggressively reduced, the sparsity of the matrices is lost. The computational gain will thus be limited. To overcome this problem, interface reduction can be applied such that truly compact models can be obtained.

2.3. SYSTEM-LEVEL AND LOCAL-LEVEL INTERFACE REDUCTION METHODS

The interface reduction techniques aim to reduce the size of the CB model by decreasing the number of interface DoFs. In principle, the interface reduction techniques can be applied both on substructure level as well as on assembly level. In this section, the commonly used interface reduction techniques on system level (Castanier *et al.*, 2001) and substructure level (Hong *et al.*, 2013) will be briefly discussed.

2.3.1. SYSTEM-LEVEL INTERFACE REDUCTION

The system-level interface reduction was first proposed in (Craig Jr & Chang, 1977) and was further discussed in (Castanier *et al.*, 2001, Bourquin, 1992, Balmès, 1996). As a starting point, we recall the assembled EoMs in (2.18) for the CB models. By fixing the internal DoFs for all subcomponents, we obtain

$$\widetilde{\mathbf{M}}^{BB}_{\mathcal{CB}}\ddot{\mathbf{q}}^{B}_{\mathcal{CB}}+\widetilde{\mathbf{K}}^{BB}_{\mathcal{CB}}\mathbf{q}^{B}_{\mathcal{CB}}=\widetilde{\mathbf{g}}^{B}_{\mathcal{CB}}, \tag{2.19}$$

where $\widetilde{\mathbf{M}}^{BB}_{\mathcal{CB}} \in \mathbb{R}^{n^B_{\mathcal{CB}}\times n^B_{\mathcal{CB}}}, \widetilde{\mathbf{K}}^{BB}_{\mathcal{CB}} \in \mathbb{R}^{n^B_{\mathcal{CB}}\times n^B_{\mathcal{CB}}}$ are the interface partition of the assembled mass and stiffness matrices in (2.18). This equation is used to find the interface behavior. Hence, the interface modes can be computed from a secondary eigenvalue analysis of (2.19) as

$$\left(\widetilde{\mathbf{K}}^{BB}_{\mathcal{CB}}-\widetilde{\omega}^2_j\widetilde{\mathbf{M}}^{BB}_{\mathcal{CB}}\right)\widetilde{\boldsymbol{\phi}}_j=\mathbf{0}, \quad j=1,\ldots,n^B_{\mathcal{CB}}, \tag{2.20}$$

where the system-level characteristic constraint (SCC) modes $\widetilde{\boldsymbol{\Phi}}_{\mathcal{SL}} \in \mathbb{R}^{n^B_{\mathcal{CB}}\times m^B_{\mathcal{SL}}}$ are defined here as a truncated set of the eigenvectors as $\widetilde{\boldsymbol{\Phi}}_{\mathcal{SL}}=[\widetilde{\boldsymbol{\phi}}_1,\ldots,\widetilde{\boldsymbol{\phi}}_{m^B_{\mathcal{SL}}}]$, with $m^B_{\mathcal{SL}} \ll n^B_{\mathcal{CB}}$. The corresponding eigenvalues can be rewritten in a diagonal matrix as $\widetilde{\boldsymbol{\omega}}^2_{\mathcal{SL}} = \mathrm{diag}(\widetilde{\omega}^2_1,\ldots,\widetilde{\omega}^2_{m^B_{\mathcal{SL}}})$.

Castanier (Castanier *et al.*, 2001) suggested that the number of interface DoFs can be reduced by using this new set of SCC modes, where a single SCC mode represents more global motion at the interface, as opposed to constraint modes. Depending on the frequency range of interest, the SCC modes can be used to generate a new CMS model with the significantly reduced number of DoFs. By taking a selected set of SCC modes, the interface DoFs are approximated by stating

$$\mathbf{q}^{B}_{\mathcal{CB}}=\widetilde{\boldsymbol{\Phi}}_{\mathcal{SL}}\boldsymbol{\eta}^{B}_{\mathcal{SL}}, \tag{2.21}$$

where $\mathbf{q}^{B}_{\mathcal{CB}}$ is reduced to a smaller set of generalized coordinates $\boldsymbol{\eta}^{B}_{\mathcal{SL}}$. Essentially, the interface dominant behavior is here given by the low-frequency vibration modes obtained by a Guyan reduction (Guyan, 1965).

Substitution of the interface reduction (2.21) into the assembly of CB equations (2.18) via a Galerkin projection then gives

$$\underbrace{\begin{bmatrix} \mathbf{I}_{\mathcal{SL}}^{BB} & \left(\widetilde{\mathbf{\Phi}}_{\mathcal{SL}}\right)^T \widetilde{\mathbf{M}}_{\mathcal{CB}}^{BI} \\ \widetilde{\mathbf{M}}_{\mathcal{CB}}^{IB} \widetilde{\mathbf{\Phi}}_{\mathcal{SL}} & \mathbf{I}_{\mathcal{CB}}^{II} \end{bmatrix}}_{\widetilde{\mathbf{M}}_{\mathcal{SL}}} \begin{bmatrix} \ddot{\boldsymbol{\eta}}_{\mathcal{SL}}^{B} \\ \ddot{\boldsymbol{\eta}}_{\mathcal{CB}}^{I} \end{bmatrix} + \underbrace{\begin{bmatrix} \widetilde{\boldsymbol{\omega}}_{\mathcal{SL}}^2 & \mathbf{0} \\ \mathbf{0} & \boldsymbol{\omega}_{\mathcal{CB}}^2 \end{bmatrix}}_{\widetilde{\mathbf{K}}_{\mathcal{SL}}} \begin{bmatrix} \boldsymbol{\eta}_{\mathcal{SL}}^{B} \\ \boldsymbol{\eta}_{\mathcal{CB}}^{I} \end{bmatrix} = \underbrace{\begin{bmatrix} \left(\widetilde{\mathbf{\Phi}}_{\mathcal{SL}}\right)^T \widetilde{\mathbf{g}}_{\mathcal{CB}}^{B} \\ \widetilde{\mathbf{g}}_{\mathcal{CB}}^{I} \end{bmatrix}}_{\widetilde{\mathbf{g}}_{\mathcal{SL}}}, \quad (2.22)$$

where the SCC modes $\widetilde{\mathbf{\Phi}}_{\mathcal{SL}}$ are assumed to be mass normalized, and the assembled stiffness matrix is now fully diagonal.

For illustration, the first two SCC modes of the ⊓-shaped model are shown in Fig. 2.2. The SCC modes exhibit a global rotation and translation at the interface DoFs. The internal DoFs follow the motion statically as dictated by the deformation at the interface. The gray color denoted statically condensed mesh. The main advantage of this method lays in the fact that the interface compatibility across coupled substructures is still exactly enforced. However, the system level reduction bears two major drawbacks. First, the stiffness and mass matrices ($\widetilde{\mathbf{K}}_{\mathcal{CB}}^{BB}$ and $\widetilde{\mathbf{M}}_{\mathcal{CB}}^{BB}$) are no longer sparse after the static condensation. Second, since the SCC modes are obtained after the system-level matrices are constructed, the SCC modes must be recomputed for all the interface DoFs, even if a design modification is performed for a single substructure. Therefore, for a large-scale system with multiple interface connections, the solution of the eigenvalue problem (2.20) is expensive, considering the large size of interface DoFs.

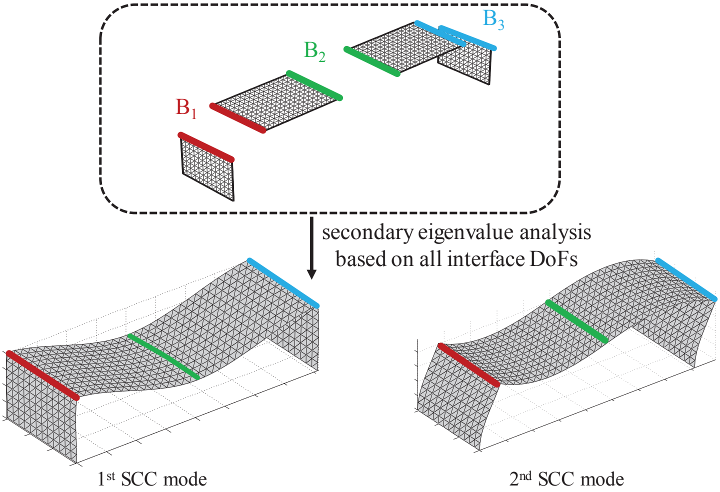

Figure 2.2: The first two SCC modes for the ⊓-shaped FE model.

2.3.2. LOCAL-LEVEL INTERFACE REDUCTION

An alternative way to achieve interface reduction was proposed in (Hong *et al.*, 2013) named as “local-level reduction". We briefly summarize the method in this section. We start with the reduced equation of motion (2.8) for the s^{th} substructure. By fixing the internal DoFs $\boldsymbol{\eta}^{I}_{(s)}$, we get

$$\widetilde{\mathbf{M}}^{BB}_{(s)}\ddot{\mathbf{q}}^{B}_{(s)} + \widetilde{\mathbf{K}}^{BB}_{(s)}\mathbf{q}^{B}_{(s)} = \widetilde{\mathbf{g}}^{B}_{(s)} + \mathbf{p}^{B}_{(s)}. \tag{2.23}$$

As for the system-level case, the local-interface reduction technique is also based on a secondary eigenvalue analysis of the free vibration of each substructure. In this case, the interaction with neighboring subcomponents is simply neglected by setting $\mathbf{p}^{B}_{(s)} = \mathbf{0}$. This results in the eigenvalue problem

$$\left(\widetilde{\mathbf{K}}^{BB}_{(s)} - \widetilde{\omega}^{2}_{j,(s)}\widetilde{\mathbf{M}}^{BB}_{(s)}\right)\widetilde{\boldsymbol{\phi}}_{j,(s)} = \mathbf{0}, \quad j = 1, \ldots, n^{B}_{(s)} \tag{2.24}$$

where a truncated set of the eigenvectors $\widetilde{\boldsymbol{\Phi}}_{\mathcal{LL},(s)} \in \mathbb{R}^{n^{B}_{(s)} \times m^{B}_{(s)}}$, called the local-level characteristic constraint (LCC) modes, is collected as $\widetilde{\boldsymbol{\Phi}}_{\mathcal{LL},(s)} = [\widetilde{\boldsymbol{\phi}}_{1,(s)}, \ldots, \widetilde{\boldsymbol{\phi}}_{m^{B}_{(s)},(s)}]$ with $m^{B}_{(s)} \ll n^{B}_{(s)}$. The LCC modes $\widetilde{\boldsymbol{\Phi}}_{\mathcal{LL},(s)}$ are used to reduce the interface DoFs for each substructure in a local sense.

Since the LCC modes are calculated without the knowledge of adjacent substructures, the subcomponent level interface reduction may result in non-conforming interfaces and may cause so-called interface locking if the reduction basis is inadequate and enforces only weak compatibility between the substructures (Gruber & Rixen, 2016). Therefore, it is important to solve the compatibility problems during the assembly step.

According to the method proposed by Hong (Hong *et al.*, 2013), the LCC modes of each interface, denoted as $\widetilde{\boldsymbol{\Phi}}^{B_i}_{\mathcal{LL}}$ for the interface B_i, are simply combined from connecting substructures. Take for instance the ⊓-shaped structure in Fig. 2.3: $\widetilde{\boldsymbol{\Phi}}^{B_1}_{\mathcal{LL}}$ contains $\widetilde{\boldsymbol{\Phi}}^{B_1}_{\mathcal{LL},(1)}$ and $\widetilde{\boldsymbol{\Phi}}^{B_1}_{\mathcal{LL},(2)}$. This augmented set of LCC modes is used as reduction basis for the interface of every connected substructure. This guarantees that the interface dynamics of each connected substructure are well described, at the cost of increasing the size of the basis. As an example, the ⊓-shaped model is again used to illustrate the procedure, see Fig. 2.3. The LCC modes are shown in different colors at the interface DoFs for each substructure. The gray mesh indicates that the internal DoFs are statically condensed. The LCC modes of each interface are simply combined from all the connecting subcomponents.

Due to the simple combination of multiple interface sets from different subsystems, the resulting reduction basis may contain linearly dependent vectors. To prevent ill-conditioning, the basis should be orthogonalized. This can be achieved by performing a further Singular Value Decomposition (SVD) for each interface B_i as

$$\mathbf{U}^{B_i}\mathbf{S}^{B_i}\left(\mathbf{D}^{B_i}\right)^{T} = \widetilde{\boldsymbol{\Phi}}^{B_i}_{\mathcal{LL}}, \tag{2.25}$$

where $\mathbf{U}^{B_i}$ and $\mathbf{S}^{B_i}$ are the left singular vectors and diagonal singular value matrix for interface B_i. In Hong's work (Hong *et al.*, 2013), only the left singular vectors corresponding to singular values larger than 0.01% of the maximum singular value are kept, and placed

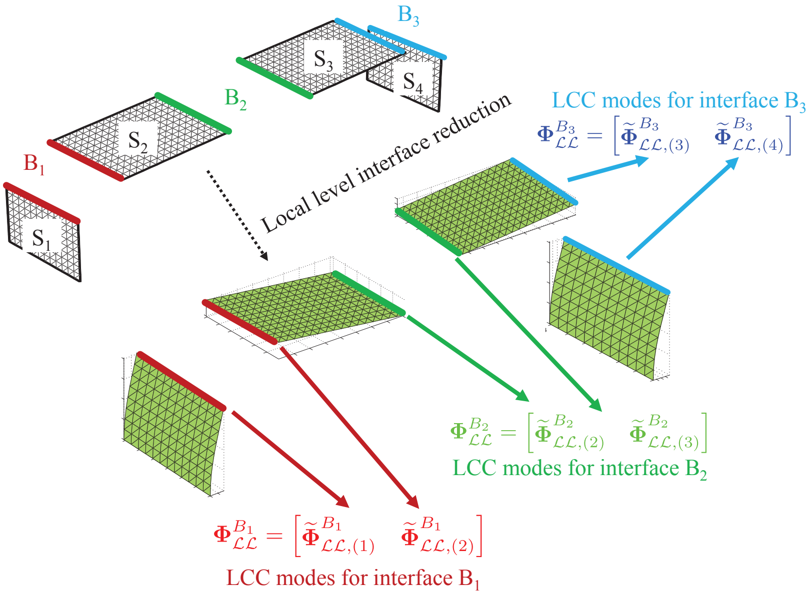

Figure 2.3: The local-level interface reduction technique (Hong *et al.*, 2013) for the ⊓-shaped model.

in $\mathbf{U}^{B_i}_{\mathcal{LL}}$. This yields the final reduction basis for all the interface DoFs as

$$\mathbf{q}^{B}_{\mathcal{CB}} = \begin{bmatrix} \mathbf{U}^{B_1}_{\mathcal{LL}} & \mathbf{0} & \mathbf{0} \\ \mathbf{0} & \ddots & \mathbf{0} \\ \mathbf{0} & \mathbf{0} & \mathbf{U}^{B_V}_{\mathcal{LL}} \end{bmatrix} \begin{bmatrix} \boldsymbol{\eta}_{B_1} \\ \vdots \\ \boldsymbol{\eta}_{B_V} \end{bmatrix} = \mathbf{U}\boldsymbol{\eta}^{B}_{\mathcal{LL}}, \tag{2.26}$$

where the subscript V is the number of interface sets. The detailed assembly procedure can be found in (Hong *et al.*, 2013), complemented with a clear example. The final reduced equation of motion can be obtained by substituting the interface reduction (2.26) to the assembly of CB equations (2.18), which gives

$$\underbrace{\begin{bmatrix} \mathbf{U}^T\tilde{\mathbf{M}}^{BB}_{\mathcal{CB}}\mathbf{U} & \mathbf{U}^T\tilde{\mathbf{M}}^{BI}_{\mathcal{CB}} \\ \tilde{\mathbf{M}}^{IB}_{\mathcal{CB}}\mathbf{U} & \mathbf{I}^{II}_{\mathcal{CB}} \end{bmatrix}}_{\tilde{\mathbf{M}}_{\mathcal{LL}}} \begin{bmatrix} \ddot{\boldsymbol{\eta}}^{B}_{\mathcal{LL}} \\ \ddot{\boldsymbol{\eta}}^{I}_{\mathcal{CB}} \end{bmatrix} + \underbrace{\begin{bmatrix} \mathbf{U}^T\tilde{\mathbf{K}}^{BB}_{\mathcal{CB}}\mathbf{U} & \mathbf{0} \\ \mathbf{0} & \boldsymbol{\omega}^2_{\mathcal{CB}} \end{bmatrix}}_{\tilde{\mathbf{K}}_{\mathcal{LL}}} \begin{bmatrix} \boldsymbol{\eta}^{B}_{\mathcal{LL}} \\ \boldsymbol{\eta}^{I}_{\mathcal{CB}} \end{bmatrix} = \underbrace{\begin{bmatrix} \mathbf{U}^T\tilde{\mathbf{g}}^{B}_{\mathcal{CB}} \\ \tilde{\mathbf{g}}^{I}_{\mathcal{CB}} \end{bmatrix}}_{\tilde{\mathbf{g}}_{\mathcal{LL}}}. \tag{2.27}$$

The *a priori* interface reduction on subcomponent level is easy to accomplish, without knowledge of the adjacent substructures. Moreover, the eigenvalue problem associated to the LCC modes is of limited size, and therefore computationally cheap. However, since the interface behavior is dependent on all components to which it is connected, the local-level interface reduction may give far less accurate results than the system-level interface reduction, since it can not properly account for the coupling between connecting subsystems.

2.4. MULTILEVEL INTERFACE REDUCTION

In order to combine the accurate system-level approach with the computationally efficient local-level method, two reduction methods based on a multilevel CB substructuring for the local subset have been discussed. Each subset is a collection of some adjacent, but not all, substructures for the entire system. This procedure localizes the interface reduction by applying a multilevel static condensation and eigenvalue analysis on interface DoFs of local subsets, and, as opposed to traditional local level techniques, does not compromise the compatibility at interfaces. In practice, it is often the case that, within the same organization, different subcomponent models have to be assembled first into larger subsystems (named as subsets here). Next, they are joined with other subsystems developed by different organizations. The multilevel approach nicely fits this scenario.

The process can be summarized as follows:

- Step 1: The global system is divided into substructures. For every substructure, a classical CB reduction basis is obtained, for which the interface DoFs are fully retained and the internal behaviors are reproduced by a combination of CMs and IVMs. This step has been explained in Section 2.2.1.

- Step 2: We group the reduced CB models of the substructures into second-level subsets, the subcomponents within each subset are assembled in parallel at this stage. For each subset, the total DoFs can be partitioned into three sets: i) *internal components of the interface DoFs* (denoted as NDoFs), which have been utilized to connect the subsystems categorized in the same subset; ii) the *boundary components of the interface DoFs* (denoted as CDoFs), which will be connected with the neighboring subsets; iii) the *internal DoFs*, which corresponds to the modal coordinates of IVMs for the subsystems within the same subset, denoted here as IDoFs. To further reduce the size of system matrices in each subset, two multilevel ROMs, named as ML1-ROM and ML2-ROM, have been discussed here. Specifically:

  ML1-ROM: For each subset, a secondary CB reduction is performed for the interface DoFs (CDoFs and NDoFs). More specifically, the NDoFs are treated as the internal component of the secondary CB reduction, and thus replaced by a truncated set of modal coordinates. The CDoFs are treated as the interface component of the secondary CB reduction and therefore retained for exact interface compatibility during the subsets assembly in the next step.

  ML2-ROM: For each subset, a secondary CB reduction is performed for all DoFs (CDoFs, NDoFs and IDoFs) within the subset. While CDoFs are the interface component of the secondary CB reduction, both NDoFs and IDoFs are the internal component of the secondary CB reduction, and therefore are further reduced.

- Step 3: The subsets are coupled together using the primal assembly. It is worth noticing that step 2 can be applied recursively in case extra assembly levels are required. For the sake of simplicity, in this work we assume that the assembled subsets obtained from step 2 will not be further connected with additional subsets. If the size of the CDoFs is still too large and a further reduction is desired, a modal truncation for the CDoFs can be performed as for the system-level reduction in Section 2.3.1.

To apply the multilevel interface reduction for an arbitrary system, we start with the stage where all the substructures are reduced with the CB method, as discussed in Section 2.2.1. The substructures within the i^{th} subset Γ_i are then assembled together in the primal way by defining a unique set of interface DoFs within the subset.

The assembly procedure is identical to the primal assembly introduced in Section 2.2.2, and will not be repeated here. The reduced EoMs are analogous to (2.18) and are written here for the i^{th} subset Γ_i as

$$\underbrace{\begin{bmatrix}\widetilde{\mathbf{M}}^{BB}_{\Gamma_i} & \widetilde{\mathbf{M}}^{BI}_{\Gamma_i}\\ \widetilde{\mathbf{M}}^{IB}_{\Gamma_i} & \mathbf{I}^{II}_{\Gamma_i}\end{bmatrix}}_{\widetilde{\mathbf{M}}_{\Gamma_i}} \begin{bmatrix}\ddot{\mathbf{q}}^{B}_{\Gamma_i}\\ \ddot{\boldsymbol{\eta}}^{I}_{\Gamma_i}\end{bmatrix} + \underbrace{\begin{bmatrix}\widetilde{\mathbf{K}}^{BB}_{\Gamma_i} & \mathbf{0}\\ \mathbf{0} & \boldsymbol{\omega}^2_{\Gamma_i}\end{bmatrix}}_{\widetilde{\mathbf{K}}_{\Gamma_i}} \begin{bmatrix}\mathbf{q}^{B}_{\Gamma_i}\\ \boldsymbol{\eta}^{I}_{\Gamma_i}\end{bmatrix} = \underbrace{\begin{bmatrix}\widetilde{\mathbf{g}}^{B}_{\Gamma_i}\\ \widetilde{\mathbf{g}}^{I}_{\Gamma_i}\end{bmatrix}}_{\widetilde{\mathbf{g}}_{\Gamma_i}} + \begin{bmatrix}\mathbf{p}^{B}_{\Gamma_i}\\ \mathbf{0}\end{bmatrix}, \quad i = 1,2,\dots,Z, \tag{2.28}$$

where the connecting force imposed by the neighboring subset is indicated by $\mathbf{p}^{B}_{\Gamma_i}$ to satisfy the force equilibrium and Z is the number of subsets for the entire system. For the i^{th} subset, $\mathbf{q}^{B}_{\Gamma_i}$ is a unique set of the interface DoFs, and $\boldsymbol{\eta}^{I}_{\Gamma_i}$ is the internal DoFs.

As mentioned in step 2, the interface DoFs $\mathbf{q}^{B}_{\Gamma_i}$ of the subset Γ_i are partitioned into 2 sets, i.e., CDoFs $\mathbf{q}^{C}_{\Gamma_i}$ and NDoFs $\mathbf{q}^{N}_{\Gamma_i}$, by expressing that $\mathbf{q}^{B}_{\Gamma_i} = \mathrm{col}(\mathbf{q}^{C}_{\Gamma_i}, \mathbf{q}^{N}_{\Gamma_i})$.

With this notation, Eq. (2.28) can be rewritten for an arbitrary structure with Z subsets in a generalized fashion:

$$\underbrace{\begin{bmatrix}\widetilde{\mathbf{M}}^{CC}_{\Gamma_i} & \widetilde{\mathbf{M}}^{CN}_{\Gamma_i} & \widetilde{\mathbf{M}}^{CI}_{\Gamma_i}\\ \widetilde{\mathbf{M}}^{NC}_{\Gamma_i} & \widetilde{\mathbf{M}}^{NN}_{\Gamma_i} & \widetilde{\mathbf{M}}^{NI}_{\Gamma_i}\\ \widetilde{\mathbf{M}}^{IC}_{\Gamma_i} & \widetilde{\mathbf{M}}^{IN}_{\Gamma_i} & \mathbf{I}^{II}_{\Gamma_i}\end{bmatrix}}_{\widetilde{\mathbf{M}}_{\Gamma_i}} \begin{bmatrix}\ddot{\mathbf{q}}^{C}_{\Gamma_i}\\ \ddot{\mathbf{q}}^{N}_{\Gamma_i}\\ \ddot{\boldsymbol{\eta}}^{I}_{\Gamma_i}\end{bmatrix} + \underbrace{\begin{bmatrix}\widetilde{\mathbf{K}}^{CC}_{\Gamma_i} & \widetilde{\mathbf{K}}^{CN}_{\Gamma_i} & \mathbf{0}\\ \widetilde{\mathbf{K}}^{NC}_{\Gamma_i} & \widetilde{\mathbf{K}}^{NN}_{\Gamma_i} & \mathbf{0}\\ \mathbf{0} & \mathbf{0} & \boldsymbol{\omega}^2_{\Gamma_i}\end{bmatrix}}_{\widetilde{\mathbf{K}}_{\Gamma_i}} \begin{bmatrix}\mathbf{q}^{C}_{\Gamma_i}\\ \mathbf{q}^{N}_{\Gamma_i}\\ \boldsymbol{\eta}^{I}_{\Gamma_i}\end{bmatrix} = \underbrace{\begin{bmatrix}\widetilde{\mathbf{g}}^{C}_{\Gamma_i}\\ \widetilde{\mathbf{g}}^{N}_{\Gamma_i}\\ \widetilde{\mathbf{g}}^{I}_{\Gamma_i}\end{bmatrix}}_{\widetilde{\mathbf{g}}_{\Gamma_i}} + \begin{bmatrix}\mathbf{p}^{C}_{\Gamma_i}\\ \mathbf{0}\\ \mathbf{0}\end{bmatrix}. \tag{2.29}$$

To further reduce the size of system matrices in (2.29), a secondary CB projection is applied at each subset independently. As mentioned in step 2, we discussed two ROMs for the multilevel interface reduction techniques. To assemble the neighboring subsets in a fully compatible way, CDoFs $\mathbf{q}^{C}_{\Gamma_i}$ are treated as the interface for the CB reduction, and thus are not reduced in both methods.

For ML1-ROM, a secondary CB reduction is performed only for the interface DoFs (CDoFs $\mathbf{q}^{C}_{\Gamma_i}$ and NDoFs $\mathbf{q}^{N}_{\Gamma_i}$) by stating

$$\begin{bmatrix}\mathbf{q}^{C}_{\Gamma_i}\\ \mathbf{q}^{N}_{\Gamma_i}\\ \boldsymbol{\eta}^{I}_{\Gamma_i}\end{bmatrix} = \begin{bmatrix}\mathbf{I} & \mathbf{0} & \mathbf{0}\\ \widetilde{\boldsymbol{\Psi}}^{NC}_{\Gamma_i} & \widetilde{\boldsymbol{\Phi}}^{NN}_{\Gamma_i} & \mathbf{0}\\ \mathbf{0} & \mathbf{0} & \mathbf{I}\end{bmatrix} \begin{bmatrix}\mathbf{q}^{C}_{\Gamma_i}\\ \boldsymbol{\eta}^{N}_{\Gamma_i}\\ \boldsymbol{\eta}^{I}_{\Gamma_i}\end{bmatrix}, \tag{2.30}$$

where the modes $\widetilde{\boldsymbol{\Psi}}^{NC}_{\Gamma_i}$ are denoted here as *the interface-level constraint modes* (ILCMs), and the modes $\widetilde{\boldsymbol{\Phi}}^{NN}_{\Gamma_i}$ are called *the interface-level internal vibration modes* (ILIVMs). The ILCMs $\widetilde{\boldsymbol{\Psi}}^{NC}_{\Gamma_i}$ and ILIVMs $\widetilde{\boldsymbol{\Phi}}^{NN}_{\Gamma_i}$ are calculated as

$$\widetilde{\boldsymbol{\Psi}}^{NC}_{\Gamma_i} = -\left(\widetilde{\mathbf{K}}^{NN}_{\Gamma_i}\right)^{-1} \widetilde{\mathbf{K}}^{NC}_{\Gamma_i} \quad \text{and} \quad \widetilde{\mathbf{K}}^{NN}_{\Gamma_i}\widetilde{\boldsymbol{\Phi}}^{NN}_{\Gamma_i} - \widetilde{\mathbf{M}}^{NN}_{\Gamma_i}\widetilde{\boldsymbol{\Phi}}^{NN}_{\Gamma_i}\boldsymbol{\varsigma}^2_{\Gamma_i} = \mathbf{0}. \tag{2.31}$$

The ILIVMs $\widetilde{\boldsymbol{\Phi}}_{\Gamma_i}^{NN}$ are truncated based on the frequency range of interest and $\boldsymbol{\varsigma}_{\Gamma_i}^2$ is the corresponding diagonal eigenfrequency matrix. It is worth noticing that the size of eigenvalue problems (2.31) is much smaller than that of the system-level counterpart (2.20), and therefore computationally less demanding.

For ML2-ROM, a secondary CB reduction is performed for all DoFs within the i^{th} subset, the NDoFs $\mathbf{q}_{\Gamma_i}^N$ and IDoFs $\boldsymbol{\eta}_{\Gamma_i}^I$ are merged together and further reduced during the modal truncation. The CB reduction can be expressed as

$$\begin{bmatrix} \mathbf{q}_{\Gamma_i}^C \\ \mathbf{q}_{\Gamma_i}^N \\ \boldsymbol{\eta}_{\Gamma_i}^I \end{bmatrix} = \begin{bmatrix} \mathbf{I} & \mathbf{0} \\ \widetilde{\boldsymbol{\Psi}}_{\Gamma_i}^{NC} & \widetilde{\boldsymbol{\Phi}}_{\Gamma_i}^{NM} \\ \mathbf{0} & \widetilde{\boldsymbol{\Phi}}_{\Gamma_i}^{IM} \end{bmatrix} \begin{bmatrix} \mathbf{q}_{\Gamma_i}^C \\ \boldsymbol{\eta}_{\Gamma_i}^M \end{bmatrix}, \tag{2.32}$$

where $\widetilde{\boldsymbol{\Phi}}_{\Gamma_i}^{NM}$ and $\widetilde{\boldsymbol{\Phi}}_{\Gamma_i}^{IM}$ are the rows of *merged internal vibration modes* $\widetilde{\boldsymbol{\Phi}}_{\Gamma_i}^{M}$ (MIVMs) corresponding to NDoFs and IDoFs, respectively. To calculate the MIVMs, the eigenvalue analysis is applied to the ROM in Eq. (2.29) when CDoFs $\mathbf{q}_{\Gamma_i}^C$ are fixed, as

$$\left[\begin{matrix} \widetilde{\mathbf{K}}_{\Gamma_i}^{NN} & \mathbf{0} \\ \mathbf{0} & \boldsymbol{\omega}_{\Gamma_i}^2 \end{matrix}\right] \begin{bmatrix} \widetilde{\boldsymbol{\Phi}}_{\Gamma_i}^{NM} \\ \widetilde{\boldsymbol{\Phi}}_{\Gamma_i}^{IM} \end{bmatrix} - \begin{bmatrix} \widetilde{\mathbf{M}}_{\Gamma_i}^{NN} & \widetilde{\mathbf{M}}_{\Gamma_i}^{NI} \\ \widetilde{\mathbf{M}}_{\Gamma_i}^{IN} & \mathbf{I}_{\Gamma_i}^{II} \end{bmatrix} \begin{bmatrix} \widetilde{\boldsymbol{\Phi}}_{\Gamma_i}^{NM} \\ \widetilde{\boldsymbol{\Phi}}_{\Gamma_i}^{IM} \end{bmatrix} \boldsymbol{\tau}_{\Gamma_i}^2 = \mathbf{0}, \tag{2.33}$$

where the MIVMs $\widetilde{\boldsymbol{\Phi}}_{\Gamma_i}^{M}$ are truncated, as before, based on the frequency range of interest, and $\boldsymbol{\tau}_{\Gamma_i}^2$ is the corresponding diagonal eigenfrequency matrix.

It should be noticed here that the computational cost of eigenvalue solution in (2.33) is slightly more expensive compared to its counterpart in (2.31), since the IDoFs $\boldsymbol{\eta}_{\Gamma_i}^I$ are also included. However, the size of $\boldsymbol{\eta}_{\Gamma_i}^I$ will not be large assuming that the internal DoFs of each subsystem have already been significantly reduced during the CB projection as discussed in Section 2.2.1. Therefore, the computational cost of Eq. (2.33) will still be small when compared to its counterpart (2.20) in SL-ROM.

By substituting the interface CB reduction for ML1-ROM (2.30) and ML2-ROM (2.32) into (2.29) and projecting, we obtain

$$\begin{bmatrix} \overline{\mathbf{M}}_{\Gamma_i}^{CC} & \overline{\mathbf{M}}_{\Gamma_i}^{CN} & \overline{\mathbf{M}}_{\Gamma_i}^{CI} \\ \overline{\mathbf{M}}_{\Gamma_i}^{NC} & \mathbf{I}_{\Gamma_i}^{NN} & \overline{\mathbf{M}}_{\Gamma_i}^{NI} \\ \overline{\mathbf{M}}_{\Gamma_i}^{IC} & \overline{\mathbf{M}}_{\Gamma_i}^{IN} & \mathbf{I}_{\Gamma_i}^{II} \end{bmatrix} \begin{bmatrix} \ddot{\mathbf{q}}_{\Gamma_i}^C \\ \ddot{\boldsymbol{\eta}}_{\Gamma_i}^N \\ \ddot{\boldsymbol{\eta}}_{\Gamma_i}^I \end{bmatrix} + \begin{bmatrix} \overline{\mathbf{K}}_{\Gamma_i}^{CC} & \mathbf{0} & \mathbf{0} \\ \mathbf{0} & \boldsymbol{\varsigma}_{\Gamma_i}^2 & \mathbf{0} \\ \mathbf{0} & \mathbf{0} & \boldsymbol{\omega}_{\Gamma_i}^2 \end{bmatrix} \begin{bmatrix} \mathbf{q}_{\Gamma_i}^C \\ \boldsymbol{\eta}_{\Gamma_i}^N \\ \boldsymbol{\eta}_{\Gamma_i}^I \end{bmatrix} = \begin{bmatrix} \overline{\mathbf{g}}_{\Gamma_i}^C \\ \overline{\mathbf{g}}_{\Gamma_i}^N \\ \overline{\mathbf{g}}_{\Gamma_i}^I \end{bmatrix} + \begin{bmatrix} \mathbf{p}_{\Gamma_i}^C \\ \mathbf{0} \\ \mathbf{0} \end{bmatrix} \tag{2.34}$$

for ML1-ROM and

$$\begin{bmatrix} \overline{\mathbf{M}}_{\Gamma_i}^{CC} & \overline{\mathbf{M}}_{\Gamma_i}^{CM} \\ \overline{\mathbf{M}}_{\Gamma_i}^{MC} & \mathbf{I}_{\Gamma_i}^{MM} \end{bmatrix} \begin{bmatrix} \ddot{\mathbf{q}}_{\Gamma_i}^C \\ \ddot{\boldsymbol{\eta}}_{\Gamma_i}^M \end{bmatrix} + \begin{bmatrix} \overline{\mathbf{K}}_{\Gamma_i}^{CC} & \mathbf{0} \\ \mathbf{0} & \boldsymbol{\tau}_{\Gamma_i}^2 \end{bmatrix} \begin{bmatrix} \mathbf{q}_{\Gamma_i}^C \\ \boldsymbol{\eta}_{\Gamma_i}^M \end{bmatrix} = \begin{bmatrix} \overline{\mathbf{g}}_{\Gamma_i}^C \\ \overline{\mathbf{g}}_{\Gamma_i}^M \end{bmatrix} + \begin{bmatrix} \mathbf{p}_{\Gamma_i}^C \\ \mathbf{0} \end{bmatrix} \tag{2.35}$$

for ML2-ROM, where the formulation of all partitioned matrices and vectors can be easily derived from the Galerkin projection, and will not be discussed here.

The reduced EoMs for the entire system are analogous to (2.18), by selecting a unique set of CDoFs $\mathbf{q}_{\Gamma}^C$ and applying the primal assembly. The reduced EoMs are directly written here as

$$\begin{bmatrix} \overline{\mathbf{M}}_\Gamma^{CC} & \overline{\mathbf{M}}_\Gamma^{CN} & \overline{\mathbf{M}}_\Gamma^{CI} \\ \overline{\mathbf{M}}_\Gamma^{NC} & \mathbf{I}_\Gamma^{NN} & \overline{\mathbf{M}}_\Gamma^{NI} \\ \overline{\mathbf{M}}_\Gamma^{IC} & \overline{\mathbf{M}}_\Gamma^{IN} & \mathbf{I}_{\mathcal{CB}}^{II} \end{bmatrix} \begin{bmatrix} \ddot{\mathbf{q}}_\Gamma^C \\ \ddot{\boldsymbol{\eta}}_\Gamma^N \\ \ddot{\boldsymbol{\eta}}_{\mathcal{CB}}^I \end{bmatrix} + \begin{bmatrix} \overline{\mathbf{K}}_\Gamma^{CC} & \mathbf{0} & \mathbf{0} \\ \mathbf{0} & \boldsymbol{\varsigma}^2 & \mathbf{0} \\ \mathbf{0} & \mathbf{0} & \boldsymbol{\omega}_{\mathcal{CB}}^2 \end{bmatrix} \begin{bmatrix} \mathbf{q}_\Gamma^C \\ \boldsymbol{\eta}_\Gamma^N \\ \boldsymbol{\eta}_{\mathcal{CB}}^I \end{bmatrix} = \begin{bmatrix} \overline{\mathbf{g}}_\Gamma^C \\ \overline{\mathbf{g}}_\Gamma^N \\ \overline{\mathbf{g}}_{\mathcal{CB}}^I \end{bmatrix} \tag{2.36}$$

for ML1-ROM, and

$$\begin{bmatrix} \overline{\mathbf{M}}_\Gamma^{CC} & \overline{\mathbf{M}}_\Gamma^{CM} \\ \overline{\mathbf{M}}_\Gamma^{MC} & \mathbf{I}_\Gamma^{MM} \end{bmatrix} \begin{bmatrix} \ddot{\mathbf{q}}_\Gamma^C \\ \ddot{\boldsymbol{\eta}}_\Gamma^M \end{bmatrix} + \begin{bmatrix} \overline{\mathbf{K}}_\Gamma^{CC} & \mathbf{0} \\ \mathbf{0} & \boldsymbol{\tau}^2 \end{bmatrix} \begin{bmatrix} \mathbf{q}_\Gamma^C \\ \boldsymbol{\eta}_\Gamma^M \end{bmatrix} = \begin{bmatrix} \overline{\mathbf{g}}_\Gamma^C \\ \overline{\mathbf{g}}_\Gamma^M \end{bmatrix} \tag{2.37}$$

for ML2-ROM, where we have $\boldsymbol{\varsigma}^2 = \mathrm{diag}(\boldsymbol{\varsigma}_{\Gamma_1}^2, \dots, \boldsymbol{\varsigma}_{\Gamma_Z}^2)$, $\boldsymbol{\tau}^2 = \mathrm{diag}(\boldsymbol{\tau}_{\Gamma_1}^2, \dots, \boldsymbol{\tau}_{\Gamma_Z}^2)$, $\boldsymbol{\eta}_\Gamma^N = \mathrm{col}\left(\boldsymbol{\eta}_{\Gamma_1}^N, \dots, \boldsymbol{\eta}_{\Gamma_Z}^N\right)$ and $\boldsymbol{\eta}_\Gamma^M = \mathrm{col}\left(\boldsymbol{\eta}_{\Gamma_1}^M, \dots, \boldsymbol{\eta}_{\Gamma_Z}^M\right)$.

If a further reduction of the CDoFs $\mathbf{q}_\Gamma^C$ is still desired, we can apply the system-level interface reduction technique as discussed in Section 2.3.1. By fixing $\boldsymbol{\eta}_\Gamma^N$ and $\boldsymbol{\eta}_{\mathcal{CB}}^I$ in Eq. (2.36) or fixing $\boldsymbol{\eta}_\Gamma^M$ in Eq. (2.37) , we get

$$\overline{\mathbf{M}}_\Gamma^{CC} \ddot{\mathbf{q}}_\Gamma^C + \overline{\mathbf{K}}_\Gamma^{CC} \mathbf{q}_\Gamma^C = \overline{\mathbf{g}}_\Gamma^C, \tag{2.38}$$

where $\overline{\mathbf{M}}_\Gamma^{CC} \in \mathbb{R}^{n_\Gamma^C \times n_\Gamma^C}, \overline{\mathbf{K}}_\Gamma^{CC} \in \mathbb{R}^{n_\Gamma^C \times n_\Gamma^C}$ are the mass and stiffness matrices when all DoFs are statically condensed to the CDoFs, and n_Γ^C is the size of vector $\mathbf{q}_\Gamma^C$. Then the motion of $\mathbf{q}_\Gamma^C$ is approximated by performing a modal truncation as

$$\mathbf{q}_\Gamma^C = \overline{\boldsymbol{\Phi}}_\Gamma^{CC} \boldsymbol{\eta}_\Gamma^C, \quad \text{with} \quad \left(\overline{\mathbf{K}}_\Gamma^{CC} - \upsilon_j^2 \overline{\mathbf{M}}_\Gamma^{CC}\right) \overline{\boldsymbol{\phi}}_{j,\Gamma}^{CC} = \mathbf{0}, \quad j = 1, \dots, n_\Gamma^C \tag{2.39}$$

where the *interface-level characteristic constraint* (ILCC) modes $\overline{\boldsymbol{\Phi}}_\Gamma^{CC} = [\overline{\boldsymbol{\phi}}_{1,\Gamma}^{CC}, \dots, \overline{\boldsymbol{\phi}}_{m_\Gamma^C,\Gamma}^{CC}]$ are a truncated set of the eigenvectors, with $m_\Gamma^C \ll n_\Gamma^C$. The corresponding eigenvalues can be rewritten in a diagonal matrix form as $\boldsymbol{\upsilon}^2 = \mathrm{diag}(\upsilon_1^2, \dots, \upsilon_{m_\Gamma^C}^2)$.

Substitution of the interface reduction (2.39) to (2.36) and (2.37) via a Galerkin projection then gives the final reduced EoMs for ML1-ROM as

$$\underbrace{\begin{bmatrix} \mathbf{I}_\Gamma^{CC} & (\overline{\boldsymbol{\Phi}}_\Gamma^{CC})^T \overline{\mathbf{M}}_\Gamma^{CN} & (\overline{\boldsymbol{\Phi}}_\Gamma^{CC})^T \overline{\mathbf{M}}_\Gamma^{CI} \\ \overline{\mathbf{M}}_\Gamma^{NC} \overline{\boldsymbol{\Phi}}_\Gamma^{CC} & \mathbf{I}_\Gamma^{NN} & \overline{\mathbf{M}}_\Gamma^{NI} \\ \overline{\mathbf{M}}_\Gamma^{IC} \overline{\boldsymbol{\Phi}}_\Gamma^{CC} & \overline{\mathbf{M}}_\Gamma^{IN} & \mathbf{I}_{\mathcal{CB}}^{II} \end{bmatrix}}_{\overline{\mathbf{M}}_{\mathcal{ML}1}} \begin{bmatrix} \ddot{\boldsymbol{\eta}}_\Gamma^C \\ \ddot{\boldsymbol{\eta}}_\Gamma^N \\ \ddot{\boldsymbol{\eta}}_{\mathcal{CB}}^I \end{bmatrix} + \underbrace{\begin{bmatrix} \boldsymbol{\upsilon}^2 & \mathbf{0} & \mathbf{0} \\ \mathbf{0} & \boldsymbol{\varsigma}^2 & \mathbf{0} \\ \mathbf{0} & \mathbf{0} & \boldsymbol{\omega}_{\mathcal{CB}}^2 \end{bmatrix}}_{\overline{\mathbf{K}}_{\mathcal{ML}1}} \begin{bmatrix} \boldsymbol{\eta}_\Gamma^C \\ \boldsymbol{\eta}_\Gamma^N \\ \boldsymbol{\eta}_{\mathcal{CB}}^I \end{bmatrix} = \underbrace{\begin{bmatrix} (\overline{\boldsymbol{\Phi}}_\Gamma^{CC})^T \overline{\mathbf{g}}_\Gamma^C \\ \overline{\mathbf{g}}_\Gamma^N \\ \overline{\mathbf{g}}_{\mathcal{CB}}^I \end{bmatrix}}_{\overline{\mathbf{g}}_{\mathcal{ML}1}}, \tag{2.40}$$

and for ML2-ROM as

$$\underbrace{\begin{bmatrix} \mathbf{I}_\Gamma^{CC} & (\overline{\boldsymbol{\Phi}}_\Gamma^{CC})^T \overline{\mathbf{M}}_\Gamma^{CM} \\ \overline{\mathbf{M}}_\Gamma^{MC} \overline{\boldsymbol{\Phi}}_\Gamma^{CC} & \mathbf{I}_\Gamma^{MM} \end{bmatrix}}_{\overline{\mathbf{M}}_{\mathcal{ML}2}} \begin{bmatrix} \ddot{\boldsymbol{\eta}}_\Gamma^C \\ \ddot{\boldsymbol{\eta}}_\Gamma^M \end{bmatrix} + \underbrace{\begin{bmatrix} \boldsymbol{\upsilon}^2 & \mathbf{0} \\ \mathbf{0} & \boldsymbol{\tau}^2 \end{bmatrix}}_{\overline{\mathbf{K}}_{\mathcal{ML}2}} \begin{bmatrix} \boldsymbol{\eta}_\Gamma^C \\ \boldsymbol{\eta}_\Gamma^M \end{bmatrix} = \underbrace{\begin{bmatrix} (\overline{\boldsymbol{\Phi}}_\Gamma^{CC})^T \overline{\mathbf{g}}_\Gamma^C \\ \overline{\mathbf{g}}_\Gamma^M \end{bmatrix}}_{\overline{\mathbf{g}}_{\mathcal{ML}2}}. \tag{2.41}$$

As can be noticed, the reduced stiffness matrices in both (2.40) and (2.41) are both fully diagonal, as it is the case in (2.22) when adopting the system-level interface reduction. Here, we stress that the effort in obtaining (2.40) and (2.41) is lower than its counterpart in the system level approach discussed in section 2.3.1.

For illustration, we take the ⊓-shaped model in Fig. 2.4 as an example. The CB-reduced subsystems are grouped into 2 local subsets: subset Γ_1, comprising substructures S_1 and S_2, and subset Γ_2, comprising substructures S_3 and S_4. The interface DoFs of the ⊓-shaped model are here partitioned into 3 components as B_1, B_2 and B_3. In this model, the interface B_2 acts as *the boundary component of the interface DoFs* (CDoFs), which connects the subsets Γ_1 and Γ_2. We show the different reduction basis of these two multilevel interface reduction techniques in Fig. 2.4.

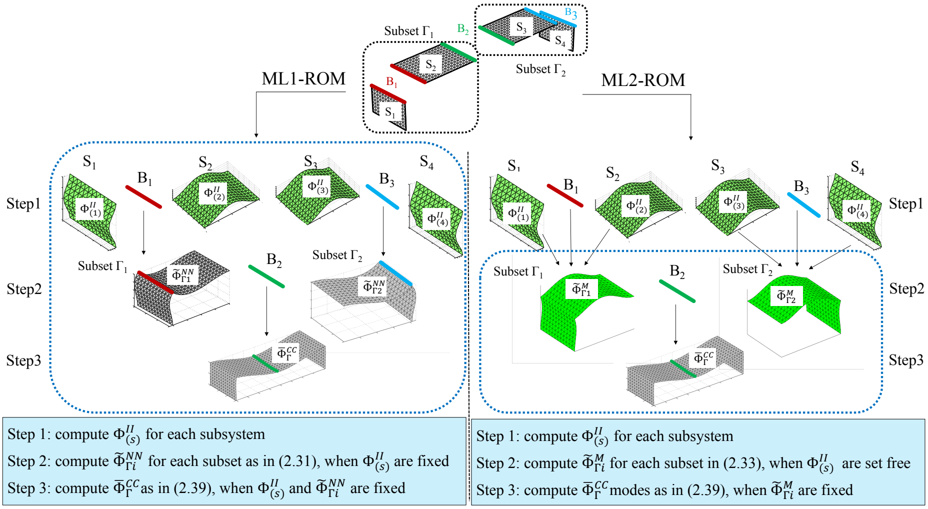

Step 1: compute $\Phi^{II}_{(s)}$ for each subsystem
Step 2: compute $\tilde{\Phi}^{NN}_{\Gamma i}$ for each subset as in (2.31), when $\Phi^{II}_{(s)}$ are fixed
Step 3: compute $\bar{\Phi}^{CC}_{\Gamma}$as in (2.39), when $\Phi^{II}_{(s)}$ and $\tilde{\Phi}^{NN}_{\Gamma i}$ are fixed

Step 1: compute $\Phi^{II}_{(s)}$ for each subsystem
Step 2: compute $\tilde{\Phi}^{M}_{\Gamma i}$ for each subset in (2.33), when $\Phi^{II}_{(s)}$ are set free
Step 3: compute $\bar{\Phi}^{CC}_{\Gamma}$modes as in (2.39), when $\tilde{\Phi}^{M}_{\Gamma i}$ are fixed

Figure 2.4: Illustration of the two multilevel interface reduction techniques (ML1-ROM and ML2-ROM) for the ⊓-shaped model.

In the next section, a detailed analysis of the computational cost associated to different interface reduction techniques will be given. We show the computational advantages of the multilevel interface reduction methods, as compared to the system-level and local-level approach.

2.5. COMPUTATIONAL COMPLEXITY

We estimate here the computational cost associated to the multilevel interface reduction and compare it to the system and local level approaches. We start with the given CB basis in (2.8) and reduced EoMs in (2.18), which are the foundation for all the interface reduction methods.

For SL-ROM, the solution of eigenvalue problems for the interface partition of the assembled CB matrices in (2.20) is the most involved operation. For the dense matrices

$\widetilde{\mathbf{K}}^{BB}_{\mathcal{CB}}$ and $\widetilde{\mathbf{M}}^{BB}_{\mathcal{CB}}$, the solution of the eigenvalue problem takes $\mathcal{O}\left[\left(n^{B}_{\mathcal{CB}}\right)^3\right]$ flops using QR and QZ methods (Golub & Van L., 2012), where $n^{B}_{\mathcal{CB}}$ is the number of a unique set of all interface DoFs.

For LL-ROM, the secondary eigenvalue analysis in (2.24) is performed for the interface DoFs of each subsystem locally. Take the s^{th} subsystem for instance, it takes $\mathcal{O}\left[(n^{B}_{(s)})^3\right]$ flops for the eigenvalue analysis for the dense matrices $\widetilde{\mathbf{K}}^{BB}_{(s)}$ and $\widetilde{\mathbf{M}}^{BB}_{(s)}$, where $n^{B}_{(s)}$ is the number of interface DoFs for the s^{th} substructure. To prevent ill conditioning, in (2.25) a singular value decomposition is used to reshape the LCC modes $\widetilde{\mathbf{\Phi}}^{B_i}_{\mathcal{LL}}$ for each interface set B_i, which will take $\mathcal{O}\left[n^{B_i}\times\left(m^{B_i}\right)^2\right]$ flops (Holmes *et al.*, 2007), where n^{B_i} is the number of DoFs at interface B_i and m^{B_i} is the number of truncated LCC modes from substructures connecting through interface B_i.

For ML1-ROM, solving the eigenvalue problem in (2.31) of the interface-level subset Γ_i takes $\mathcal{O}\left[(n^{N}_{\Gamma_i})^3\right]$ flops, where $n^{N}_{\Gamma_i}$ is the size of vector $\mathbf{q}^{N}_{\Gamma_i}$ for the subset Γ_i. For ML2-ROM, solving the eigenvalue problem in (2.33) takes $\mathcal{O}\left[(n^{N}_{\Gamma_i}+m^{I}_{\Gamma_i})^3\right]$ flops, where $m^{I}_{\Gamma_i}$ is the number of IVMs of the subsystems within the subset Γ_i. In general, the IVMs in each subsystem has been efficiently truncated so that $m^{I}_{\Gamma_i}\ll n^{N}_{\Gamma_i}$. Therefore, the extra computational cost associated to ML2-ROM, when compared to ML1-ROM, will be only marginal. The solution of interface-level CMs in (2.31) for subset Γ_i is the same for both ML1-ROM and ML2-ROM. It requires the factorization of the dense matrix $\widetilde{\mathbf{K}}^{NN}_{\Gamma_i}$, which is also computationally expensive. In fact, the complexity of the factorization of a dense $n^{N}_{\Gamma_i}\times n^{N}_{\Gamma_i}$ matrix is given by $\mathcal{O}\left[(n^{N}_{\Gamma_i})^{2.38}\right]$ flops, see (Coppersmith & Winograd, 1990). If a further reduction of the CDoFs $\mathbf{q}^{C}_{\Gamma}$ is desired, the eigenvalue analysis in (2.39) will take an extra $\mathcal{O}\left[(n^{C}_{\Gamma})^3\right]$ operations, where n^{C}_{Γ} is the size of vector $\mathbf{q}^{C}_{\Gamma}$.

All the estimated costs are summarized in Table 2.1. It shows that the computational cost of the different techniques mainly depends on the number of interface DoFs involved in the reduction procedures. As opposed to the system-level interface reduction, the local-level and multilevel methods can be applied for each substructure/subset in parallel. For clarity, we labelled the parallelizable operations for each substructure/subset with the symbol || in Table 2.1. Each of these models are of significantly smaller size as compared to the full model. Therefore, the computational cost for the LL-ROM, ML1-ROM and ML2-ROM only depends on the maximum cost associated to the largest subcomponent/subset. Given a system with large number of substructures and interface sets, it always holds that

$$n^{B}_{\mathcal{CB}}>\max\left(n^{B}_{(s)}\right),\quad n^{B}_{\mathcal{CB}}>\max\left(n^{B_i}\right),\quad \text{with}\quad s=1,\ldots,H;\ i=1,\ldots,V, \tag{2.42}$$

when the SL-ROM and LL-ROM are compared, and

$$n^{B}_{\mathcal{CB}}>n^{C}_{\Gamma},\quad n^{B}_{\mathcal{CB}}>\max\left(n^{N}_{\Gamma_j}\right),\quad n^{B}_{\mathcal{CB}}>\max\left(n^{N}_{\Gamma_j}+m^{I}_{\Gamma_j}\right),\quad \text{with}\quad j=1,\ldots,Z, \tag{2.43}$$

when we compared the performance between SL-ROM and ML1-ROM or ML2-ROM.

Eq. (2.42) and (2.43) indicate that the number of interface DoFs for the entire system is much larger than the one of a single substructure/subset. This highlights the potential

Table 2.1: Computational cost estimation of the most expensive operations of different interface reduction techniques

Method	significant operations		
SL-ROM	eigenvalue analysis in (2.20) $\mathcal{O}\left[\left(n^B_{\mathcal{CB}}\right)^3\right]$		
LL-ROM	eigenvalue analysis in (2.24) $\mathcal{O}\left[(n^B_{(s)})^3\right] \quad \|$	singular value decomposition in (2.25) $\mathcal{O}\left[n^{B_i} \times \left(m^{B_i}\right)^2\right] \quad \|$	
ML1-ROM	eigenvalue analysis in (2.31) $\mathcal{O}\left[(n^N_{\Gamma_i})^3\right] \quad \|$	matrix factorization in (2.31) $\mathcal{O}\left[(n^N_{\Gamma_i})^{2.38}\right] \quad \|$	eigenvalue analysis in (2.39) $\mathcal{O}\left[(n^C_\Gamma)^3\right]$
ML2-ROM	eigenvalue analysis in (2.33) $\mathcal{O}\left[(n^N_{\Gamma_i} + m^I_{\Gamma_i})^3\right] \quad \|$	matrix factorization in (2.31) $\mathcal{O}\left[(n^N_{\Gamma_i})^{2.38}\right] \quad \|$	eigenvalue analysis in (2.39) $\mathcal{O}\left[(n^C_\Gamma)^3\right]$

computational savings of performing the local-level and multilevel interface reduction techniques with respect to the system-level interface reduction, when parallel computation is performed for each substructure/subset with a much smaller size.

In this work, we also compare the computational efficiency of different interface reduction methods when a transient analysis is performed on the so obtained ROMs. The implicit Newmark method is adopted for the time integration, with parameters $\alpha = \frac{1}{2}$ and $\beta = \frac{1}{4}$. The detailed procedure of the Newmark method can be found in (Geradin & Rixen, 1997). The Rayleigh damping for damping matrix is adopted, and the coefficients are chosen to match a modal damping of 0.02 for the first two modes (see (Jain *et al.*, 2017) for details).

2.6. NUMERICAL EXAMPLES

In order to assess the accuracy of the different methods, we compare the eigenfrequencies and eigenmodes obtained by using different ROMs for two numerical examples. The linear dynamic response is further investigated in Section 2.6.2. In particular, we refer to the full model (i.e. without reduction) as Full; the CB-reduced model (without interface reduction) as CB-ROM; the system level, local level and two multilevel reduced models are denoted by SL-ROM, LL-ROM, ML1-ROM and ML2-ROM, respectively.

2.6.1. THE DOUBLE-⊓ SHAPED FE MODEL

A double-⊓ shaped FE model that consists of 9 subcomponents is here considered. The geometry of the structure is shown in Fig. 2.5. The length is $L = 0.4064$ m, the width is $W = 0.3048$ m, the height is $H = 0.2030$ m, and the thickness is $t_h = 0.003175$ m. The Young modulus is $E = 7.31 \times 10^{10}$ Pa, the Poisson's ratio is $\nu = 0.33$, and the density is $\rho = 2795.7$ kg.m^{-3}. The structure has been divided into 9 substructures (S_1 to S_9), which are connected through 8 interface sets (B_1 to B_8). For the multilevel interface reduction, the interface sets are further split into 3 subsets (Γ_1 to Γ_3). The structure is meshed with triangular flat shell elements with 6 DoFs per node. The resulting FE model has a total of 8814 DoFs, including $n^B_{\mathcal{CB}}$=624 interface DoFs and $n^I_{\mathcal{G}}$=8190 internal DoFs, with $n^I_{\mathcal{G}} = \sum_{s=1}^{9} n^I_{(s)}$. The system has been clamped at two ends.

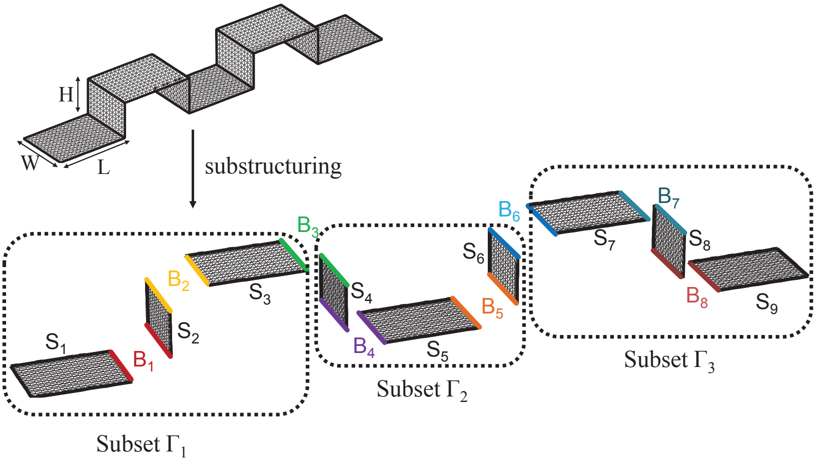

Figure 2.5: Illustration of the double-⊓ shaped FE model.

We are interested in the first 30 eigenfrequencies and eigenmodes of the system. For the CB-ROM, the first $m^I_{(s)}$=10 IVMs $\boldsymbol{\Phi}^{II}_{(s)}$ are selected for each substructure, and thus the number of internal DoFs is reduced from $n^I_{\mathcal{G}}$=8190 to $m^I_{\mathcal{CB}}$=90 DoFs, while all the $n^B_{\mathcal{CB}}$=624 interface DoFs are retained without reduction. The 624 CMs are replaced with the first $m^B_{\mathcal{SL}}$=80 SCC modes $\widetilde{\boldsymbol{\Phi}}_{\mathcal{SL}}$ by applying further system-level interface reduction methods for the SL-ROM. The LL-ROM is constructed by replacing the CMs in each substructure with the first $m^B_{(s)}$=12 LCC modes $\widetilde{\boldsymbol{\Phi}}_{\mathcal{LL},(s)}$. By using a SVD for each interface set to guard against ill conditioning and using the threshold discussed previously, finally 145 interface modes are retained in the reduction basis. The ML1-ROM is formed by $m^N_{\Gamma_i}$=20 interface-level IVMs $\widetilde{\boldsymbol{\Phi}}^{NN}_{\Gamma_i}$ for each subset (Γ_1 to Γ_3) together with m^C_{Γ}=20 ILCC modes $\overline{\boldsymbol{\Phi}}^{CC}_{\Gamma}$. The ML2-ROM is formed by the first 50 MIVMs $\widetilde{\boldsymbol{\Phi}}^{M}_{\Gamma_i}$ for each subset and m^C_{Γ}=20 ILCC modes $\overline{\boldsymbol{\Phi}}^{CC}_{\Gamma}$. We determine the number of kept modes for different interface reduction methods in such a way that SL-ROM, ML1-ROM and ML2-ROM all result in 170 modes in the final reduction basis. For illustration, the number of DoFs for different ROMs is summarized in Table 2.2. The first 30 eigenfrequencies and the corresponding relative error with respect to the full model are shown in Fig. 2.6. Note that any ROM featuring interface reduction will not be more accurate than its parent CB-ROM. As can be seen in Fig. 2.6(b), the eigenfrequency error for all the considered ROMs is below 2% for the first 30 frequencies. Except for the LL-ROM, the other considered ROMs keep the error within 0.1 %. The SL-ROM, ML1-ROM and ML2-ROM lead to an accuracy orders of magnitude better in the low-frequency range, when compared to the LL-ROM, although the latter one includes much more interface modes than the SL-ROM, ML1-ROM and ML2-ROM do.

Table 2.2: Number of modal coordinates of the double-⊓ shaped model for different ROMs

ROMs	number of modal coordinates			total DoFs
CB-ROM	$\mathbf{q}^B_{\mathcal{CB}}$	$\boldsymbol{\eta}^I_{\mathcal{CB}}$		$\text{col}(\mathbf{q}^B_{\mathcal{CB}}, \boldsymbol{\eta}^I_{\mathcal{CB}})$
	624	90		714
SL-ROM	$\boldsymbol{\eta}^B_{\mathcal{SL}}$	$\boldsymbol{\eta}^I_{\mathcal{CB}}$		$\text{col}(\boldsymbol{\eta}^B_{\mathcal{SL}}, \boldsymbol{\eta}^I_{\mathcal{CB}})$
	80	90		170
LL-ROM	$\boldsymbol{\eta}^B_{\mathcal{LL}}$	$\boldsymbol{\eta}^I_{\mathcal{CB}}$		$\text{col}(\boldsymbol{\eta}^B_{\mathcal{LL}}, \boldsymbol{\eta}^I_{\mathcal{CB}})$
	145	90		235
ML1-ROM	$\boldsymbol{\eta}^C_{\Gamma}$	$\boldsymbol{\eta}^N_{\Gamma}$	$\boldsymbol{\eta}^I_{\mathcal{CB}}$	$\text{col}(\boldsymbol{\eta}^C_{\Gamma}, \boldsymbol{\eta}^N_{\Gamma}, \boldsymbol{\eta}^I_{\mathcal{CB}})$
	20	60	90	170
ML2-ROM	$\boldsymbol{\eta}^C_{\Gamma}$	$\boldsymbol{\eta}^M_{\Gamma}$		$\text{col}(\boldsymbol{\eta}^C_{\Gamma}, \boldsymbol{\eta}^M_{\Gamma})$
	20	150		170

An eigenfrequency comparison is usually carried out in conjunction with a comparison of the associate mode shapes. One commonly used method for comparing mode shape vectors is the modal assurance criterion (MAC) (Allemang & Brown, 1982). When the mode shape vectors are mass-normalized, it is more appropriate to use the mass weighted MAC, which computes the vector correlation between a pair of mode shapes from full model $\boldsymbol{\Phi}_{i,full}$ and ROM $\boldsymbol{\Phi}_{j,red}$ as

$$\text{MAC}_{ij} = \frac{|\boldsymbol{\Phi}^T_{i,full}\mathbf{M}\boldsymbol{\Phi}_{j,red}|^2}{\left(\boldsymbol{\Phi}^T_{i,full}\mathbf{M}\boldsymbol{\Phi}_{i,full}\right)\left(\boldsymbol{\Phi}^T_{j,red}\mathbf{M}\boldsymbol{\Phi}_{j,red}\right)}. \tag{2.44}$$

Along the diagonal terms one finds the matching modes, while the off-diagonal terms show the correlation between non-matching modes. Ideally, matching mode shapes should have a MAC value close to one, whereas cross-correlating different mode shapes should give a value close to zero. The relative mode error ϵ_i of the i^{th} mode $\boldsymbol{\Phi}_{i,red}$ is thus calculated based on the matching modes as $\epsilon_i = 1 - \text{MAC}_{ii}$. The relative mode error of the interface ROMs are shown in Fig. 2.7. The SL-ROM, ML1-ROM and ML2-ROM all yield good results for the first 30 modes. Although LL-ROM contains more interface modes in the reduction basis, the relative mode error for the LL-ROM is substantial for the higher frequency modes.

2.6.2. NACA AIRFOIL WING BOX STRUCTURE

We consider here a thin-walled wing box structure proposed in (Jain *et al.*, 2017) and shown in Fig. 2.8. The cross section features a NACA 0012 profile; the structure is stiffened with ribs along the chord direction and spars along the longitudinal direction. The structure is meshed with triangular flat shell elements with 6 DoFs per node, resulting in 135570 DoFs and 49968 elements for the full model. The Young Modulus is $E = 70$ GPa,

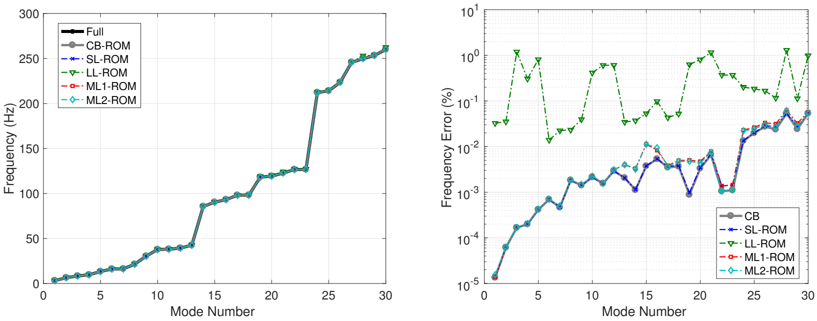

(a) First 30 eigenfrequencies (b) Relative error for the first 30 frequencies

Figure 2.6: First 30 eigenfrequencies and the corresponding relative error of the CB-ROM, SL-ROM, LL-ROM, ML1-ROM and ML2-ROM.

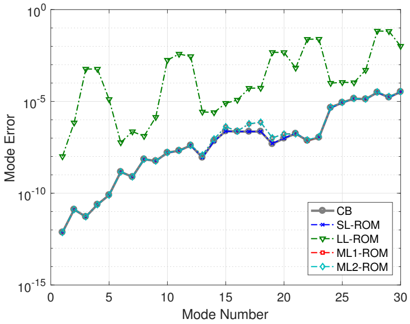

Figure 2.7: Relative mode error of the ROMs, compared to the full model.

the Poisson' ratio is $\nu = 0.33$, and the density is $\rho = 2700$ kg/m^3. A uniform thickness of $t_h = 1.5$ mm is adopted across the whole structure. The wing has a total length of 5 m and is cantilevered at one end. The significantly large number of DoFs of the full model allows to appreciate the computational advantages associated to interface reduction.

The wing box is then divided into 600 substructures, connected through 792 interface sets. The subdivision of the wing-box structure is illustrated in Fig. 2.8(c). Note that this subdivision could in fact reflect a common industrial scenario, where rather detailed FE models of each component might exist for component sizing and stress analysis. The DoFs of the full model are split into $n^B_{\mathcal{CB}}$=28944 interface DoFs and $n^I_{\mathcal{G}}$=106626 internal DoFs. We first investigated the accuracy of the frequency and mode of the assembled systems using different interface reduction techniques. The linear response of the wing box is analyzed when a spatially uniform, multi-harmonic pressure load is applied locally on the structure skin at an area highlighted in Fig. 2.8(a). The dynamic load function is given as

$$g\{t\} = 1000 \sum_{i=1}^{15} \left(1 - \frac{(i-1)^2}{392}\right) \sin\left(\omega_i \times t\right), \quad \text{with} \quad \omega_i = 250 \times \left(\frac{i}{15}\right)^2. \qquad (2.45)$$

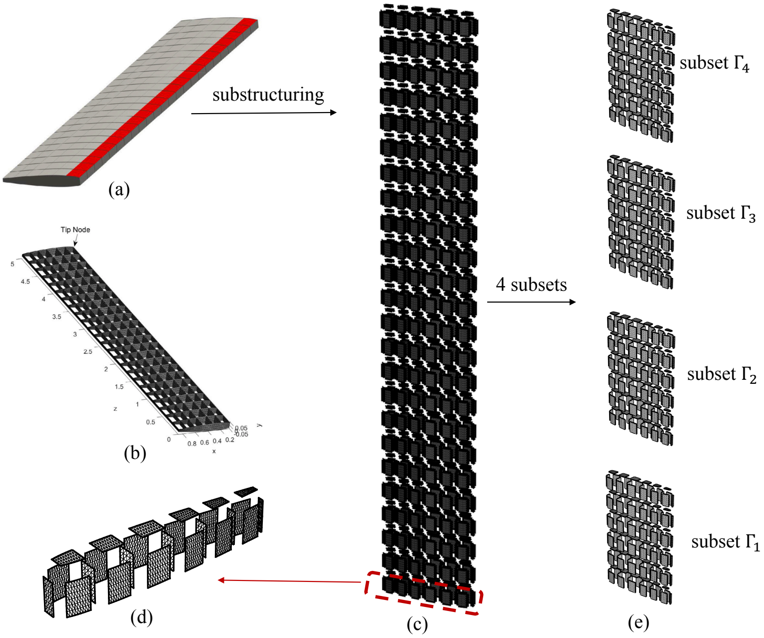

Figure 2.8: Illustration of the wing box structure. A pressure load is applied at the highlighted area as in (a). The skin panels are removed for a clear view in (b) and the tip node is highlighted. The wing-box structure is divided into 600 substructures as in (c). The 25 subsystems associated to one wing section are then plotted in (d). For multilevel interface reduction, 600 substructures are evenly grouped into 4 subsets, as shown in (e).

The number of retained IVMs for each substructure is determined by a frequency cut-off criterion: only IVMs associated to frequencies lower than 1500 Hz are kept in the reduced-order basis (ROB) of each substructure. The CB-ROM therefore reduces the internal DoFs from $n^I_{\mathcal{G}}$=106626 to $m^I_{\mathcal{CB}}$=1440. The SL-ROM is built with the same frequency cut-off criterion by including the SCC modes $\widetilde{\mathbf{\Phi}}_{\mathcal{SL}}$ associated to frequencies lower than 1500 Hz. This results into keeping the first $m^B_{\mathcal{SL}}$=1170 SCC modes in the final reduction basis. As for the ML1-ROM and ML2-ROM, all the substructures are collected into 4 subsets (Γ_1 to Γ_4), as shown in Fig. 2.8(e). The same frequency cut-off criterion is again utilized here. For ML1-ROM, the interface DoFs are further reduced by replacing the $n^B_{\mathcal{CB}}$=28944 CMs with the first $m^N_{\Gamma_i} = 168$ interface-level IVMs $\widetilde{\mathbf{\Phi}}^{NN}_{\Gamma_i}$ for subset (Γ_1 to Γ_3), $m^N_{\Gamma_i} = 180$ interface-level IVMs for subset Γ_4 together with the first m^C_{Γ}=153 ILCC modes $\overline{\mathbf{\Phi}}^{CC}_{\Gamma}$. This results in shrinking the interface DoFs from 28944 to 837. For ML2-ROM, the internal DoFs of each subset are reduced by using $m^M_{\Gamma_i} = 369$ merged IVMs $\widetilde{\mathbf{\Phi}}^{M}_{\Gamma_i}$ for subset (Γ_1 to Γ_3), and $m^M_{\Gamma_4} = 373$ merged IVMs for subset Γ_4. The number of CDoFs are reduced by including the first m^C_{Γ}=153 ILCC modes $\overline{\mathbf{\Phi}}^{CC}_{\Gamma}$. It will result in 1480 internal

DoFs and 153 interface DoFs in total for ML2-ROM. The LL-ROM is constructed by replacing the CMs in each substructure with the LCC modes $\widetilde{\mathbf{\Phi}}_{\mathcal{LL},(s)}$ up to 1500 Hz in each subsystem. Given the large number of substructures and interface sets, the LL-ROM would result in a large number of LCC modes. By using a SVD for each interface set to guard against ill conditioning and using threshold discussed previously, finally 22716 interface modes are retained in the reduction basis. For illustration, the number of modal coordinates of the different ROMs is summarized in Table 2.3.

Table 2.3: Number of modal coordinates of the wing-box model for different ROMs

ROMs	number of modal coordinates			total DoFs
CB-ROM	$\mathbf{q}^B_{\mathcal{CB}}$ 28944	$\boldsymbol{\eta}^I_{\mathcal{CB}}$ 1440		col$(\mathbf{q}^B_{\mathcal{CB}}, \boldsymbol{\eta}^I_{\mathcal{CB}})$ 30384
SL-ROM	$\boldsymbol{\eta}^B_{\mathcal{SL}}$ 1170	$\boldsymbol{\eta}^I_{\mathcal{CB}}$ 1440		col$(\boldsymbol{\eta}^B_{\mathcal{SL}}, \boldsymbol{\eta}^I_{\mathcal{CB}})$ 2610
LL-ROM	$\boldsymbol{\eta}^B_{\mathcal{LL}}$ 22716	$\boldsymbol{\eta}^I_{\mathcal{CB}}$ 1440		col$(\boldsymbol{\eta}^B_{\mathcal{LL}}, \boldsymbol{\eta}^I_{\mathcal{CB}})$ 24156
ML1-ROM	$\boldsymbol{\eta}^C_{\Gamma}$ 153	$\boldsymbol{\eta}^N_{\Gamma}$ 684	$\boldsymbol{\eta}^I_{\mathcal{CB}}$ 1440	col$(\boldsymbol{\eta}^C_{\Gamma}, \boldsymbol{\eta}^N_{\Gamma}, \boldsymbol{\eta}^I_{\mathcal{CB}})$ 2277
ML2-ROM	$\boldsymbol{\eta}^C_{\Gamma}$ 153	$\boldsymbol{\eta}^M_{\Gamma}$ 1480		col$(\boldsymbol{\eta}^C_{\Gamma}, \boldsymbol{\eta}^M_{\Gamma})$ 1633

The first 120 eigenfrequencies and corresponding relative errors are shown in Fig. 2.9. The mode shape error is also presented in Fig. 2.10. As indicated in Fig. 2.9(b) and 2.10, the SL-ROM, ML1-ROM and ML2-ROM can all lead to a good approximation by keeping relative frequency error below 0.5% for the first 120 frequencies (up to 460 Hz). The SL-ROM has slightly better accuracy compared to the ML1-ROM and ML2-ROM, especially at the frequency range of the applied load function (0-250 Hz). The LL-ROM fails to provide a satisfactory frequency approximation, although it includes 22716 interface modes.

The time history of the displacement for the tip node in Fig. 2.8(b) is shown in Fig. 2.11. In addition, we also show the root mean square (RMS) error ϵ_{RMS} at an arbitrary time step t_i defined as

$$\epsilon_{RMS}\{t_i\} = \sqrt{\frac{1}{n}\left(||\mathbf{q}_x\{t_i\} - \overline{\mathbf{q}}_x\{t_i\}||^2 + ||\mathbf{q}_y\{t_i\} - \overline{\mathbf{q}}_y\{t_i\}||^2 + ||\mathbf{q}_z\{t_i\} - \overline{\mathbf{q}}_z\{t_i\}||^2\right)} \qquad (2.46)$$

where $\mathbf{q}_x, \mathbf{q}_y, \mathbf{q}_z$ and $\overline{\mathbf{q}}_x, \overline{\mathbf{q}}_y, \overline{\mathbf{q}}_z$ are the x, y, z component of of the node displacement from the full and ROMs, respectively (rotational DoFs are excluded).

As observed in Fig. 2.11, while LL-ROM is inaccurate, all the other interface reduction techniques are able to reproduce the full solution. The RMS error better highlights the difference in performance between the various methods. It can be noticed that SL-ROM can reproduce the full solution as accurately as the CB-ROM (i.e., without interface

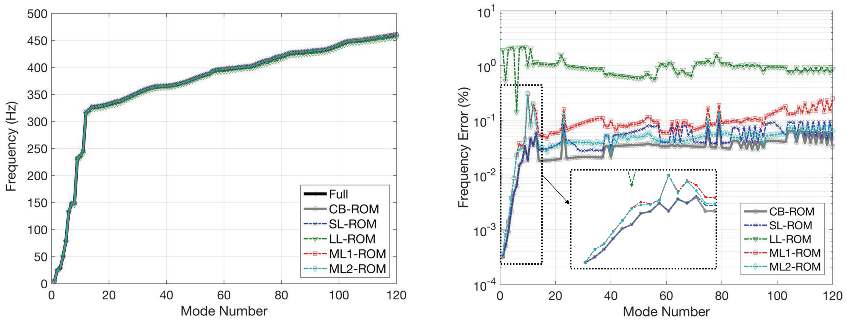

(a) First 120 eigenfrequencies (b) Relative error for the first 120 frequencies

Figure 2.9: First 120 eigenfrequencies and the corresponding relative error of the CB-ROM, SL-ROM, LL-ROM, ML1-ROM, and ML2-ROM.

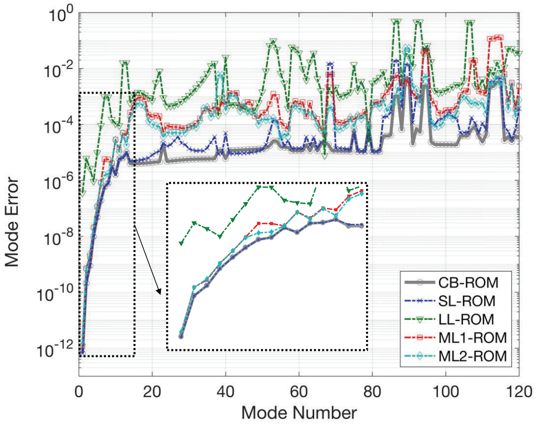

Figure 2.10: Relative mode error of the ROMs, compared to the full model.

reduction). While ML1-ROM and ML2-ROM can both produce a satisfactory approximation, the accuracy of ML2-ROM is slightly better than that of ML1-ROM.

2.6.3. COMPUTATIONAL EFFICIENCY

The computational complexity of the different interface reduction methods has been detailedly discussed in Section 2.5. In this subsection we compare the computational time required by each of the methods proposed. All simulations are performed in MATLAB® R2015, on the TU Delft cluster, equipped with 8-core Intel® Xeon® CPUs (E5-2630v3) @ 2.4 GHz and 128 GB RAM.

Table 2.4 compares the computational cost for the wing box structure in Section 2.6.2. The complexity comparisons have been split into 3 parts: i) the construction of reduction basis for different substructuring methods, which are done *offline*; ii) the frequency analysis of the assembled system; iii) the transient analysis of the response so-

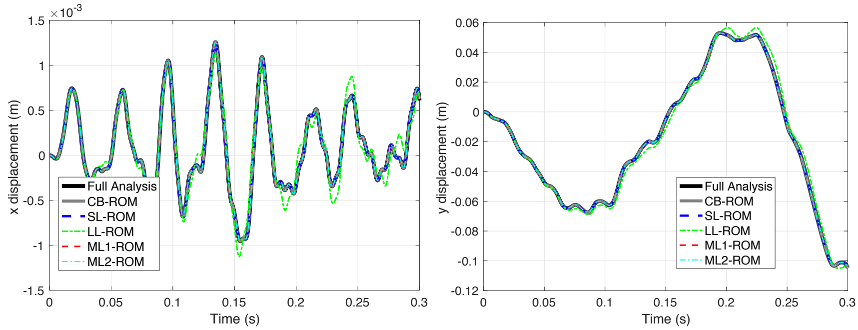

(a) x displacement at the tip node (b) y displacement at the tip node

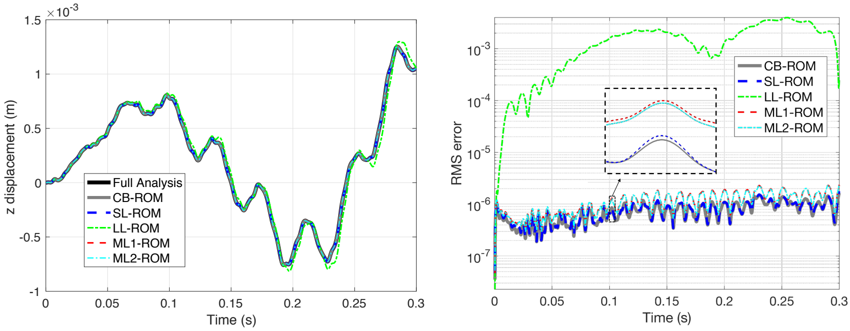

(c) z displacement at the tip node (d) RMS error

Figure 2.11: Time history of solution (displacement) in x, y, z direction at the tip-node of the wing-box structure, and the corresponding RMS error.

lution, which would be regarded as *online* analysis. Obviously, the full analysis does not carry any offline costs. The reduction basis for each substructure and each subset can be parallelized. Note that, in this particular example, the same substructures and subsets are instanced many times along the structure, so one needs to compute the reduction basis only once for each repeated set. In a more general case, because of the possibility of parallelization, the computational cost is mainly dependent on the most time-consuming subsystems or subsets, see Table 2.1. The computational efficiency is measured by the speed up factor, defined as

$$\mathcal{S} = \frac{\mathcal{C}_{on} t_{full}}{\mathcal{C}_{off} t_{off} + \mathcal{C}_{on} t_{on}}, \quad \text{with} \quad \mathcal{C}_{off} + \mathcal{C}_{on} = 1. \tag{2.47}$$

The offline calculation cost is neglected by setting $\mathcal{S}_1 : \mathcal{C}_{off} = 0, \mathcal{C}_{on} = 1$. The so obtained speed up factor $\mathcal{S}_1$ is justified when the same ROM is used for many different load cases. Alternatively one can set an equal weightage to offline and online costs, i.e., $\mathcal{S}_2 : \mathcal{C}_{off} = 0.5, \mathcal{C}_{on} = 0.5$. This covers the limit case in which the ROM is used only once. In addition, the accuracy of different ROMs is measured in terms of global relative errors (GRE) by

Table 2.4: Computational time of wing-box structure for the CB-ROM, SL-ROM, LL-ROM, ML1-ROM and ML2-ROM.

CPU Time (s)	Full	CB-ROM	SL-ROM	LL-ROM	ML1-ROM	ML2-ROM
ROB construction (*offline*)	-	1.70	578.13	6.17	24.51	34.98
Frequency analysis	74.88	46.50	3.51	27.60	1.79	0.86
Transient analysis (*online*)	387.20	200.80	120.10	113.69	53.35	35.42
Speed up factor $\mathcal{S}_1$	-	1.92	3.22	3.41	7.26	10.93
Speed up factor $\mathcal{S}_2$	-	1.91	0.55	3.23	4.85	5.50
GRE_x (%)	-	0.0466	0.0506	28.86	0.1112	0.1058
GRE_y (%)	-	0.0033	0.0034	8.10	0.0050	0.0049
GRE_z (%)	-	0.0050	0.0052	10.09	0.0162	0.0149

defining

$$\mathrm{GRE}_\diamond = \frac{\sqrt{\sum_t \left[\mathbf{q}_\diamond\{t\} - \bar{\mathbf{q}}_\diamond\{t\}\right]^T \left[\mathbf{q}_\diamond\{t\} - \bar{\mathbf{q}}_\diamond\{t\}\right]}}{\sqrt{\sum_t \mathbf{q}_\diamond\{t\}^T \mathbf{q}_\diamond\{t\}}} \times 100\%, \tag{2.48}$$

where subscript $\diamond$ designates the displacement of the full solution $\mathbf{q}$ and reduced solution $\bar{\mathbf{q}}$ in the x, y and z direction, respectively.

The computational time of the frequency analysis and transient analysis cannot be significantly reduced by the CB-ROM, although the internal DoFs are greatly reduced. In this wing-box example, the size of interface and internal DoFs is comparable, and therefore the system matrices of CB-ROM still contain a large number of interface DoFs.

From the results shown in Table 2.4, one can see that all interface reduction methods do deliver a slight advantage with respect of CB-ROM for frequency analysis, also when offline cost is considered. In particular, for this specific case, the ML1-ROM and ML2-ROM cut the computation time of the frequencies by factors (46.5+1.7)/(1.79+24.51)= 1.83 and (46.5+1.7)/(34.98+0.86)=1.34, respectively. LL-ROM provides similar figures, but was shown to be inaccurate. SL-ROM, on the contrary, requires large offline computations and therefore is not competitive against CB-ROM.

The major advantage in performing interface reduction comes in fact when transient analysis is needed, as can be seen by looking at the speed up factors reported in Table 2.4. It is emphasized here that the final size of ROMs, and therefore the computational savings depend on the cut-off criterion previously introduced in section 2.6.2. To this respect, the ML2-ROM features the smallest size, and therefore results in the best speed-up factor $\mathcal{S}_1$ of 10.93. In both ML1-ROM and ML2-ROM, the offline computational cost can be reduced by setting up smaller, parallelizable problems relative to each subset. The frequency analysis and online (transient analysis) computational cost are reduced owing to the final system matrices with much smaller size.

The GRE is also shown in Table 2.4. The SL-ROM offers a reduced solution almost as accurate as the CB-ROM. The LL-ROM, on the other side, is largely inaccurate. The multilevel interface reduction methods ML1-ROM and ML2-ROM still guarantee good accuracy while increasing the speed. In particular, ML2-ROM is more accurate, and faster, than ML1-ROM, but requires larger offline calculations. It should also be noted here that the obtained results for ML1-ROM and ML2-ROM depend on the subset division. An attempt of finding the best division to maximize the speed up was not made in this work.

The selection of the "best" interface reduction method is somewhat problem dependent. Here, we attempt to give guidelines by making the following observations.

- SL-ROM: the system level interface reduction is preferred when high accuracy is required and the offline cost can be neglected, i.e., the speed up factor $\mathcal{S}_1$ is justified. Therefore, SL-ROM is suitable for problems in which the size of interface DoFs is moderate, and the ROM needs to be constructed only once.

- LL-ROM: Although its accuracy is the worst when compared to its counterparts, LL-ROM is still an option if one is interested in the low frequency spectrum of systems featuring a limited number of substructures, which are connected through simple patterns, as the double-$\sqcap$ shaped FE model discussed in section 2.6.1. Therefore, the LL-ROM may be applied for relatively simple systems during the design process, when design changes occur in some parts of the structure, and thus the ROM has to be frequently rebuilt. The LL-ROM benefits from a cheap offline cost. However, it is not applicable when the substructures are connected through numerous interfaces, as the method does not properly consider the contributions of neighboring subcomponents.

- ML1-ROM, ML2-ROM: these two methods provide good speed up and accuracy for both frequency and transient analysis. Therefore, they are applicable for problems where both accuracy and computational efficiency are of concern. They are suitable for the design process, when changes occur within few local subsets. In this case, only the ROBs relative to the modified parts need to be rebuilt. ML2-ROM is more accurate and faster (online) than ML1-ROM, at a price of a slightly increased offline cost.

2.7. CONCLUSIONS

In this chapter, we summarize the existing interface reduction methods and especially present the multilevel interface reduction techniques for complex systems featuring multiple subcomponents and a large number of interface DoFs. The main idea is to group subcomponents into different subsets, and perform a secondary CB reduction for the resulting subset DoFs. The methods localize the interface reduction by applying a multilevel static condensation and eigenvalue analysis on each subset in parallel. As opposed to traditional local level technique, the multilevel interface reduction methods better consider the interaction between interfaces. Because of this, the multilevel interface reduction techniques provide accuracy comparable to system level interface reduction methods. At the same time, these techniques enable computational time saving by setting up smaller, parallelizable problems relative to each subset. Two variants of the multilevel interface reduction techniques (ML1-ROM and ML2-ROM) are investigated.

In ML1-ROM, a secondary CB reduction is performed for the interface DoFs of each subset. In ML2-ROM, the same CB reduction is performed for all DoFs of each subset. We assessed the methods both on eigenvalues calculations and numerical time integration. When a frequency cut-off criterion is applied for the selection of modes, the ML2-ROM results in smaller (and therefore faster) and more accurate ROM. This comes at the expense of a slightly larger offline cost.

All the interface reduction techniques have been tested for the rather complex numerical examples featuring several subcomponents and large meshes. The multilevel methods outperform the system level interface reduction in terms of achievable speedup, while delivering comparable accuracy. We indicate that the multilevel methods are particularly useful when dealing with systems featuring large and multi-connected interfaces. In cases of simpler and smaller interfaces, we provide guidelines for the choice of the most suited reduction method.

3

ENHANCED CRAIG-BAMPTON METHOD WITH INTERFACE REDUCTION FOR GEOMETRIC NONLINEAR STRUCTURES

In this chapter, we present an enhanced Craig-Bampton substructuring technique for the reduction of geometric nonlinear dynamics analysis of multi-component structures. The proposed method is a natural extension of the standard Craig-Bampton method and system-level interface reduction by augmenting the fixed-interface modes of each subsystem and the characteristic constraint modes of the assembled system with their corresponding modal derivatives in parallel. The interface degrees of freedom are thus dramatically reduced. The modal derivatives of the fixed-interface modes and characteristic constraint modes can describe the geometrical nonlinear behavior, for the internal components and interface components respectively. We construct the reduced tensors for the projected force in parallel across substructures. The size of reduced tensors for each subsystem is much smaller than the size of the final reduced basis. Therefore, computational savings and storage memory reduction for both online and offline computation can be achieved. This framework also enables the flexibility for reduced model construction, by only adding modal derivatives to the selected substructures undergoing nonlinear deformations. The presented numerical examples show excellent agreement along the transient dynamic response between the reduced order model and the full-order model. Significant computational gains were obtained when combining the reduced-order model with substructure-level modal tensorial forms of the nonlinear forces.

This chapter is based on the paper "Wu, L., Tiso, P., van Keulen, F., 2018. A Modal Derivatives Enhanced Craig-Bampton Method for Geometric Nonlinear Structures. (submitted to Computers & Structures)"

3.1. INTRODUCTION

Dynamic responses of complex structures can nowadays be accurately analyzed with the assistance of advanced numerical simulation. However, with the ever-increasing demand for larger and more densely meshed models, the total CPU time required for a single simulation could severely hinder the design process. Moreover, the presence of elastic nonlinearities significantly increases the computational cost, as the nonlinear load vector and tangent operator need to be calculated and factorized at every step of the time integration. In this context, model order reduction (MOR) is a must to bring the computational cost to a manageable level.

Often, the system at hand consists of several *substructures* (also called *subsystems*). In this case, one can resort to component mode synthesis (CMS) techniques (Klerk *et al.*, 2008) to reduce the size of the problem. Among other approaches, the Craig-Bampton (CB) method (Bampton & Craig, 1968), which combines the concepts of component-wise analysis and model reduction, is widely used in industry and academia. The CB method approximates the behavior of each subsystem by constructing a reduction basis with two distinct contributions, namely i) a set of constraint modes (CMs) representing the static deformation when interface displacements are individually applied, and ii) internal vibration modes (IVMs) obtained by fixing the component at the interface. A dual extension, which enforces compatibility across the substructures in a weak sense, has been proposed in (Rixen, 2004) under the name of Dual CB. Recently, Kim (Kim & Lee, 2015) enhanced the CB method by considering the effect of residual substructure modes. However, the extension of CB method for nonlinear systems remains an open research topic.

In a linear context, the dynamics of the system can be effectively represented by a linear combination of few, carefully selected modes. Among other choices, vibration modes (VMs) are very effective to reduce the size of the original model, often referred to high fidelity model (HFM). The VMs are used to form a reduced order basis (ROB) on which the equations of motion are projected. To account for geometric nonlinearity, the ROB can be enriched with modal derivatives (MDs) (Idelsohn & Cardona, 1985*a*,*b*), as shown in several contributions (Slaats *et al.*, 1995, Weeger *et al.*, 2014, Barbic & James, 2005, Barbic & Zhao, 2011, Tiso *et al.*, 2011). A static version of the MDs, i.e. obtained by neglecting the inertial effects, was proposed in (Idelsohn & Cardona, 1985*b*), and has been widely applied afterwards. As illustrated in (Weeger, 2015), the MDs are computed by differentiating twice the nonlinear static equilibrium problem along directions given by predetermined linear modes, which are assumed to accurately approximate the linear response. The possibility of extending the CB basis with the MDs has also been discussed in (Weeger, 2015, Wenneker & Tiso, 2014).

However, issues arise when the size of the reduced problem is dominated by the large number of interface DoFs. If nonlinear behavior is expected at the interface, one needs to compute MDs relative to the full set of CMs in the CB method. Unfortunately, the number of obtainable MDs grows quadratically with respect to the number of underlying linear modes, and therefore this approach quickly becomes unpractical, as the reduction basis will be dominated by a large number of the MDs corresponding to the CMs. It is therefore of significance to reduce the number of interface DoFs, by using a proper interface reduction technique.

Craig (Craig Jr & Chang, 1977) proposed three approximated methods for reducing the interface DoFs for linear systems. Castanier (Castanier *et al.*, 2001) revised one of the three methods, which involved an eigenvalue analysis of the interface DoFs using the so-called system-level characteristic constraint (SCC) modes. Later, Hong (Hong *et al.*, 2013) formulated the interface reduction in a slightly different way by generating local-level characteristic constraint (LCC) modes from mass and stiffness associated with the interface DoFs before assembly. Tran(Tran, 2001) indicated that the use of SCC modes can be extended from the fixed interface modes based substructuring to various free or hybrid interface mode based substructuring techniques, like the CMS method proposed by MacNeal (MacNeal, 1971) and later by Rubin (Rubin, 1975). The SCC modes can be selected depending on their relative importance to the ROB solution. A criterion for their selection is introduced in (David & Thomas, 2005) by extending the effective interface mass (Kammer & Triller, 1996) as a mean of evaluating the SCC modes to be retained in ROB. An optional interface reduction technique for extremely large-scale eigen-analysis of structures is introduced in (Aoyama & Yagawa, 2001), by analysing the interface VMs from two components adjacent to each interface. All the mentioned techniques have been applied to linear systems, but the extension of these methods to nonlinear cases remains challenging. Recently, Kuether (Kuether *et al.*, 2016, 2017) proposed a non-intrusive substructuring approach for geometric nonlinear structures. In order to extract the coefficients of the nonlinear reduced order model (ROM), they compute the ROM from a selected set of nonlinear static problems.

In this chapter, we construct ROMs for geometric nonlinear substructured systems by enhancing system-level interface reduction with MDs related to the IVMs of all the components and to the SCC modes as well. This allows to obtain a small-size ROM. By applying the proposed approach, we can establish the ROM without reliance on full training simulations, which are unfortunately of the size of the HFM. The focus of this work is on shell-type structures, where the geometric nonlinearities exhibit bending-stretching coupling effects. The application and efficiency of a MDs based reduction technique to complex structures, where substructuring techniques and interface reduction are not applied, has been demonstrated in many previous contributions (Weeger *et al.*, 2014, Barbic & James, 2005, Barbic & Zhao, 2011). As discussed in (Barbic & James, 2005), the reduced nonlinear force vector can be directly expressed as a polynomial function of the modal vector, by using higher-order tensors of the whole system. In this work, the reduced nonlinear force vector has been computed for each substructure and then assembled, by assigning the system-level interface modes and corresponding MDs to the relevant substructures for tensorial computations.

The remainder of this chapter is organized as follows. Section 3.2 introduces the classic CB approach. A truncated set of SCC modes is included in the reduction basis to reduce the interface DoFs, instead of considering the CMs associated with all boundary DoFs. In Section 3.3, a subset of the corresponding MDs is then calculated and extended to the linear ROB to properly consider the bending-stretching coupling effects. In Section 3.4, we discuss the computation of the reduced nonlinear force vector, which is computationally expensive. In this work, the reduced nonlinear force vector is directly expressed as a function of the generalized coordinates for each subsystem by applying matrix expansion. In Section 3.5, several numerical examples are discussed. Conclusions and outlook are provided in Section 3.6.

3.2. CRAIG-BAMPTON METHOD WITH INTERFACE REDUCTION

In this section, we first briefly outline the CB method (Bampton & Craig, 1968) for subsystems and primal assembly of the substructures. Afterwards, we apply system-level interface reduction to further reduce the size of the assembled reduced model.

Consider a nonlinear undamped system composed of H subsystems. The equation of motion (EoM) for the s^{th} substructure is written as

$$\mathbf{M}_{(s)}\ddot{\mathbf{u}}_{(s)}\{t\} + \mathbf{f}_{(s)}\left\{\mathbf{u}_{(s)}\{t\}\right\} = \mathbf{g}_{(s)}\{t\} + \mathbf{p}_{(s)}\{t\}, \quad s = 1,\ldots,H, \tag{3.1}$$

where $\mathbf{M}_{(s)}$ is the constant mass matrix, $\mathbf{f}_{(s)}$ is the nonlinear internal force vector, $\mathbf{g}_{(s)}$ is the external load, $\mathbf{p}_{(s)}$ is the vector of connecting loads imposed by neighboring subsystems and $\mathbf{u}_{(s)}$ is the vector of generalized nodal DoFs of the s^{th} decoupled nonlinear substructure. In this chapter, the argument of functional dependency is enclosed in curly brackets. For the sake of simplicity, the explicit time dependence will be omitted from here on. In this work, the mass matrices $\mathbf{M}_{(s)}$ and the external force vectors $\mathbf{g}_{(s)}$ are assumed to be configuration independent. Damping is neglected as well. The configuration-dependent tangent stiffness matrix is obtained as

$$\frac{\partial \mathbf{f}_{(s)}\{\mathbf{u}_{(s)}\}}{\partial \mathbf{u}_{(s)}} = \mathbf{K}_{(s)}\{\mathbf{u}_{(s)}\}. \tag{3.2}$$

A linearization of the system (3.1) around an equilibrium position leads to a set of linear EoMs. Without loss of generality, we assume the equilibrium configuration is $\mathbf{u}_{(s)} = \mathbf{0}$. The corresponding linear EoMs of the s^{th} subsystem are thus

$$\mathbf{M}_{(s)}\ddot{\mathbf{q}}_{(s)} + \overline{\mathbf{K}}_{(s)}\mathbf{q}_{(s)} = \mathbf{g}_{(s)} + \mathbf{p}_{(s)}, \quad s = 1,\ldots,H, \tag{3.3}$$

where $\overline{\mathbf{K}}_{(s)} = \mathbf{K}_{(s)}\{\mathbf{u}_{(s)} = \mathbf{0}\}$ is the linear stiffness matrix evaluated at equilibrium, and $\mathbf{q}_{(s)}$ is the corresponding vector of generalized nodal DoFs of the s^{th} linear substructure.

The EoM of all uncoupled subsystems can be grouped in a block-diagonal fashion for the nonlinear problem as

$$\mathbf{M}_{\mathcal{G}}\ddot{\mathbf{u}}_{\mathcal{G}} + \mathbf{f}_{\mathcal{G}}\{\mathbf{u}_{\mathcal{G}}\} = \mathbf{g}_{\mathcal{G}} + \mathbf{p}_{\mathcal{G}}, \tag{3.4}$$

and for the linear problem

$$\mathbf{M}_{\mathcal{G}}\ddot{\mathbf{q}}_{\mathcal{G}} + \overline{\mathbf{K}}_{\mathcal{G}}\mathbf{q}_{\mathcal{G}} = \mathbf{g}_{\mathcal{G}} + \mathbf{p}_{\mathcal{G}}, \tag{3.5}$$

respectively, where the subscript $\mathcal{G}$ indicates that the vectors and matrices are stacked (i.e. no assembly is performed) for the entire system.

3.2.1. CRAIG-BAMPTON METHOD

Let us now focus on the s^{th} substructure. The linear EoMs can be partitioned into internal DoFs $\mathbf{q}^{I}_{(s)} \in \mathbb{R}^{n^{I}_{(s)}}$ and boundary DoFs $\mathbf{q}^{B}_{(s)} \in \mathbb{R}^{n^{B}_{(s)}}$ with $n^{I}_{(s)} + n^{B}_{(s)} = n_{(s)}$, which gives

$$\mathbf{M}_{(s)}\ddot{\mathbf{q}}_{(s)} + \overline{\mathbf{K}}_{(s)}\mathbf{q}_{(s)} = \mathbf{g}_{(s)} + \mathbf{p}_{(s)} \Leftrightarrow \begin{bmatrix} \mathbf{M}^{BB}_{(s)} & \mathbf{M}^{BI}_{(s)} \\ \mathbf{M}^{IB}_{(s)} & \mathbf{M}^{II}_{(s)} \end{bmatrix} \begin{bmatrix} \ddot{\mathbf{q}}^{B}_{(s)} \\ \ddot{\mathbf{q}}^{I}_{(s)} \end{bmatrix} + \begin{bmatrix} \overline{\mathbf{K}}^{BB}_{(s)} & \overline{\mathbf{K}}^{BI}_{(s)} \\ \overline{\mathbf{K}}^{IB}_{(s)} & \overline{\mathbf{K}}^{II}_{(s)} \end{bmatrix} \begin{bmatrix} \mathbf{q}^{B}_{(s)} \\ \mathbf{q}^{I}_{(s)} \end{bmatrix} = \begin{bmatrix} \mathbf{g}^{B}_{(s)} \\ \mathbf{g}^{I}_{(s)} \end{bmatrix} + \begin{bmatrix} \mathbf{p}^{B}_{(s)} \\ \mathbf{0} \end{bmatrix}. \tag{3.6}$$

Typically, the number of boundary DoFs is much smaller than the number of internal DoFs ($n^B_{(s)} \ll n^I_{(s)}$). In the CB method, the dynamics of a substructure is described by a truncated set of IVMs, combined with a set of CMs which provide the connection to the neighboring subsystems. In order to calculate the CMs and IVMs as done in (Bampton & Craig, 1968), we assume that the external forces $\mathbf{g}_{(s)}$ are $\mathbf{0}$ since we are interested in the free vibration of the system.

The IVMs $\mathbf{\Phi}^{II}_{(s)}$ are obtained by solving the internal eigenvalue problem associated to free vibrations with fixed interface The CMs $\mathbf{\Psi}^{IB}_{(s)}$ represent the static responses of the internal DoFs that result from applying a unit displacement at one interface DoF while keeping the other interface DoFs fixed.

By means of $\mathbf{\Phi}^{II}_{(s)}$ and $\mathbf{\Psi}^{IB}_{(s)}$ we generate a projection basis for the s^{th} substructure, where the interface DoFs $\mathbf{q}^B_{(s)}$ are retained without reduction, as

$$\mathbf{q}_{(s)} = \begin{bmatrix} \mathbf{q}^B_{(s)} \\ \mathbf{q}^I_{(s)} \end{bmatrix} = \begin{bmatrix} \mathbf{I}^{BB}_{(s)} & \mathbf{0} \\ \mathbf{\Psi}^{IB}_{(s)} & \mathbf{\Phi}^{II}_{(s)} \end{bmatrix} \begin{bmatrix} \mathbf{q}^B_{(s)} \\ \boldsymbol{\eta}^I_{(s)} \end{bmatrix} \triangleq \mathbf{X}_{(s)} \boldsymbol{\gamma}_{(s)}, \tag{3.7}$$

where $\boldsymbol{\eta}^I_{(s)}$ is the vector of modal coordinates associated to the IVMs, $\mathbf{X}_{(s)}$ and $\boldsymbol{\gamma}_{(s)}$ are the CB reduction matrix and corresponding generalized coordinate vector of the s^{th} subsystem, respectively. The matrix $\mathbf{I}^{BB}_{(s)} \in \mathbb{R}^{n^B_{(s)} \times n^B_{(s)}}$ is an identity matrix. The reduced substructures need now to be assembled to form the system model.

3.2.2. PRIMAL ASSEMBLY OF COMPONENT MODELS

The CB transformations (3.7) for each substructure can be collected for the entire system in a block-diagonal form as

$$\mathbf{q}_{\mathcal{G}} = \mathbf{X}_{\mathcal{G}} \boldsymbol{\gamma}_{\mathcal{G}}, \tag{3.8}$$

where $\mathbf{X}_{\mathcal{G}} = \text{diag}(\mathbf{X}_{(1)}, \dots, \mathbf{X}_{(H)})$ is a block-diagonal matrix consisting of all substructure CB reduction matrices, and $\boldsymbol{\gamma}_{\mathcal{G}} = \text{col}(\boldsymbol{\gamma}_{(1)}, \dots, \boldsymbol{\gamma}_{(H)})$ is the stacked set of the generalized coordinates of subsystems for the global system.

The subsystems are here assembled in a primal manner (Voormeeren, 2012), i.e. a new reduced set of generalized coordinates of the assembled system $\boldsymbol{\xi}_{\mathcal{CB}}$ for the CB model is defined as

$$\boldsymbol{\xi}_{\mathcal{CB}} = \text{col}\left(\mathbf{q}^B_{\mathcal{CB}}, \boldsymbol{\eta}^I_{\mathcal{CB}}\right), \quad \text{with} \quad \boldsymbol{\eta}^I_{\mathcal{CB}} = \text{col}\left(\boldsymbol{\eta}^I_{(1)}, \dots, \boldsymbol{\eta}^I_{(H)}\right), \tag{3.9}$$

where $\mathbf{q}^B_{\mathcal{CB}} \in \mathbb{R}^{n^B_{\mathcal{CB}}}$ is a unique choice of all interface DoFs $\text{col}(\mathbf{q}^B_{(1)}, \dots, \mathbf{q}^B_{(H)})$ and $\boldsymbol{\eta}^I_{\mathcal{CB}} \in \mathbb{R}^{m^I_{\mathcal{CB}}}$ contains the internal generalized coordinates of all substructures. For the internal vibration modes, it holds that $m^I_{\mathcal{CB}} = \sum_{s=1}^{H} m^I_{(s)}$ since the internal DoFs of each substructure are independent. The compatibility condition ensures no relative motion between the boundaries of connected substructures.

To couple the adjacent subsystems in a primal way, the matching interface DoFs for any pair of adjacent substructure should have the same displacement, while the summation of the corresponding interface force vectors should be equal to zero. The primal EoMs of the coupled system can be obtained from a Galerkin projection as

$$\underbrace{\mathbf{L}^T_{\mathcal{CB}} \mathbf{X}^T_{\mathcal{G}} \mathbf{M}_{\mathcal{G}} \mathbf{X}_{\mathcal{G}} \mathbf{L}_{\mathcal{CB}}}_{\tilde{\mathbf{M}}_{\mathcal{CB}}} \ddot{\boldsymbol{\xi}}_{\mathcal{CB}} + \underbrace{\mathbf{L}^T_{\mathcal{CB}} \mathbf{X}^T_{\mathcal{G}} \overline{\mathbf{K}}_{\mathcal{G}} \mathbf{X}_{\mathcal{G}} \mathbf{L}_{\mathcal{CB}}}_{\tilde{\mathbf{K}}_{\mathcal{CB}}} \boldsymbol{\xi}_{\mathcal{CB}} = \underbrace{\mathbf{L}^T_{\mathcal{CB}} \mathbf{X}^T_{\mathcal{G}} \mathbf{g}_{\mathcal{G}}}_{\tilde{\mathbf{g}}_{\mathcal{CB}}}, \tag{3.10}$$

where $\mathbf{L}_{\mathcal{CB}}$ is the Boolean matrix primal assembly operator, and the connected force vectors from neighboring systems are eliminated to satisfy the force equilibrium condition. The matrices $\widetilde{\mathbf{M}}_{\mathcal{CB}}$, $\widetilde{\mathbf{K}}_{\mathcal{CB}}$ and $\widetilde{\mathbf{g}}_{\mathcal{CB}}$ are the assembled mass matrix, stiffness matrix, and load vector obtained after applying the CB substructuring and primal assembly.

The matrices and vectors $\widetilde{\mathbf{M}}_{\mathcal{CB}}$, $\widetilde{\mathbf{K}}_{\mathcal{CB}}$ and $\widetilde{\mathbf{g}}_{\mathcal{CB}}$ can be further partitioned into interface coordinates $\mathbf{q}^{B}_{\mathcal{CB}}$ and internal coordinates $\boldsymbol{\eta}^{I}_{\mathcal{CB}}$. The reduced EoMs (3.10) are therefore rewritten in a partitioned form as

$$\begin{bmatrix} \widetilde{\mathbf{M}}^{BB}_{\mathcal{CB}} & \widetilde{\mathbf{M}}^{BI}_{\mathcal{CB}} \\ \widetilde{\mathbf{M}}^{IB}_{\mathcal{CB}} & \mathbf{I}^{II}_{\mathcal{CB}} \end{bmatrix} \begin{bmatrix} \ddot{\mathbf{q}}^{B}_{\mathcal{CB}} \\ \ddot{\boldsymbol{\eta}}^{I}_{\mathcal{CB}} \end{bmatrix} + \begin{bmatrix} \widetilde{\mathbf{K}}^{BB}_{\mathcal{CB}} & \mathbf{0} \\ \mathbf{0} & \boldsymbol{\omega}^{2}_{\mathcal{CB}} \end{bmatrix} \begin{bmatrix} \mathbf{q}^{B}_{\mathcal{CB}} \\ \boldsymbol{\eta}^{I}_{\mathcal{CB}} \end{bmatrix} = \begin{bmatrix} \widetilde{\mathbf{g}}^{B}_{\mathcal{CB}} \\ \widetilde{\mathbf{g}}^{I}_{\mathcal{CB}} \end{bmatrix}, \tag{3.11}$$

where $\boldsymbol{\omega}^{2}_{\mathcal{CB}} = \mathrm{diag}(\boldsymbol{\omega}^{2}_{(1)}, \ldots, \boldsymbol{\omega}^{2}_{(H)})$ and $\mathbf{I}^{II}_{\mathcal{CB}} \in \mathbb{R}^{m^{I}_{\mathcal{CB}} \times m^{I}_{\mathcal{CB}}}$ is the identity matrix. The detailed formulation of the partitioned matrices $\widetilde{\mathbf{M}}^{BB}_{\mathcal{CB}}$ and $\widetilde{\mathbf{K}}^{BB}_{\mathcal{CB}}$ can be found in (Voormeeren, 2012), and will be not discussed here. If the finite element mesh is sufficiently fine and many substructures with distributed interfaces are considered, the size of these reduced system-level matrices is dominated by the interface DoFs. To overcome this problem, we can apply the system-level interface reduction such that truly compact models can be obtained.

3.2.3. SYSTEM-LEVEL INTERFACE REDUCTION

The system-level interface reduction was first proposed in (Craig Jr & Chang, 1977) and was further discussed in (Castanier *et al.*, 2001). As a starting point, we recall the assembled EoMs in (3.11) for the CB models. By fixing the internal DoFs for all subsystems, we obtain

$$\widetilde{\mathbf{M}}^{BB}_{\mathcal{CB}} \ddot{\mathbf{q}}^{B}_{\mathcal{CB}} + \widetilde{\mathbf{K}}^{BB}_{\mathcal{CB}} \mathbf{q}^{B}_{\mathcal{CB}} = \widetilde{\mathbf{g}}^{B}_{\mathcal{CB}}, \tag{3.12}$$

where $\widetilde{\mathbf{M}}^{BB}_{\mathcal{CB}} \in \mathbb{R}^{n^{B}_{\mathcal{CB}} \times n^{B}_{\mathcal{CB}}}, \widetilde{\mathbf{K}}^{BB}_{\mathcal{CB}} \in \mathbb{R}^{n^{B}_{\mathcal{CB}} \times n^{B}_{\mathcal{CB}}}$ are the interface partition of the assembled mass and stiffness matrices in (3.11). This equation is used to find the vibration behaviour at the interface DoFs. Hence, the interface modes can be computed from the eigenvalue analysis of (3.12) as

$$\left(\widetilde{\mathbf{K}}^{BB}_{\mathcal{CB}} - \widetilde{\omega}^{2}_{j} \widetilde{\mathbf{M}}^{BB}_{\mathcal{CB}}\right) \widetilde{\boldsymbol{\phi}}^{BB}_{j} = \mathbf{0}, \quad j = 1, \ldots, n^{B}_{\mathcal{CB}}, \tag{3.13}$$

where the system-level characteristic constraint (SCC) modes $\widetilde{\boldsymbol{\Phi}}^{BB} \in \mathbb{R}^{n^{B}_{\mathcal{CB}} \times m^{B}_{\mathcal{CC}}}$ are defined here as a truncated set of low-frequency eigenvectors $\widetilde{\boldsymbol{\Phi}}^{BB} = [\widetilde{\boldsymbol{\phi}}^{BB}_{1}, \ldots, \widetilde{\boldsymbol{\phi}}^{BB}_{m^{B}_{\mathcal{CC}}}]$, with $m^{B}_{\mathcal{CC}} \ll n^{B}_{\mathcal{CB}}$. The corresponding eigenvalues can be rewritten in diagonal matrix as $\widetilde{\boldsymbol{\omega}}^{2}_{\mathcal{CC}} = \mathrm{diag}(\widetilde{\omega}^{2}_{1}, \ldots, \widetilde{\omega}^{2}_{m^{B}_{\mathcal{CC}}})$.

Castanier (Castanier *et al.*, 2001) proposed to use this new set of SCC modes to reduce the interface DoFs, where a single SCC mode represents more global motion, as opposed to constraint modes. Depending on the frequency range of interest, the SCC modes can be used to generate a new CMS model with significantly reduced number of DoFs. By taking a selected set of SCC modes, the generalized modal coordinates $\boldsymbol{\xi}_{\mathcal{CB}}$ are approximated by stating

$$\boldsymbol{\xi}_{\mathcal{CB}} = \begin{bmatrix} \mathbf{q}^{B}_{\mathcal{CB}} \\ \boldsymbol{\eta}^{I}_{\mathcal{CB}} \end{bmatrix} = \begin{bmatrix} \widetilde{\boldsymbol{\Phi}}^{BB} & \mathbf{0} \\ \mathbf{0} & \mathbf{I} \end{bmatrix} \begin{bmatrix} \boldsymbol{\eta}^{B}_{\mathcal{CC}} \\ \boldsymbol{\eta}^{I}_{\mathcal{CB}} \end{bmatrix} \triangleq \mathbf{X}_{\mathcal{CC}} \boldsymbol{\xi}_{\mathcal{CC}}, \tag{3.14}$$

where $\mathbf{q}^{B}_{\mathcal{CB}}$ is reduced to a smaller set of generalized coordinates $\boldsymbol{\eta}^{B}_{\mathcal{CC}}$, while $\mathbf{X}_{\mathcal{CC}}$ and $\boldsymbol{\xi}_{\mathcal{CC}}$ are the compact expression of the reduction matrix and corresponding generalized coordinate vector after reduction via the secondary eigenvalue analysis.

The substitution of the interface reduction (3.14) into the assembly of CB equations (3.10) via a Galerkin projection then gives the final assembled EoMs for a linear system:

$$\underbrace{\mathbf{X}^{T}_{\mathcal{CC}}\mathbf{L}^{T}_{\mathcal{CB}}\mathbf{X}^{T}_{\mathcal{G}}\mathbf{M}_{\mathcal{G}}\mathbf{X}_{\mathcal{G}}\mathbf{L}_{\mathcal{CB}}\mathbf{X}_{\mathcal{CC}}}_{\widetilde{\mathbf{M}}_{\mathcal{CC}}}\ddot{\boldsymbol{\xi}}_{\mathcal{CC}}+\underbrace{\mathbf{X}^{T}_{\mathcal{CC}}\mathbf{L}^{T}_{\mathcal{CB}}\mathbf{X}^{T}_{\mathcal{G}}\overline{\mathbf{K}}_{\mathcal{G}}\mathbf{X}_{\mathcal{G}}\mathbf{L}_{\mathcal{CB}}\mathbf{X}_{\mathcal{CC}}}_{\widetilde{\mathbf{K}}_{\mathcal{CC}}}\boldsymbol{\xi}_{\mathcal{CC}}=\underbrace{\mathbf{X}^{T}_{\mathcal{CC}}\mathbf{L}^{T}_{\mathcal{CB}}\mathbf{X}^{T}_{\mathcal{G}}\mathbf{g}_{\mathcal{G}}}_{\widetilde{\mathbf{g}}_{\mathcal{CC}}}. \tag{3.15}$$

The final modal transformation, after applying the system-level interface reduction, can be expressed as

$$\mathbf{q}_{\mathcal{G}}=\left(\mathbf{X}_{\mathcal{G}}\mathbf{L}_{\mathcal{CB}}\mathbf{X}_{\mathcal{CC}}\right)\boldsymbol{\xi}_{\mathcal{CC}}. \tag{3.16}$$

The displacement compatibility and force equilibrium can be satisfied by directly considering the primal assembly operator $\mathbf{L}_{\mathcal{CB}}$ in the reduction basis in (3.16). Therefore the final reduced EoMs in (3.15) can also be obtained by directly substituting the reduction basis (3.16) into the global and uncoupled system (3.5).

Without loss of generality, we can derive the partitioned format of reduction basis for an arbitrary structure containing H substructures as

$$\mathbf{q}^{\mathcal{G}}=\begin{bmatrix}\mathbf{q}^{B}_{(1)}\\ \mathbf{q}^{I}_{(1)}\\ \vdots\\ \mathbf{q}^{B}_{(H)}\\ \mathbf{q}^{I}_{(H)}\end{bmatrix}=\underbrace{\begin{bmatrix}\mathbf{I}^{BB}_{(1)} & \mathbf{0} & \dots & \mathbf{0} & \mathbf{0}\\ \boldsymbol{\Psi}^{IB}_{(1)} & \boldsymbol{\Phi}^{II}_{(1)} & \dots & \mathbf{0} & \mathbf{0}\\ \vdots & \vdots & \ddots & \vdots & \vdots\\ \mathbf{0} & \mathbf{0} & \dots & \mathbf{I}^{BB}_{(H)} & \mathbf{0}\\ \mathbf{0} & \mathbf{0} & \dots & \boldsymbol{\Psi}^{IB}_{(H)} & \boldsymbol{\Phi}^{II}_{(H)}\end{bmatrix}}_{\mathbf{X}_{\mathcal{G}}}\underbrace{\begin{bmatrix}\mathbf{L}^{BB}_{(1)} & \mathbf{0} & \dots & \mathbf{0}\\ \mathbf{0} & \mathbf{I}^{II}_{(1)} & \dots & \mathbf{0}\\ \vdots & \vdots & \ddots & \vdots\\ \mathbf{L}^{BB}_{(H)} & \mathbf{0} & \dots & \mathbf{0}\\ \mathbf{0} & \mathbf{0} & \dots & \mathbf{I}^{II}_{(H)}\end{bmatrix}}_{\mathbf{L}_{\mathcal{CB}}}\underbrace{\begin{bmatrix}\widetilde{\boldsymbol{\Phi}}^{BB} & \mathbf{0} & \dots & \mathbf{0}\\ \mathbf{0} & \mathbf{I}^{II}_{(1)} & \dots & \mathbf{0}\\ \vdots & \vdots & \ddots & \vdots\\ \mathbf{0} & \mathbf{0} & \dots & \mathbf{I}^{II}_{(H)}\end{bmatrix}}_{\mathbf{X}_{\mathcal{CC}}}\begin{bmatrix}\boldsymbol{\eta}^{B}_{\mathcal{CC}}\\ \boldsymbol{\eta}^{I}_{(1)}\\ \vdots\\ \boldsymbol{\eta}^{I}_{(H)}\end{bmatrix}=\begin{bmatrix}\widetilde{\boldsymbol{\Phi}}^{BB}_{(1)} & \mathbf{0} & \dots & \mathbf{0}\\ \widetilde{\boldsymbol{\Phi}}^{IB}_{(1)} & \boldsymbol{\Phi}^{II}_{(1)} & \dots & \mathbf{0}\\ \vdots & \vdots & \ddots & \vdots\\ \widetilde{\boldsymbol{\Phi}}^{BB}_{(H)} & \mathbf{0} & \dots & \mathbf{0}\\ \widetilde{\boldsymbol{\Phi}}^{IB}_{(H)} & \mathbf{0} & \dots & \boldsymbol{\Phi}^{II}_{(H)}\end{bmatrix}\begin{bmatrix}\boldsymbol{\eta}^{B}_{\mathcal{CC}}\\ \boldsymbol{\eta}^{I}_{(1)}\\ \vdots\\ \boldsymbol{\eta}^{(H)}_{i}\end{bmatrix} \tag{3.17}$$

where the matrices $\mathbf{X}_{\mathcal{G}}$, $\mathbf{L}_{\mathcal{CB}}$ and $\mathbf{X}_{\mathcal{CC}}$ are all written here as partitioned forms. $\mathbf{L}^{BB}_{(s)}$ is the interface-level Boolean matrix to select $\mathbf{q}^{B}_{(s)}$ of the s^{th} substructure from the global interface DoFs $\mathbf{q}^{B}_{\mathcal{CB}}$.

The first column of the reduction basis in (3.17) contains the SCC modes of the entire system, which are denoted here as $\widetilde{\boldsymbol{\Phi}}_{\mathcal{CC}}$. In (3.17), $\widetilde{\boldsymbol{\Phi}}_{\mathcal{CC}}$ has been partitioned as $\widetilde{\boldsymbol{\Phi}}^{BB}_{(s)}$ and $\widetilde{\boldsymbol{\Phi}}^{IB}_{(s)}$ of the s^{th} substructure, according to the corresponding interface and internal DoFs, respectively. It holds that

$$\widetilde{\boldsymbol{\Phi}}^{BB}_{(s)}=\mathbf{L}^{BB}_{(s)}\widetilde{\boldsymbol{\Phi}}^{BB}\quad\text{and}\quad\widetilde{\boldsymbol{\Phi}}^{IB}_{(s)}=\boldsymbol{\Psi}^{IB}_{(s)}\mathbf{L}^{BB}_{(s)}\widetilde{\boldsymbol{\Phi}}^{BB}=\boldsymbol{\Psi}^{IB}_{(s)}\widetilde{\boldsymbol{\Phi}}^{BB}_{(s)}. \tag{3.18}$$

As observed in (3.18), $\widetilde{\boldsymbol{\Phi}}^{IB}_{(s)}$ presents a linear combination of all CMs $\boldsymbol{\Psi}^{IB}_{(s)}$, and exhibits the geometrically *linear* deformation of internal DoFs according to the shape of interface DoFs $\widetilde{\boldsymbol{\Phi}}^{BB}_{(s)}$. The second to last columns of the reduction basis in (3.17) represent the ROBs containing the IVMs of each substructure.

For illustration, we consider here the structure shown in Fig. 3.1. The structure is composed of two substructures ($\mathbf{S}_1$ and $\mathbf{S}_2$) and connected together through the interface $\mathbf{q}^{B}_{\mathcal{G}}$. The reduction basis contains three sets of modes: a truncated set of SCC modes exhibiting global deformations of the assembled system, and a truncated set of IVMs for each of the two substructures.

In principle, the reduced EoMs of a nonlinear system can be similarly obtained by substituting (3.17) into the nonlinear EoMs of the entire and uncoupled system in (3.4)

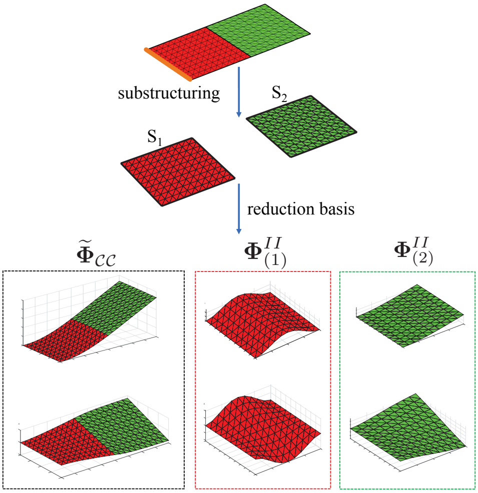

Figure 3.1: Illustration of the reduction basis of a two sub-component shell structure. The structure is cantilevered at the end of S_1. The first two SCC modes of the assembled system and the first two IVMs of each substructure have been plotted here.

through a Galerkin projection. However, a ROM based solely on low-frequency SCC mode and IVMs would perform poorly when geometric nonlinearities are considered, because they can not capture bending-stretching couplings effectively. A remedy of this shortcoming is discussed in the next section.

3.3. ENHANCED CRAIG-BAMPTON TECHNIQUE WITH MODAL DERIVATIVES

The classic CB basis with interface reduction, constructed with the low-frequency SCC modes and IVMs, is not well-suited for the reduction of geometrical nonlinear systems. Take the two-components shell structure in Fig. 3.1 as an example. The first few SCC modes and IVMs exhibit bending dominant displacement fields. This would require the inclusion of membrane dominant modes in the basis to capture the geometric nonlinear effect. These modes will be high frequency vibration modes. However, since one does not know in advance their corresponding eigenfrequency, their extraction is difficult and expensive, as many modes need to be computed. Also, for more complex and realistic components, the distinction between axial and bending/twisting dominated modes can be difficult to establish.

As discussed in the introduction, MDs are effective additions to the reduction basis to capture geometric nonlinear behavior. Originally proposed in (Idelsohn & Cardona, 1985*a*,*b*), the MDs are defined by differentiating the nonlinear eigenvalue problem with respect to the modal amplitudes. This generates somewhat cumbersome expressions, as the derivatives of frequencies need also to be computed. Slaats (Slaats *et al.*, 1995) stated that multiplication of all masses by the same factor does not influence the shape of the MDs, provided the mass matrix is constant (the inertia terms are assumed to be configuration independent). Related to this property, a simplified definition is also given by neglecting these inertia related terms. This technique is usually addressed as the “definition without mass consideration", or more recently, “static modal derivatives" (Jain *et al.*, 2017). Most of the authors (Weeger *et al.*, 2014, Barbic & James, 2005, Barbic & Zhao, 2011, Tiso *et al.*, 2011, Wu & Tiso, 2016, Weeger, 2015) applying MDs for MOR have been using this simplified definition, since the elastic effects, instead of the inertia effects, are generally the key factor to trigger the geometrical nonlinearities (Haller & Ponsioen, 2017). Because inertial effects are often neglected, many researchers prefer to compute the MDs from the static nonlinear problems directly, as in the Remark 1 of (Rutzmoser *et al.*, 2017), as well as in (Jain *et al.*, 2017, Weeger *et al.*, 2016). In this paper, we follow the same fashion and derive all the static MDs in both substructure-level and assembled-level.

One of the key aspects of this work is the enhancement of both SCC modes and IVMs with the corresponding MDs, as described in this section.

3.3.1. MODAL DERIVATIVES ENHANCED BASIS

In this work, we consider the static linearized problem of a single substructure. The static equilibrium equation of the s^{th} subsystem

$$\overline{\mathbf{K}}^{II}_{(s)}\mathbf{q}^{I}_{(s)} = \mathbf{g}^{I}_{(s)} \tag{3.19}$$

is obtained by fixing the interface DoFs. By assuming that the external force vector is a superposition of stiffness-weighted IVMs as

$$\mathbf{g}^{I}_{(s)} = \overline{\mathbf{K}}^{II}_{(s)}\mathbf{\Phi}^{II}_{(s)}\mathbf{y}_{(s)}, \tag{3.20}$$

the corresponding linear displacement $\mathbf{q}^{I}_{(s)}$ lives in a subspace spanned by the truncated IVMs $\mathbf{\Phi}^{II}_{(s)}$. If the external load vector $\mathbf{g}^{I}_{(s)}$ can be expressed as in (3.20), then the reduction $\mathbf{q}^{I}_{(s)} = \mathbf{\Phi}^{II}_{(s)}\eta^{I}_{(s)}$ is exact for linear static problems.

We are now looking for the solution of a nonlinear static problem with the same external load condition:

$$\mathbf{f}^{I}_{(s)}\left\{\mathbf{u}^{I}_{(s)}\right\} = \mathbf{g}^{I}_{(s)} \quad \text{and} \quad \mathbf{g}^{I}_{(s)} = \overline{\mathbf{K}}^{II}_{(s)}\mathbf{\Phi}^{II}_{(s)}\mathbf{y}_{(s)}, \tag{3.21}$$

where the interface DoFs are fixed, and the external load vector is still a linear superposition of the truncated IVMs. For the nonlinear force vector $\mathbf{f}^{I}_{(s)}$, it should hold that $\mathbf{f}^{I}_{(s)}\left\{\mathbf{u}^{I}_{(s)} = \mathbf{0}\right\} = \mathbf{0}$, as assumed in Section 3.2.1.

It is difficult to find a closed-form solution $\mathbf{u}^{I}_{(s)}\left\{\mathbf{y}_{(s)}\right\}$ for (3.21). However, by assuming that the nonlinear displacement vector $\mathbf{u}^{I}_{(s)}$ is C^2 differentiable with respect to modal amplitude vector $\mathbf{y}_{(s)}$, we can write a Taylor expansion around $\mathbf{y}_{(s)} = \mathbf{0}$ as

$$\mathbf{u}^{I}_{(s)}\left\{\mathbf{y}_{(s)}\right\} = \mathbf{0} + \sum_{j=1}^{m^{I}_{(s)}} \left.\frac{\partial\, \mathbf{u}^{I}_{(s)}}{\partial\, y_{j,(s)}}\right|_{0} y_{j,(s)} + \frac{1}{2}\sum_{j=1}^{m^{I}_{(s)}}\sum_{l=1}^{m^{I}_{(s)}} \left.\frac{\partial^2 \mathbf{u}^{I}_{(s)}}{\partial y_{j,(s)}\, \partial y_{l,(s)}}\right|_{0} y_{j,(s)}\, y_{l,(s)} + \mathcal{O}(||\mathbf{y}_{(s)}||^3), \tag{3.22}$$

where $y_{j,(s)}$ is the j^{th} modal parameter in the vector $\mathbf{y}_{(s)}$ of the s^{th} subsystem.

In order to find the derivatives in (3.22), we first notice that both sides of (3.21) are functions of the modal amplitudes $\mathbf{y}_{(s)}$, and then differentiate both sides of (3.21) with respect to $y_{j,(s)}$ as

$$\frac{\mathrm{d}\mathbf{f}^I_{(s)}}{\mathrm{d}\mathbf{u}^I_{(s)}}\frac{\partial \mathbf{u}^I_{(s)}}{\partial y_{j,(s)}} = \frac{\partial \mathbf{g}^I_{(s)}}{\partial y_{j,(s)}} = \overline{\mathbf{K}}^{II}_{(s)}\boldsymbol{\phi}^{II}_{j,(s)}, \tag{3.23}$$

where $\boldsymbol{\phi}^{II}_{j,(s)}$ is the vector of j^{th} mode in the truncated set of IVMs. Evaluating 3.23 around $\mathbf{y}_{(s)} = \mathbf{0}$, we obtain

$$\overline{\mathbf{K}}^{II}_{(s)}\left.\frac{\partial \mathbf{u}^I_{(s)}}{\partial y_{j,(s)}}\right|_0 = \overline{\mathbf{K}}^{II}_{(s)}\boldsymbol{\phi}^{II}_{j,(s)} \quad \Rightarrow \quad \left.\frac{\partial \mathbf{u}^I_{(s)}}{\partial y_{j,(s)}}\right|_0 = \boldsymbol{\phi}^{II}_{j,(s)}, \tag{3.24}$$

i.e. the first derivatives of the nonlinear displacement vector $\mathbf{u}^I_{(s)}$ with respect to $\mathbf{y}_{(s)}$ are the truncated set of IVMs.

Since we assume that $\mathbf{u}^I_{(s)}$ is C^2 differentiable with respect to $\mathbf{y}_{(s)}$, we can differentiate both sides of (3.23) again with respect to $y_{l,(s)}$ by stating

$$\left(\frac{\mathrm{d}^2\mathbf{f}^I_{(s)}}{\mathrm{d}(\mathbf{u}^I_{(s)})^2}\frac{\partial \mathbf{u}^I_{(s)}}{\partial y_{l,(s)}}\right)\frac{\partial \mathbf{u}^I_{(s)}}{\partial y_{j,(s)}} + \frac{\mathrm{d}\mathbf{f}^I_{(s)}}{\mathrm{d}\mathbf{u}^I_{(s)}}\frac{\partial^2 \mathbf{u}^I_{(s)}}{\partial y_{l,(s)}\partial y_{j,(s)}} = \mathbf{0}. \tag{3.25}$$

It should be noticed that the second derivatives of the load vector with respect to the modal amplitudes (i.e. the right hand side of the equation) is a null vector since we assume the load vector is a linear superposition of the selected modes. Evaluation at $\mathbf{y}_{(s)} = \mathbf{0}$ will give

$$\left(\left.\frac{\mathrm{d}^2\mathbf{f}^I_{(s)}}{\mathrm{d}(\mathbf{u}^I_{(s)})^2}\right|_0 \boldsymbol{\phi}^{II}_{l,(s)}\right)\boldsymbol{\phi}^{II}_{j,(s)} + \overline{\mathbf{K}}^{II}_{(s)}\left.\frac{\partial^2 \mathbf{u}^I_{(s)}}{\partial y_{l,(s)}\partial y_{j,(s)}}\right|_0 = \mathbf{0}. \tag{3.26}$$

Note that $\left.\frac{\mathrm{d}^2\mathbf{f}^I_{(s)}}{\mathrm{d}(\mathbf{u}^I_{(s)})^2}\right|_0 \boldsymbol{\phi}^{II}_{l,(s)}$ is the directional derivative of internal tangent stiffness matrix $\mathbf{K}^{II}_{(s)}$ with respect to modal amplitude $y_{l,(s)}$ of mode $\boldsymbol{\phi}^{II}_{l,(s)}$, i.e.

$$\left.\frac{\mathrm{d}^2\mathbf{f}^I_{(s)}}{\mathrm{d}(\mathbf{u}^I_{(s)})^2}\right|_0 \boldsymbol{\phi}^{II}_{l,(s)} = \left.\frac{\mathrm{d}\mathbf{K}^{II}_{(s)}}{\mathrm{d}\mathbf{u}^I_{(s)}}\right|_0 \cdot \left.\frac{\partial \mathbf{u}^I_{(s)}}{\partial y_{l,(s)}}\right|_0 = \left.\frac{\partial \mathbf{K}^{II}_{(s)}}{\partial y_{l,(s)}}\right|_0 = \lim_{y_{l,(s)}\to 0}\frac{1}{y_{l,(s)}}\left[\mathbf{K}^{II}_{(s)}\left\{\boldsymbol{\phi}^{II}_{l,(s)}y_{l,(s)}\right\} - \overline{\mathbf{K}}^{II}_{(s)}\right]. \tag{3.27}$$

The second derivatives of the nonlinear responses with respect to the modal amplitudes $\left.\frac{\partial^2 \mathbf{u}^I_{(s)}}{\partial y_{l,(s)}\partial y_{j,(s)}}\right|_0$ can be obtained from the solution of Eq (3.26) as

$$\left.\frac{\partial^2 \mathbf{u}^I_{(s)}}{\partial y_{l,(s)}\partial y_{j,(s)}}\right|_0 = -\left(\overline{\mathbf{K}}^{II}_{(s)}\right)^{-1}\left.\frac{\partial \mathbf{K}^{II}_{(s)}}{\partial y_{l,(s)}}\right|_0 \boldsymbol{\phi}^{II}_{j,(s)} \triangleq \boldsymbol{\vartheta}^{II}_{jl,(s)}. \tag{3.28}$$

The obtained vector $\left.\frac{\partial^2 \mathbf{u}^I_{(s)}}{\partial y_{l,(s)}\partial y_{j,(s)}}\right|_0$ is the MD, and is denoted here as $\boldsymbol{\vartheta}^{II}_{jl,(s)}$.

The Taylor expression (3.22) is now rewritten as

$$\mathbf{u}^{I}_{(s)}\left\{\mathbf{y}_{(s)}\right\} = \sum_{j=1}^{m^{I}_{(s)}} \boldsymbol{\phi}^{II}_{j,(s)} y_{j,(s)} + \frac{1}{2} \sum_{j=1}^{m^{I}_{(s)}} \sum_{l=1}^{m^{I}_{(s)}} \boldsymbol{\vartheta}^{II}_{jl,(s)} y_{j,(s)} y_{l,(s)}. \tag{3.29}$$

At this stage, a linear basis consisting of IVMs and MDs could be then used to reduce the internal dynamics of each component. The reduction basis is then written as

$$\begin{bmatrix} \boldsymbol{\phi}^{II}_{1,(s)} & \cdots & \boldsymbol{\phi}^{II}_{m^{I}_{(s)},(s)} & \cdots & \boldsymbol{\vartheta}^{II}_{jl,(s)} & \cdots \end{bmatrix} \triangleq \begin{bmatrix} \boldsymbol{\Phi}^{II}_{(s)} & \boldsymbol{\Theta}^{II}_{(s)} \end{bmatrix}, \tag{3.30}$$

where $\boldsymbol{\Theta}^{II}_{(s)} \in \mathbb{R}^{n^{I}_{(s)} \times r^{I}_{(s)}}$ is a matrix containing the MDs, and $r^{I}_{(s)}$ is the number of MDs included in $\boldsymbol{\Theta}^{II}_{(s)}$. According to Clairaut's theorem (also called Schwarz's theorem), the second order derivatives $\frac{\mathrm{d}^2 \mathbf{f}^{I}_{(s)}}{\mathrm{d}(\mathbf{u}^{I}_{(s)})^2}$ in (3.27) are symmetric because the internal force vector $\mathbf{f}^{I}_{(s)} \in C^2(\mathbb{R}^{n^{I}_{(s)}}, \mathbb{R}^{n^{I}_{(s)}})$. Therefore, it can be proven that the MDs are also symmetric, i.e. $\boldsymbol{\vartheta}^{II}_{jl,(s)} = \boldsymbol{\vartheta}^{II}_{lj,(s)}$. Interested readers can find the details in (Weeger, 2015). It should be noticed that the symmetry only holds for the static MDs, i.e., when the inertial effects are neglected and the tangent stiffness matrix is symmetric. Given $m^{I}_{(s)}$ IVMs in the reduction basis, a maximum number of $r^{I}_{(s)} = m^{I}_{(s)}(m^{I}_{(s)}+1)/2$ MDs can be calculated, and inserted in the matrix $\boldsymbol{\Theta}^{II}_{(s)}$. Indeed, including MDs in the reduction basis will increase the number of modal coordinates quadratically with respect to the number of IVMs ($m^{I}_{(s)}$) in the basis. The internal displacement of the s^{th} substructure, when the interface is fixed, is then approximated as

$$\mathbf{u}^{I}_{(s)} = \begin{bmatrix} \boldsymbol{\Phi}^{II}_{(s)} & \boldsymbol{\Theta}^{II}_{(s)} \end{bmatrix} \begin{bmatrix} \boldsymbol{\eta}^{I}_{(s)} \\ \boldsymbol{\zeta}^{I}_{(s)} \end{bmatrix}. \tag{3.31}$$

It is emphasized that Eq. (3.29) is a special instance of the general linear manifold defined by (3.31). The modal amplitudes of the MDs are enslaved to those of the IVMs in (3.29), while they are free to assume any value in (3.31). Therefore, the approximate solution based on (3.31) will generally be better than the approximation obtained with (3.29) through Galerkin projection, at the price of adding extra modal coordinates $\boldsymbol{\zeta}^{I}_{(s)}$.

The inclusion of MDs with respect to IVMs is not enough to describe the geometric nonlinear behavior occurring at the interface, since all the corresponding MDs are fixed at the interface. The basis of SCC modes of the assembled system can be enriched with the corresponding MDs in the same fashion as

$$\mathbf{u}_{\mathcal{G}} = \begin{bmatrix} \widetilde{\boldsymbol{\Phi}}_{CC} & \widetilde{\boldsymbol{\Theta}}_{CC} \end{bmatrix} \begin{bmatrix} \boldsymbol{\eta}^{B}_{CC} \\ \boldsymbol{\zeta}^{B}_{CC} \end{bmatrix}, \tag{3.32}$$

where $\widetilde{\boldsymbol{\Theta}}_{CC} \in \mathbb{R}^{n_{\mathcal{G}} \times r^{B}_{CC}}$ are the modal derivatives corresponding to the SCC mode for the assembled system. The number of MDs included in the matrix $\widetilde{\boldsymbol{\Theta}}_{CC}$ is denoted by r^{B}_{CC}. The computation of $\widetilde{\boldsymbol{\Theta}}_{CC}$ follows an analogous procedure as for $\boldsymbol{\Theta}^{II}_{(s)}$.

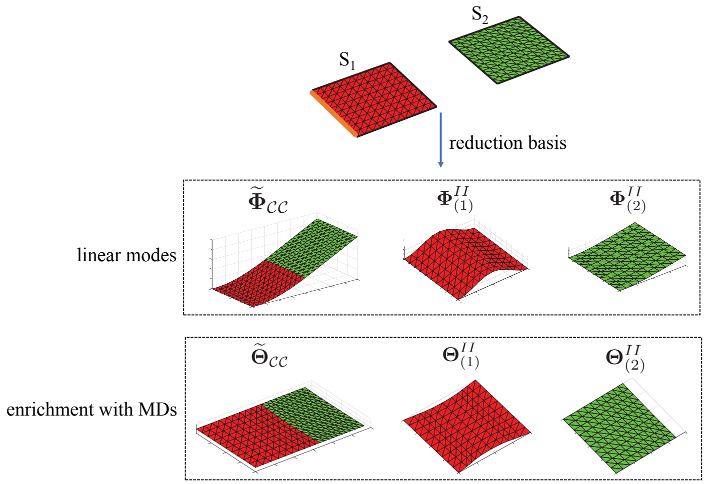

Figure 3.2: Illustration of the enhanced reduction basis of a two substructures shell structure.

By combining (3.31) and (3.32), we obtain the enhanced Craig-Bampton (ECB) basis $\mathbf{V} \in \mathbb{R}^{n_{\mathcal{G}} \times z_{\mathcal{G}}}$ for the entire system as

$$\mathbf{u}_{\mathcal{G}} = \begin{bmatrix} \mathbf{u}^B_{(1)} \\ \mathbf{u}^I_{(1)} \\ \vdots \\ \mathbf{u}^B_{(H)} \\ \mathbf{u}^I_{(H)} \end{bmatrix} = \begin{bmatrix} \widetilde{\boldsymbol{\Phi}}^{BB}_{(1)} & \widetilde{\boldsymbol{\Theta}}^{BB}_{(1)} & \mathbf{0} & \mathbf{0} & \dots & \mathbf{0} & \mathbf{0} \\ \widetilde{\boldsymbol{\Phi}}^{IB}_{(1)} & \widetilde{\boldsymbol{\Theta}}^{IB}_{(1)} & \boldsymbol{\Phi}^{II}_{(1)} & \boldsymbol{\Theta}^{II}_{(1)} & \dots & \mathbf{0} & \mathbf{0} \\ \vdots & \vdots & \vdots & \vdots & \ddots & \vdots & \vdots \\ \widetilde{\boldsymbol{\Phi}}^{BB}_{(H)} & \widetilde{\boldsymbol{\Theta}}^{BB}_{(H)} & \mathbf{0} & \mathbf{0} & \dots & \mathbf{0} & \mathbf{0} \\ \widetilde{\boldsymbol{\Phi}}^{IB}_{(H)} & \widetilde{\boldsymbol{\Theta}}^{IB}_{(H)} & \mathbf{0} & \mathbf{0} & \dots & \boldsymbol{\Phi}^{II}_{(H)} & \boldsymbol{\Theta}^{II}_{(H)} \end{bmatrix} \begin{bmatrix} \boldsymbol{\eta}^B_{CC} \\ \boldsymbol{\zeta}^B_{CC} \\ \boldsymbol{\eta}^I_{(1)} \\ \boldsymbol{\zeta}^I_{(1)} \\ \vdots \\ \boldsymbol{\eta}^I_{(H)} \\ \boldsymbol{\zeta}^I_{(H)} \end{bmatrix} \triangleq \mathbf{V}\boldsymbol{\xi}_{ECB} \qquad (3.33)$$

where each block column of modes in (3.17) is now augmented with corresponding MDs in (3.33), with $z_{\mathcal{G}} = m^B_{CC} + r^B_{CC} + \sum_{s=1}^{H}(m^I_{(s)} + r^I_{(s)})$. The blocks $\widetilde{\boldsymbol{\Theta}}^{BB}_{(s)} \in \mathbb{R}^{n^B_{(s)} \times r^B_{CC}}$ and $\widetilde{\boldsymbol{\Theta}}^{IB}_{(s)} \in \mathbb{R}^{n^I_{(s)} \times r^B_{CC}}$ are the rows of MDs $\widetilde{\boldsymbol{\Theta}}_{CC}$ corresponding to the interface DoFs and internal DoFs of the s^{th} subsystem, respectively.

To illustrate the proposed approach, Fig. 3.2 shows the enhanced reduction basis of the two-component shell structure shown before. Compared to Fig. 3.1, the MDs corresponding to the SCC modes and IVMs have been appended to the original linear basis. The MDs capture the inherent stretching effects with respect to the bending dominant modes of the flat structure.

The final reduced EoMs for the entire system can be obtained by substituting (3.33) into the nonlinear EoMs of the entire uncoupled system (3.4) through Galerkin projection as

$$\underbrace{\mathbf{V}^T\mathbf{M}_{\mathcal{G}}\mathbf{V}}_{\widetilde{\mathbf{M}}_{ECB}}\ddot{\boldsymbol{\xi}}_{ECB}+\underbrace{\mathbf{V}^T\mathbf{f}_{\mathcal{G}}\left\{\mathbf{V}\boldsymbol{\xi}_{ECB}\right\}}_{\widetilde{\mathbf{f}}_{ECB}}=\underbrace{\mathbf{V}^T\mathbf{g}_{\mathcal{G}}}_{\widetilde{\mathbf{g}}_{ECB}}, \tag{3.34}$$

where $\widetilde{\mathbf{M}}_{ECB} \in \mathbb{R}^{z_{\mathcal{G}} \times z_{\mathcal{G}}}$, $\widetilde{\mathbf{f}}_{ECB} \in \mathbb{R}^{z_{\mathcal{G}}}$ and $\widetilde{\mathbf{g}}_{ECB} \in \mathbb{R}^{z_{\mathcal{G}}}$ are the mass matrices, internal force vector and external force vector of the nonlinear reduced model.

3.3.2. OPTIMAL MODAL DERIVATIVES BASIS SELECTION

The basic idea of MDs selection criterion, formalized in (Tiso, 2011, Jain *et al.*, 2017) and named maximum modal interaction (MMI), is to estimate the modal interaction between different modes based on a linear modal solution with the same load condition. Following this idea, we first calculate the modal amplitudes of different modes related to the same external load condition for a linearized calculation, which is computationally cheap to obtain. Next, we build a weighting matrix for the SCC modes

$$\widetilde{\mathbf{W}}_{ij,\,\mathcal{CC}}=\int_0^T\left|\eta^B_{i,\mathcal{CC}}\{t\}\,\eta^B_{j,\mathcal{CC}}\{t\}\right|\mathrm{d}t, \tag{3.35}$$

and for the IVMs

$$\mathbf{W}_{ij,(s)}=\int_0^T\left|\eta^I_{i,(s)}\{t\}\,\eta^I_{j,(s)}\{t\}\right|\mathrm{d}t, \tag{3.36}$$

respectively, where $[0,T]$ is the time interval over which the simulation is performed. Here, $\widetilde{\mathbf{W}}_{ij,\mathcal{CC}}$ and $\mathbf{W}_{ij,(s)}$ represents the weight of the corresponding MDs with respect to the SCC modes and IVMs in the s^{th} subsystem, respectively, and $\boldsymbol{\eta}^B_{i,\mathcal{CC}}$ and $\boldsymbol{\eta}^I_{i,(s)}$ are the time varying amplitude of the i^{th} SCC modes and IVMs in the s^{th} subsystem when the linear reduced system (3.11) is excited with the external load over the time range $[0,T]$.

The magnitudes of the entries of the weighting matrices give an indication of potential modal interaction of the modes in a nonlinear analysis with the same load condition. We assume that if the relative weightage between two arbitrary modes is high for the given time span, then the interaction between these two modes in the nonlinear regime is likely to be strong. Therefore, the inclusion of the MDs associated to such modes in the reduction basis is necessary. We rank the relative importance of all MDs in the same fashion.

It should be noted that, although the MMI selection criterion uses weights to rank the MDs in terms of relative importance, it does not yield a truncation threshold. Thus, there is a need for further work in this area. Since the MMI criterion only relies on the modal amplitudes obtained from a linear, modal analysis with the same load conditions, the computational cost for this criterion is marginal. However, the MMI criterion ranks MDs associated to IVMs of each substructure independently. This criterion is not the absolute selection criterion for all the MDs. Thus, there is a need for further work in this area. Moreover, since the selection of the MDs depends on the external load used to simulate the linearized model, the sensitivity of the modes selection with respect to the load condition should be further investigated, especially for cases where multiple loads need to be evaluated.

3.4. COMPUTATIONAL EFFICIENCY FOR REDUCED TIME INTEGRATION

The reduction in computational time that could be achieved by applying the proposed reduction method will be discussed in this section. We use here an implicit Newmark scheme for the time integration, with parameters $\mu = \frac{1}{2}, \beta = \frac{1}{4}$. For the sake of completeness, the Newmark iteration scheme (Geradin & Rixen, 1997) for the full system, also called high fidelity model (HFM), is summarized in Algorithm 1.

Algorithm 1 Newmark time integration algorithm for the HFM (no substructuring)

```
Input: Intial condition:$\mathbf{u}_0, \dot{\mathbf{u}}_0$;   Newmark scheme parameters:$\mu, \beta, T, \Delta t$;
    Residual tolerance:$\epsilon$; Mass matrix:$\mathbf{M}$; external load:$\mathbf{g}\{t\}$
Output: Nonlinear response: $\mathbf{u}\{t\}$
 1: $\ddot{\mathbf{u}}_0 = \mathbf{M}^{-1}\left(\mathbf{g}_0 - \mathbf{f}\{\mathbf{u}_0\}\right)$    ▷ Initializing $\ddot{\mathbf{u}}_0$
 2: while $t < T$ do    ▷ Time matching loop
 3:     $p+1 := p$
 4:     $t_{p+1} := t_p + \Delta t$    ▷ Time increment
 5:     $\dot{\mathbf{u}}_{p+1} := \dot{\mathbf{u}}_p + (1-\mu)\Delta t \ddot{\mathbf{u}}_p$; $\mathbf{u}_{p+1} := \mathbf{u}_p + \Delta t \dot{\mathbf{u}}_p + (0.5-\beta)\Delta t^2 \ddot{\mathbf{u}}_p$; $\ddot{\mathbf{u}}_{p+1} := \mathbf{0}$    ▷ Prediction
 6:     Update $\mathbf{f}\{\mathbf{u}_{p+1}\}$ and $\mathbf{K}\{\mathbf{u}_{p+1}\}$    ▷ Update the internal force vector and tangent stiffness matrix
 7:     $\mathbf{R}_{p+1} = \mathbf{M}\ddot{\mathbf{u}}_{p+1} + \mathbf{f}\left\{\mathbf{u}_{p+1}\right\} - \mathbf{g}_{p+1}$    ▷ Residual evaluation
 8:     if $||\mathbf{R}_{p+1}|| > \epsilon||\mathbf{f}\{\mathbf{u}_{p+1}\}||$ then    ▷ Start iteration, convergence check
 9:         $\mathbf{S}\left\{\mathbf{u}_{p+1}\right\} = \mathbf{K}\left\{\mathbf{u}_{p+1}\right\} + \frac{1}{\beta\Delta t^2}\mathbf{M}$    ▷ Calculate Jacobian matrix $\mathbf{S}$
10:         $\Delta\mathbf{u} = -\left(\mathbf{S}\left\{\mathbf{u}_{p+1}\right\}\right)^{-1}\mathbf{R}_{p+1}$    ▷ Increment calculation
11:         $\mathbf{u}_{p+1} := \mathbf{u}_{p+1} + \Delta\mathbf{u}$; $\dot{\mathbf{u}}_{p+1} := \dot{\mathbf{u}}_{p+1} + \frac{\mu}{\beta\Delta t}\Delta\mathbf{u}$; $\ddot{\mathbf{u}}_{p+1} := \ddot{\mathbf{u}}_{p+1} + \frac{1}{\beta\Delta t^2}\Delta\mathbf{u}$    ▷ Correction
12:         Update $\mathbf{f}\{\mathbf{u}_{p+1}\}$ and $\mathbf{K}\{\mathbf{u}_{p+1}\}$    ▷ Update the internal force vector and tangent stiffness matrix
13:         $\mathbf{R}_{p+1} = \mathbf{M}\ddot{\mathbf{u}}_{p+1} + \mathbf{f}\left\{\mathbf{u}_{p+1}\right\} - \mathbf{g}_{p+1}$    ▷ Residual evaluation
14:     end if    ▷ End iteration
15: end while
```

The Newton-Raphson loop is repeated during every time step until the convergence condition is satisfied. The two most time-consuming operations are: i) the update of the configuration dependent internal forces $\mathbf{f}\{\mathbf{u}\}$ and tangent stiffness matrix $\mathbf{K}\{\mathbf{u}\}$ (Line 6 and 12); ii) the increment calculation (Line 10), which requires the factorization of the large sparse symmetric matrix $\mathbf{S}\{\mathbf{u}\}$. For complicated system with a large number of DoFs, the factorization will become computational demanding. The complexity of the factorization of a sparse $n \times n$ matrix depends largely on the nature of sparseness. For instance, if the upper and lower bandwidth of the matrix can be approximated as $\sqrt{n}$, applying LU decomposition for this matrix only requires $\mathcal{O}(n^2)$ flops (Golub & Van L., 2012). Without loss of generality, the complexity of the solution of a sparse $n \times n$ system is $\mathcal{O}(s\{n\})$, where $s\{n\}$ is a function depending on the solver characteristics and matrix bandwidth.

Generally, the nonlinear force $\mathbf{f}\{\mathbf{u}\}$ and tangent stiffness operator $\mathbf{K}\{\mathbf{u}\}$ are computed for the HFM, and then projected on the reduced basis at each time-step to obtain the reduced terms $\widetilde{\mathbf{f}}_{ECB}$ and $\widetilde{\mathbf{K}}_{ECB}$, as indicated in (3.34) . The cost of these steps, unfortunately, scales with the size of the HFM. As the system becomes large, the cost of evaluating the nonlinear force and of the projection become dominant. The strategies to circumvent this problem will be discussed here.

In this work, the nonlinear forces are based on the von-Karman kinematic model, which is valid for moderate rotation and small strains (Crisfield, 1991). By doing so, the nonlinear force vector $\mathbf{f}_{(s)}\,\{\mathbf{u}_{(s)}\}$ for the s^{th} substructure can be expressed as a polynomial function of the displacement vector $\mathbf{u}_{(s)}$ as

$$\mathbf{f}_{(s)} = {}^{2}\mathbf{Q}_{(s)}\mathbf{u}_{(s)} + \left({}^{3}\mathbf{Q}_{(s)} \cdot \mathbf{u}_{(s)}\right)\mathbf{u}_{(s)} + \left[\left({}^{4}\mathbf{Q}_{(s)} \cdot \mathbf{u}_{(s)}\right) \cdot \mathbf{u}_{(s)}\right]\mathbf{u}_{(s)}\,, \tag{3.37}$$

where ${}^{2}\mathbf{Q} \in \mathbb{R}^{n_{(s)} \times n_{(s)}}$,${}^{3}\mathbf{Q} \in \mathbb{R}^{n_{(s)} \times n_{(s)} \times n_{(s)}}$ and ${}^{4}\mathbf{Q} \in \mathbb{R}^{n_{(s)} \times n_{(s)} \times n_{(s)} \times n_{(s)}}$ are constant quadratic, cubic and quartic tensors, respectively. In practice, the nonlinear force vector is calculated for each element, and then assembled to $\mathbf{f}_{(s)}$. Therefore, ${}^{2}\mathbf{Q}_{(s)}$, ${}^{3}\mathbf{Q}_{(s)}$ and ${}^{4}\mathbf{Q}_{(s)}$ are sparse tensors.

Of course, significant time savings could be achieved if $\widetilde{\mathbf{f}}_{ECB}$ is expressed as function of the modal coordinates only. The reduced force vector is formed by assembling projected nonlinear forces of each component, as

$$\widetilde{\mathbf{f}}_{ECB} = \mathbf{V}^{T}\mathbf{f}_{\mathcal{G}} = \sum_{s=1}^{H} \mathbf{V}_{(s)}^{T}\mathbf{f}_{(s)}, \tag{3.38}$$

where $\mathbf{V}_{(s)} \in \mathbb{R}^{n_{(s)} \times z_{\mathcal{G}}}$ are the rows of the reduction basis matrix $\mathbf{V}$ corresponding to the s^{th} subsystem, and $z_{\mathcal{G}}$ is the total number of modes for the global system . These matrices are in fact obtained by assigning local reduction basis $\widetilde{\mathbf{V}}_{(s)}$ through a localization Boolean matrix $\mathbf{L}_{(s)}$ as

$$\mathbf{V}_{(s)} = \widetilde{\mathbf{V}}_{(s)}\mathbf{L}_{(s)}. \tag{3.39}$$

Here, $\widetilde{\mathbf{V}}_{(s)} \in \mathbb{R}^{n_{(s)} \times z_{(s)}}$ only contains the non-zero columns of the matrix $\mathbf{V}_{(s)}$, with $z_{(s)} = m_{CC}^{B} + r_{CC}^{B} + m_{(s)}^{I} + r_{(s)}^{I}$ and $\mathbf{L}_{(s)} \in \mathbb{R}^{z_{(s)} \times z_{\mathcal{G}}}$. Specifically,

$$\mathbf{V}_{(s)} = \begin{bmatrix} \widetilde{\mathbf{\Phi}}_{(s)}^{BB} & \widetilde{\mathbf{\Theta}}_{(s)}^{BB} & \dots & \mathbf{0} & \dots & \mathbf{0} & \mathbf{0} & \dots & \mathbf{0} & \dots \\ \widetilde{\mathbf{\Phi}}_{(s)}^{IB} & \widetilde{\mathbf{\Theta}}_{(s)}^{IB} & \dots & \mathbf{0} & \dots & \mathbf{\Phi}_{(s)}^{II} & \mathbf{\Theta}_{(s)}^{II} & \dots & \mathbf{0} & \dots \end{bmatrix} \quad \text{and} \quad \widetilde{\mathbf{V}}_{(s)} = \begin{bmatrix} \widetilde{\mathbf{\Phi}}_{(s)}^{BB} & \widetilde{\mathbf{\Theta}}_{(s)}^{BB} & \mathbf{0} & \mathbf{0} \\ \widetilde{\mathbf{\Phi}}_{(s)}^{IB} & \widetilde{\mathbf{\Theta}}_{(s)}^{IB} & \mathbf{\Phi}_{(s)}^{II} & \mathbf{\Theta}_{(s)}^{II} \end{bmatrix}. \tag{3.40}$$

By applying (3.39), the reduced force vector $\widetilde{\mathbf{f}}_{ECB}$ in (3.38) is calculated by stating

$$\widetilde{\mathbf{f}}_{ECB} = \sum_{s=1}^{H} \mathbf{L}_{(s)}^{T}\widetilde{\mathbf{V}}_{(s)}^{T}\mathbf{f}_{(s)} \triangleq \sum_{s=1}^{H} \mathbf{L}_{(s)}^{T}\widetilde{\mathbf{f}}_{(s)}, \quad \text{with} \quad \widetilde{\mathbf{f}}_{(s)} = \widetilde{\mathbf{V}}_{(s)}^{T}\mathbf{f}_{(s)}. \tag{3.41}$$

According to (3.33), the displacement vector $\mathbf{u}(s)$ of each subsystem can be expressed as a function of the modal coordinates as

$$\mathbf{u}_{(s)} = \mathbf{V}_{(s)}\boldsymbol{\xi}_{ECB} = \widetilde{\mathbf{V}}_{(s)}\mathbf{L}_{(s)}\boldsymbol{\xi}_{ECB} \triangleq \widetilde{\mathbf{V}}_{(s)}\boldsymbol{\xi}_{(s)}, \quad \text{with} \quad \boldsymbol{\xi}_{(s)} = \text{col}(\boldsymbol{\eta}_{CC}^{B}, \boldsymbol{\zeta}_{CC}^{B}, \boldsymbol{\eta}_{(s)}^{I}, \boldsymbol{\zeta}_{(s)}^{I}). \tag{3.42}$$

Substituting (3.37) and (3.42) into (3.41), the nonlinear force vector $\widetilde{\mathbf{f}}_{(s)}$ can be expressed as

$$\widetilde{\mathbf{f}}_{(s)} = {}^2\widetilde{\mathbf{Q}}_{(s)}\boldsymbol{\xi}_{(s)} + \left({}^3\widetilde{\mathbf{Q}}_{(s)} \cdot \boldsymbol{\xi}_{(s)}\right)\boldsymbol{\xi}_{(s)} + \left[\left({}^4\widetilde{\mathbf{Q}}_{(s)} \cdot \boldsymbol{\xi}_{(s)}\right) \cdot \boldsymbol{\xi}_{(s)}\right]\boldsymbol{\xi}_{(s)} \tag{3.43}$$

where ${}^2\widetilde{\mathbf{Q}}_{(s)} \in \mathbb{R}^{z_{(s)} \times z_{(s)}}$, ${}^3\widetilde{\mathbf{Q}}_{(s)} \in \mathbb{R}^{z_{(s)} \times z_{(s)} \times z_{(s)}}$ and ${}^4\widetilde{\mathbf{Q}}_{(s)} \in \mathbb{R}^{z_{(s)} \times z_{(s)} \times z_{(s)} \times z_{(s)}}$ are the constant quadratic, third-order and forth-order tensors, respectively. The reduced tangent stiffness matrix $\widetilde{\mathbf{K}}_{ECB}$ is calculated in the same fashion

$$\widetilde{\mathbf{K}}_{ECB} = \frac{\partial \widetilde{\mathbf{f}}_{ECB}}{\partial \boldsymbol{\xi}_{ECB}} = \sum_{s=1}^{H} \left(\mathbf{L}_{(s)}^T\, {}^2\widetilde{\mathbf{Q}}_{(s)}\mathbf{L}_{(s)} + 2\mathbf{L}_{(s)}^T \left({}^3\widetilde{\mathbf{Q}}_{(s)} \cdot \boldsymbol{\xi}_{(s)}\right)\mathbf{L}_{(s)} + 3\mathbf{L}_{(s)}^T \left[\left({}^4\widetilde{\mathbf{Q}}_{(s)} \cdot \boldsymbol{\xi}_{(s)}\right) \cdot \boldsymbol{\xi}_{(s)}\right]\mathbf{L}_{(s)}\right) \triangleq \sum_{s=1}^{H} \mathbf{L}_{(s)}^T \widetilde{\mathbf{K}}_{(s)}\mathbf{L}_{(s)}. \tag{3.44}$$

The tensors ${}^2\widetilde{\mathbf{Q}}_{(s)}$, ${}^3\widetilde{\mathbf{Q}}_{(s)}$ and ${}^4\widetilde{\mathbf{Q}}_{(s)}$ can be precomputed *offline*, once the enhanced CB reduction basis $\mathbf{V}$ is determined. For multi-component structures, the final size of the reduction basis $z_{\mathcal{G}}$ can be too large for the tensor construction for the whole system.

In this chapter, the offline construction of reduced tensors for the projected forces is parallelized across substructures, thus achieving computational savings and storage memory reduction by noticing $\max(z_{(s)}) < z_{\mathcal{G}}$, as compared to the case when the tensorial reduced expressions are computed for the whole system, as for instance in (Barbic & James, 2005).

The time integration of the reduced system using Newmark integration is summarized in Algorithm 2. By updating the nonlinear force vectors and stiffness matrices directly in terms of reduced modal coordinates (Line 7 and 16) for each subsystem in parallel, the related computational cost is significantly reduced. Meanwhile, the effort in increment calculation is also reduced, because the associated system of equations for the reduced coordinates increment $\Delta\boldsymbol{\xi}$ of a generic corrector step (Line 13) is of much smaller size. The computational cost of the increment calculation involves the factorization of dense $z_{\mathcal{G}} \times z_{\mathcal{G}}$ matrix. The complexity of the factorization of a dense $z_{\mathcal{G}} \times z_{\mathcal{G}}$ matrix is given by $\mathcal{O}(z_{\mathcal{G}}^{2.38})$, see (Coppersmith & Winograd, 1990). A substantial computational cost reduction can be achieved for the time integration, compared to the full analysis without substructuring techniques, when $z_{\mathcal{G}} \ll n$.

Alternatively, hyper reduction techniques can also be used to reduce the computational cost associated with computing the reduced nonlinear terms, by, for instance, using the Energy Conserving Sampling and Weighting (ECSW) method (Farhat *et al.*, 2014, 2015). In that case, however, one needs to resort on training sets obtained from full system runs, which are completely avoided here by exploiting the structure of the nonlinear terms.

3.5. NUMERICAL EXAMPLES

Two sets of numerical examples are presented in this section to show the effectiveness of the proposed approach. Firstly, we consider a cantilevered plate modeled with shell elements, and consisting of two substructures. Secondly, we consider a more complex double-clamped structure divided into 4 substructures. In our discussion, we use the following labelling to refer to the various solutions obtained:

- *HFM-L*: response obtained from the full linear model;
- *HFM-NL*: response obtained from the full nonlinear model;

Algorithm 2 Newmark time iteration scheme for the entire system using ECB techniques

```
Input: Intial condition:$\boldsymbol{\xi}_0, \dot{\boldsymbol{\xi}}_0$;   Newmark parameters:$\mu, \beta, T, \Delta t$;   Mass matrix:$\mathbf{M}_{\mathcal{G}}$;
    Resudual tolerance:$\epsilon$;   ECB reduction basis:$\mathbf{V}$;   Boolean matrices:$\mathbf{L}_{(s)}$;
    external load:$\mathbf{g}_{\mathcal{G}}\{t\}$
Output: Nonlinear response: $\mathbf{u}\{t\}$
$\widetilde{\mathbf{M}}_{ECB} := \mathbf{V}^T\mathbf{M}_{\mathcal{G}}\mathbf{V}$; $\widetilde{\mathbf{g}}_{ECB}\{t\} := \mathbf{V}^T\mathbf{g}_{\mathcal{G}}\{t\}$   ▷ Calculate reduced mass matrices and external load vectors in advance
while $t < T$ do   ▷ Time matching loop
    $p + 1 := p$
    $t_{p+1} := t_p + \Delta t$   ▷ Time increment
    $\dot{\boldsymbol{\xi}}_{p+1} := \dot{\boldsymbol{\xi}}_p + (1-\mu)\Delta t\ddot{\boldsymbol{\xi}}_p$; $\boldsymbol{\xi}_{p+1} := \boldsymbol{\xi}_p + \Delta t\dot{\boldsymbol{\xi}}_p + (0.5-\beta)\Delta t^2\ddot{\boldsymbol{\xi}}_p$; $\ddot{\boldsymbol{\xi}}_{p+1} := \mathbf{0}$   ▷ Prediction
    for s=1 to H do
        Update $\widetilde{\mathbf{f}}_{(s)}$ and $\widetilde{\mathbf{K}}_{(s)}$ for each subsystem, using Eq. (3.43) and (3.44)
    end for
    $\widetilde{\mathbf{f}}_{ECB}\{\boldsymbol{\xi}_{p+1}\} = \sum_{s=1}^{H} \mathbf{L}_{(s)}^T\widetilde{\mathbf{f}}_{(s)}$ ;   $\widetilde{\mathbf{K}}_{ECB}\{\boldsymbol{\xi}_{p+1}\} = \sum_{(s)=1}^{H} \mathbf{L}_{(s)}^T\widetilde{\mathbf{K}}_{(s)}\mathbf{L}_{(s)}$ ;   ▷ Assembly
    $\widetilde{\mathbf{Re}}_{p+1} = \widetilde{\mathbf{M}}_{ECB}\ddot{\boldsymbol{\xi}}_{p+1} + \widetilde{\mathbf{f}}_{ECB}\{\boldsymbol{\xi}_{p+1}\} - \widetilde{\mathbf{g}}_{ECB}\{t_{p+1}\}$   ▷ Residual Evaluation
    if $||\widetilde{\mathbf{Re}}_{p+1}|| > \epsilon||\widetilde{\mathbf{f}}_{ECB}||$ then   ▷ Convergence check
        $\widetilde{\mathbf{S}}\{\boldsymbol{\xi}_{p+1}\} = \widetilde{\mathbf{K}}_{ECB}\{\boldsymbol{\xi}_{p+1}\} + \frac{1}{\beta\Delta t^2}\widetilde{\mathbf{M}}_{ECB}$   ▷ Calculate reduced Jacobian matrix $\widetilde{\mathbf{S}}$
        $\Delta\boldsymbol{\xi} = -\left(\widetilde{\mathbf{S}}\{\boldsymbol{\xi}_{p+1}\}\right)^{-1}\widetilde{\mathbf{Re}}_{p+1}$   ▷ Increment calculation
        $\boldsymbol{\xi}_{p+1} := \boldsymbol{\xi}_{p+1} + \Delta\boldsymbol{\xi}$; $\dot{\boldsymbol{\xi}}_{p+1} := \dot{\boldsymbol{\xi}}_{p+1} + \frac{\mu}{\beta\Delta t}\Delta\boldsymbol{\xi}$; $\ddot{\boldsymbol{\xi}}_{p+1} := \ddot{\boldsymbol{\xi}}_{p+1} + \frac{1}{\beta\Delta t^2}\Delta\boldsymbol{\xi}$   ▷ Correction
        for s=1 to H do
            Update $\widetilde{\mathbf{f}}_{(s)}$ and $\widetilde{\mathbf{K}}_{(s)}$ for each subsystem, using Eq. (3.43) and (3.44)
        end for
        $\widetilde{\mathbf{f}}_{ECB}\{\boldsymbol{\xi}_{p+1}\} = \sum_{s=1}^{H} \mathbf{L}_{(s)}^T\widetilde{\mathbf{f}}_{(s)}$ ;   $\widetilde{\mathbf{K}}_{ECB}\{\boldsymbol{\xi}_{p+1}\} = \sum_{(s)=1}^{H} \mathbf{L}_{(s)}^T\widetilde{\mathbf{K}}_{(s)}\mathbf{L}_{(s)}$ ;   ▷ Assembly
        $\widetilde{\mathbf{Re}}_{p+1} = \widetilde{\mathbf{M}}_{ECB}\ddot{\boldsymbol{\xi}}_{p+1} + \widetilde{\mathbf{f}}_{ECB}\{\boldsymbol{\xi}_{p+1}\} - \widetilde{\mathbf{g}}_{ECB}\{t_{p+1}\}$   ▷ Residual Evaluation
    end if
    $\mathbf{u}_{p+1} = \mathbf{V}\boldsymbol{\xi}_{p+1}$;   $\dot{\mathbf{u}}_{p+1} = \mathbf{V}\dot{\boldsymbol{\xi}}_{p+1}$;   $\ddot{\mathbf{u}}_{p+1} = \mathbf{V}\ddot{\boldsymbol{\xi}}_{p+1}$;
end while
```

- *CB-L*: response of the CB-reduced linear model with interface reduction;
- *CB-NL*: response of the reduced nonlinear model obtained by projection on the classic CB basis (without modal derivatives).
- *ECB-NL*: response of the reduced nonlinear model obtained by projection on the enhanced CB basis (with modal derivatives);

In this section, all the models contain elastic bodies meshed with triangular FE shell elements featuring 3 nodes per element and 6 DoFs per node. The set of DoFs can be

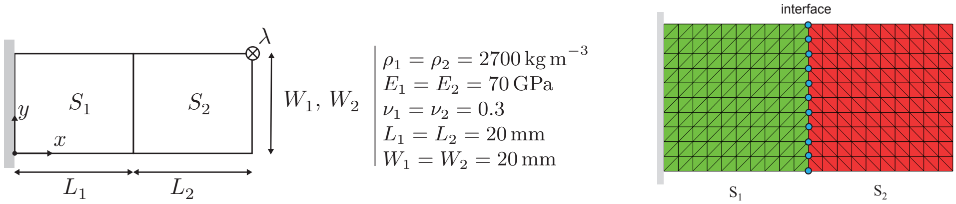

(a) shell model and materials (b) description of right graph

Figure 3.3: Sketch of the tested numerical example with corresponding material properties and mesh size. The interface nodes are highlighted using blue dots. The length is $L_1 = L_2 = 20$ mm, the width is $W_1 = W_2 = 20$ mm. The Young's modulus is $E_1 = E_2 = 70$ GPa, the Poisson's ratio is $\nu_1 = \nu_2 = 0.3$, and the density is $\rho_1 = \rho_2 = 2700$ kg.m^{-3}.

divided into a membrane and a bending part, as formulated by Allman in (Allman, 1976) and (Allman, 1988). The detailed implementation of the shell element can be found in (Tiso, 2006).

3.5.1. TWO-COMPONENT CANTILEVER PLATE

The two-component cantilever plate example was originally proposed in (Wenneker & Tiso, 2014). The geometry, material properties and mesh are shown in Fig. 3.3. The whole structure is divided into two substructures S_i with $i = 1, 2$, and each substructure has different thickness. A step load in $z-$direction with amplitude g is applied to the indicated tip node. This model has a total of 1386 DoFs, $n^{B}_{\mathcal{CB}}$ =66 interface DoFs and $n^{I}_{\mathcal{G}}$ =1320 internal DoFs for two substructures.

We consider here two cases, referred to as Model-I(1) and Model-I(2), respectively. For Model-I(1), a thick substructure S_1 is cantilevered at one edge and then connected with a relatively thin substructure S_2 at the other edge. This model is shown in Fig. 3.4(a). When a step load is imposed at the free edge of Model-I(1), it is expected that S_1 will deform in the linear range, while S_2 will exhibit nonlinear behavior. For Model-I(2), one edge of the thin substructure S_1 is fully restrained, and the other edge is connected with a relatively thick substructure S_2. This model is illustrated in Fig. 3.4(b). When a step load is imposed at the free edge of Model-I(2), the thin substructure S_1 will deform in the nonlinear range, while the thick substructure S_2 will mainly undergo finite rigid body motion. The displacement in the $z-$direction at the loaded node of both Model-I(1) and Model-I(2) is shown in Fig. 3.4. For both cases, the linear response (HFM-L) and nonlinear response (HFM-NL) are clearly different, thus confirming that the applied load triggers significant nonlinear behavior.

As mentioned in Section 3.3.2, the MMI selection criterion does not yield the optimal number of MDs that need to be included in the basis to reproduce the solution with a satisfactory accuracy. In this study, we determine the number of IVMs, SCC modes and MDs remained in the ROMs according to the user's experience. For consistency of the two cases, we kept 5 IVMs and 10 corresponding MDs for the thick plate (relative stiff substructure); 10 IVMs and 20 corresponding MDs for the thin plate (relative flexible substructure); and 10 SCC modes and 10 corresponding MDs for the assembled system. The various ROMs considered for the two cases are listed in Table 3.1 and 3.2.

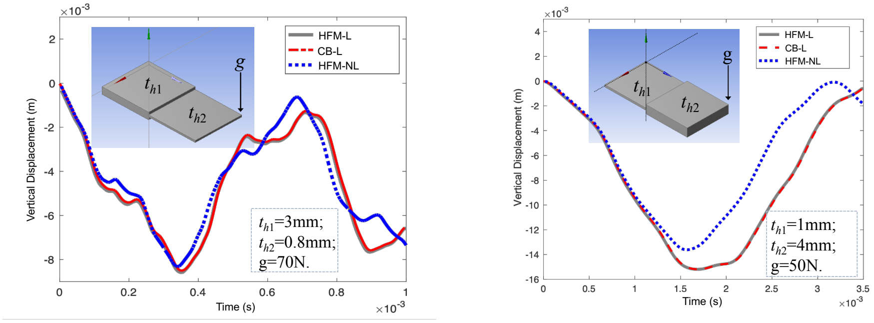

(a) Model-I(1)

(b) Model-I(2)

Figure 3.4: Dynamic responses for Model-I(1) and Model-I(2), comparison of the full linear (HFM-L), full nonlinear (HFM-NL), and linear Craig-Bampton (CB-L) method. The excellent agreement between HFM-L and CB-L confirms the effectiveness of the linear reduction basis.

Table 3.1: Reduction basis and number of DoFs for Model-I(1)

	S_1	S_2	interface	
CB-L	number of IVMs		number of SCC modes	total DoFs
	5	10	10	25
ECB_1-NL	number of IVMs		number of SCC modes	total DoFs
	5	10	10	
	number of MDs		number of MDs	65
	10	20	10	
ECB_2-NL	number of IVMs		number of SCC modes	total DoFs
	5	10	10	
	number of MDs		number of MDs	45
	0	20	0	
ECB_3-NL	number of IVMs		number of CMs	total DoFs
	5	10	66	
	number of MDs		number of MDs	111
	10	20	0	
CB-NL	number of IVMs		number of SCC modes	total DoFs
	50	50	66	166

Table 3.2: Reduction basis and number of DoFs for Model-I(2)

	S_1	S_2	interface	
CB-L	number of IVMs		number of SCC modes	total DoFs
	10	5	10	25
ECB_1-NL	number of IVMs		number of SCC modes	total DoFs
	10	5	10	
	number of MDs		number of MDs	65
	20	10	10	
ECB_2-NL	number of IVMs		number of SCC modes	total DoFs
	10	5	10	
	number of MDs		number of MDs	55
	20	0	10	
ECB_3-NL	number of IVMs		number of CMs	total DoFs
	10	5	66	
	number of MDs		number of MDs	111
	20	10	0	
CB-NL	number of IVMs		number of SCC modes	total DoFs
	50	50	66	166

MODEL-I(1): THICK-THIN SHELL STRUCTURE

The various ROM considered for this example are listed in Table 3.1. We first establish an accurate ROM for the HFM-L model. By including only $m^B_{CC} = 10$ SCC modes, $m^I_{(1)} = 5$ IVMs for S_1 and $m^I_{(2)} = 10$ IVMs for S_2 in the ROM (indicated as CB-L), a satisfactory accuracy can be obtained, as shown in Fig. 3.4(a).

The reduced nonlinear response obtained with ECB basis (ECB-NL) is then shown in Fig. 3.5(a). As noted earlier, the reduction basis size grows quadratically with respect to the number of IVMs and SCC modes if all corresponding MDs are included in the basis. However, only a few of these MDs might be significant for capturing the nonlinear behavior. We applied here the MMI criterion discussed in Section 3.3.2. The obtained ranking is shown in Fig. 3.6. Here, we select the first $r^B_{CC} = 10$ MDs corresponding to the SCC modes, $r^I_{(1)} = 10$ internal MDs for S_1, and $r^I_{(2)} = 20$ internal MDs for S_2 in the ROM. This ROM is labelled as ECB_1-NL. As it can be observed in Fig. 3.5(a), the results obtained in ECB_1-NL are in very good agreement with the HFM-NL reference.

As discussed, S_1 is expected to feature small displacements and therefore behave linearly. The thin substructure S_2, on the other hand, undergoes large deflections, and needs to be modelled nonlinearly. Therefore, MDs related to SCC modes and MDs for the IVMs of S_1 could be neglected in the reduction basis. This is confirmed by comparing the approximation between the results obtained by the ROM labelled ECB_1-NL and ECB_2-NL. In ECB_2-NL, the MDs related to SCC modes and MDs for the IVMs of S_1 are not included in the basis. As can be seen, there is no appreciable degradation of accuracy between the responses of ECB_1-NL and ECB_2-NL.

In one relevant work (Wenneker & Tiso, 2014), the MDs associated to the IVMs are

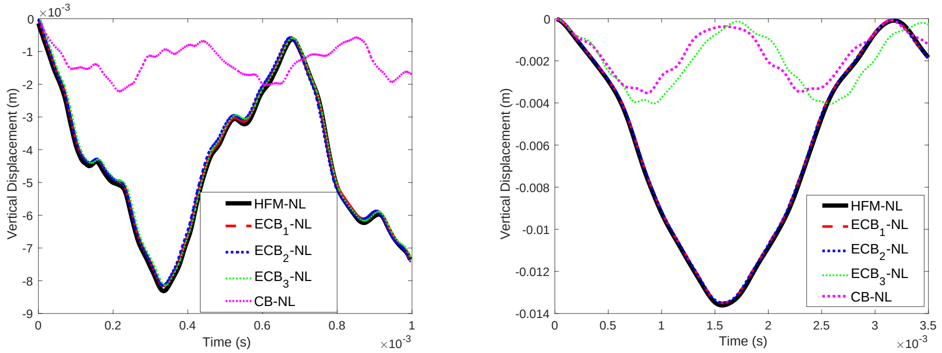

(a) Model-I(1) (b) Model-I(2)

Figure 3.5: Nonlinear dynamic responses of different reduction basis for Model-I(1) and Model-I(2), compared to the full nonlinear solution.

added in the classic CB reduction basis, while the interface reduction, as well as the MDs associated to the SCC modes are not applied. It is therefore interesting to compare the ROM in (Wenneker & Tiso, 2014) (denoted as ECB$_3$-NL) with the ROM proposed here. For Model-I(1), ECB$_3$-NL can also produce accurate results. However, ECB$_3$-NL features the drawback of a larger size of interface DoFs, as compared to ECB$_1$-NL.

On the contrary, a ROM based on classic CB reduction (indicated as CB-NL) containing all $n^B_{\mathcal{CB}} = 66$ CMs and as many as the first $m^I_{(1)} = m^I_{(2)} = 50$ IVMs for each subsystem (without MDs) yields very poor results, in spite of the fact that the size of the reduction basis is remarkably larger than the ECB$_2$-NL. This confirms the effectiveness of MDs in capturing the nonlinear effects while yielding a reduction basis of reasonable size.

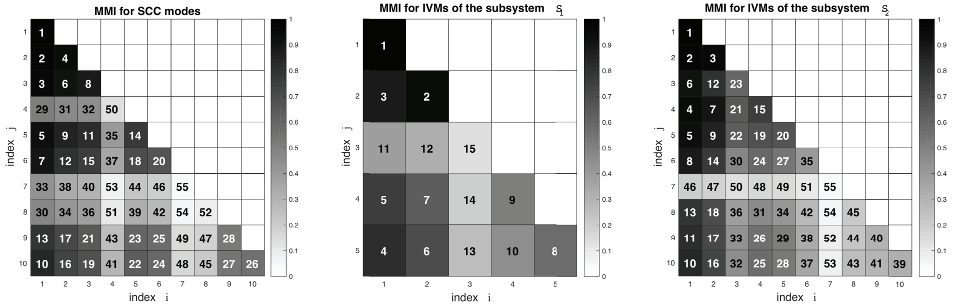

MMI for SCC modes

index j \ index i	1	2	3	4	5	6	7	8	9	10
1	1									
2	2	4								
3	3	6	8							
4	29	31	32	50						
5	5	9	11	35	14					
6	7	12	15	37	18	20				
7	33	38	40	53	44	46	55			
8	30	34	36	51	39	42	54	52		
9	13	17	21	43	23	25	49	47	28	
10	10	16	19	41	22	24	48	45	27	26

MMI for IVMs of the subsystem S_1

index j \ index i	1	2	3	4	5
1	1				
2	3	2			
3	11	12	15		
4	5	7	14	9	
5	4	6	13	10	8

MMI for IVMs of the subsystem S_2

index j \ index i	1	2	3	4	5	6	7	8	9	10
1	1									
2	2	3								
3	6	12	23							
4	4	7	21	15						
5	5	9	22	19	20					
6	8	14	30	24	27	35				
7	46	47	50	48	49	51	55			
8	13	18	36	31	34	42	54	45		
9	11	17	33	26	29	38	52	44	40	
10	10	16	32	25	28	37	53	43	41	39

Figure 3.6: Ranking and weights obtained by the MMI criterion for all MDs corresponding to the SCC modes and IVMs of each substructure, respectively, for Model-I(1). The gray intensity indicates the relative importance of MDs. The numbers denote the ranking for the MDs. The upper triangular terms are not shown because of the symmetry of the MDs.

MODEL-I(2): THIN-THICK SHELL STRUCTURE

This model consists of a clamped thin substructure S_1 and a relatively thick substructure S_2. The thin substructure S_1 experiences large deformations and thus needs to be described nonlinearly, while S_2 will mainly undergo large rigid rotations. In model-I(2), the MDs related to the SCC modes, which indicate the global rigid rotation and translation, are of great significance during the nonlinear analysis.

The CB-L can accurately describe the full linear response as shown in Fig. 3.4(b). This linear basis is taken as the one guaranteeing sufficient accuracy for the linear model.

The reduced nonlinear response obtained with different ECB basis is shown in Fig. 3.5(b). In ECB$_1$-NL, the reduced response is in good agreement with the full nonlinear solution. The MDs were ranked using the MMI criterion, as done for the Model-I(1). The display of the ranking is omitted here for sake of compactness.

The thick plate S_2 mainly undergoes rigid body motion, which is described by the SCC modes in the ROM. The corresponding in-plane motion should be considered by the corresponding MDs associated to the SCC modes. By noticing that S_2 features relatively small displacement and rotation when the interface-related motion is excluded, we applied another ROM where the MDs corresponding to the IVMs of S_2 are removed from the reduction basis. This ROM is denoted by ECB$_2$-NL. Indeed, practically identical accuracy can still be obtained in ECB$_2$-NL.

In ECB$_3$-NL, we form the reduction basis with 10 IVMs plus 20 MDs for S_1, 5 IVMs plus 10 MDs for S_2, as well as 66 CMs for all interface DoFs. As shown in Fig.3.5(b), ECB$_3$-NL fails to reproduce the response obtained from HFM-NL. Although ECB$_3$-NL includes all interface DoFs, the CMs only describe the geometrically linear deformation of the internal DoFs because of the imposed perturbation at the interface DoFs. On the contrary, the MDs associated to the SCC modes are able to consider the geometrically nonlinear behavior of the internal DoFs when the interface DoFs deform according to the shape of the SCC modes. The reduced size and improved accuracy of ECB$_1$-NL, as compared to ECB$_3$-NL, indicate the superiority of the proposed approach with respect to the nonlinear CB method in (Wenneker & Tiso, 2014).

As done in the previous case, the results are also compared with a ROM comprising all $n^B_{\mathcal{CB}} = 66$ CMs and as many as the first $m^I_{(1)} = m^I_{(2)} = 50$ IVMs (indicated as CB-NL). In spite of the large size of the reduction basis, this model is not yielding accurate results.

For both Model-I(1) and Model-I(2), piratically identical accuracy can be obtained between ECB$_1$-NL and ECB$_2$-NL, while ECB$_2$-NL features less number of DoFs. It indicates that the ECB approach offers the flexibility for ROM construction, as the necessary nonlinear ingredients (i.e., MDs) can be added only for the substructures featuring geometrically nonlinear behavior.

3.5.2. DOUBLE-CLAMPED SHELL STRUCTURE

We consider here the FE model of a double-clamped structure (henceforth referred to as Model-II), shown in Fig. 3.7. The FE model has a total of 25344 DoFs, $n^B_{\mathcal{CB}}$ =192 interface DoFs and $n^I_{\mathcal{G}}$ =25152 internal DoFs. A pressure P$\{t\}$ = 2000sin(143.42t) Pa is applied at substructure S_1 and S_2. The vertical displacement at Node A and the horizonal displacement at Node B are monitored. The coordinates of node A ($x = 0$ m; $y = 0.35$ m; $z = 0$ m) and node B ($x = 0.07$ m; $y = 0.14$ m; $z = 0.032$ m) have been shown in Fig 3.7(a).

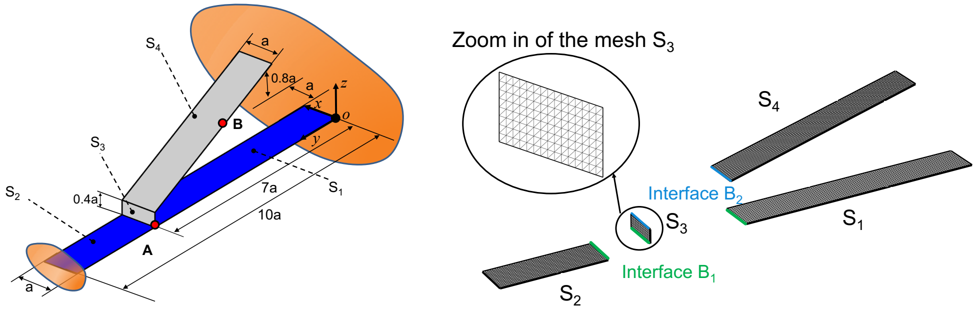

(a) sketch of Model-II (b) FE model of 4 substructures

Figure 3.7: Illustration of Model-II. The geometric parameter is $a = 50$ mm, the Young modulus is $E = 69$ GPa, the Poisson's ratio is $\nu = 0.33$, the density is $\rho = 2700$ kg.m^{-3}, and the thickness of the shell structure is $t_h = 2$ mm. The displacements of the Node A and Node B are monitored.

The different ROBs for the both linear and nonlinear analysis are listed in Table 3.3. Fig. 3.8 shows a remarkable difference in the dynamic response between a linear and a nonlinear analysis of the HFM, confirming that the system vibrates in the nonlinear regime. In this case, we considered all the substructures to be nonlinear. It can be also seen that a linear reduction basis (indicated as CB-L) consisting of $n^B_{CC} = 10$ SCC modes and $m^I_{(1)} = m^I_{(2)} = m^I_{(3)} = m^I_{(4)} = 10$ IVMs for all substructures can accurately approximate the full linear response.

Table 3.3: Reduction basis and number of DoFs for Model-II

	S_1	S_2	S_3	S_4	interface	
CB-L	number of IVMs				number of SCC modes	total DoFs
	10	10	10	10	10	50
ECB$_1$-NL	number of IVMs				number of SCC modes	total DoFs
	10	10	10	10	10	
	number of MDs				number of MDs	125
	15	15	15	15	15	
ECB$_2$-NL	number of IVMs				number of CMs	total DoFs
	10	10	10	10	192	
	number of MDs				number of MDs	292
	15	15	15	15	0	
CB-NL	number of IVMs				number of CMs	total DoFs
	50	50	50	50	192	392

The nonlinear response of the full model is compared with the response obtained with ECB-NL. The linear reduction basis is augmented with the first $r^I_{(1)} = r^I_{(2)} = r^I_{(3)} = r^I_{(4)} = 15$ MDs of the IVMs of S_1 to S_4, as well as the first $r^B_{CC} = 15$ MDs of the SCC modes

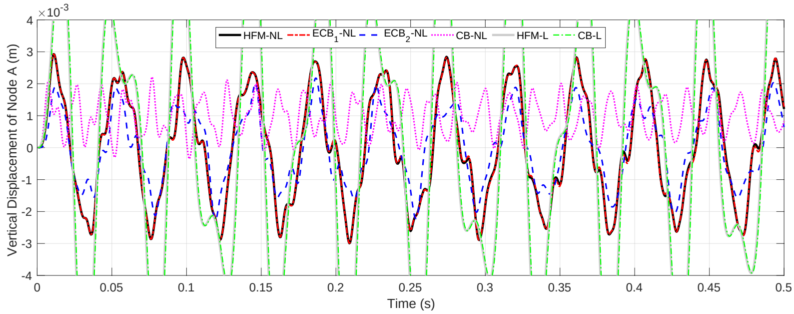

(a) vertical response at Node A

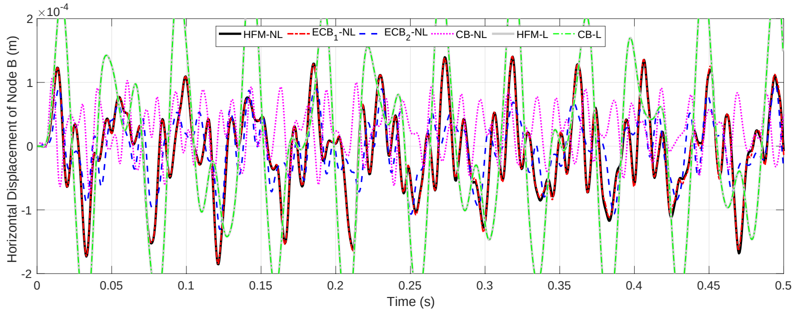

(b) horizontal response at Node B

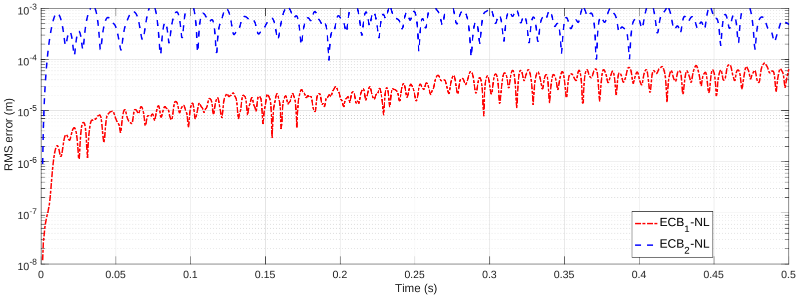

(c) RMS errors comparison

Figure 3.8: Dynamic responses and RMS error for Model-II, comparison of the full and reduced model, for both linear and nonlinear analysis.

of the assembled system. The results are shown in Fig. 3.8. The ECB-NL shows a good agreement with the HFM-NL model, confirming that the MDs are able to describe the essential nonlinear effect of the elastic geometric nonlinearities. As for the other cases, the responses in CB-NL, where all $n_{\mathcal{CB}}^{B} = 192$ CMs and as many as the first $m_{(1)}^{I} = m_{(2)}^{I} = m_{(3)}^{I} = m_{(4)}^{I} = 50$ IVMs are included in 4 substructures, failed to produce good results.

It is also interesting to compare the proposed substructuring technique with its counterpart in (Wenneker & Tiso, 2014), where the SCC modes and the corresponding MDs are replaced with the full set of CMs. The corresponding ROM is denoted as ECB$_2$-NL. Although the accuracy of ECB$_2$-NL is improved when compared to its counterpart of CB-NL, the dynamic response of ECB$_2$-NL is still not as accurate as the one of ECB$_1$-NL. The comparison between ECB$_1$-NL and ECB$_2$-NL indicates the superiority of the SCC modes plus the corresponding MDs to consider the geometrically nonlinear behavior of the internal DoFs triggered by the interface motions. The CMs, on the other hand, merely present the geometrically linear motion of the internal DoFs because of the perturbation at the interface DoFs.

To further investigate the approximation accuracy of the ROMs for all DoFs along the integration time, the root-mean square (RMS) error of different ROMs, defined as

$$\epsilon_{RMS}\{t\} = \sqrt{\frac{1}{n}\left(||\mathbf{u}_x\{t\} - \overline{\mathbf{u}}_x\{t\}||^2 + ||\mathbf{u}_y\{t\} - \overline{\mathbf{u}}_y\{t\}||^2 + ||\mathbf{u}_z\{t\} - \overline{\mathbf{u}}_z\{t\}||^2\right)}\,, \tag{3.45}$$

has been plotted in Fig. 3.8(c), where $\mathbf{u}\{t\}$ and $\overline{\mathbf{u}}\{t\}$ are the vector of displacement at the time t, obtained from the full nonlinear and reduced solution, respectively. The subscripts $\star_x$, $\star_y$ and $\star_z$ indicate directional components of $\mathbf{u}$ and $\overline{\mathbf{u}}$ along the OX, OY, OZ axis. The ECB$_1$-NL is more accurate than ECB$_2$-NL over the entire time interval, even though more modes are included in ECB$_2$-NL. Since the modes and corresponding MDs are computed at the equilibrium position and never updated during the time integration, the approximation accuracy of ECB$_1$-NL decreases when we increase the time interval, as observed in the RMS error of ECB$_1$-NL. To obtain better accuracy for a longer time interval, a periodic basis updating of the tangent modes and corresponding MDs can be applied, as denoted in (Idelsohn & Cardona, 1985*b*) for the entire system without substructuring, paying for the price of extra offline cost.

3.5.3. COMPUTATIONAL EFFICIENCY

In this section, we compare the computational time between the HFM-NL and the ECB-NL, together with the global relative errors (GRE) defined as

$$GRE_m = \frac{\sqrt{\sum_t \left(\mathbf{u}\{t\} - \tilde{\mathbf{u}}\{t\}\right)^T \mathbf{M}\left(\mathbf{u}\{t\} - \tilde{\mathbf{u}}\{t\}\right)}}{\sqrt{\sum_t \mathbf{u}\{t\}^T \mathbf{M} \mathbf{u}\{t\}}} \times 100\%, \tag{3.46}$$

where $\mathbf{u}\{t\}$ and $\tilde{\mathbf{u}}\{t\}$ are the vector of displacement at the time t, obtained from the full nonlinear and reduced solution, respectively. The mass matrix $\mathbf{M}$ provides a relevant normalisation for the generalised displacements, which could be a combination of physical displacements and rotations, as the shell models applied here. This error measure was first introduced in (Farhat *et al.*, 2014) and then slightly modified in (Jain *et al.*, 2017). All simulations are performed in MATLAB® R2015, on the a cluster equipped with 8-core Intel® Xeon® CPUs (E5-2630v3) @ 2.4 GHz and 128 GB RAM.

Table 3.4 compares the computational cost of all the numerical examples of Section 5. The computational cost for the proposed ECB method has been split into the *offline* and *online* cost, where the offline cost corresponds to the extra computational efforts required to construct the ROM. The most time consuming operations in the offline calculation are the construction of the reduction basis as in (3.33), which is denoted here as

t_{off_1}, and the calculation of the higher-order tensors in (3.43), which is denoted as t_{off_2}. The online calculation corresponds to the time integration of the ROM, which is denoted as t_{on}. Obviously, the full analysis does not carry any offline costs.

Table 3.4: Computational cost for numerical examples using ECB$_1$-NL for all models.

Numerical models	Full analysis	ECB method			speed up factor		GRE
		offline		online			
	$t_{full}(s)$	$t_{off1}(s)$	$t_{off2}(s)$	$t_{on}(s)$	$\mathcal{S}_1$	$\mathcal{S}_2$	GRE$_m$(%)
Model-I(1)	65.36	1.41	20.33	5.78	11.31	2.38	1.52
Model-I(2)	70.59	1.26	22.88	7.23	9.76	2.25	1.31
Model-II	6767	31.9	269	110.82	61.06	16.43	2.54

The computational efficiency is measured in terms of speed up factor, defined as

$$\mathcal{S} = \frac{\mathcal{C}_{on} t_{full}}{\mathcal{C}_{off}(t_{off_1} + t_{off_2}) + \mathcal{C}_{on} t_{on}}, \quad \text{with} \quad \mathcal{C}_{off} + \mathcal{C}_{on} = 1, \tag{3.47}$$

$\mathcal{C}_{off}$ and $\mathcal{C}_{on}$ being weight-factors for the offline and online stages, respectively. The offline calculation cost is neglected by setting $\mathcal{C}_{off} = 0, \mathcal{C}_{on} = 1$. The so obtained speed up factor, denoted as $\mathcal{S}_1$, is justified when the same ROM is used for many different load cases. Alternatively, one can set an equal weightage to offline and online costs, i.e., $\mathcal{S}_2 : \mathcal{C}_{off} = 0.5, \mathcal{C}_{on} = 0.5$. This covers the limit case in which the ROM is used only once.

The results are summarized in Table 3.4. It can be observed that the proposed ECB approach not only approximates the full solution with a high accuracy, but also efficiently reduces the computational time. As expected and discussed in Section 3.4, the speed up factor is significantly larger for the Model-II case, which features a relatively large number of DoFs. This reflects the situation encountered in practical applications where large models are expected. With a longer time interval during the nonlinear MOR, the speed up factor S_2 increases owing to the unchanged offline cost and enhanced online savings. The GRE, on the other hand, will also increase without a periodic basis updating. Therefore, a balance between the approximation accuracy and computational efficiency should be determined according to the user's demand.

3.6. CONCLUSIONS

We have proposed a novel MOR technique for multi-components FE models featuring geometric nonlinearities. The proposed method is a natural extension of the standard CB method and system-level interface reduction, obtained by enriching the CB linear reduction basis with MDs of both the IVMs and SCC modes. The MDs are capable of describing the most significant contributions to geometric nonlinear behavior, for both internal and interface DoFs. Moreover, this substructuring framework also allows to consider nonlinearities only for selected substructures undergoing nonlinear deformations, as shown in Section 3.5.1. Moreover, the MD paradigm allows to distinguish between nonlinear behavior due to rigid body rotations and elastic deflection, thus revealing the relative importance of the two contributions. This has been illustrated by the simple yet comprehensive examples in Section 3.5. We mitigated the quadratic growth of the size of the MD basis by applying a simple MMI ranking criterion to rank the relative importance of the MDs.

The reduced nonlinear force vector, which is computationally expensive, is here directly expressed as a function of the reduced generalized DoFs. A substantial computational cost reduction and memory savings can be achieved by setting much smaller tensors for each subsystem in parallel.

The proposed technique allows highly efficient modeling of complex structures with geometric nonlinearities by yielding a ROM with a significantly reduced number of generalized DoFs. The presented numerical examples highlight the performance improvements of the extended CB method with respect to the standard CB reduction.

4

NONLINEAR MODEL ORDER REDUCTION FOR FLEXIBLE MULTIBODY DYNAMICS: A MODAL DERIVATIVES APPROACH

In Chapter 2 and 3, the Craig–Bampton method with interface reduction was applied to couple the different reduced components without rigid body motion. In this chapter, an effective reduction technique is presented for flexible multibody systems, for which the elastic deflection could not be considered small. We consider here planar beam systems undergoing large rotations, in the floating frame description. The proposed method enriches the classical linear reduction basis with modal derivatives stemming from the derivative of the eigenvalue problem. Based on the linear projection, the configuration-dependent internal force can be expressed as cubic polynomials in the reduced coordinates. Coefficients of these polynomials can be precomputed for efficient run-time evaluation. The numerical results show that the modal derivatives are essential for the correct approximation of the nonlinear elastic deflection with respect to the body reference. The proposed reduction method constitutes a natural and effective extension of the classical linear modal reduction in the floating frame.

This chapter is based on the paper "Wu, L., Tiso, P.: Nonlinear model order reduction for flexible multibody dynamics: a modal derivatives approach. Multibody System Dynamics 36(4), 405-425 (2016)."

4.1. Introduction

The floating frame of reference (FFR), which follows a mean rigid body motion of an arbitrary flexible component, is widely applied in flexible multibody systems (FMBS) (Wasfy & Noor, 2003). The major advantage of floating reference, when compared with the corotational frame of reference (CFR), is the ability to naturally allow Model Order Reduction (MOR): the local generalized coordinates can be expressed as a linear combination of a small number of modes.

The traditional FFR approach combined with linear elastic finite element (FE) models was illustrated by Shabana (Shabana, 2005). This formulation has been used to numerous problems featuring large rigid body displacement but small deflections. However, nonlinear effects due to elastic geometric nonlinearities are not incorporated in this method, and can not be ignored in many FMBS applications. In (Bakr & Shabana, 1986, Nada *et al.*, 2010), the classical geometric stiffness, obtained from an expression for the strain energy that includes only some higher-order terms of the strain tensor, was included in the motion equations. This approximation ignores the foreshortening displacement, and may lead to diverging solutions in applications involving large deflections and large axial forces (Mayo *et al.*, 1995). Mayo (Mayo & Domínguez, 1996) extended this formulation and obtained additional geometric stiffness matrix and nonlinear elastic force vectors. The inclusion of this effects improved both the axial and transverse response.

The FE discretization of the elastic bodies in FFR introduces a large number of degrees of freedom (DoFs), and the simulation of the multibody system becomes computationally expensive, especially when the internal forces are nonlinear. Therefore, an essential step in the modeling of FMBS is the reduction of the elastic DoFs. While the traditional linear MOR methods have been widely applied in FFR formulation (Shabana, 2005, Bakr & Shabana, 1986), some other non-modal model reduction techniques have also been used in large scale industrial models in the last few years (Fehr & Eberhard, 2011, Fischer & Eberhard, 2014, Holzwarth & Eberhard, 2015). However, efficient reduction techniques with elastic geometrical nonlinearities in FFR formulation still remain a relevant research topic, given the broad range of applications tackled by FMBS. One proposed approach, under the name of *ad-hoc modes*, is to specifically select some axial vibration modes, in addition to low-frequency bending and torsion modes, and include them in the reduction basis in order to properly account for the nonlinear membrane response (Rizzi & Przekop, 2008, Li *et al.*, 2009). However, the frequencies of fundamental axial modes are normally much higher than the ones associated to bending modes. The extraction of such modes is difficult and expensive, and therefore not practical for realistic applications. Along this line, Holm-Jϕrgensen (Holm-Jørgensen & Nielsen, 2009) extended the truncated modal basis with a quasi-static correction, assuming that the high-frequency elastic modes only cause quasi-static displacements. Similar approaches were previously proposed by Schwertassek (Schwertassek *et al.*, 1999*a*,*b*). A set of suitable quasi-comparison function, by combining eigenfunctions and static modes, is used in the FFR formulation applying Ritz method. This method was further applied to the deployment of a solar panel array by Wallrapp (Wallrapp & Wiedemann, 2002).

Higher-order modes, also known as modal derivatives (MDs), have been proved to be an efficient approach to enrich the modal basis and represent the effects of nonlinearity (Idelsohn & Cardona, 1985*a*,*b*, Slaats *et al.*, 1995). This method has been successfully applied in the inertial frame description, to solve nonlinear problems without large rigid body motion. Interesting applications are also found in computer graphics and haptics (Barbic & James, 2005, Barbic & Zhao, 2011). Recently, this method has also been extended from the planar beam element to a general three-dimensional shell element implementation in inertial frame (Tiso, 2011).

In this chapter, a reduction method based on the enrichment of reduction basis constituted of vibration modes with modal derivatives is presented. The FFR formulation is considered here. The elastic nonlinearity is modeled by employing full quadratic Green strain expression, and the MDs can be interpreted as a static correction of the selected vibration modes that represent the nonlinear forces with respect to the body reference correctly. The proposed technique is implemented with the Craig-Bampton method on the floating frame (Liew *et al.*, 1996, Cardona, 2000), to give a exact compatibility at boundaries. The effectiveness of the proposed method will be illustrated through several numerical examples.

4.2. FLOATING FRAME OF REFERENCE FORMULATION

The proposed method is illustrated by planar beam systems featuring multiple components. The following assumptions have been made:

1. we consider only Euler-Bernoulli beam theory;
2. the material nonlinearities are not taken into consideration;
3. damping is neglected.

4.2.1. KINEMATIC DESCRIPTION

In the FFR description, the absolute motion of an arbitrary point on element P_j of the s^{th} body is described as the superposition of the motion of the body coordinate $O^{(s)}X^{(s)}Y^{(s)}$ and the position of the points with respect to the body reference, as shown in Fig. 4.1. The definition of body coordinate $O^{(s)}X^{(s)}Y^{(s)}$ is not unique, we adopt here the nodal fixed frame (Nikravesh, 2005): the origin of the body coordinate is fixed to one node of the s^{th} body, and the $O^{(s)}X^{(s)}$ axis connects the origin to the end node. The position vector $\mathbf{r}^{j,(s)}$ of the point of element P_j on s^{th} body can be defined in FFR formulation as

$$\mathbf{r}^{j,(s)} = \mathbf{R}^{(s)} + \mathbf{A}^{(s)}\mathbf{N}^{j,(s)}(\mathbf{e}_0^{j,(s)} + \mathbf{q}_f^{j,(s)}), \tag{4.1}$$

where $\mathbf{R}^{(s)}$ represents the position of origin of body system $O^{(s)}X^{(s)}Y^{(s)}$ with respect to global system OXY, $\mathbf{A}^{(s)}$ is the transformation matrix from $O^{(s)}X^{(s)}Y^{(s)}$ to OXY, $\mathbf{N}^{j,(s)}$ are the FE shape functions, $\mathbf{e}_0^{j,(s)}$ is the nodal coordinate vector in the undeformed state and $\mathbf{q}_f^{j,(s)}$ is the vector of relative DoFs at the nodal points. In the presented 2D framework, the transformation matrix $\mathbf{A}^{(s)}$ depends only on the angle $\theta^{(s)}$. The kinetic energy $\mathcal{T}^{j,(s)}$ for element P_j on s^{th} body is defined as

$$\mathcal{T}^{j,(s)} = \frac{1}{2}\int_{V^{j,(s)}} \rho^{j,(s)}(\dot{\mathbf{r}}^{j,(s)})^T\dot{\mathbf{r}}^{j,(s)}dV^{j,(s)}, \tag{4.2}$$

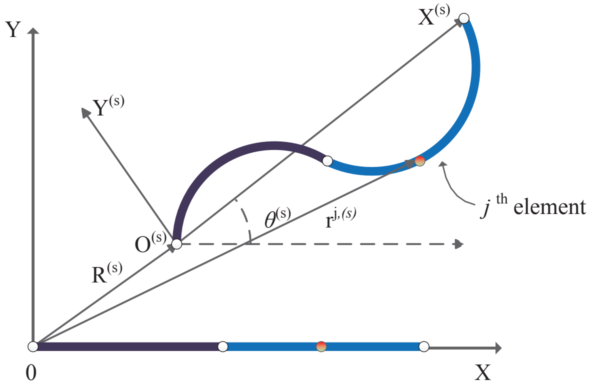

Figure 4.1: Generalized coordinates expression in FFR

where the velocity $\dot{\mathbf{r}}^{j,(s)}$ is given by

$$\dot{\mathbf{r}}^{j,(s)} = \dot{\mathbf{R}}^{(s)} + \dot{\mathbf{A}}^{(s)}\mathbf{N}^{j,(s)}(\mathbf{e}_0^{j,(s)} + \mathbf{q}_f^{j,(s)}) + \mathbf{A}^{(s)}\mathbf{N}^{j,(s)}\dot{\mathbf{q}}_f^{j,(s)}, \tag{4.3}$$

and $\dot{\mathbf{A}}^{(s)} = \mathbf{A}_\theta^{(s)}\dot{\theta}^{(s)}$, $\mathbf{A}_\theta^{(s)}$ is the derivatives of the rotation matrix with respect to $\theta^{(s)}$. Global quantities (therefore not equipped with index j) are obtained with standard FE assembly.

The equations of motion for the entire multibody system can be derived from Lagrange's equations

$$\frac{d}{dt}\left(\frac{\partial \mathcal{T}}{\partial \dot{\mathbf{q}}}\right)^T - \left(\frac{\partial \mathcal{T}}{\partial \mathbf{q}}\right)^T + \left(\frac{\partial \mathcal{U}}{\partial \mathbf{q}}\right)^T + \mathbf{C}_q^T\boldsymbol{\lambda} = \mathbf{g}, \tag{4.4}$$

where $\mathcal{T}$ and $\mathcal{U}$ are, respectively, the kinetic energy and strain energy for the entire system; $\mathbf{C}_q$ is the constraint Jacobian matrix, obtained from the constraint equation $\mathbf{C}(\mathbf{q}) = \mathbf{0}$; $\boldsymbol{\lambda}$ is the vector of Lagrange multipliers, representing the constraint forces; $\mathbf{g}$ is the vector of externally applied forces; t indicates time; $\mathbf{q}$ is the vector of the body generalized coordinates, formed as $\mathbf{q}^T = [\mathbf{q}^{(1)^T} \dots \mathbf{q}^{(N)^T}]$. Here, N is the number of bodies forming the system. Furthermore, $\mathbf{q}^{(s)}$ can be divided as

$$\mathbf{q}^{(s)^T} = \begin{bmatrix}\mathbf{q}_r^{(s)^T} & \mathbf{q}_f^{(s)^T}\end{bmatrix} = \begin{bmatrix}\mathbf{R}^{(s)^T} & \theta^{(s)} & \mathbf{q}_f^{(s)^T}\end{bmatrix}, \tag{4.5}$$

where $\mathbf{q}_r^{(s)} \in \mathbb{R}^3$ refers to the displacement and orientation of the body coordinate, $\mathbf{q}_f^{(s)} \in \mathbb{R}^{n_{(s)}}$ refers to the elastic displacement in the body coordinate, and $n_{(s)}$ is the corresponding number of elastic DoFs. For the remainder of this chapter, we focus on one single body and drop the superscript (s) for the sake of clarify.

The inertia coupling between the body coordinates $\mathbf{q}_r$ and elastic coordinates $\mathbf{q}_f$ leads to inertia terms which are configuration and velocity dependent

$$\frac{d}{dt}\left(\frac{\partial \mathcal{T}}{\partial \dot{\mathbf{q}}}\right)^T - \left(\frac{\partial \mathcal{T}}{\partial \mathbf{q}}\right)^T = \mathbf{M}\{\mathbf{q}\}\ddot{\mathbf{q}} - \mathbf{Q}_v\{\mathbf{q}, \dot{\mathbf{q}}\}, \tag{4.6}$$

where **M** is the configuration-dependent mass matrix, and $\mathbf{Q}_v$ is the quadratic velocity vector. The argument of functional dependency is enclosed in curly brackets.The details of the derivation can be found in Appendix A.1.

4.2.2. NONLINEAR STRAIN EXPRESSION

For a planar Euler-Bernoulli beam, the strain energy $\mathcal{U}$ could be written as (Sharf, 1996)

$$\mathcal{U} = \frac{1}{2}\int_0^L EA\varepsilon_{xx}^2\,\mathrm{d}x, \tag{4.7}$$

where E is Young's modulus; A is the cross sectional area of beam; L is the length and ε_{xx} is the axial strain.

The axial strain of an Euler-Bernoulli beam is given by Green-Lagrange strain expression (Reddy, 2004)

$$\varepsilon_{xx} = \frac{\partial u}{\partial x} + \frac{1}{2}\left[\left(\frac{\partial u}{\partial x}\right)^2 + \left(\frac{\partial v}{\partial x}\right)^2\right], \tag{4.8}$$

where u and v are, respectively, the axial and transverse displacement at any point of the cross section. Furthermore, the displacement field can be typically specified by the following linearized form

$$\begin{cases} u = u_0 - y\dfrac{\partial v_0}{\partial x} \\ v = v_0 \end{cases}, \tag{4.9}$$

where subscription $(\star)_0$ indicates the position at the centroid of the cross section, and y is the transverse coordinate. We adopt here the moderate rotations, von Kármán kinematic, which states that axial deformations and curvature are small compared to the bending rotation

$$\frac{1}{2}\left(\frac{\partial u}{\partial x}\right)^2 \ll \frac{\partial u}{\partial x}, \frac{1}{2}\left(\frac{\partial v}{\partial x}\right)^2. \tag{4.10}$$

Therefore, the quadratic strain expression applied in this work is suitable for the model with small to moderate deflections (Sharf, 1999)

$$\varepsilon_{xx} = \frac{\partial u}{\partial x} + \frac{1}{2}\left(\frac{\partial v}{\partial x}\right)^2 = \frac{\partial u_0}{\partial x} - y\frac{\partial^2 v_0}{\partial x^2} + \frac{1}{2}\left(\frac{\partial v_0}{\partial x}\right)^2. \tag{4.11}$$

In case of isotropic linear elastic material, the strain energy could be expressed as

$$\begin{aligned}\mathcal{U} = &\frac{1}{2}\int_0^L EA\Big(\frac{\partial u_0}{\partial x}\Big)^2\mathrm{d}x + \frac{1}{2}\int_0^L EI\left(\frac{\partial^2 v_0}{\partial x^2}\right)^2\mathrm{d}x \\ &+ \frac{1}{2}\int_0^L EA\frac{\partial u_0}{\partial x}\left(\frac{\partial v_0}{\partial x}\right)^2\mathrm{d}x + \frac{1}{2}\int_0^L \frac{EA}{4}\left(\frac{\partial v_0}{\partial x}\right)^4\mathrm{d}x,\end{aligned} \tag{4.12}$$

where I is the moment of inertia.

The classical linear strain energy expression, which is commonly applied in the FFR, only contains first and second order integrals in (4.12). The last two integrals in (4.12) are cubic and quartic functions of displacements, respectively. Once the FE discretization and assembly are applied, the elastic forces here can be directly generated from the differentiation of strain energy $\mathcal{U}$ as

$$\mathbf{f}_{nl} = \left(\frac{\partial \mathcal{U}}{\partial \mathbf{q}}\right)^T = \begin{bmatrix} \mathbf{0} & \mathbf{0} \\ \mathbf{0} & \mathbf{K}_L \end{bmatrix} \begin{bmatrix} \mathbf{q}_r \\ \mathbf{q}_f \end{bmatrix} + \begin{bmatrix} \mathbf{0} \\ \mathbf{Q}_f \end{bmatrix}, \tag{4.13}$$

where the internal force vector $\mathbf{f}_{nl}$ is a third-order polynomial function of the DoFs $\mathbf{q}_f$, and it can be divided into two contributions: the first term contains the classical linear internal forces, while the second term $\mathbf{Q}_f$ contains the higher order geometric nonlinear terms.

4.2.3. EQUATIONS OF MOTION

The equations of motion could be obtained by simply substituting (4.6) and (4.13) into (4.4), and written as

$$\mathbf{M}\{\mathbf{q}\}\ddot{\mathbf{q}} - \mathbf{Q}_v\{\mathbf{q},\dot{\mathbf{q}}\} + \mathbf{f}_{nl}\{\mathbf{q}\} + \mathbf{C}_q^T\boldsymbol{\lambda} = \mathbf{g}, \tag{4.14}$$

or more compactly,

$$\mathbf{M}\ddot{\mathbf{q}} + \mathbf{f}_{nl} + \mathbf{C}_q^T\boldsymbol{\lambda} = \mathbf{G}, \tag{4.15}$$

where $\mathbf{G} = \mathbf{g} + \mathbf{Q}_v$. The explicit dependency on $\mathbf{q}$ is here dropped for clarity. Equation (4.15) can be conveniently written in a partitioned form in terms of a coupled set of reference and elastic coordinates:

$$\begin{bmatrix} \mathbf{M}_{rr} & \mathbf{M}_{rf} \\ \mathbf{M}_{fr} & \mathbf{M}_{ff} \end{bmatrix} \begin{bmatrix} \ddot{\mathbf{q}}_r \\ \ddot{\mathbf{q}}_f \end{bmatrix} + \begin{bmatrix} \mathbf{0} & \mathbf{0} \\ \mathbf{0} & \mathbf{K}_L \end{bmatrix} \begin{bmatrix} \mathbf{q}_r \\ \mathbf{q}_f \end{bmatrix} + \begin{bmatrix} \mathbf{0} \\ \mathbf{Q}_f \end{bmatrix} + \begin{bmatrix} \mathbf{C}_{qr}^T \\ \mathbf{C}_{qf}^T \end{bmatrix} \boldsymbol{\lambda} = \begin{bmatrix} \mathbf{G}_r \\ \mathbf{G}_f \end{bmatrix}. \tag{4.16}$$

In multibody dynamics, the constraints are often differentiated twice with respect to time and incorporated in the inertial terms (Shabana, 2005, Bakr & Shabana, 1986). Then, additional regularization for constraint equations is required to ensure that the constraints are satisfied on the displacement and velocity level. This constraint regularization could be avoided by solving the original constraints (usually nonlinear) together with the equations of motion

$$\begin{cases} \mathbf{Re}\{\mathbf{q},\boldsymbol{\lambda}\} = \mathbf{M}\ddot{\mathbf{q}} + \mathbf{f}_{nl} + \mathbf{C}_q^T\boldsymbol{\lambda} - \mathbf{G} = \mathbf{0} \\ \mathbf{C}\{\mathbf{q}\} = \mathbf{0} \end{cases}. \tag{4.17}$$

Since the constraints will generally introduce infinite stiffness into the system, it is necessary to use unconditionally stable time integration schemes (Holm-Jørgensen & Nielsen, 2009). Usually, the constraints are acting only on specific boundary nodes. It is therefore convenient to further partition the elastic DoFs as $\mathbf{q}_f^T = [\mathbf{q}_b^T \quad \mathbf{q}_i^T]$, where the subscripts $(\star)_b$ and $(\star)_i$ replace $(\star)_f$ to represent boundary and internal DoFs. $\mathbf{q}_b \in \mathbb{R}^{n_b}$, $\mathbf{q}_i \in \mathbb{R}^{n_i}$ and $n = n_b + n_i$. The constraint Jacobian matrix can then be written as

$$\mathbf{C}_q = \begin{bmatrix} \mathbf{C}_{qr} & \mathbf{C}_{qb} & \mathbf{0}_{qi} \end{bmatrix}, \tag{4.18}$$

where the zero block matrix $\mathbf{0}_{qi}$ indicates that no constraints are acting on the internal DoFs. Equation (4.16) can then be partitioned in the same fashion as

$$\begin{bmatrix} \mathbf{M}_{rr} & \mathbf{M}_{rb} & \mathbf{M}_{ri} \\ \mathbf{M}_{br} & \mathbf{M}_{bb} & \mathbf{M}_{bi} \\ \mathbf{M}_{ir} & \mathbf{M}_{ib} & \mathbf{M}_{ii} \end{bmatrix} \begin{bmatrix} \ddot{\mathbf{q}}_r \\ \ddot{\mathbf{q}}_b \\ \ddot{\mathbf{q}}_i \end{bmatrix} + \begin{bmatrix} \mathbf{0} & \mathbf{0} & \mathbf{0} \\ \mathbf{0} & \mathbf{K}_{bb} & \mathbf{K}_{bi} \\ \mathbf{0} & \mathbf{K}_{ib} & \mathbf{K}_{ii} \end{bmatrix} \begin{bmatrix} \mathbf{q}_r \\ \mathbf{q}_b \\ \mathbf{q}_i \end{bmatrix} + \begin{bmatrix} \mathbf{0} \\ \mathbf{Q}_b \\ \mathbf{Q}_i \end{bmatrix} + \begin{bmatrix} \mathbf{C}_{qr}^T \\ \mathbf{C}_{qb}^T \\ \mathbf{0} \end{bmatrix} \boldsymbol{\lambda} = \begin{bmatrix} \mathbf{G}_r \\ \mathbf{G}_b \\ \mathbf{G}_i \end{bmatrix}. \tag{4.19}$$

4.3. NONLINEAR MODEL ORDER REDUCTION

In the classical application of modal analysis in FFR (Bakr & Shabana, 1986), the elastic displacement field $\mathbf{q}_f$ is represented as a linear combination of mode shapes. In this section, we discuss the extension of the well-known Craig-Bampton method for the effective reduction of flexible multibody systems characterized by elastic geometric nonlinearities.

4.3.1. CRAIG-BAMPTON METHOD

In order not to introduce any error in the constraints during the modal transformation, we adopt here the well known Craig-Bampton method (Bampton & Craig, 1968) for the reduction of the internal elastic DoFs. The reduction can be written as

$$\mathbf{q}_f = \begin{bmatrix} \mathbf{q}_b \\ \mathbf{q}_i \end{bmatrix} = \begin{bmatrix} \mathbf{I} & \mathbf{0} \\ \boldsymbol{\Psi} & \boldsymbol{\Phi} \end{bmatrix} \begin{bmatrix} \mathbf{q}_b \\ \boldsymbol{\eta} \end{bmatrix}, \tag{4.20}$$

where constraint modes $\boldsymbol{\Psi} \in \mathbb{R}^{n_i \times n_b}$

$$\boldsymbol{\Psi} = -\mathbf{K}_{ii}^{-1}\mathbf{K}_{ib} \tag{4.21}$$

are used to account for local effects at boundaries. In the linear modal analysis, the fixed interface modes $\boldsymbol{\Phi}$ only contains m vibration modes (VMs) of the system when constrained at the interface (i.e. $\mathbf{q}_b = \mathbf{0}$), solution of the eigenvalue problem:

$$\left(\mathbf{K}_{ii} - \omega_j^2 \mathbf{M}_{ii}\right)\boldsymbol{\phi}_j = \mathbf{0}, \tag{4.22}$$

where ω_j is the j^{th} eigenfrequency and $\boldsymbol{\phi}_j$ is the associated VM. In (4.20), $\boldsymbol{\eta} \in \mathbb{R}^m$ is a vector of modal coordinates. The reduction will be achieved by forming $\boldsymbol{\Phi}$ only with $m \ll n_i$ internal VMs. In practice, the reduction is performed on each component of the multibody system independently.

4.3.2. AUGMENTED REDUCTION BASIS WITH MODAL DERIVATIVES

Although Craig-Bampton method has been successfully applied in the FFR formulation in (Liew *et al.*, 1996), the reduction basis in (4.20) is usually linearized around a reference equilibrium position.

In geometric nonlinear systems, linear VMs usually fail to accurately reproduce the motion because of their inability to account for bending-stretching coupling caused by finite deflections. Typically, low-frequency bending dominated VMs must be accompanied by axial modes to accommodate for such effects. Axial VMs can be in principle calculated. However, their extraction is expensive since they are typically associated to much higher frequencies with respect to the bending modes. In addition, for more complex and realistic components, the distinction between axial and bending/twisting dominated modes can be difficult to establish.

To overcome this difficulty, modal derivatives (MDs) stemming from VMs can be appended to the existing linear reduction basis $\mathbf{\Phi}$, as shown in (Idelsohn & Cardona, 1985*a*,*b*). When the internal DoFs $\mathbf{q}_i$ can not be considered small, we first assume a nonlinear mapping $\mathbf{\Gamma}$ between the modal coordinate vector $\boldsymbol{\eta}$ and internal DoFs vector $\mathbf{q}_i$

$$\mathbf{q}_i \approx \mathbf{\Psi}\mathbf{q}_b + \mathbf{\Gamma}\{\boldsymbol{\eta}\}, \tag{4.23}$$

which gives

$$\mathrm{d}\mathbf{q}_i = \mathbf{\Psi}\mathrm{d}\mathbf{q}_b + \frac{\partial \mathbf{\Gamma}}{\partial \boldsymbol{\eta}}\mathrm{d}\boldsymbol{\eta} = \mathbf{\Psi}\mathrm{d}\mathbf{q}_b + \mathcal{X}\{\boldsymbol{\eta}\}\mathrm{d}\boldsymbol{\eta}, \tag{4.24}$$

where $\mathcal{X}(\boldsymbol{\eta})$ is a configuration dependent matrix of modes. The mapping (4.23) can be expanded in Taylor series around the equilibrium position

$$\mathbf{q}_i \approx \mathbf{\Psi}\mathbf{q}_b + \sum_{j=1}^{m} \left.\frac{\partial \mathbf{\Gamma}}{\partial \eta_j}\right|_{eq} \eta_j + \sum_{j=1}^{m}\sum_{k=1}^{m} \frac{1}{2}\left.\frac{\partial^2 \mathbf{\Gamma}}{\partial \eta_j \partial \eta_k}\right|_{eq} \eta_j \eta_k, \tag{4.25}$$

where the derivatives of the DoFs vector $\mathbf{q}_i$ with respect to the modal amplitudes η_j around the equilibrium position are assumed to be the truncated vibration modes, i.e.,

$$\left.\frac{\partial \mathbf{\Gamma}}{\partial \eta_j}\right|_{eq} = \mathcal{X}_j\{\mathbf{0}\} = \boldsymbol{\phi}_j, \tag{4.26}$$

and

$$\left.\frac{\partial^2 \mathbf{\Gamma}}{\partial \eta_j \partial \eta_k}\right|_{eq} = \left.\frac{\partial \mathcal{X}_j}{\partial \eta_k}\right|_{eq} = \boldsymbol{\vartheta}_{jk}, \tag{4.27}$$

where (4.26) represents the linear VM $\boldsymbol{\phi}_j$ (i.e., calculated at the equilibrium), and (4.27) gives the corresponding MDs, denoted here as $\boldsymbol{\vartheta}_{jk}$, which represent how $\mathcal{X}_j$ changes because of an imposed perturbation in the shape $\mathcal{X}_k$, at equilibrium. Equation (4.25) can therefore be written as

$$\mathbf{q}_i \approx \mathbf{\Psi}\mathbf{q}_b + \sum_{j=1}^{m} \boldsymbol{\phi}_j \eta_j + \sum_{j=1}^{m}\sum_{k=1}^{m} \frac{1}{2}\boldsymbol{\vartheta}_{jk}\eta_j\eta_k. \tag{4.28}$$

The MDs can be computed analytically by differentiating the linearized eigenvalue problem with respect to the modal amplitudes. It has already been shown that the inertia related terms can be neglected (Idelsohn & Cardona, 1985*a*,*b*, Slaats *et al.*, 1995). In this case, the MDs could be interpreted as a static correction, and are calculated by solving

$$\boldsymbol{\vartheta}_{jk} = -\mathbf{K}_{ii}^{-1} \left.\frac{\partial \mathbf{K}_{ii}^{nl}}{\partial \eta_k}\right|_{eq} \boldsymbol{\phi}_j. \tag{4.29}$$

Since the system is fixed at its boundary nodes by applying a nodal-fixed frame in FFR, the internal stiffness matrix $\mathbf{K}_{ii}$ is nonsingular. By neglecting all the inertia terms, it can be proved that MDs are symmetrical, i.e., $\boldsymbol{\vartheta}_{jk} = \boldsymbol{\vartheta}_{kj}$. Therefore, given m VMs, $r = m(m+1)/2$ MDs can be calculated.

In order to properly capture the contribution of the nonlinearity, we now augment reduction basis for the internal DoFs with a set of MDs collected in the matrix $\boldsymbol{\Theta}$, by loosing the quadratic mapping (4.28) between VMs and MDs and adding additional modal coordinates $\boldsymbol{\xi}$

$$\mathbf{q}_i \approx \boldsymbol{\Psi}\mathbf{q}_b + \boldsymbol{\Phi}\boldsymbol{\eta} + \boldsymbol{\Theta}\boldsymbol{\xi}. \tag{4.30}$$

Note that, although the number of MDs r grows quadratically with the number of chosen VMs m, it is possible to use simple selection criteria that indicate the most significant k MDs for the given analysis (Tiso, 2011). The reduction basis for an arbitrary body is therefore written as

$$\mathbf{q} = \begin{bmatrix} \mathbf{q}_r \\ \mathbf{q}_b \\ \mathbf{q}_i \end{bmatrix} = \begin{bmatrix} \mathbf{I} & \mathbf{0} & \mathbf{0} & \mathbf{0} \\ \mathbf{0} & \mathbf{I} & \mathbf{0} & \mathbf{0} \\ \mathbf{0} & \boldsymbol{\Psi} & \boldsymbol{\Phi} & \boldsymbol{\Theta} \end{bmatrix} \begin{bmatrix} \mathbf{q}_r \\ \mathbf{q}_b \\ \boldsymbol{\eta} \\ \boldsymbol{\xi} \end{bmatrix}. \tag{4.31}$$

Once the reduction basis (4.31) has been derived, the equations of motion (4.19) can be evaluated and projected to obtain a model of greatly reduced dimensions. Unfortunately, this procedure is inefficient since the cost for the evaluation of the nonlinear terms (i.e., inertial and elastic forces) scales with the size of the *nodal* coordinates: the nonlinear terms have to be computed in nodal coordinates and then projected on the reduced subspace. In our case, the nonlinear terms are written directly in terms of the modal coordinates. This is discussed in detail in the next section.

4.3.3. PRECOMPUTING POLYNOMIAL COEFFICIENTS

The adopted kinematic model yields a multivariate third-order polynomial expression of the nonlinear elastic forces $\mathbf{Q}_f$. A generic component Q_f^I can be written as

$$Q_f^I = Q_1^{Iij} q_f^i q_f^j + Q_2^{Iijl} q_f^i q_f^j q_f^l, \tag{4.32}$$

where $\mathbf{Q}_1 \in \mathbb{R}^{n\times n\times n}$, $\mathbf{Q}_2 \in \mathbb{R}^{n\times n\times n\times n}$ are constant third order and fourth order tensor coefficients with generic components Q_1^{Iij} and Q_2^{Iijl}. We adopted here the Einstein summation convention over the repeated indexes in the superscript.

Consequently, with the modal transformation of the form $\mathbf{q}_f = \mathbf{V}\boldsymbol{\gamma}$, where

$$\mathbf{V} = \begin{bmatrix} \mathbf{I} & \mathbf{0} & \mathbf{0} \\ \boldsymbol{\Psi} & \boldsymbol{\Phi} & \boldsymbol{\Theta} \end{bmatrix}, \tag{4.33}$$

and

$$\boldsymbol{\gamma}^T = [\mathbf{q}_b^T \quad \boldsymbol{\eta}^T \quad \boldsymbol{\xi}^T], \tag{4.34}$$

the reduced internal forces $\overline{\mathbf{Q}}_f = \mathbf{V}^T\mathbf{Q}_f\{\mathbf{V}\boldsymbol{\gamma}\}$ is a multivariate cubic polynomial in reduced coordinates $\boldsymbol{\gamma}$

$$\begin{aligned} \overline{Q}_f^I &= V^{iI}Q_f^i = V^{iI}{Q_1}^{ijl}V^{jp}V^{ls}\gamma^p\gamma^s + V^{iI}{Q_2}^{ijlv}V^{jp}V^{ls}V^{vw}\gamma^p\gamma^s\gamma^w \\ &= \overline{Q}_1^{Ips}\gamma^p\gamma^s + \overline{Q}_2^{Ipsw}\gamma^p\gamma^s\gamma^w, \end{aligned} \tag{4.35}$$

where $\overline{\mathbf{Q}}_1 \in \mathbb{R}^{\nu\times\nu\times\nu}$, $\overline{\mathbf{Q}}_2 \in \mathbb{R}^{\nu\times\nu\times\nu\times\nu}$ are constant third order and forth order tensor coefficients in the reduced coordinates with $\nu = n_b + m + k$. Similarly, each component of the reduced tangent stiffness matrix $\overline{\mathbf{K}}_{nl}$ is also a multivariate quadratic polynomial in $\boldsymbol{\gamma}$

$$\overline{K}_{nl}^{IJ} = \overline{K}_L^{IJ} + \overline{K}_3^{IJl}\gamma^l + \overline{K}_4^{IJls}\gamma^l\gamma^s, \tag{4.36}$$

with constant tensor coefficients $\overline{\mathbf{K}}_3 \in \mathbb{R}^{\nu\times\nu\times\nu}$, $\overline{\mathbf{K}}_4 \in \mathbb{R}^{\nu\times\nu\times\nu\times\nu}$. The constant linear stiffness can be expressed as

$$\overline{\mathbf{K}}_L = \mathbf{V}^T\mathbf{K}_L\mathbf{V}. \tag{4.37}$$

The tensors $\overline{\mathbf{Q}}_1$, $\overline{\mathbf{Q}}_2$, $\overline{\mathbf{K}}_3$, $\overline{\mathbf{K}}_4$ and $\overline{\mathbf{K}}_L$ can be precomputed offline for efficient runtime evaluation.

4.3.4. REDUCED EQUATIONS

The reduced equations are obtained via a classical Galerkin projection, i.e the residual obtained by introducing (4.31) in (4.16) is projected onto the same reduced basis used for the approximation of the displacements. As discussed in the previous section, it is possible to precompute the nonlinear terms to directly obtain modal terms rather than performing the full evaluation and projection. The resulting reduced equations are written as

$$\begin{bmatrix} \mathbf{M}_{rr} & \overline{\mathbf{M}}_{rf} \\ \overline{\mathbf{M}}_{fr} & \overline{\mathbf{M}}_{ff} \end{bmatrix} \begin{bmatrix} \ddot{\mathbf{q}}_r \\ \ddot{\boldsymbol{\gamma}} \end{bmatrix} + \begin{bmatrix} \mathbf{0} & \mathbf{0} \\ \mathbf{0} & \overline{\mathbf{K}}_L \end{bmatrix} \begin{bmatrix} \mathbf{q}_r \\ \boldsymbol{\gamma} \end{bmatrix} + \begin{bmatrix} \mathbf{0} \\ \overline{\mathbf{Q}}_f \end{bmatrix} + \begin{bmatrix} \mathbf{C}_{qr}^T \\ \overline{\mathbf{C}}_{qf}^T \end{bmatrix} \boldsymbol{\lambda} = \begin{bmatrix} \mathbf{G}_r \\ \overline{\mathbf{G}}_f \end{bmatrix}, \tag{4.38}$$

where

$$\overline{\mathbf{M}}_{rf} = \overline{\mathbf{M}}_{fr}^T = \mathbf{M}_{rf}\mathbf{V}; \quad \overline{\mathbf{M}}_{ff} = \mathbf{V}^T\mathbf{M}_{ff}\mathbf{V}; \quad \overline{\mathbf{G}}_f = \mathbf{V}^T\mathbf{G}_f.$$

Note that $\overline{\mathbf{C}}_{qf}$ only contains non-zero terms on the column corresponding to the boundary DoFs $\mathbf{q}_b$.

Because of the inertia coupling between the reference motion of the body and the elastic deformation of elements, also the inertia related terms $\overline{\mathbf{M}}_{rf}$, $\overline{\mathbf{M}}_{fr}$ and $\overline{\mathbf{G}}_f$ will be configuration dependent. Similar to the elastic terms, the inertial terms can also be directly expressed in modal coordinates. The detailed formulation of the reduced mass matrix and quadratic velocity vector is reported in Appendix A.2.

The detailed MOR procedure proposed is illustrated in Fig.4.2 on a flexible slider crank mechanism. The end nodes in both crank and connecting rod are treated as boundary nodes: their corresponding DoFs will not be transformed to modal coordinates. The material and geometrical properties are taken from the numerical example in Section 4.4.3. From Fig.4.2 we can see that the first few VMs feature bending displacements only, while the corresponding MDs, which describe the second-order nonlinearities, exhibit longitudinal displacement only.

4.4. NUMERICAL EXAMPLES

Three numerical examples are presented in this section to show the effectiveness of the proposed approach. The reduced solutions in the FFR are not only compared with the

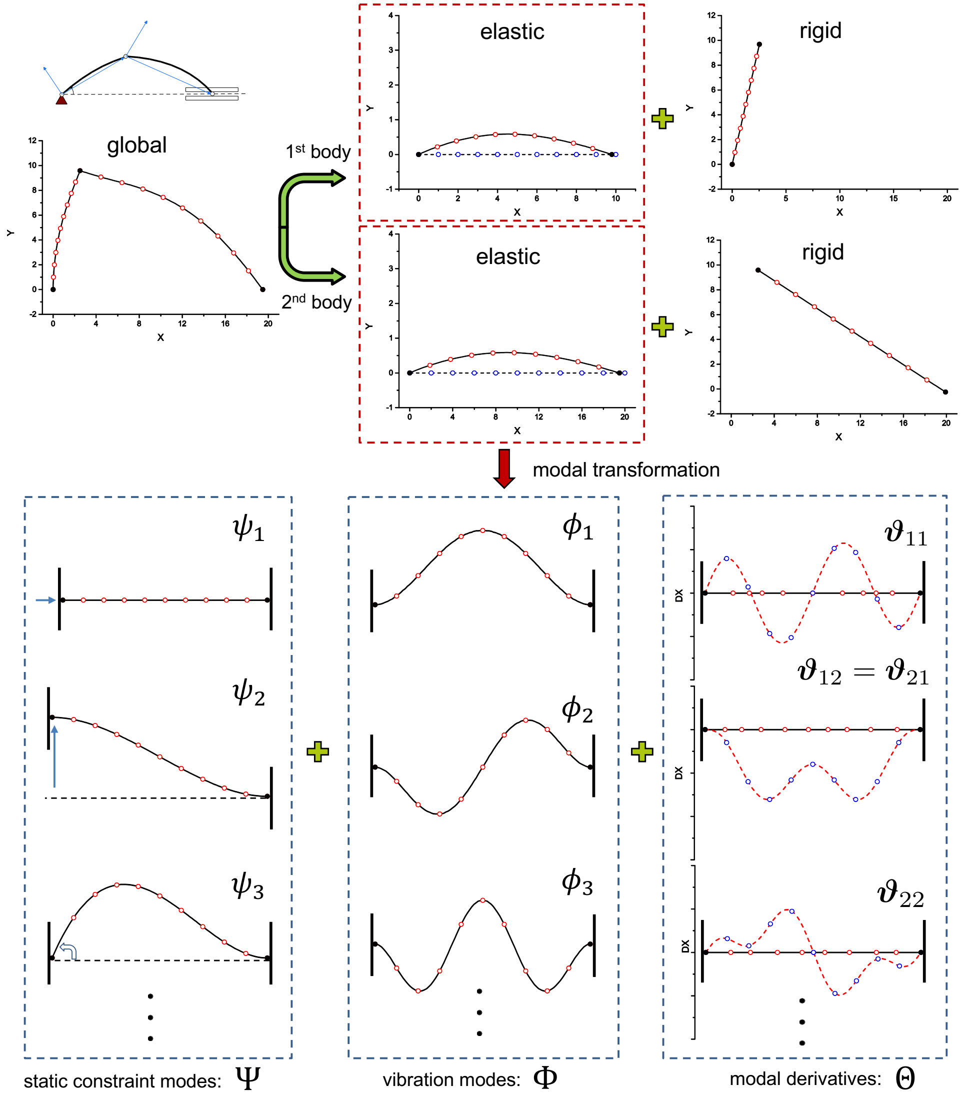

Figure 4.2: Detailed modal transformation procedure for a slider crank mechanism in FFR. To further highlight the MDs, the axial displacement DX (red dot line with blue node) is plotted here as a function of node position. The actual mesh deformation is shown as well. Note the axial-only contribution of the MDs that capture the necessary second order effect of the geometric nonlinearity associated to bending-only VMs.

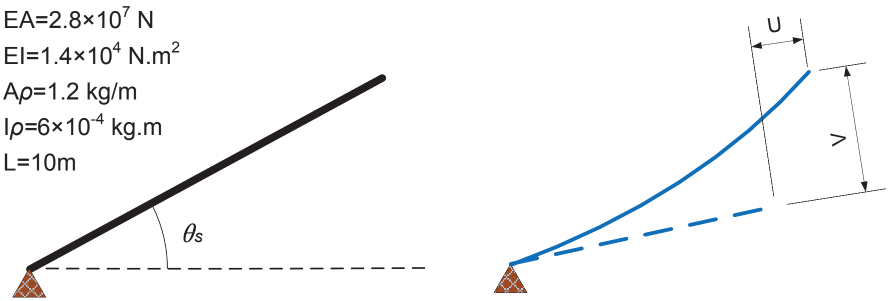

Figure 4.3: The spin-up beam and two components of its tip displacement: U and V

corresponding full solutions, but also with the response obtained by using a Corotational Frame of Reference (CFR) formulation. The CFR is a more general and expensive framework that is able to deal with arbitrary large elastic deflection. This allows to assess that the magnitude of the elastic deflections are within the validity of the adopted approximated von Karman kinematic model. We considered here the CFR formulation discussed in (Le *et al.*, 2011) as a reference, where cubic shape functions are used to derive both the inertia and elastic terms. Recently, this formulation has also been successfully extended to the dynamic analysis of 3D flexible beam with good accuracy (Le *et al.*, 2014).

4.4.1. TEST 1: ROTATING BEAM

The dynamic analysis of a rotating beam, which has been used as a benchmark in many papers dealing with flexible beams and geometric nonlinearities (Simo & V. Q., 1986, Hsiao *et al.*, 1994, Galvanetto & Crisfield, 1996, Kim *et al.*, 2013), is here presented. The geometry of the beam and the corresponding material properties are shown in Fig. 4.3. An imposed end rotation θ_s is applied as:

$$\theta_s = \begin{cases} \frac{\omega_s}{T_s}\left[\frac{1}{2}t^2 + \left(\frac{T_s}{2\pi}\right)^2\left(\cos\left(\frac{2\pi t}{T_s}\right) - 1\right)\right], & t < T_s \\ \omega_s\left(t - \frac{T_s}{2}\right). & t > T_s \end{cases} \tag{4.39}$$

The beam reaches steady state motion after T_s second and then rotates at a constant angular velocity ω_s. Transient responses are computed for $T_s = 15$ s, and for angular velocity $\omega_s = 6$ rad/sec.

In order to make a comprehensive comparison, this example is analyzed by different approaches: 1.the CFR is taken as reference solution; 2. the nonlinear floating frame is mentioned as the full analysis (denoted as NLFFR); 3. the linear floating frame is performed by neglecting the nonlinear internal forces $\mathbf{Q}_f$ in equation of motion (denoted as LFFR); 4. the modal derivatives based reduction solution is applied in nonlinear floating frame, where the modal basis is composed by the first 10 VMs and 10 MDs corresponding to the first 4 VMs (denoted as 10VMs+10MDs); 5. a reduced solution obtained with the first 20 VMs (denoted as 20VMs) is also calculated. The two components of the tip

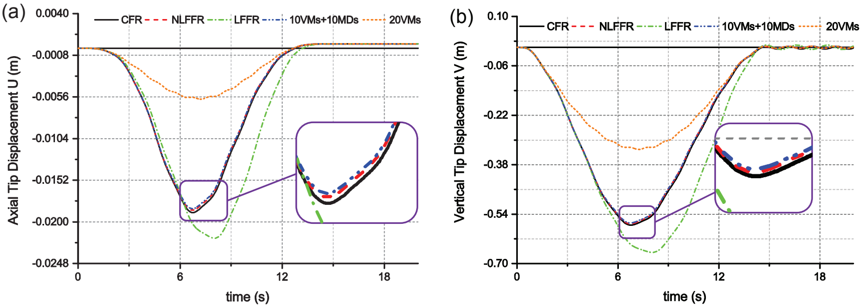

Figure 4.4: Time history for two components of the tip displacement relative to the spin-up beam. (a) Axial Tip Displacement U. (b) Vertical Tip Displacement V

displacement vector are shown in Fig. 4.4.

The results obtained with the NLFFR are in very good agreement with the CFR solution and clearly differ from the LFFR response, to confirm that the adopted kinematic model is adequate for the problem at hand, see Fig. 4.4 . Furthermore, the proposed modal derivatives based reduction method with 10VMs and 10MDs shows a good agreement with the reference solution. On the contrary, if only the first 20VMs are applied in the reduced basis, a clear difference can be observed.

To offer a further insight, some other reduced models with different modal basis are compared with the full analysis (NLFFR), as shown in Fig. 4.5. The comparison is performed between different reduction basis of the same size. The tip displacements components are shown. In addition, the root mean square (RMS) error ϵ_{RMS} relative to the entire displacement vector is shown, calculated as:

$$\epsilon_{RMS}\{t\} = \sqrt{\frac{1}{n}\left[\sum_{i=1}^{n}(u_i\{t\} - \overline{u}_i\{t\})^2 + \sum_{i=1}^{n}(w_i\{t\} - \overline{w}_i\{t\})^2\right]} \tag{4.40}$$

where u_i, w_i and $\overline{u}_i, \overline{w}_i$, are the horizontal and vertical components of the node displacement from the full and reduced models.

The reduced basis with 10 VMs enriched by 6 MDs (indicated as 10VMs+6MDs) yields much better results when compared to the reduced solution obtained with 16VMs. In addition, by increasing the reduction basis with two additional MDs (10VMs+8MDs), the results show a marked improvement, while the results are almost unchanged if two additional VMs are added in the 18VMs cases. In some related work (Rizzi & Przekop, 2008, Li *et al.*, 2009), high-frequency axial vibration modes (AVMs) are specifically added to the basis in order to properly account for the nonlinear bending-stretching coupling. It is therefore interesting to compare this approach with the method proposed here. We form the reduction basis with first 10 VMs and the first 8 AVMs. The eigenfrequencies associated to the AVMs are reported in Table 4.1. Note that the frequency range of interest has to be extended from 145 Hz to almost 2100 Hz. In addition, the obtained results do not match the accuracy given by the 10VMs+8MDs case. Therefore, we can conclude that in order to reproduce the nonlinear behaviour, MDs based reduction basis provides better accuracy than an equal size reduction constructed with AVMs.

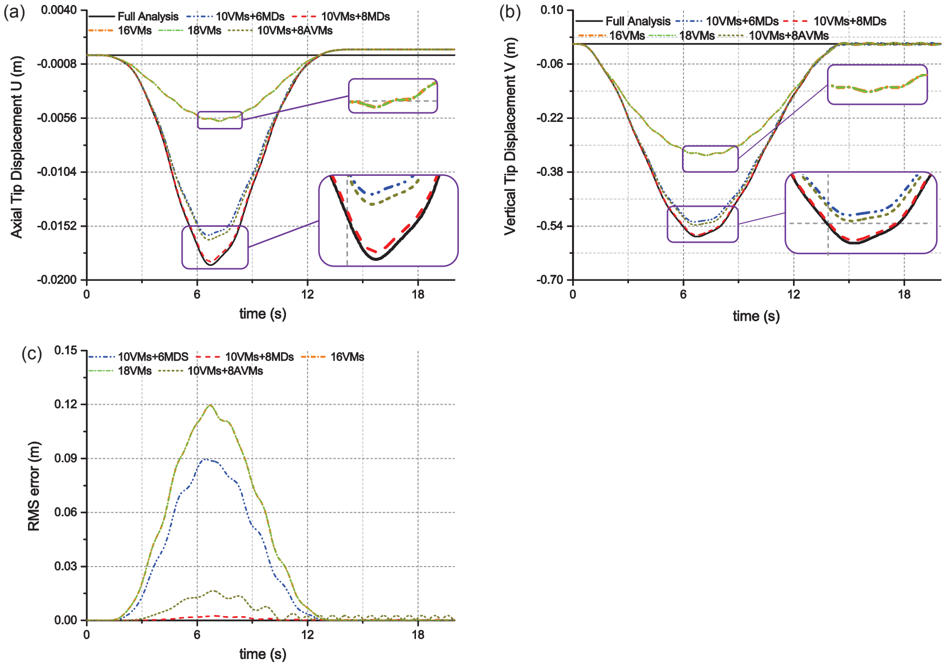

Figure 4.5: The comparison of the spin-up beam under different reduced models. (a) Axial Tip Displacement U. (b) Vertical Tip Displacement V. (c) RMS error of the displacement field

Table 4.1: Frequencies of the first 10 VMs and additional 8 AVMs

Mode Shapes	1VM	2VM	⋯	10VM	1AVM	2AVM	⋯	8AVM
Frequency(Hz)	2.650	8.589	⋯	145.171	362.318	603.963	⋯	2059.050

4.4.2. TEST 2: SWINGING RUBBER BAR

We consider here a slender rubber beam connected to a fixed inertial frame via a joint and exposed to a constant gravitational force. The beam is initially at rest in horizontal position. The material and geometric properties of the beam are taken from (Lang *et al.*, 2011, Schulze *et al.*, 2013): E=5 × 10^6 N/m^2, ρ=1.1× 10^3 kg/m^3, L = 1.0 m. The cross section is circular with a radius of 5 mm. The analysis is performed for a time interval of 1 second with a fixed time step ΔT of 0.001 seconds.

The dynamic response is shown in Fig. 4.6. The full response is compared with reduced basis formed with the first 5 VMs plus 10 MDs, as well as 15 VMs, respectively. As shown in Fig. 4.6, a reduction basis containing 5 VMs plus 10 MDs clearly outperforms a basis of the same size formed with 15 VMs only.

The RMS error ϵ_{RMS} of four reduced models with different modal basis is shown in Fig. 4.7. The number of VMs is fixed and equal to 5, while the number of MDs is increased

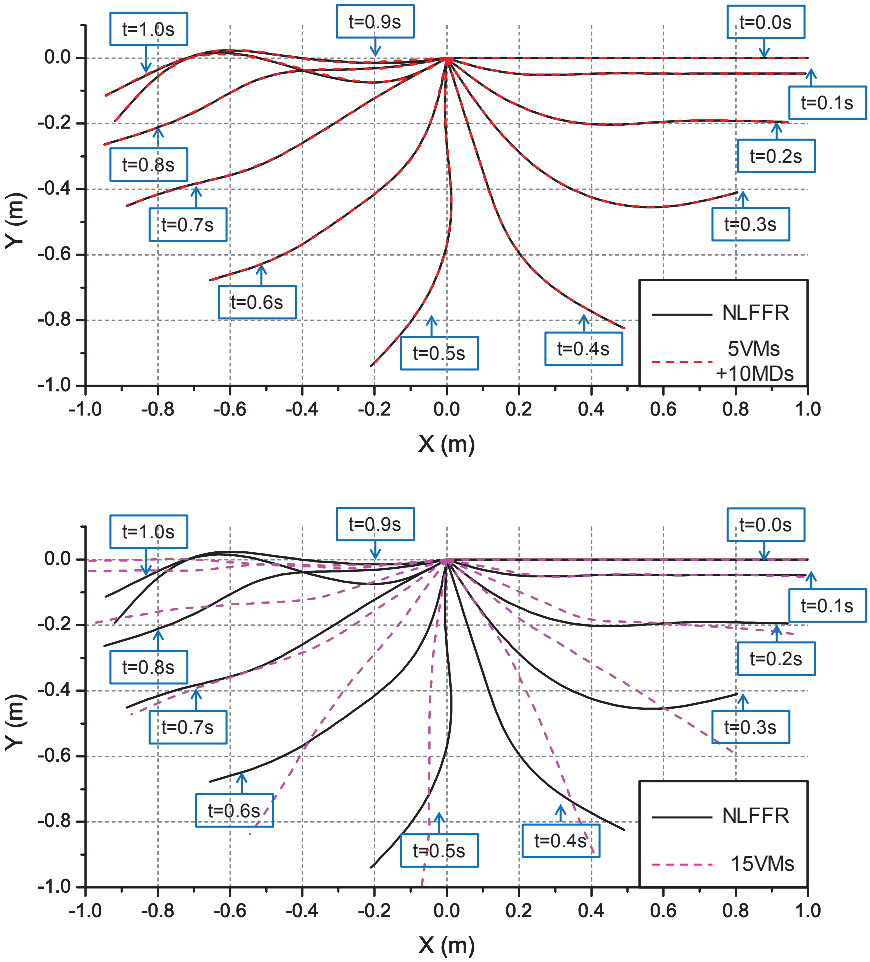

Figure 4.6: Response of a swinging rubber beam during the first second: (a) 5VMs+10MDs vs. full analysis; (b) 15VMs vs. full analysis

to include the contribution of the first 2,3 and 4 VMs, respectively. The error rapidly decreases as more MDs associated to the low frequency VMs are included in the basis.

4.4.3. TEST 3: FLEXIBLE SLIDER CRANK MECHANISM

In the third numerical example, a flexible slider-crank mechanism is analyzed. The system is depicted in Fig.4.8 together with the material and geometric properties. The connection rod is constrained to the crank at the left end by a joint, and is fixed in vertical direction at the right end. A constant angular acceleration is prescribed to the crank such that the rotation θ_s reaches 270 degrees after 5 seconds, as shown in Fig. 4.9(a). At this point, the angular rotation of the crank is locked and the system starts to exhibit elastic

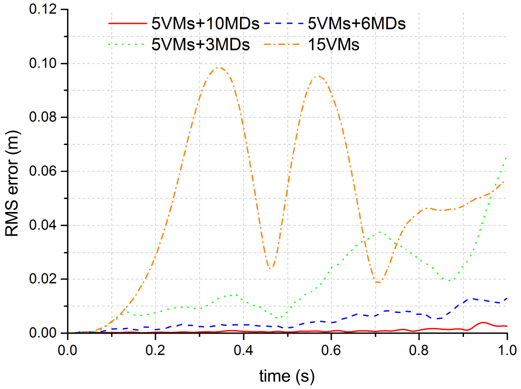

Figure 4.7: RMS error of the different modal basis in the swinging rubber bar example

oscillations in the geometric nonlinear range.

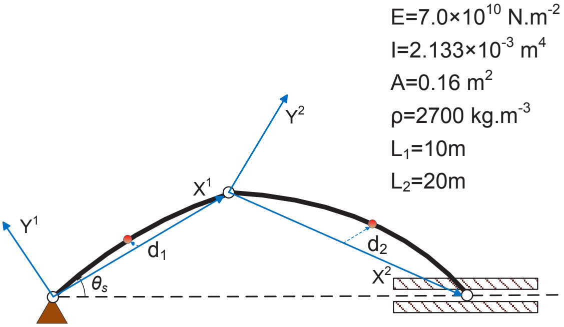

Figure 4.8: The deformed configuration of a slider crank mechanism

In the FFR model, two fixed nodal frames are attached to the crank and rod respectively. The two end nodes of both crank and rod are set as the boundary nodes, and therefore 6 constraint modes are present in the reduced model for each substructure.

The elastic deflection of the middle point of both the crank and rod is shown in Fig. 4.9. The results obtained with the CFR have been set as a reference to check the accuracy of the full analysis in FFR. The reduction basis is formed with 5 VMs and 10 MDs (relative to the first 4 VMs) for both substructures, and the obtained results are compared with the case when only first 15 VMs are used.

The response of the system during the first 5 seconds (i.e., before the rotation locking) exhibits mainly rigid motion, and therefore both of the two reduced models show accurate results. After the locking, the elastic deflections are large and the reduction basis featuring only VMs is not able to reproduce the full solution, while the reduced basis

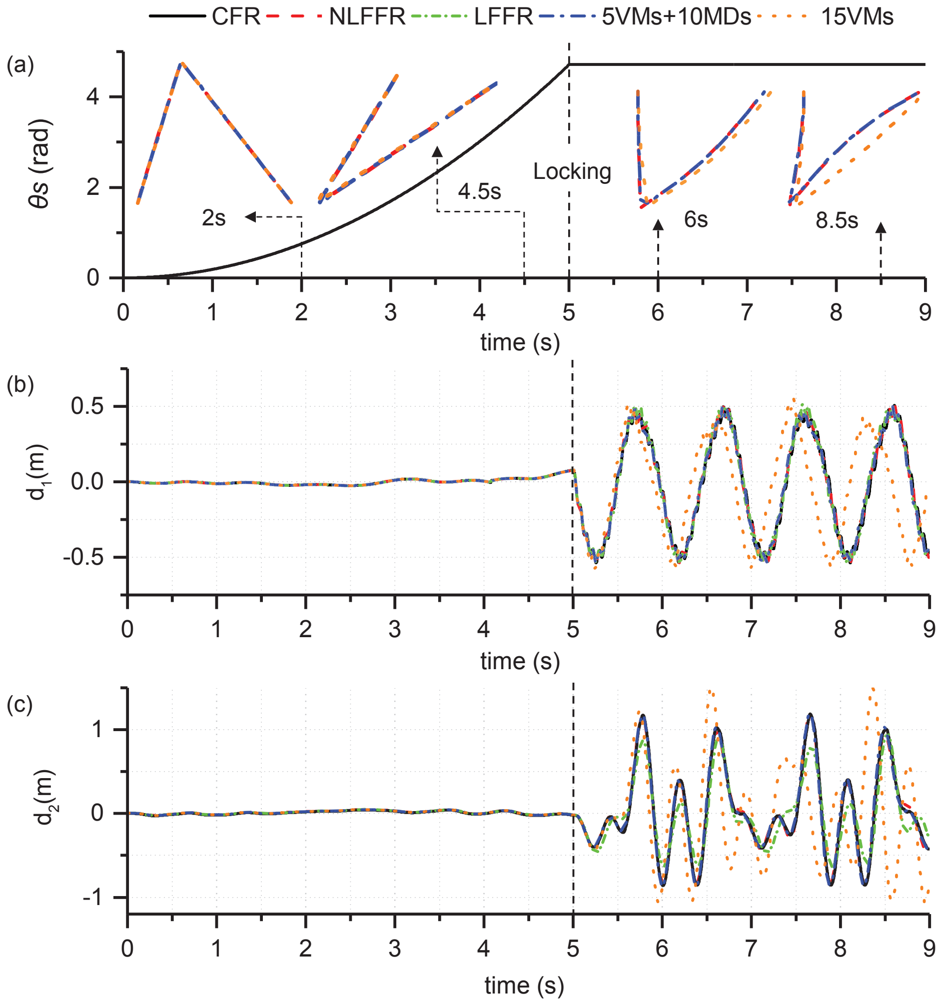

Figure 4.9: The elastic deflection of the flexible slider crank mechanism using different formulations: (a) prescribed rotational angular during the a 9 second time span; (b) the deflection d_1 of the middle point of the flexible crank; (c) the deflection d_2 of the middle point of the flexible rod. In (a), snapshots of the flexible crank-rod system are shown at 2s, 4.5s, 6s, 8.5s.

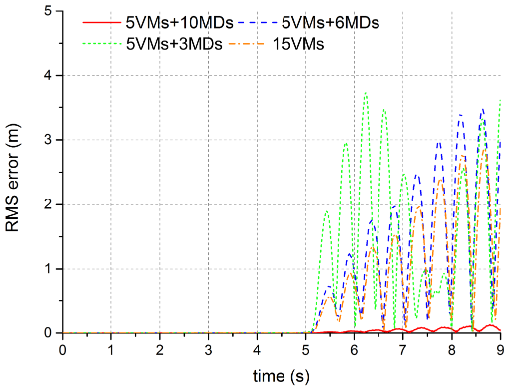

Figure 4.10: RMS error of the different modal basis in the flexible slider crank example

formed with VMs and MDs yields very good results, as can be seen in Fig. 4.9.

The RMS error between the full and reduced solutions is computed also for this example in order to gain additional insight on the properties of the reduction basis, see Fig. 4.10. It can be noticed that, if not enough MDs are included in the reduction basis, the reduced solution is of poor accuracy. This could be attributed to the fact that the impulsive load generated by the rotation locking triggers the large response of the first few VMs, and therefore their interactions, which is given by the corresponding MDs, must be properly included in the basis.

4.4.4. COMPUTATIONAL EFFICIENCY

In this section, the computational efficiency is compared between the nonlinear modal analysis with augmented basis (VMs+MDs) and the full nonlinear FEM analysis (NLFFR). The performance is measured in terms of computational time for Test 1: rotating beam. All the simulations are performed on software MATLAB® R2012b, on an Intel® Core™ i5-3470 @ 3.2GHz and 16GB RAM machine.

Table 4.2 compares the CPU time required for Test 1. The simulations are performed for 20s with a time step $\Delta t = 0.02s$. As shown in Table 4.2, the computational time in the case of nonlinear modal analysis mainly depends on the size of selected model reduction bases, and only slightly arises with the increase of element number owing to the time spend on modal transformation . Therefore, a substantial CPU time reduction can be achieved for application characterised by a large number of elements, which is typically the case for realistic applications.

4.5. CONCLUSIONS

We propose a model order reduction method for the dynamic analysis of flexible multibody systems featuring large overall motion and nonlinear elastic deflection, which can be described with the von Kármán kinematic assumption in the body reference. The equations of motion are written in the floating frame of reference (FFR) for each flexible

Table 4.2: CPU time for the Test 1: rotating beam, between full model and reduced model

Element number	100	200	300	400	500
Full analysis (s)	52.511	123.502	165.847	204.683	251.598
Modal analysis with 10VMs plus 10MDs (s)	64.280	71.259	72.555	72.900	79.832

component. This enables the description of the elastic motion with an internal reduction basis complemented with interface modes, which allow the connection between the bodies via constraints. The internal basis of linear vibration modes (VMs) is enriched with modal derivatives (MDs), which describe the essential nonlinear contributions for the elastic geometric nonlinearities induced by the VMs.

The reduced basis is formed by enriching a classical Craig-Bampton reduction with MDs relative to the VMs considered for each component. Subsequently, the reduced equations of motion are obtained with a Galerkin projection.

The reduction in computational time is obtained by the substantial reduction in size of the governing equations of motion. This results in the solution of a much smaller system during the time integration via the implicit scheme. Moreover, the polynomial form of the nonlinear elastic forces allows the offline computation of the reduced nonlinear terms directly in modal coordinates.

The presented numerical examples highlight the superior performances of the proposed approach with respect to classical reduction with VMs only. It is worth noting that the *ad-hoc* inclusion of axial vibration modes in the reduction basis does not provide results as accurate as the ones obtained with the proposed approach. The proposed method extends the common practice of linear modal analysis to systematically tackle geometric nonlinear multibody problems. As a consequence, the proposed technique does not require expensive sampling of the full solution to form the reduction basis, as necessary in several model order reduction techniques based on the proper orthogonal decomposition.

The proposed approach does not pose additional conceptual difficulties for the extension into three dimensional cases. In this case, it is recommended to resort on the mean-axis definition for the floating frame of reference. This choice could be more practical than the nodal fixed frame, as the best choice of the specified fixed nodes in the nodal fixed frame is not straightforward in three dimensional cases. Also, the MDs have been successfully calculated for three dimensional models (Tiso, 2011, Weeger *et al.*, 2014) in inertia frame, to solve nonlinear problems without the large rigid body motion. It is worth mentioning that the benefits of the proposed technique will be even more apparent for tridimensional problems that would feature, in general, larger finite element meshes and therefore provide larger gains from the adopted modal approach.

5

A MODAL DERIVATIVES ENHANCED RUBIN SUBSTRUCTURING METHOD FOR GEOMETRIC NONLINEAR MULTIBODY SYSTEMS

This chapter presents a novel model order reduction technique for 3D flexible multibody systems featuring nonlinear elastic behavior. We adopt the mean-axis floating frame approach in combination with an enhanced Rubin substructuring technique for the construction of the reduction basis. The standard Rubin reduction basis is augmented with the modal derivatives of both free-interface vibration modes and attachment modes to consider the bending-stretching coupling effects for each flexible body. The mean-axis frame generally yields relative displacements and rotations of smaller magnitude when compared to the one obtained by the nodal-fixed floating frame. This positively impacts the accuracy of the reduction basis. Also, the enhanced Rubin method better considers the geometrical nonlinearities at the interfaces than the modal derivatives enhanced Craig-Bampton method, as it comprises vibration modes and modal derivatives featuring free motion of the interface. The coupling between free-interface modes and attachment modes is also considered. Numerical tests show that the proposed technique can reproduce the full solutions with satisfying accuracy and online speed up. The proposed technique results in a more accurate reduced-order model than its counterpart obtained with the enhanced Craig-Bampton, nodal-fixed floating frame method in Chapter 4. However, the mean-axis formulation produces non-sparse operators and increases the offline costs.

This chapter is based on the paper "Wu, L., Tatsis, K. , Chatzi, E., van Keulen, F., & Tiso, P. , A modal derivatives enhanced Rubin substructuring method for geometric nonlinear multibody systems. (submitted to Multibody System Dynamics, minor revision)".

5.1. INTRODUCTION

The simulation of flexible multibody systems (FMBS) often relies on finite element (FE) discretization of flexible components, which are then embedded into a floating frame of reference (FFR) formulation (Shabana, 1997, Wasfy & Noor, 2003). The FFR represents the position of each body as a superposition of two components: *i*) the motion of the reference frame which follows the overall rigid body motion of the flexible body; *ii*) the relative motion of the flexible body with respect to the reference frame. The resulting models often comprise a large number of degrees of freedom (DoFs), which render time integration schemes extremely costly. A relevant example of unaffordable computational burden could be found in the simulation of large-scale offshore wind turbines. To assess their fatigue life, thousands of load cases need to be simulated, resulting in disproportionally large computation times. At present, this can be achieved only by relying on extremely simplified beam models that reduce the computational cost to a bearable level. Such models do not inherit the complexity of the actual three-dimensional model of the blade, and, as a result, the complex dynamic behavior may not be appropriately represented. For this reason, many model order reduction (MOR) strategies for three-dimensional FMBS have been proposed in the past. These techniques are based on classic modal truncation (Shabana, 2005, Bakr & Shabana, 1986) or singular value decomposition (SVD) based MOR techniques as in (Fehr & Eberhard, 2011, Fischer & Eberhard, 2014, Holzwarth & Eberhard, 2015). In (Brüls *et al.*, 2007), a global modal parametrization based MOR method is proposed, where the motion of the FMBS is described in terms of configuration dependent modes. Using this reduction method, the nonlinear holonomic constraints are naturally satisfied without the adoption of Lagrange Multipliers. However, in most of the MOR techniques, the elastic behavior is assumed to be linear. As discussed in (Shabana, 2005), the linear MOR with FFR formulation is only suitable for structures featuring large rigid body motions but small relative displacements with respect to the reference frame, as well as slow rotational speeds. For FMBS featuring high rigid body rotation rates, the centrifugal force is of great significance, and therefore, the centrifugal stiffening effect and foreshortening effect have to be considered.

For many FMBS applications involving finite but moderate relative rotations with respect to the reference frame, neglecting geometrical nonlinearities may lead to incorrect and even diverging solutions (Mayo *et al.*, 1995, Mayo & Domínguez, 1996). In (Nada *et al.*, 2010), the geometrical nonlinearities are introduced in the equations of motion. As a result, the internal force vector and tangent matrix need to be recomputed for every iteration within each time step, therefore significantly impacting the computational cost. It is then a must to extend the linear MOR methods to the geometric nonlinear regime for three-dimensional FMBS.

When one substructure of the FMBS features geometric nonlinear behavior, dominant low-frequency modes are not sufficient for adequately representing the relative motion with respect to the reference frame. Typically, large slender structures exhibit coupling between bending and axial displacements when excited in the nonlinear regime. The corresponding bending-stretching coupling could be in principle provided by adding membrane-dominant (usually high-frequency) modes to the bending-dominant (typically low-frequency) modes based reduction basis. For flat structures, where each vibration mode exhibits purely bending or membrane displacement, such membrane modes can be easily identified and added to the reduced-order basis (ROB). The inclusion of these so-called *ad hoc* modes has been applied in the FFR formulation in (Rizzi & Przekop, 2008, Li *et al.*, 2009). However, for more complex geometries, the extraction of such modes is *i*) challenging, as it is not straightforward to identify membrane-dominated modes, and *ii*) expensive, as several modes need to be extracted.

In previous work (Wu & Tiso, 2016), the linear Craig-Bampton (CB) substructuring basis (Bampton & Craig, 1968) was enriched with modal derivatives (MDs) (Idelsohn & Cardona, 1985*a*,*b*) corresponding to low-frequency fixed-interface modes. The augmented ROB was capable of capturing both the rigid body motions and the nonlinear relative displacement of the FMBS effectively. The nonlinear MOR technique was applied for nodal-fixed frame reference (Nikravesh, 2005), which is the most straightforward implementation of the FFR formulation. In this case, the reference frame is attached to specified nodes of the moving body. However, for complex structures, e.g. discretized with shell and solid elements, it is difficult to determine the optimal node whereon the reference frame should be attached. This arbitrary definition of the nodal-fixed frame results in significantly different relative displacements and rotations with respect to the reference frame (Nikravesh, 2005), and ultimately degrades the accuracy if the relative displacement and rotations are too large.

The use of mean-axis frame (Cavin & Dusto, 1977), which alleviates the need for the reference frame to be attached to a specified node of the structure, aims at minimizing the relative kinetic energy with respect to the reference frame. As a result, the largest relative displacement and rotation observed from a mean-axis frame will be smaller than the largest one observed when standing at the origin of the nodal-fixed frame, as underlined in (Nikravesh, 2005). This is especially relevant when one assumes geometrical nonlinearities based on the von Kármán kinematic assumption, which is suitable for small strains and moderate rotations (Sharf, 1999) with respect to the reference frame. Since the MDs are obtained from a truncated Taylor expansion of the nonlinear static equilibrium around the reference position (Weeger *et al.*, 2014, 2016) and are not updated during the time integration, the accuracy of using MDs will be determined by how far the structure departs from the equilibrium position. Therefore, the use of MDs further supports the argument of using the mean-axis formulation.

In this chapter, the standard Rubin substructuring technique (Rubin, 1975) is enhanced with MDs and then implemented on the mean-axis frame formulation for the construction of ROMs for the FMBS featuring moderate relative displacements and rotations with respect to the reference frame. Each body is reduced by forming the ROB with attachment modes, free-interface modes, and corresponding MDs. The Rubin method fits the mean-axis formulation more naturally than the CB method when applied to the geometric nonlinear problem, for two reasons. First, the Rubin method is based on a truncated set of free-interface vibration modes, which naturally describe the elastic deformation of the component with respect to the reference frame (i.e., free-interface deformation with respect to the reference frame as in mean-axis frame formulation). Second, the nonlinear behavior occurring at the interface is better represented by MDs of both free-interface modes and attachment modes (related to the Rubin method) than by MDs of fixed interface modes coming from the CB method. In (Wenneker & Tiso, 2014), the inclusion of only the MDs relative to rigid body modes (i.e., vibration modes of zero frequency) in the ROB significantly increases the accuracy. In our approach, the MDs relative to rigid body modes are avoided since the rigid body motion has already been described by the reference frame motion. Therefore, a ROB of very limited size can be achieved.

This chapter is organized as follows. Section 5.2 describes the FFR description featuring geometric nonlinearities. The nodal-fixed and mean-axis frame are applied to the FFR formulation in Section 5.3. The assembled EoMs of all FMBS, as well as the holonomic joint constraints, are presented in Section 5.4. The nonlinear MOR method based on the enhanced Rubin method is proposed in Section 5.5. Section 5.6 shows numerical examples to assess the accuracy of the present formulation, especially emphasizing the improvements with respect to (Wu & Tiso, 2016). Finally, conclusions are given in Section 5.7.

5.2. EQUATIONS OF MOTION IN FLOATING FRAME OF REFERENCE

In the FFR formulation, we describe the absolute motion of an arbitrary point $P^{j,(s)}$ on the j^{th} finite element of the s^{th} body as the superposition of the motion of the reference frame $O^{(s)}X^{(s)}Y^{(s)}Z^{(s)}$ and the position of the point with respect to the reference frame, as shown in Fig. 5.1. The position vector $\mathbf{r}^{j,(s)} \in \mathbb{R}^3$ of the point $P^{j,(s)}$ is defined as

$$\mathbf{r}^{j,(s)} = \mathbf{R}^{(s)} + \mathbf{A}^{(s)}\mathbf{u}^{j,(s)} = \mathbf{R}^{(s)} + \mathbf{A}^{(s)}\mathbf{N}^{j,(s)}\left(\mathbf{q}_0^{j,(s)} + \mathbf{q}_f^{j,(s)}\right), \tag{5.1}$$

where $\mathbf{R}^{(s)} \in \mathbb{R}^3$ represents the position of origin of the reference frame $O^{(s)}X^{(s)}Y^{(s)}Z^{(s)}$ with respect to global frame $OXYZ$, $\mathbf{u}^{j,(s)} \in \mathbb{R}^3$ is the relative nodal position of $P^{j,(s)}$ with respect to the reference frame, and $\mathbf{A}^{(s)} \in \mathbb{R}^{3\times 3}$ is the transformation matrix from the reference frame $O^{(s)}X^{(s)}Y^{(s)}Z^{(s)}$ to the global frame $OXYZ$. The matrix of shape functions in the reference frame is indicated by $\mathbf{N}^{j,(s)} \in \mathbb{R}^{3\times n_e}$, where n_e is the number of DoFs per element, $\mathbf{q}_0^{j,(s)} \in \mathbb{R}^{n_e}$ is the vector of nodal coordinates in the undeformed state and $\mathbf{q}_f^{j,(s)} \in \mathbb{R}^{n_e}$ is the vector of relative DoFs of the j^{th} element. For the remainder of this chapter, we drop the superscript $\star^{(s)}$ for the sake of clarify, unless it is necessary to distinguish between different bodies in the FMBS.

The rotation matrix $\mathbf{A}$ is defined as

$$\mathbf{A} = \begin{bmatrix} 1-2\theta_2^2-2\theta_3^2 & 2(\theta_1\theta_2-\theta_0\theta_3) & 2(\theta_1\theta_3+\theta_0\theta_2) \\ 2(\theta_1\theta_2+\theta_0\theta_3) & 1-2\theta_1^2-2\theta_3^2 & 2(\theta_2\theta_3-\theta_0\theta_1) \\ 2(\theta_1\theta_3-\theta_0\theta_2) & 2(\theta_2\theta_3+\theta_0\theta_1) & 1-2\theta_1^2-2\theta_2^2 \end{bmatrix}, \tag{5.2}$$

where the four Euler parameters $\boldsymbol{\theta} = \mathrm{col}(\theta_0, \theta_1, \theta_2, \theta_3)$ are used:

$$\theta_0 = \cos\frac{\theta}{2}, \; \theta_1 = v_1 \sin\frac{\theta}{2}, \; \theta_2 = v_2 \sin\frac{\theta}{2}, \; \theta_3 = v_3 \sin\frac{\theta}{2}, \quad \text{with } \theta_0^2+\theta_1^2+\theta_2^2+\theta_3^3 = 1.$$

Here, the function col(...) indicates the column stacking of vectors or scalar quantities. The unit vector along the rotation axis is given by $\mathbf{v} = \mathrm{col}(v_1, v_2, v_3)$ and θ is the rotation angle. The axis of rotation along $\mathbf{v}$ and the rotation angle θ are defined for each flexible body separately.

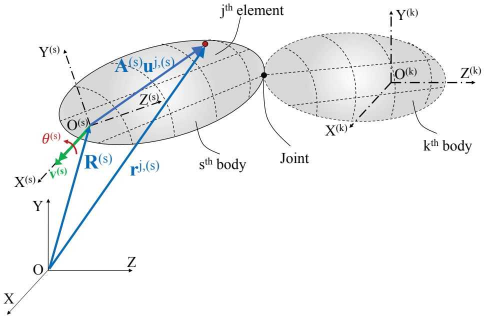

Figure 5.1: Generalized coordinates expression in floating frame of reference. Two bodies are coupled through a joint. The absolute position of an arbitrary point (red) in the j^{th} element of the s^{th} body is shown.

The absolute velocity $\dot{\mathbf{r}}^j$ is given by

$$\begin{aligned}\dot{\mathbf{r}}^j &= \dot{\mathbf{R}} + \dot{\mathbf{A}}\mathbf{N}^j(\mathbf{q}_0^j + \mathbf{q}_f^j) + \mathbf{A}\mathbf{N}^j\dot{\mathbf{q}}_f^j \\ &= \begin{bmatrix}\mathbf{I} & \mathcal{B}^j\{\boldsymbol{\theta},\mathbf{q}_f^j\} & \mathbf{A}\mathbf{N}^j\end{bmatrix}\begin{bmatrix}\dot{\mathbf{R}} \\ \dot{\boldsymbol{\theta}} \\ \dot{\mathbf{q}}_f^j\end{bmatrix},\end{aligned} \tag{5.3}$$

where the argument of functional dependency is enclosed in curly brackets. The second term in (5.3) is rewritten as

$$\dot{\mathbf{A}}\mathbf{N}^j(\mathbf{q}_0^j + \mathbf{q}_f^j) = \mathcal{B}^j\{\boldsymbol{\theta},\mathbf{q}_f^j\}\dot{\boldsymbol{\theta}}, \tag{5.4}$$

in order to isolate the velocity terms $\dot{\boldsymbol{\theta}}$. The matrix $\mathcal{B}^j$ is thus a function of $\boldsymbol{\theta}$, $\mathbf{q}_f^j$ and $\mathbf{q}_0^j$. The dependency of $\mathcal{B}^j$ on $\mathbf{q}_0^j$ will not be explicitly expressed since $\mathbf{q}_0^j$ is constant for each FE model.

The kinetic energy $\mathcal{T}^j$ for the j^{th} element can be evaluated by

$$\mathcal{T}^j = \frac{1}{2}\int_{V^j}\rho^j(\dot{\mathbf{r}}^j)^{\mathrm{T}}\dot{\mathbf{r}}^j\,dV^j = \frac{1}{2}(\dot{\mathbf{q}}^j)^{\mathrm{T}}\mathbf{M}^j\dot{\mathbf{q}}^j, \tag{5.5}$$

where $\mathbf{q}^j = \mathrm{col}(\mathbf{R}\,,\,\boldsymbol{\theta}\,,\,\mathbf{q}_f^j)$ and ρ^j is the density of the element material. The mass matrix $\mathbf{M}^j$ is configuration-dependent. The kinetic energy of the s^{th} body can be determined by summing up the kinetic energy $\mathcal{T}^j$ of all its elements. The mass matrix $\mathbf{M}$ of the s^{th} body is obtained by standard FE assembly. The vector $\mathbf{q} = \mathrm{col}(\mathbf{R},\boldsymbol{\theta},\mathbf{q}_f)$ indicates the generalized coordinates of a single flexible body, where $\mathbf{q}_f \in \mathbb{R}^n$ refers to the total relative DoFs in the reference frame and n is the number of relative DoFs.

The equations of motion (EoMs) for each flexible body can be derived from Lagrange's equations as

$$\frac{d}{dt}\left(\frac{\partial\mathcal{T}}{\partial\dot{\mathbf{q}}}\right)^{\mathrm{T}} - \left(\frac{\partial\mathcal{T}}{\partial\mathbf{q}}\right)^{\mathrm{T}} + \left(\frac{\partial\mathcal{U}}{\partial\mathbf{q}}\right)^{\mathrm{T}} = \mathbf{g}, \tag{5.6}$$

where $\mathcal{T}$ and $\mathcal{U}$ are the kinetic energy and strain energy, respectively; $\mathbf{g}$ is the vector of externally applied generalized loads. At this stage, the flexible bodies (if more than one) have not been assembled and the prescribed motions of the flexible bodies have not been imposed yet.

The EoMs (5.6) can be rewritten in matrix form as

$$\mathbf{M}\{\mathbf{q}\}\ddot{\mathbf{q}} - \mathbf{Q}_v\{\mathbf{q}, \dot{\mathbf{q}}\} + \mathbf{f}\{\mathbf{q}\} = \mathbf{g}, \tag{5.7}$$

where $\mathbf{Q}_v$ is the quadratic velocity vector, which includes the effect of apparent forces (such as centrifugal force and Coriolis force), and $\mathbf{f}$ is the nonlinear elastic force vector. The quadratic velocity vector $\mathbf{Q}_v$ results from the inertia coupling between the motion $\mathrm{col}(\mathbf{R}, \boldsymbol{\theta})$ of the reference frame and the relative motion $\mathbf{q}_f$.

In this work, we adopt the von Kármán kinematic assumption for geometric nonlinearities, which is suitable for small strains and moderate rotations (Sharf, 1999). The elastic force $\mathbf{f}$ can be directly derived from the differentiation of the strain energy and may be written as a third-order polynomial function of the relative DoFs $\mathbf{q}_f$.

Equation (5.7) can be conveniently written in a partitioned form that highlights the coupling between $\mathrm{col}(\mathbf{R}, \boldsymbol{\theta})$ and $\mathbf{q}_f$, as

$$\begin{bmatrix} \mathbf{M}_{RR} & \mathbf{M}_{R\theta} & \mathbf{M}_{Rf} \\ & \mathbf{M}_{\theta\theta} & \mathbf{M}_{\theta f} \\ \text{sym} & & \mathbf{M}_{ff} \end{bmatrix} \begin{bmatrix} \ddot{\mathbf{R}} \\ \ddot{\boldsymbol{\theta}} \\ \ddot{\mathbf{q}}_f \end{bmatrix} - \begin{bmatrix} (\mathbf{Q}_v)_R \\ (\mathbf{Q}_v)_\theta \\ (\mathbf{Q}_v)_f \end{bmatrix} + \begin{bmatrix} \mathbf{0} \\ \mathbf{0} \\ \mathbf{f}_f \end{bmatrix} = \begin{bmatrix} \mathbf{g}_R \\ \mathbf{g}_\theta \\ \mathbf{g}_f \end{bmatrix}, \tag{5.8}$$

where the explicit dependency on $\mathbf{q}$ is dropped for clarity. The subscripts $\star_R$, $\star_\theta$ and $\star_f$ indicate the partitions corresponding to $\mathbf{R}$, $\boldsymbol{\theta}$ and $\mathbf{q}_f$, respectively.

In this work, we rigidize the interface by rigidly linking each interface set with a reference virtual node, and expressing all relative interface DoFs $\mathbf{q}_{b_p}$ at the p^{th} interface set through 6 DoFs $\mathbf{q}_{v_p} \in \mathbb{R}^6$ (3 translational DoFs and 3 rotational DoFs) of the virtual node, as illustrated in Fig. 5.2. The 6 DoFs $\mathbf{q}_{v_p}$ represent the relative translations and rotations of the virtual node with respect to the reference frame. The rigid body constraints are commonly applied at the interface, when the flexible bodies are connected through rigid joints.

To be specific, we split the relative DoFs $\mathbf{q}_f \in \mathbb{R}^n$ in the s^{th} body into the sets of relative interface DoFs $\mathbf{q}_b \in \mathbb{R}^{n_b}$ and relative internal DoFs $\mathbf{q}_i \in \mathbb{R}^{n_i}$ as

$$\mathbf{q}_f = \mathrm{col}(\mathbf{q}_b, \mathbf{q}_i) = \mathrm{col}(\mathbf{q}_{b_1}, \dots, \mathbf{q}_{b_w}, \mathbf{q}_i), \tag{5.9}$$

where the interface DoFs $\mathbf{q}_b$ have been further divided into different interface sets from $\mathbf{q}_{b_1} \in \mathbb{R}^{n_{b_1}}$ to $\mathbf{q}_{b_w} \in \mathbb{R}^{n_{b_w}}$, and w is the number of interface sets. It holds that $n_{b_1} + \cdots + n_{b_w} = n_b$. The transformation from DoFs $\mathbf{q}_b$ of all interface nodes to the DoFs $\mathbf{q}_v$ of all virtual nodes can be written as

$$\mathbf{q}_b = \begin{bmatrix} \mathbf{q}_{b_1} \\ \vdots \\ \mathbf{q}_{b_w} \end{bmatrix} = \underbrace{\begin{bmatrix} \mathbf{L}_{v_1} & & \\ & \ddots & \\ & & \mathbf{L}_{v_w} \end{bmatrix}}_{\mathbf{L}_v} \underbrace{\begin{bmatrix} \mathbf{q}_{v_1} \\ \vdots \\ \mathbf{q}_{v_w} \end{bmatrix}}_{\mathbf{q}_v}, \tag{5.10}$$

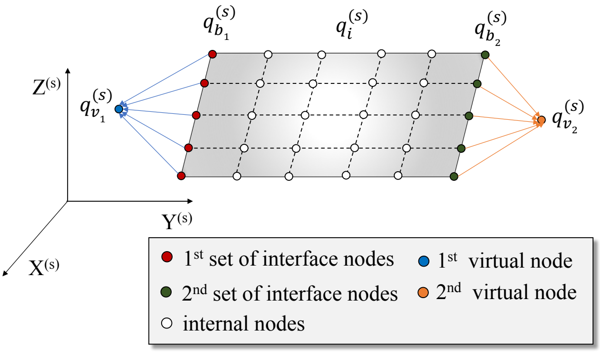

Figure 5.2: Illustration of the "rigidizing" the interface sets of the s^{th} body. The flexible body contains two sets of interface DoFs. The relative DoFs $\mathbf{q}_{b_1}^{(s)}, \mathbf{q}_{b_2}^{(s)}$ of the two interface sets are described by the relative DoFs $\mathbf{q}_{v_1}^{(s)}, \mathbf{q}_{v_2}^{(s)}$ of their corresponding virtual nodes w.r.t. the reference frame, respectively.

where $\mathbf{L}_v \in \mathbb{R}^{n_b \times n_v}$ is the transformation matrix of the entire interface DoFs, and n_v is the number of DoFs for all virtual nodes. Matrix $\mathbf{L}_v$ is calculated according to the position of each interface node. The detailed expression of the transformation matrix $\mathbf{L}_v$ is discussed in Appendix B.

It should be noticed that the FE models, without imposed constraints, allow relative rigid body motion of the the flexible bodies with respect to the body reference. In the FFR formulation, however, the rigid body motion has already been described by the translation and rotation of the reference frame. To define a unique displacement field, we need to eliminate redundant DoFs, by imposing a set of reference constraints. This is discussed in the next section.

5.3. FLOATING FRAME DEFINITION

We now briefly summarize the nodal-fixed definition (Nikravesh, 2005) and the mean-axis definition (Cavin & Dusto, 1977) of the FFR, together with the embedding technique utilized to impose the constraints introduced by the mean-axis frame definition.

5.3.1. NODAL-FIXED FRAME

The nodal-fixed frame is commonly applied since its definition is straightforward. In this work, the origin of the reference frame is attached to a specified node of the moving body, i.e. no relative translations and rotations of the attached node with respect to the reference frame are allowed. The choice of the attached node is not unique. Here, we choose the virtual node of the k^{th} interface set. Mathematically, this is simply done by fixing the 6 relative DoFs $\mathbf{q}_{v_k}$ of the corresponding virtual node with respect to the reference frame as

$$\mathbf{q}_{v_k} = \mathbf{0}, \tag{5.11}$$

which corresponds to 6 scalar constraints. For illustration, we show the kinematic description of a crank-shaft system for the nodal-fixed floating frame in Fig. 5.3. The grey mesh denotes the rigid body motion of each body, defined by the position and orientation of the reference frame. When “standing" at the origin of the reference frame, one observes the relative displacements and rotations of the body as the flexible body is clamped at the origin of the frame.

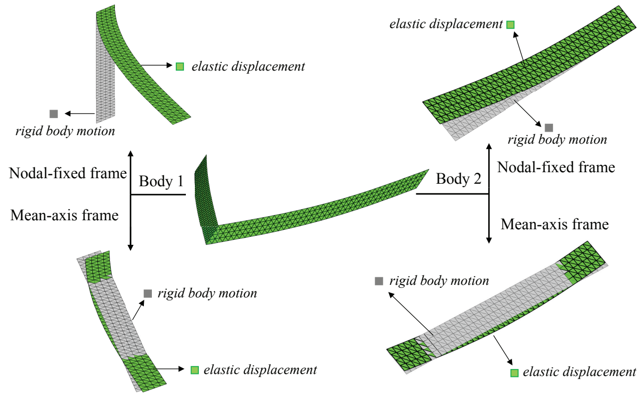

Figure 5.3: The kinematic description of a crank-shaft system (middle) for both nodal-fixed frame (top) and mean-axis frame (bottom).

5.3.2. MEAN-AXIS FRAME

If an approximated kinematic model for only moderate relative rotations formulation is adopted, as the case of the von Kármán model in the present work, one should try to keep the relative rotations with respect to the reference frame as small as possible. Since the magnitude of the relative displacements and rotations with respect to the nodal-fixed frame largely depends on the choice of the attachment node, the mean-axis floating frame is a more clever choice. Unlike the nodal-fixed frame, the mean-axis frame imposes constraint condition as a function of relative DoFs at each body impartially. The basic idea is to locate the reference frame in such a way that the relative kinetic energy is minimum with respect to an observer stationed on the reference frame. The relative kinetic energy of the j^{th} element in the s^{th} flexible body is defined as (Agrawal & Shabana, 1986)

$$\mathcal{T}_r = \sum_j \mathcal{T}_r^j = \sum_j \frac{1}{2} \int_{V^j} \rho^j (\dot{\mathbf{u}}_f^j)^{\mathrm{T}} \dot{\mathbf{u}}_f^j \mathrm{d}V^j. \tag{5.12}$$

According to (5.3), the relative velocity $\dot{\mathbf{u}}_f^j$ of an arbitrary point in the j^{th} element is rewritten by stating

$$\dot{\mathbf{u}}_f^j = \mathbf{N}^j \dot{\mathbf{q}}_f^j = (\mathbf{A})^{\mathrm{T}} \left[\dot{\mathbf{r}}^j - \dot{\mathbf{R}} - \mathcal{B}^j \dot{\boldsymbol{\theta}} \right]. \tag{5.13}$$

Therefore, the relative kinetic energy $\mathcal{T}_r$ can be expressed as

$$\mathcal{T}_r = \sum_j \frac{1}{2} \int_{V^j} \rho^j \left[\dot{\mathbf{r}}^j - \dot{\mathbf{R}} - \mathcal{B}^j \dot{\boldsymbol{\theta}} \right]^{\mathrm{T}} \left[\dot{\mathbf{r}}^j - \dot{\mathbf{R}} - \mathcal{B}^j \dot{\boldsymbol{\theta}} \right] \mathrm{d}V^j. \tag{5.14}$$

If $\dot{\mathbf{R}}$ and $\dot{\boldsymbol{\theta}}$ are to satisfy the mean-axis condition, the kinetic energy $\mathcal{T}_r$ should be minimum. As discussed for instance in (Agrawal & Shabana, 1986), we first rewrite the time derivatives of the Euler parameters as a function of the angular velocity vector $\boldsymbol{\omega}$, i.e.,

$$\boldsymbol{\omega} = 2\mathbf{E}\dot{\boldsymbol{\theta}}, \tag{5.15}$$

with

$$\mathbf{E} = \begin{bmatrix} -\theta_1 & \theta_0 & \theta_3 & -\theta_2 \\ -\theta_2 & -\theta_3 & \theta_0 & \theta_1 \\ -\theta_3 & \theta_2 & -\theta_1 & \theta_0 \end{bmatrix}, \quad \boldsymbol{\omega} = \begin{bmatrix} \omega_1 \\ \omega_2 \\ \omega_3 \end{bmatrix} = \begin{bmatrix} 2(\theta_3\dot{\theta}_2 - \theta_2\dot{\theta}_3 - \theta_1\dot{\theta}_0 + \theta_0\dot{\theta}_1) \\ 2(\theta_1\dot{\theta}_3 + \theta_0\dot{\theta}_2 - \theta_3\dot{\theta}_1 - \theta_2\dot{\theta}_0) \\ 2(\theta_2\dot{\theta}_1 - \theta_3\dot{\theta}_0 + \theta_0\dot{\theta}_3 - \theta_1\dot{\theta}_2) \end{bmatrix}.$$

Then, the minimum for $\mathcal{T}_r$ can be found by posing

$$\frac{\partial \mathcal{T}_r}{\partial \dot{\mathbf{R}}} = \mathbf{0}; \quad \text{and} \quad \frac{\partial \mathcal{T}_r}{\partial \boldsymbol{\omega}} = \mathbf{0}. \tag{5.16}$$

Eq. (5.16) yields 6 constraint equations to satisfy the mean-axis condition. In (Agrawal & Shabana, 1986), the mean-axis constraint equations are further simplified and finally linearized as a function of $\dot{\mathbf{q}}_f$, which is the time derivatives of the relative DoFs with respect to reference frame. The approximated mean-axis condition is expressed as

$$\mathbf{S}\dot{\mathbf{q}}_f = \mathbf{0}. \tag{5.17}$$

where $\mathbf{S} \in \mathbb{R}^{6\times n}$ is a matrix of constant parameters, usually referred to as inertia integrals. The detailed derivation and linearization from (5.16) to (5.17) are given in Appendix C.

In order to express the mean-axis condition in terms of $\mathbf{q}_f$, the time integral of (5.17) is applied to obtain

$$\mathbf{S}\mathbf{q}_f = \mathbf{0}. \tag{5.18}$$

By applying the mean-axis frame condition (5.18), the flexible body can no longer undergo rigid body motion with respect to the reference frame. For illustration, the kinematic description of a crank-shaft system for mean-axis frame is also given in Fig. 5.3. In the mean-axis frame, the relative displacement and rotation (green mesh) of the body exhibit a interface-free vibration with respect to the reference frame (grey mesh). Generally, the relative displacement and rotation observed from a mean-axis frame will be smaller than their counterparts observed from the nodal-fixed floating frame, as discussed in (Nikravesh, 2005).

5.3.3. EMBEDDING OF MEAN-AXIS AND INTERFACE CONSTRAINTS

While enforcing Eq. (5.11) for nodal-fixed frame is straightforward, the treatment of Eq. (5.18) requires more attention, since the constraint conditions are expressed as an explicit form of all relative DoFs $\mathbf{q}_f$. By noticing that the mean-axis frame only yields linear constraints, we apply the so-called *embedding techniques* (Shabana, 2005) to obtain a minimum number of equations expressed in terms of independent coordinates. As mentioned in (Pereira & Proenca, 1991), the process of imposing all the reference conditions is actually equivalent to static condensation, where the slave variables are eliminated.

We can define the generalized DoFs vector $\mathbf{q}_g$ as

$$\mathbf{q}_g = \mathrm{col}(\mathbf{q}_v\,,\, \mathbf{q}_b\,,\, \mathbf{q}_i) = \mathrm{col}(\mathbf{q}_{m,v}\,,\, \mathbf{q}_{s,b}\,,\, \mathbf{q}_{m,i}\,,\, \mathbf{q}_{s,i}) \tag{5.19}$$

where the virtual, boundary and internal DoFs are further split into independent (master) and dependent (slave) sets of coordinates, denoted by the subscript $\star_m$ and $\star_s$, respectively. Note that all interface DoFs $\mathbf{q}_b$ are set as slave DoFs $\mathbf{q}_{s,b}$ and the DoFs of the virtual nodes are set as master DoFs $\mathbf{q}_{m,v}$ since $\mathbf{q}_{s,b}$ are determined by $\mathbf{q}_{m,v}$.

The rigid interface condition in (5.10) and mean-axis frame constraint in (5.18) can be written together as

$$\underbrace{\begin{bmatrix} \mathbf{L}_v & -\mathbf{I} & \mathbf{0} & \mathbf{0} \\ \mathbf{0} & \mathbf{S}_{s,b} & \mathbf{S}_{m,i} & \mathbf{S}_{s,i} \end{bmatrix}}_{\mathbf{D}} \underbrace{\begin{bmatrix} \mathbf{q}_{m,v} \\ \mathbf{q}_{s,b} \\ \mathbf{q}_{m,i} \\ \mathbf{q}_{s,i} \end{bmatrix}}_{\mathbf{q}_g} = \mathbf{0}, \tag{5.20}$$

where $\mathbf{D} \in \mathbb{R}^{(n_b+6)\times(n_v+n_b+n_i)}$ is the Jacobian matrix of all constraint conditions with respect to the generalized DoFs $\mathbf{q}_g$ in the mean-axis frame, and the $\mathbf{S}$ matrix has been partitioned accordingly. Eq. (5.20) can also be written as

$$\mathbf{D}_s\mathbf{q}_s + \mathbf{D}_m\mathbf{q}_m = \mathbf{0}, \tag{5.21}$$

where

$$\mathbf{q}_s = \mathrm{col}(\mathbf{q}_{s,b}\,,\, \mathbf{q}_{s,i}) \quad \text{and} \quad \mathbf{q}_m = \mathrm{col}(\mathbf{q}_{m,v}\,,\, \mathbf{q}_{m,i}), \tag{5.22}$$

and the matrices $\mathbf{D}_s$ and $\mathbf{D}_m$ contain the columns of $\mathbf{D}$ corresponding to slave DoFs $\mathbf{q}_s \in \mathbb{R}^{n_b+6}$ and master DoFs $\mathbf{q}_m \in \mathbb{R}^{n_m}$, respectively, and n_m are the number of master DoFs. The generalized DoFs $\mathbf{q}_g$ can then be written as a function of $\mathbf{q}_m$ as

$$\mathbf{q}_g = \begin{bmatrix} \mathbf{q}_m \\ \mathbf{q}_s \end{bmatrix} = \begin{bmatrix} \mathbf{I} \\ -(\mathbf{D}_s)^{-1}\mathbf{D}_m \end{bmatrix} \mathbf{q}_m = \mathbf{H}_m\mathbf{q}_m, \tag{5.23}$$

where $\mathbf{H}_m$ is the generalized condensation matrix. Finally, according to (5.23), the relative DoFs $\mathbf{q}_f$ can be directly written as a function of the master DoFs $\mathbf{q}_m$ as

$$\mathbf{q}_f = \mathbf{H}_{fm}\mathbf{q}_m, \tag{5.24}$$

where $\mathbf{H}_{fm}$ contains the rows of $\mathbf{H}_m$ corresponding to $\mathbf{q}_f$.

By substituting (5.24) into (5.8) and performing a Galerkin projection, we can obtain the EoMs as

$$\underbrace{\begin{bmatrix} \mathbf{M}_{RR} & \mathbf{M}_{R\theta} & \mathbf{M}_{Rm} \\ & \mathbf{M}_{\theta\theta} & \mathbf{M}_{\theta m} \\ \text{sym} & & \mathbf{M}_{mm} \end{bmatrix}}_{\tilde{\mathbf{M}}} \underbrace{\begin{bmatrix} \ddot{\mathbf{R}} \\ \ddot{\boldsymbol{\theta}} \\ \ddot{\mathbf{q}}_m \end{bmatrix}}_{\ddot{\tilde{\mathbf{q}}}} - \underbrace{\begin{bmatrix} (\mathbf{Q}_v)_R \\ (\mathbf{Q}_v)_\theta \\ (\mathbf{Q}_v)_m \end{bmatrix}}_{\tilde{\mathbf{Q}}_v} + \underbrace{\begin{bmatrix} \mathbf{0} \\ \mathbf{0} \\ \mathbf{f}_m \end{bmatrix}}_{\tilde{\mathbf{f}}} = \underbrace{\begin{bmatrix} \mathbf{g}_R \\ \mathbf{g}_\theta \\ \mathbf{g}_m \end{bmatrix}}_{\tilde{\mathbf{g}}}, \tag{5.25}$$

where

$$\mathbf{M}_{mm} = (\mathbf{H}_{fm})^{\mathrm{T}} \mathbf{M}_{ff} \mathbf{H}_{fm}, \quad \mathbf{M}_{Rm} = \mathbf{M}_{Rf} \mathbf{H}_{fm}, \quad \mathbf{f}_m = (\mathbf{H}_{fm})^{\mathrm{T}} \mathbf{f}_f$$

$$\mathbf{g}_m = (\mathbf{H}_{fm})^{\mathrm{T}} \mathbf{g}_f, \quad \mathbf{M}_{\theta m} = \mathbf{M}_{\theta f} \mathbf{H}_{fm}, \quad (\mathbf{Q}_v)_m = (\mathbf{H}_{fm})^{\mathrm{T}} (\mathbf{Q}_v)_f.$$

In (5.25), the EoMs are expressed in terms of only the master DoFs $\mathbf{q}_m$. The $\tilde{\star}$ refers to quantities relative to a flexible body constrained on the mean-axis frame. The constraint condition in (5.20) will be identically satisfied. This procedure is referred as the *embedding technique* in (Shabana, 2005). This embedding technique is not as computationally efficient as using Lagrange multipliers, since the condensed stiffness and mass matrices are not sparse. However, it is strongly preferred when applying MOR for the relative DoFs, as any mode extracted from Eq. (5.25) and used to form the reduction basis would satisfy the mean axis and rigid interface condition exactly.

5.4. FLEXIBLE MULTIBODY EQUATIONS

Holonomic joint constraints are applied to connect neighbouring bodies and/or impose prescribed motion through virtual nodes. For instance, a rigid connection between j^{th} and k^{th} bodies can be imposed as

$$\mathbf{C}\{\mathbf{R}, \boldsymbol{\theta}, \mathbf{q}_{m,v}\} = \mathbf{R}^{(j)} + \mathbf{A}^{(j)} \mathbf{N}_v^{(j)} (\mathbf{q}_{0,v}^{(j)} + \mathbf{q}_{m,v}^{(j)}) - \mathbf{R}^{(k)} - \mathbf{A}^{(k)} \mathbf{N}_v^{(k)} (\mathbf{q}_{0,v}^{(k)} + \mathbf{q}_{m,v}^{(k)}) = \mathbf{0}, \tag{5.26}$$

where $\mathbf{q}_{0,v}$ and $\mathbf{q}_{m,v}$ are the initial position and relative DoFs of the connecting virtual nodes, respectively, and $\mathbf{N}_v$ here is equal to the Boolean matrix of selecting the translation DoFs.

It is emphasized here that the joint constraints are not imposed at the internal DoFs $\mathbf{q}_{m,i}$. The constraint Jacobian matrix can thus be written as

$$\mathbf{C}_q = \frac{\partial \mathbf{C}}{\partial \tilde{\mathbf{q}}} = \begin{bmatrix} \dfrac{\partial \mathbf{C}}{\partial \mathbf{R}} & \dfrac{\partial \mathbf{C}}{\partial \boldsymbol{\theta}} & \dfrac{\partial \mathbf{C}}{\partial \mathbf{q}_{m,v}} & \mathbf{0}_i \end{bmatrix} = \begin{bmatrix} \mathbf{C}_R & \mathbf{C}_\theta & \mathbf{C}_m \end{bmatrix}, \tag{5.27}$$

where $\mathbf{0}_i$ reflects that the constraints are not imposed on the internal DoFs $\mathbf{q}_{m,i}$ and $\mathbf{C}_m = \begin{bmatrix} \frac{\partial \mathbf{C}}{\partial \mathbf{q}_{m,v}} & \mathbf{0}_i \end{bmatrix}$. The joint constraints (usually nonlinear) are included with Lagrange multipliers $\boldsymbol{\lambda}$ as

$$\begin{cases} \begin{bmatrix} \mathbf{M}_{RR}^{(s)} & \mathbf{M}_{R\theta}^{(s)} & \mathbf{M}_{Rm}^{(s)} \\ & \mathbf{M}_{\theta\theta}^{(s)} & \mathbf{M}_{\theta m}^{(s)} \\ \text{sym} & & \mathbf{M}_{mm}^{(s)} \end{bmatrix} \begin{bmatrix} \ddot{\mathbf{R}}^{(s)} \\ \ddot{\boldsymbol{\theta}}^{(s)} \\ \ddot{\mathbf{q}}_m^{(s)} \end{bmatrix} - \begin{bmatrix} (\mathbf{Q}_v^{(s)})_R \\ (\mathbf{Q}_v^{(s)})_\theta \\ (\mathbf{Q}_v^{(s)})_m \end{bmatrix} + \begin{bmatrix} \mathbf{0} \\ \mathbf{0} \\ \mathbf{f}_m^{(s)} \end{bmatrix} + \begin{bmatrix} (\mathbf{C}_R^{(s)})^{\mathrm{T}} \\ (\mathbf{C}_\theta^{(s)})^{\mathrm{T}} \\ (\mathbf{C}_m^{(s)})^{\mathrm{T}} \end{bmatrix} \boldsymbol{\lambda} = \begin{bmatrix} \mathbf{g}_R^{(s)} \\ \mathbf{g}_\theta^{(s)} \\ \mathbf{g}_m^{(s)} \end{bmatrix} \\ \text{for} \quad s = 1, \ldots, \mathcal{H}, \\ \mathbf{C}\{\mathbf{R}, \boldsymbol{\theta}, \mathbf{q}_{m,v}\} = \mathbf{0}, \end{cases} \tag{5.28}$$

where $\mathcal{H}$ is the number of bodies in the FMBS.

5.5. ENHANCED RUBIN SUBSTRUCTURING METHOD

The inertial terms of (5.28) are configuration dependent and therefore need to be updated at every time step during time integration. Likewise, when geometric nonlinearities have to be considered, also the internal force vector $\mathbf{f}_m$ is configuration dependent.

The computational cost of large size nonlinear FMBS using the FFR reference may thus become significant, and MOR is required. The idea is to reduce the size of $\mathbf{q}_m$ for each body by expressing them as a combination of modes computed after suppressing the rigid body motion of the floating frame, see (Wu & Tiso, 2016, Shabana, 2005, 1986). The EoMs for each body in (5.28) can thus be simplified by suppressing col$(\mathbf{R},\boldsymbol{\theta})$ as

$$\mathbf{M}_{mm}\ddot{\mathbf{q}}_m + \mathbf{f}_m\{\mathbf{q}_m\} = \mathbf{g}_m - \mathbf{C}_m^{\mathrm{T}}\boldsymbol{\lambda}. \tag{5.29}$$

By fixing the rigid body motion of the frame, the quadratic velocity terms $(\mathbf{Q}_v)_m$ and the couplings between rigid body motion and relative displacement vanish. The last term in (5.29) represents the connecting forces which are imposed only at the virtual node DoFs. The last term can be further rewritten as

$$-\mathbf{C}_m^{\mathrm{T}}\boldsymbol{\lambda} = \mathbf{B}^{\mathrm{T}}\mathbf{g}_v, \tag{5.30}$$

where $\mathbf{B} \in \mathbb{R}^{n_v \times n_m}$ is the local-Boolean matrix that selects the interface DoFs $\mathbf{q}_v$ from $\mathbf{q}_m$, and $\mathbf{g}_v \in \mathbb{R}^{n_v}$ is the interface force imposed at the virtual node.

Furthermore, we linearized (5.29) as

$$\mathbf{M}_{mm}\ddot{\mathbf{q}}_m + \mathbf{K}_{mm}\mathbf{q}_m = \mathbf{g}_m + \mathbf{B}^{\mathrm{T}}\mathbf{g}_v, \tag{5.31}$$

where

$$\mathbf{K}_{mm} = \left.\frac{\mathrm{d}\mathbf{f}_m}{\mathrm{d}\mathbf{q}_m}\right|_{\mathbf{0}} = (\mathbf{H}_{fm})^{\mathrm{T}} \left.\frac{\mathrm{d}\mathbf{f}_f}{\mathrm{d}\mathbf{q}_f}\right|_{\mathbf{0}} \frac{\mathrm{d}\mathbf{q}_f}{\mathrm{d}\mathbf{q}_m} = (\mathbf{H}_{fm})^{\mathrm{T}}\mathbf{K}_{ff}\mathbf{H}_{fm}$$

is the linear stiffness matrix after the constraint embedding, and $\mathbf{K}_{ff}$ is the linear sparse stiffness matrix of the body. In general, $\mathbf{K}_{mm}$ is not a sparse matrix.

5.5.1. AUGMENTED RUBIN REDUCTION BASES WITH MODAL DERIVATIVES

In this section, we extend the standard Rubin substructuring method by augmenting the associated reduction basis with MDs to properly consider geometric nonlinear effects. The ROBs are established for each body separately.

The MDs were first proposed in (Idelsohn & Cardona, 1985*a*,*b*) for a single structure not undergoing rigid body motion, by differentiating the eigenvalue problem associated to the free vibration with respect to the modal amplitude. Slaats (Slaats *et al.*, 1995) noticed that neglecting the inertial terms when computing the MDs could still yield satisfactory results. Related to this property, a simplified definition of MDs is also given by neglecting these inertia related terms. This technique is usually addressed as the *definition without mass consideration*, or more recently, *static* MDs (Jain *et al.*, 2017). A more theoretical grounding of the validity of MDs is given in (Haller & Ponsioen, 2017).

When the inertial terms are neglected, Eq. (5.29) becomes

$$\mathbf{f}_m\{\mathbf{q}_m\} = \mathbf{g}_m + \mathbf{B}^{\mathrm{T}}\mathbf{g}_v. \tag{5.32}$$

We assume here that the external load $\mathbf{g}_m$ can be written as a stiffness-scaled linear superposition of the free-interface modes (FVMs) as

$$\mathbf{g}_m = \mathbf{K}_{mm}\boldsymbol{\Phi}\boldsymbol{\eta}, \tag{5.33}$$

where the FVMs $\mathbf{\Phi}$ can be obtained by solving the linear eigenvalue problem associated to (5.31):

$$\left(\mathbf{K}_{mm} - \nu_j^2 \mathbf{M}_{mm}\right) \boldsymbol{\phi}_j = \mathbf{0}, \tag{5.34}$$

where ν_j is the j^{th} eigenfrequency and $\boldsymbol{\phi}_j$ is the corresponding FVM. Generally, a truncated set of the first r_m FVMs is selected in the reduction basis $\mathbf{\Phi} \in \mathbb{R}^{n_m \times r_m}$ based on the frequency range of interest. The reduction will be achieved by letting $r_m \ll n_m$. Note that $\mathbf{\Phi}$ does not contain any rigid body motion since the system has already been fully constrained, see Section 5.3.

By substituting (5.33) into (5.32), we obtain a static nonlinear problem

$$\mathbf{f}_m\{\mathbf{q}_m\} = \mathbf{K}_{mm}\mathbf{\Phi}\boldsymbol{\eta} + \mathbf{B}^{\mathrm{T}}\mathbf{g}_\nu = \begin{bmatrix}\mathbf{K}_{mm}\mathbf{\Phi} & \mathbf{B}^{\mathrm{T}}\end{bmatrix}\boldsymbol{\zeta}, \quad \text{with} \quad \boldsymbol{\zeta} = \mathrm{col}(\boldsymbol{\eta}, \mathbf{g}_\nu) \tag{5.35}$$

where static response $\mathbf{q}_m$ is determined by the modal amplitude $\boldsymbol{\zeta} \in \mathbb{R}^{r_m+n_\nu}$. Instead of finding a solution of (5.35), we assume that $\mathbf{q}_m$ is C^2 differentiable with respect to the modal parameter $\boldsymbol{\zeta}$ and we expand $\mathbf{q}_m$ into a Taylor series around equilibrium position as

$$\mathbf{q}_m\{\boldsymbol{\zeta}\} = \sum_{j=1}^{r_m+n_\nu} \left.\frac{\partial \mathbf{q}_m}{\partial \zeta_j}\right|_{\mathbf{0}} \zeta_j + \frac{1}{2}\sum_{j=1}^{r_m+n_\nu}\sum_{k=1}^{r_m+n_\nu} \left.\frac{\partial^2 \mathbf{q}_m}{\partial \zeta_j \partial \zeta_k}\right|_{\mathbf{0}} \zeta_j \zeta_k + \mathcal{O}(||\boldsymbol{\zeta}||^3), \tag{5.36}$$

where ζ_j is the j^{th} component of the modal parameter $\boldsymbol{\zeta}$.

In order to find the derivatives in (5.36) we differentiate both sides of (5.35) with respect to $\boldsymbol{\zeta}$, and evaluate them around the equilibrium position as

$$\frac{\mathrm{d}\mathbf{f}_m}{\mathrm{d}\mathbf{q}_m}\frac{\partial \mathbf{q}_m}{\partial \boldsymbol{\zeta}} = \begin{bmatrix}\mathbf{K}_{mm}\mathbf{\Phi} & \mathbf{B}^{\mathrm{T}}\end{bmatrix} \quad \rightarrow \quad \left.\frac{\partial \mathbf{q}_m}{\partial \boldsymbol{\zeta}}\right|_{\mathbf{0}} = \begin{bmatrix}\mathbf{\Phi} & \mathbf{K}_{mm}^{-1}\mathbf{B}^{\mathrm{T}}\end{bmatrix}, \tag{5.37}$$

where $\mathbf{K}_{mm}^{-1}$ exists as rigid body motions are suppressed. This procedure distinguishes from the standard Rubin method, where a pseudo-inverse matrix needs to be computed due to the presence of rigid body modes. The matrix $\mathbf{\Psi} = \mathbf{K}_{mm}^{-1}\mathbf{B}^{\mathrm{T}}$, $\mathbf{\Psi} \in \mathbb{R}^{n_m \times n_\nu}$ includes the so-called attachment modes (AMs). The AMs represent deformations due to the unit generalized force at one interface DoF and zero to all other interface DoFs. Therefore, the connecting interface force vector $\mathbf{g}_\nu$ represents the modal amplitudes of the AMs $\mathbf{\Psi}$.

The expression (5.37) can be compactly written as

$$\left.\frac{\partial \mathbf{q}_m}{\partial \boldsymbol{\zeta}}\right|_{\mathbf{0}} = \begin{bmatrix}\mathbf{\Phi} & \mathbf{\Psi}\end{bmatrix} = \mathbf{X}, \tag{5.38}$$

where $\mathbf{X}$ is the Rubin ROB. In order to calculate the second-order derivatives of $\mathbf{q}_m$ with respect to $\boldsymbol{\zeta}$, we differentiate (5.35) twice as

$$\frac{\mathrm{d}\mathbf{f}_m}{\mathrm{d}\mathbf{q}_m}\frac{\partial^2 \mathbf{q}_m}{\partial \zeta_j \partial \zeta_k} + \frac{\mathrm{d}^2\mathbf{f}_m}{\mathrm{d}(\mathbf{q}_m)^2}\frac{\partial \mathbf{q}_m}{\partial \zeta_j}\frac{\partial \mathbf{q}_m}{\partial \zeta_k} = \mathbf{0}. \tag{5.39}$$

Evaluating (5.39) around the equilibrium position gives

$$\mathbf{K}_{mm}\left.\frac{\partial^2 \mathbf{q}_m}{\partial \zeta_j \partial \zeta_k}\right|_{\mathbf{0}} + \left.\frac{\mathrm{d}^2\mathbf{f}_m}{\mathrm{d}(\mathbf{q}_m)^2}\right|_{\mathbf{0}}\left.\frac{\partial \mathbf{q}_m}{\partial \zeta_j}\right|_{\mathbf{0}}\left.\frac{\partial \mathbf{q}_m}{\partial \zeta_k}\right|_{\mathbf{0}} = \mathbf{0}, \tag{5.40}$$

where the right hand side of (5.40) is a null vector, since the external load and interface forces are assumed to be a linear superposition of the modal parameters $\boldsymbol{\zeta}$.

The second derivatives of the nonlinear response with respect to the modal amplitudes $\left.\frac{\partial^2 \mathbf{q}_m}{\partial \zeta_j \partial \zeta_k}\right|_{\mathbf{0}}$ are the MDs, computed from (5.40) as

$$\boldsymbol{\vartheta}_{jk} = \left.\frac{\partial^2 \mathbf{q}_m}{\partial \zeta_j \partial \zeta_k}\right|_{\mathbf{0}} = -(\mathbf{K}_{mm})^{-1} \left.\frac{\mathrm{d}^2 \mathbf{f}_m}{\mathrm{d}(\mathbf{q}_m)^2}\right|_{\mathbf{0}} \mathbf{X}_j \mathbf{X}_k, \tag{5.41}$$

and it holds that $\boldsymbol{\vartheta}_{jk} = \boldsymbol{\vartheta}_{kj}$, see (Weeger *et al.*, 2016).

Having defined the AMs, FVMs and corresponding MDs, $\mathbf{q}_m$ can be approximated by the second-order Taylor expansion in (5.36) as

$$\mathbf{q}_m = \sum_{j=1}^{r_m+n_v} \mathbf{X}_j \zeta_j + \frac{1}{2} \sum_{j=1}^{r_m+n_v} \sum_{k=1}^{r_m+n_v} \boldsymbol{\vartheta}_{jk} \zeta_j \zeta_k, \tag{5.42}$$

which constitutes a quadratic manifold for $\mathbf{q}_m$ in the $\boldsymbol{\zeta}$ space. In this work, we will not directly apply (5.42), as done, for instance, in (Jain *et al.*, 2017, Rutzmoser *et al.*, 2017). Instead, the MDs will be included in the ROB as additional independent modes to reproduce geometric nonlinearities. [1]

The relative DoFs vector $\mathbf{q}_m$ with respect to the floating frame is then given by

$$\mathbf{q}_m = \boldsymbol{\Psi} \mathbf{g}_v + \boldsymbol{\Phi} \boldsymbol{\eta} + \boldsymbol{\Theta} \boldsymbol{\xi}, \tag{5.43}$$

where $\boldsymbol{\Theta}$ is the matrix containing the vectors of independent MDs, and $\boldsymbol{\xi}$ is the modal coordinates vector associated to the MDs in $\boldsymbol{\Theta}$. Since the MDs are calculated around the equilibrium position and will not be updated during the time integration, the accuracy of using the modal transformation in (5.43) will be determined by how far the structure departs from reference position.

For illustration, some representative modes of the ROB for the crank-shaft system are shown in Fig. 5.4. For the first body, the ROB is constructed as done in (Wu & Tiso, 2016), i.e., a nodal-fixed frame is applied, and the enhanced CB method is applied. The origin of the reference frame is attached to the interface B_1. Therefore, the fixed-interface modes $\boldsymbol{\Phi}^{(1)}$, MDs $\boldsymbol{\Theta}^{(1)}$ are fixed at interface B_1 and B_2. The compatibility with neighboring bodies are considered by the constraint modes (CMs) $\boldsymbol{\Psi}^{(1)}$. The mean-axis frame is utilized to describe the motion of the second body. The corresponding FVMs $\boldsymbol{\Phi}^{(2)}$, MDs $\boldsymbol{\Theta}^{(2)}$ and AMs $\boldsymbol{\Psi}^{(2)}$ exhibit free vibration at the interface sets B_2 and B_3. It should be noted that all modes are obtained after the mean-axis constraints are included. Therefore, the FVMs in the ROB of the mean-axis frame model contain no rigid body motions. While these low-frequency FVMs of the flat plate models contain bending-dominant vibrations, the corresponding MDs exhibit membrane-dominant vibrations to properly model the nonlinear effects.

In order to assemble the reduced components, Eq. (5.43) should contain only modal amplitudes. Further transformation is applied to replace the force vector $\mathbf{g}_v$ with the

---

[1] Note that the number of obtainable MDs grows quadratically with respect to the number of modes contained in the Rubin basis $\mathbf{X}$. In (Jain *et al.*, 2017), two MDs selection criteria are discussed with the goal of selecting only a relevant subset of all possible MDs and therefore reduce the ROB size.

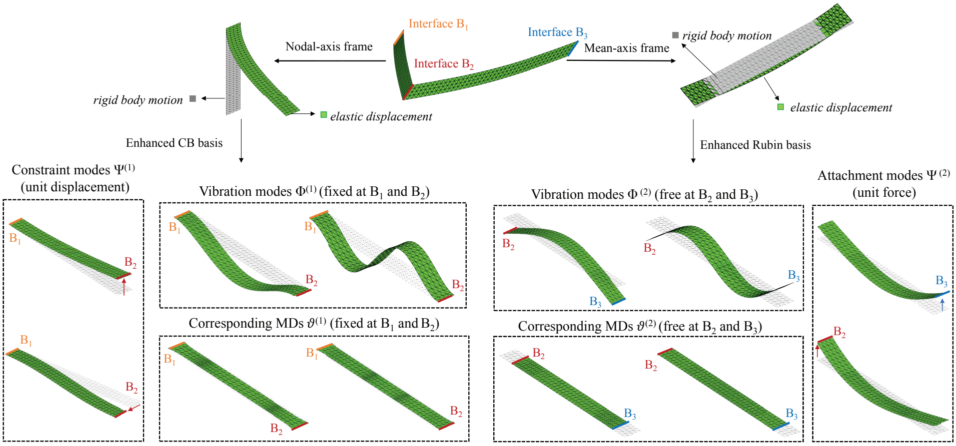

Figure 5.4: The nonlinear ROBs for the crank shaft system. The first body (left) and its corresponding enhanced CB ROB is illustrated using the nodal-fixed frame, while the second body (right) and its corresponding enhanced Rubin ROB is illustrated using the mean-axis frame.

interface DoFs vector $\mathbf{q}_{m,v}$. The interface partition of (5.43) is

$$\mathbf{q}_{m,v} = \mathbf{B}\mathbf{q}_m = \boldsymbol{\Psi}_v \mathbf{g}_v + \boldsymbol{\Phi}_v \boldsymbol{\eta} + \boldsymbol{\Theta}_v \boldsymbol{\xi}, \tag{5.44}$$

where $\boldsymbol{\Psi}_v$, $\boldsymbol{\Phi}_v$ and $\boldsymbol{\Theta}_v$ are the rows of the AMs, FVMs and MDs associated to the interface DoFs, respectively. The interface force vector $\mathbf{g}_v$ can thus be expressed as

$$\mathbf{g}_v = (\boldsymbol{\Psi}_v)^{-1}(\mathbf{q}_{m,v} - \boldsymbol{\Phi}_v \boldsymbol{\eta} - \boldsymbol{\Theta}_v \boldsymbol{\xi}). \tag{5.45}$$

By substituting (5.45) into (5.43) and recalling (5.22), the interface DoFs $\mathbf{q}_{m,v}$ can be retained in the final coordinates transformation as

$$\mathbf{q}_m = \begin{bmatrix} \mathbf{q}_{m,v} \\ \mathbf{q}_{m,i} \end{bmatrix} = \begin{bmatrix} \mathbf{I} & \mathbf{0} & \mathbf{0} \\ \boldsymbol{\Psi}_{iv} & \boldsymbol{\Phi}_i - \boldsymbol{\Psi}_{iv}\boldsymbol{\Phi}_v & \boldsymbol{\Theta}_i - \boldsymbol{\Psi}_{iv}\boldsymbol{\Theta}_v \end{bmatrix} \begin{bmatrix} \mathbf{q}_{m,v} \\ \boldsymbol{\eta} \\ \boldsymbol{\xi} \end{bmatrix} = \mathbf{V}_f \boldsymbol{\gamma}_f, \tag{5.46}$$

where $\boldsymbol{\Psi}_{iv} = \boldsymbol{\Psi}_i(\boldsymbol{\Psi}_v)^{-1}$, $\boldsymbol{\Psi}_i$, $\boldsymbol{\Phi}_i$ and $\boldsymbol{\Theta}_i$ are the internal components of the AMs, FVMs and MDs, respectively. $\mathbf{V}_f$ and $\boldsymbol{\gamma}_f$ are the final ROB and generalized DoFs vector for the enhanced Rubin reduction, when geometric nonlinearity is considered.

5.5.2. REDUCED EQUATION OF MOTION

The final reduced EoMs for the s^{th} substructure can be obtained by substituting (5.46) into (5.28) and performing a Galerkin projection as

$$\underbrace{\begin{bmatrix} \mathbf{M}_{RR}^{(s)} & \mathbf{M}_{R\theta}^{(s)} & \overline{\mathbf{M}}_{Rf}^{(s)} \\ & \mathbf{M}_{\theta\theta}^{(s)} & \overline{\mathbf{M}}_{\theta f}^{(s)} \\ \text{sym} & & \overline{\mathbf{M}}_{ff}^{(s)} \end{bmatrix}}_{\overline{\mathbf{M}}^{(s)}} \underbrace{\begin{bmatrix} \ddot{\mathbf{R}}^{(s)} \\ \ddot{\boldsymbol{\theta}}^{(s)} \\ \ddot{\boldsymbol{\gamma}}_f^{(s)} \end{bmatrix}}_{\ddot{\overline{\mathbf{q}}}^{(s)}} - \underbrace{\begin{bmatrix} (\mathbf{Q}_v^{(s)})_R \\ (\mathbf{Q}_v^{(s)})_\theta \\ (\overline{\mathbf{Q}}_v^{(s)})_f \end{bmatrix}}_{\overline{\mathbf{Q}}_v^{(s)}} + \underbrace{\begin{bmatrix} \mathbf{0} \\ \mathbf{0} \\ \bar{\mathbf{f}}_f^{(s)} \end{bmatrix}}_{\bar{\mathbf{f}}^{(s)}} + \underbrace{\begin{bmatrix} (\mathbf{C}_R^{(s)})^{\mathrm{T}} \\ (\mathbf{C}_\theta^{(s)})^{\mathrm{T}} \\ (\overline{\mathbf{C}}_f^{(s)})^{\mathrm{T}} \end{bmatrix}}_{(\overline{\mathbf{C}}^{(s)})^{\mathrm{T}}} \boldsymbol{\lambda} = \underbrace{\begin{bmatrix} \mathbf{g}_R^{(s)} \\ \mathbf{g}_\theta^{(s)} \\ \bar{\mathbf{g}}_f^{(s)} \end{bmatrix}}_{\bar{\mathbf{g}}^{(s)}} \tag{5.47}$$

with

$$\overline{\mathbf{M}}_{ff}^{(s)} = (\mathbf{V}_f^{(s)})^{\mathrm{T}} \mathbf{M}_{mm}^{(s)} \mathbf{V}_f^{(s)}, \quad \overline{\mathbf{M}}_{Rf}^{(s)} = \mathbf{M}_{Rm}^{(s)} \mathbf{V}_f^{(s)}, \quad \overline{\mathbf{C}}_f^{(s)} = \mathbf{C}_m^{(s)} \mathbf{V}_f^{(s)}, \quad \bar{\mathbf{f}}_f^{(s)} = (\mathbf{V}_f^{(s)})^{\mathrm{T}} \mathbf{f}_m^{(s)}$$
$$\bar{\mathbf{g}}_f^{(s)} = (\mathbf{V}_f^{(s)})^{\mathrm{T}} \mathbf{g}_m^{(s)}, \quad \overline{\mathbf{M}}_{\theta f}^{(s)} = \mathbf{M}_{\theta m}^{(s)} \mathbf{V}_f^{(s)}, \quad (\overline{\mathbf{Q}}_v^{(s)})_f = (\mathbf{V}_f^{(s)})^{\mathrm{T}} (\mathbf{Q}_v^{(s)})_m.$$

All nonlinear terms in (5.47) can be directly expressed as a function of the modal coordinates $\mathrm{col}(\mathbf{R}^{(s)}, \boldsymbol{\theta}^{(s)}, \boldsymbol{\gamma}_f^{(s)})$ by a tensorial form as in (Wu & Tiso, 2016).

The nonlinear force vector $\bar{\mathbf{f}}_f^{(s)}$, whose update is the most time consuming operation during each iteration of the time integration, can be directly expressed as

$$\bar{\mathbf{f}}_f^{(s)} = {}^2\mathcal{W}^{(s)} \boldsymbol{\gamma}_f^{(s)} + \left({}^3\mathcal{W}^{(s)} \cdot \boldsymbol{\gamma}_f^{(s)}\right) \cdot \boldsymbol{\gamma}_f^{(s)} + \left[\left({}^4\mathcal{W}^{(s)} \cdot \boldsymbol{\gamma}_f^{(s)}\right) \cdot \boldsymbol{\gamma}_f^{(s)}\right] \cdot \boldsymbol{\gamma}_f^{(s)}, \tag{5.48}$$

where the tensors ${}^2\mathcal{W}^{(s)} \in \mathbb{R}^{r_g^{(s)} \times r_g^{(s)}}$, ${}^3\mathcal{W}^{(s)} \in \mathbb{R}^{r_g^{(s)} \times r_g^{(s)} \times r_g^{(s)}}$ and ${}^4\mathcal{W}^{(s)} \in \mathbb{R}^{r_g^{(s)} \times r_g^{(s)} \times r_g^{(s)} \times r_g^{(s)}}$ are constant quadratic, cubic and quartic tensors, respectively, and $r_g^{(s)}$ is the number of modes in the enhanced ROB $\mathbf{V}_f^{(s)}$. The tensors ${}^2\mathcal{W}^{(s)}$, ${}^3\mathcal{W}^{(s)}$ and ${}^4\mathcal{W}^{(s)}$ can be calculated *offline*, once the reduction basis of each flexible body is determined.

The system reduced EoMs can be obtained by assembling the contribution from each body and by appending the constraint conditions, as

$$\begin{cases} \overline{\mathbf{M}}^{(s)} \ddot{\overline{\mathbf{q}}}^{(s)} - \overline{\mathbf{Q}}_v^{(s)} + \bar{\mathbf{f}}^{(s)} + (\overline{\mathbf{C}}^{(s)})^{\mathrm{T}} \boldsymbol{\lambda} = \bar{\mathbf{g}}^{(s)}, \quad \text{for} \quad s = 1, \dots, \mathcal{H} \\ \mathbf{C}\{\mathbf{R}, \boldsymbol{\theta}, \mathbf{q}_{m,v}\} = \mathbf{0}. \end{cases} \tag{5.49}$$

It is emphasized here that the constraint equation $\mathbf{C} = \mathbf{0}$ is not projected onto the reduced basis, and therefore, exact interface compatibility has been guaranteed.

In this work, we use the implicit Newmark scheme for the time integration of (5.49). The constraint equation is treated as discussed in (Meek & Liu, 1995). Substantial computational cost reduction can be achieved, in comparison to full analysis, thanks to the reduction in size and the efficient treatment of the nonlinear terms (5.48).

5.6. NUMERICAL EXAMPLES

In this section, two numerical examples are presented to assess the performance of the proposed reduction method. All the models contain elastic bodies meshed with triangular FE shell elements (Tiso, 2006) featuring 3 nodes per element and 6 DoFs per node. In our discussion, the following labelling is utilized to refer to the solutions obtained from different approaches, namely:

- MFR-HFM-L/NL: linear/nonlinear response of the high fidelity model (HFM) obtained from mean-axis floating frame of reference (MFR);
- NFR-HFM-L/NL: linear/nonlinear response of the HFM obtained by nodal-fixed floating frame of reference (NFR);
- MFR-ERubin-NL: nonlinear response of ROMs obtained by projection on the enhanced Rubin basis (with MDs) for MFR, as discussed in this work;
- NFR-ECB-NL: nonlinear response of the ROMs obtained by projection on the enhanced Craig-Bampton basis (with MDs) for NFR, as discussed in (Wu & Tiso, 2016);
- MFR-Rubin-NL: nonlinear response of ROMs obtained by the projection on the standard Rubin basis (without MDs) for MFR;
- NFR-CB-NL: nonlinear response of ROMs obtained by the projection on the standard CB basis (without MDs) for NFR.

5.6.1. MODEL 1: ROTATING BEAM

We consider here the dynamic analysis of a rotating beam, which has been used as a benchmark in many papers dealing with flexible beams and geometric nonlinearities (Simo & V. Q., 1986, Hsiao *et al.*, 1994, Galvanetto & Crisfield, 1996, Kim *et al.*, 2013). In all the previous publications, the system shown in Fig. 5.5 was meshed with planar beam elements. The geometry of the beam and material properties are also illustrated in Fig. 5.5. An imposed end rotation θ_s with respect to OX axis is applied as:

$$\theta_s = \begin{cases} \frac{\omega_s}{T_s}\left[\frac{1}{2}t^2 + \left(\frac{T_s}{2\pi}\right)^2\left(\cos\left(\frac{2\pi t}{T_s}\right) - 1\right)\right], & t \leqslant T_s \\ \omega_s\left(t - \frac{T_s}{2}\right). & t > T_s \end{cases}$$

where $T_s = 15$ s and $\omega_s = 6$ rad/s.

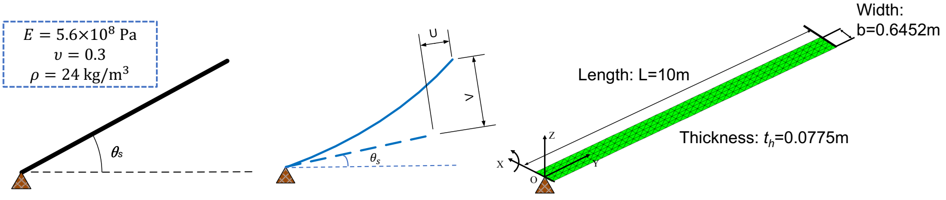

(a) rotating beam structure (b) tip displacement: U and V (c) FE model with shell elements

Figure 5.5: The kinetic description of rotating beam model with shell elements.

The nonlinear responses of the tip displacement components W, U and V (see Fig. 5.5(b)) obtained with different methods are compared. When the global position vector at the tip node $\mathbf{r}^j$ is obtained from Eq. (5.1), the tip displacement W, U and V can be calculated for this example as

$$\begin{bmatrix} W \\ U \\ V \end{bmatrix} = \begin{bmatrix} 1 & 0 & 0 \\ 0 & \cos\theta_s & -\sin\theta_s \\ 0 & \sin\theta_s & \cos\theta_s \end{bmatrix}^{\mathrm{T}} \left(\begin{bmatrix} r_X^t \\ r_Y^t \\ r_Z^t \end{bmatrix} - \begin{bmatrix} \widetilde{R}_X^t \\ \widetilde{R}_Y^t \\ \widetilde{R}_Z^t \end{bmatrix} \right) - \begin{bmatrix} \mathbf{q}_{0,X}^t \\ \mathbf{q}_{0,Y}^t \\ \mathbf{q}_{0,Z}^t \end{bmatrix}, \text{ with } \begin{bmatrix} \mathbf{q}_{0,X}^t \\ \mathbf{q}_{0,Y}^t \\ \mathbf{q}_{0,Z}^t \end{bmatrix} = \begin{bmatrix} 0 \\ 10 \\ 0 \end{bmatrix}.$$

The vector $\widetilde{\mathbf{R}}$ presents the position of virtual node of the joint, and the superscript t denotes the tip node with nodal position $\mathrm{col}(0,10,0)$ at the initial state. Notice that since the beam only rotates about the x-axis, it holds that $W = 0$.

The tip displacement components U and V are shown in Fig. 5.6. The nonlinear response obtained from the corotational frame of reference (CFR) featuring planar beam element is also included as a reference solution. The CFR (Le *et al.*, 2011) is a more general and expensive framework that is able to deal with arbitrary large elastic displacement. This reference solution is denoted as CFR-HFM-NL. From Fig. 5.6 we can observe a good agreement between the time response of the CFR-HFM-NL, NFR-HFM-NL and MFR-HFM-NL. The good agreement confirms that the adopted von Kármán kinetic assumption is adequate for this numerical example.

Table 5.1: size of ROB for the rotating beam model.

	number of modes in linear ROB	number of MDs	total DoFs
NFR-ECB-NL	10	10	20
MFR-ERubin-NL	10	10	20
NFR-CB-NL	50	0	50
MFR-Rubin-NL	50	0	50

In addition, the accuracy of all ROMs is compared to the HFMs. For illustration, the number of modes for different ROMs is listed in Table 5.1. Since the origin of the NFR is fixed at the hinge, no interface modes (i.e. constraint modes) are included in the NFR-ECB-NL. The MDs enhanced substructuring method for both nodal-fixed frame and mean-axis frame (i.e., NFR-ECB-NL and MFR-ERubin-NL) can achieve a good approximation of the reference solution. On the contrary, the standard substructuring techniques (without MDs) for both nodal-fixed and mean-axis frame (i.e., NFR-CB-NL and MFR-Rubin-NL) fail to reproduce the full response, even though as many as 50 modes are included in the ROBs.

To further compare the effectiveness of the ROMs between nodal-fixed frame and mean-axis frame, the root-mean square (RMS) error, defined as

$$\epsilon_{RMS}\{t_i\} = \sqrt{\frac{1}{n}\left(||\mathbf{r}_X\{t_i\} - \bar{\mathbf{r}}_X\{t_i\}||^2 + ||\mathbf{r}_Y\{t_i\} - \bar{\mathbf{r}}_Y\{t_i\}||^2 + ||\mathbf{r}_Z\{t_i\} - \bar{\mathbf{r}}_Z\{t_i\}||^2\right)} \tag{5.50}$$

is plotted in Fig. 5.7(a) for $\omega_s = 6$ rad/s, and the relative error (RE), defined as

$$RE = \frac{\sqrt{\sum_t (\mathbf{r}\{t\} - \bar{\mathbf{r}}\{t\})^{\mathrm{T}} (\mathbf{r}\{t\} - \bar{\mathbf{r}}\{t\})}}{\sqrt{\sum_t \mathbf{r}^{\mathrm{T}}\{t\}\mathbf{r}\{t\}}} \times 100\% \tag{5.51}$$

is plotted in Fig. 5.7(b) for ω_s ranging from 6 rad/s to 12 rad/s. Here, $\mathbf{r}$ and $\bar{\mathbf{r}}$ are the global position vectors obtained from the HFM and ROMs, respectively. The subscripts $\star_X$, $\star_Y$, $\star_Z$ indicate directional components along the OX, OY, OZ axis. As can be observed in Fig. 5.7 (a), although both the ROMs with nodal-fixed frame and mean-axis frame can reproduce the full solution with satisfactory accuracy (RMS errors below

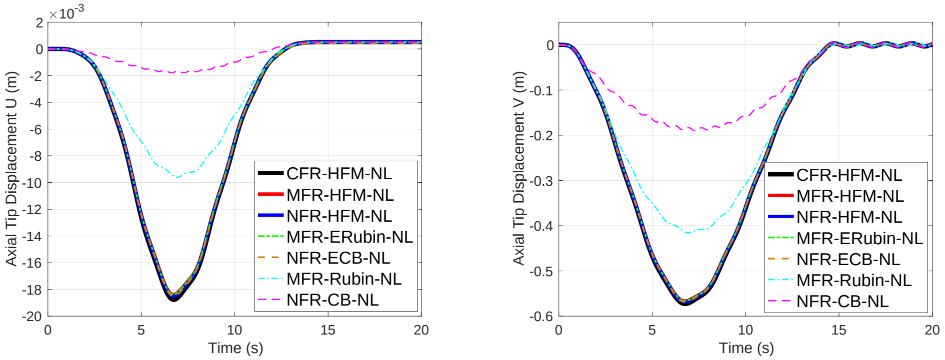

(a) tip displacement U

(b) tip displacement V

Figure 5.6: Time history of the tip displacement relative to the spin-up beam. The ROMs featuring MDs (i.e., MFR-ERubin-NL and NFR-ECB-NL) yield the accurate approximations of their corresponding HFM solutions.

1.5×10^{-4}), the MFR-ERubin-NL is more accurate (RMS error below 2×10^{-5}) than NFR-ECB-NL, for a ROM of the same size. As can be seen in Fig 5.7 (b), when the rotational velocity parameter ω_s increases from 6 rad/s to 12 rad/s, the REs of both NFR-ECB-NL and MFR-ERubin-NL increases since larger geometrical nonlinearities are triggered. The REs obtained from MFR-ERubin-NL are always signifcantly lower than their counterparts in NFR-ECB-NL for all the load cases. The mean-axis formulation (MFR-ERubin-NL) gives better results as the relative displacement is smaller than its counterpart in the nodal-fixed counterpart (NFR-ECB-NL). As a result, the MDs better capture nonlinear displacements in MFR-ERubin-NL.

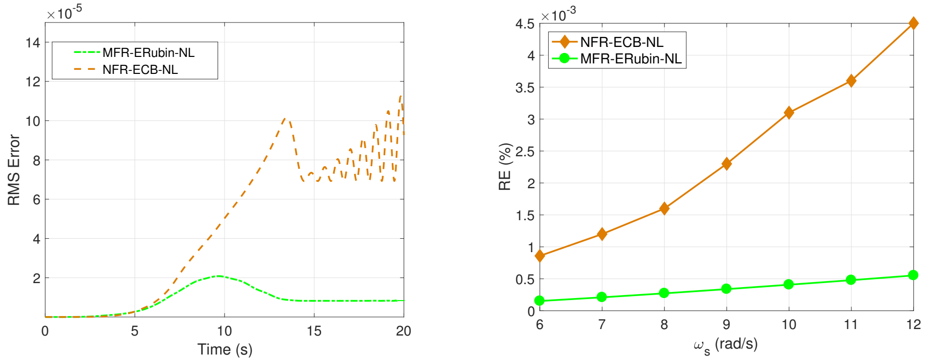

(a) RMS errors comparison with $\omega_s = 6\text{rad/s}$

(b) RE comparison for ω_s from 6rad/s to 12rad/s

Figure 5.7: Accuracy comparison between nodal-fixed frame and mean-axis frame. The REs obtained from MFR-ERubin-NL are always significantly lower than their counterparts in NFR-ECB-NL for all the load cases.

5.6.2. MODEL 2: 5MW/61.5M WIND TURBINE BLADE

We consider here a more complex example: a 61.5 m long blade of the NREL 5 MW reference wind turbine, which is originally presented in (Resor, 2013). This model is constructed by assuming constant thickness and homogeneous material. The effective material properties and geometrical parameters are shown in Fig. 5.8. Rayleigh damping (Geradin & Rixen, 1997) is adopted: a modal damping factor of 2% for the first two modes is used to determine the Rayleigh coefficients.

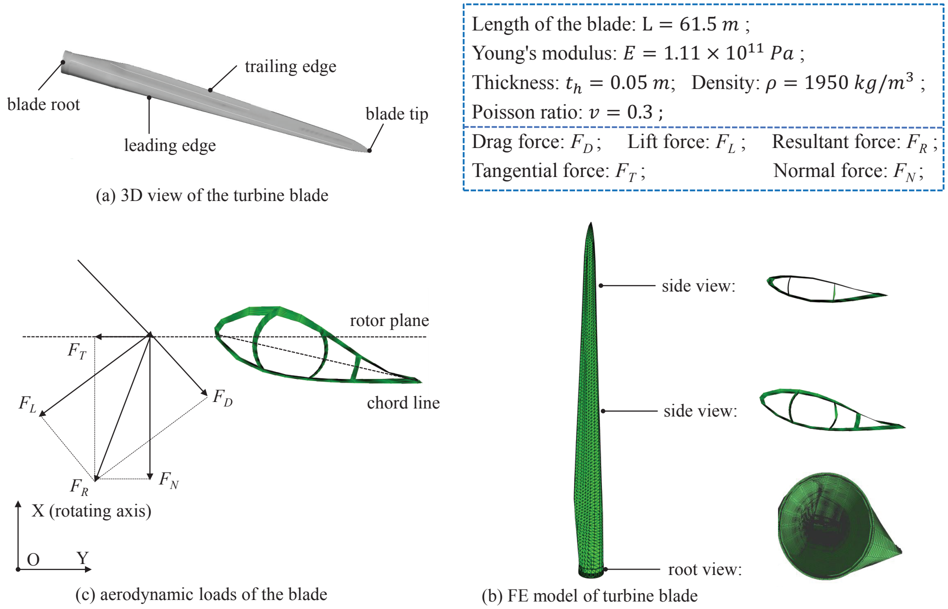

Length of the blade: L = $61.5\ m$;
Young's modulus: $E = 1.11 \times 10^{11}\ Pa$;
Thickness: $t_h = 0.05\ m$; Density: $\rho = 1950\ kg/m^3$;
Poisson ratio: $v = 0.3$;
Drag force: F_D; Lift force: F_L ; Resultant force: F_R ;
Tangential force: F_T ; Normal force: F_N;

(a) 3D view of the turbine blade

(c) aerodynamic loads of the blade

(b) FE model of turbine blade

Figure 5.8: Illustration of the 61.5 m blade of the NREL 5MW reference wind turbine. The mesh contains 3989 nodes and 8394 elements, which yields to 23934 DoFs.

The aerodynamic loads experienced by the blade are calculated using the Blade Element Momentum (BEM) theory, which constitutes a broadly adopted industrial practice for design and analysis of wind turbines. The aerodynamic loads (i.e., normal force F_N and tangential force F_T per section) are computed as discussed in (Hansen, 2015). For this example, they result in prescribed, time-varying nodal forces at the leading edge of the blade. No aero-elastic interaction is here considered. For illustration, the normal force F_N and tangential force F_T, calculated as in (Hansen, 2015), along the leading edge nodes with length L of 10 m, 33 m and 50 m, respectively, are shown in Fig. 5.9.

The blade is assumed to rotate around the x-axis with a constant speed $\Omega = 8$ rad/s and a physical time of 100 seconds is simulated. For the time integration, we use a fixed time step of 0.02 seconds, with updating of the tangential operator at each iteration within one time step, with a convergence criterion on the norm of the force residual

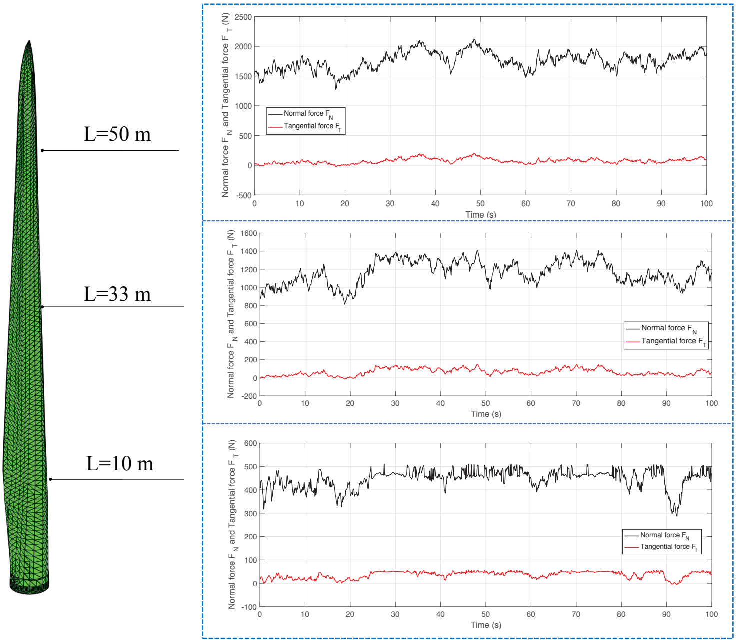

Figure 5.9: Normal forces F_N and tangential forces F_T at the leading edge nodes with $L = 10m, 33m$, and $50m$ for the first 100 seconds.

relative to the norm of the internal force vector (tolerance set to 10^{-6}).

The tip displacement W, U and V of the blade tip node obtained from the elastically linear (NFR-HFM-L, MFR-HFM-L) and nonlinear (NFR-HFM-NL, MFR-HFM-NL) HFMs are compared in Fig. 5.10. A clear difference between the linear and nonlinear tip displacement W, U and V can be observed, confirming that the blade vibrates in the nonlinear regime. On the other hand, the relative displacements obtained from MFR-HFM-NL and NFR-HFM-NL are in good agreement.

The different ROBs for the nonlinear analysis, for both nodal-fixed frame and mean-axis frame, are listed in Table 5.2. The reduced nonlinear responses obtained from different ROMs are shown in Fig. 5.11. As can be observed, the ROMs with MDs (i.e., MFR-ERubin-NL and NFR-ECB-NL) yield much better approximations than their counterparts without MDs (i.e., MFR-Rubin-NL and NFR-CB-NL), even though much more modes are included in these latter ones. This confirms the efficiency of using MDs to account for the nonlinear effect. Furthermore, the enhanced Rubin basis performs better than the enhanced CB counterpart in the nodal-fixed frame, even though the same number of MDs are included. The better accuracy is clearly highlighted in Fig. 5.11(d), where the RMS errors of the overall displacement field are compared.

The computational time is compared between the ROMs enriched with MDs (NFR-ECB-NL and MFR-ERubin-NL) and the HFMs (NFR-HFM-NL and MFR-HFM-NL). All simulations are performed in MATLAB®R2015, on the a cluster equipped with 8-core Intel® Xeon® CPUs (E5-2630v3) @ 2.4 GHz and 128 GB RAM.

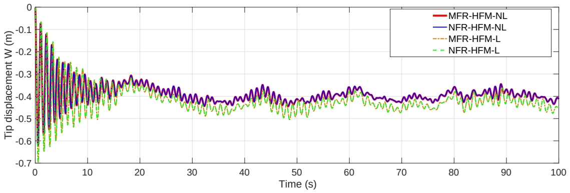

(a) elastic displacement component W at the tip node

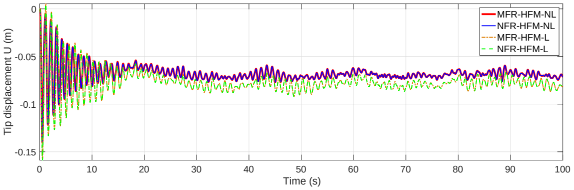

(b) elastic displacement component U at the tip node

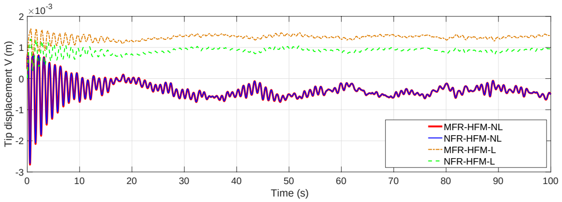

(c) elastic displacement component V at the tip node

Figure 5.10: Comparison of linear and nonlinear tip displacement W, U and V of the blade tip node. A clear difference between the linear and nonlinear responses can be observed, confirming that the blade vibrates in the nonlinear regime.

Table 5.2: Number of DoFs for the 61.5m blade model of the NREL 5 MW reference wind turbine

	number of modes in linear ROB	number of enriched MDs	total DoFs
NFR-ECB-NL	10	15	25
MFR-ERubin-NL	10	15	25
NFR-CB-NL	50	0	50
MFR-Rubin-NL	50	0	50

The computational cost of the HFM is denoted by t_{full} while the one of ROMs has been divided into three different components: *i*) the construction of the reduction basis, which is regarded as *offline cost* (t_{off1}); *ii*) the calculation of all the higher-order tensors as in (5.48), also included in the *offline cost* (t_{off2}), and *iii*) the time required for time integration, which constitutes the *online cost* (t_{on}). Clearly, the HFM does not bear any

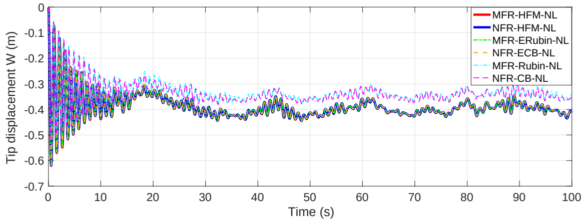

(a) elastic displacement component W at the tip node

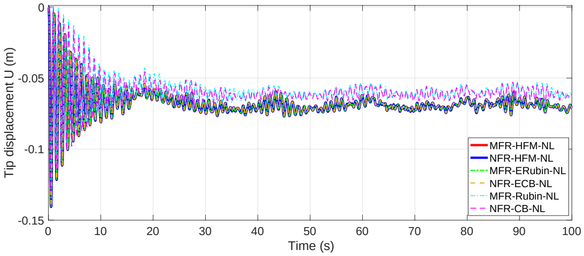

(b) elastic displacement component U at the tip node

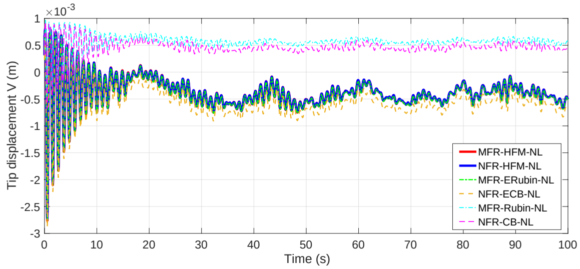

(c) elastic displacement component V at the tip node

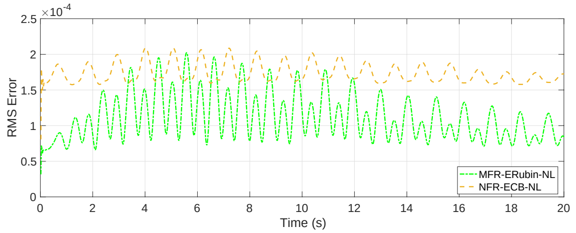

(d) RMS errors for the different ROMs

Figure 5.11: Nonlinear response of the monitored node for different ROMs. The ROMs with MDs (i.e., MFR-ERubin-NL and NFR-ECB-NL) yield much better approximations than their counterparts without MDs (i.e., MFR-Rubin-NL and NFR-CB-NL).

offline cost. The computational time is shown in Table 5.3.

Table 5.3: Computational cost for the 61.5m wind turbine blade (100s physical time).

floating frame	HFM	ROM			Number of iterations	speed up factor	
		offline		online			
	t_{full}	t_{off1}	t_{off2}	t_{on}	$\mathcal{N}$	$\mathcal{S}_1$	$\mathcal{S}_2$
mean-axis	155307s	2053s	230s	72s	10598	2157	66
nodal-fixed	49254s	13.25s	241s	125s	17758	394	129.87

A speed-up factor $\mathcal{S}$ is applied to highlight the computational efficiencies of the nonlinear MOR methods by stating

$$\mathcal{S} = \frac{\mathcal{C}_{on} t_{full}}{\mathcal{C}_{off}(t_{off_1} + t_{off_2}) + \mathcal{C}_{on} t_{on}}, \quad \text{with} \quad \mathcal{C}_{off} + \mathcal{C}_{on} = 1, \tag{5.52}$$

where $\mathcal{C}_{off}$ and $\mathcal{C}_{on}$ are weight factors for the offline and online stages, respectively. The offline calculation cost is neglected by setting $\mathcal{C}_{off} = 0, \mathcal{C}_{on} = 1$. The so obtained speed up factor, denoted as $\mathcal{S}_1$, is justified when the same ROM is used for many different load cases. Alternatively, one can set equal weights to offline and online costs, i.e., $\mathcal{S}_2 : \mathcal{C}_{off} = 0.5, \mathcal{C}_{on} = 0.5$. This covers the limit case in which the ROM is used only once. In the context of wind turbines, a considerable number of loading conditions is prescribed by the design standard IEC 61400-1 (TC88-MT, 2005), resulting in a minimum acceptable number of simulations in the order of 1880 (Hansen *et al.*, 2015). This number grows rapidly when one or more of the parameters associated with the site environmental conditions lies outside the range of IEC reference conditions and may quickly result in up to 3,200,000 simulations (Graf *et al.*, 2016). The significance of online cost becomes even more pronounced in the context of digital twin technology, which constitutes the state-of-the-art approach for lifecycle management of wind turbine structures. Such technology consists in combining a virtual system model, i.e digital twin of the wind turbine, with operational sensor data so as to afford real-time assessment of the structural condition of wind turbines, making thus $\mathcal{S}_1$ a decisive factor in comparison to $\mathcal{S}_2$.

It can be observed that the t_{full} and t_{off_1} in the mean-axis frame are much larger than their counterparts in the nodal-fixed frame, since the stiffness and mass matrices $\mathbf{M}_{mm}$ and $\mathbf{K}_{mm}$ are no longer sparse matrices due to the static condensation of the constraints in the mean-axis frame. Therefore, the eigenvalue analysis in Eq. (5.34), the calculation of MDs in Eq. (5.41), as well as tangent operator calculation in Newmark time integration are more expensive than their correspondents in the nodal-fixed frame, where only sparse matrices $\mathbf{M}_{ff}$ and $\mathbf{K}_{ff}$ are involved. t_{off_2} is similar for the mean-axis frame and nodal-fixed frame ROMs, as t_{off_2} is mainly determined by the size of ROBs, i.e., the number of modes included in the reduction basis. On the contrary, t_{on} in the mean-axis frame is much smaller than its counterpart in the nodal-fixed frame. This is due to the fact that the MFR-ERubin-NL requires fewer iterations for a given time step because of smaller relative DoFs $\mathbf{q}_f$, although NFR-ECB-NL and MFR-ERubin-NL contain the same number of modes in the ROB and their corresponding computational time per iteration is similar.

5.7. CONCLUSIONS

This chapter presents a model-order reduction technique for flexible multibody systems featuring geometric nonlinear elastic behavior. The overall motion of each body is described with the mean-axis floating frame of reference. The relative displacements of each body are then represented by enhancing the standard Rubin substructuring basis with the modal derivatives. The modal derivatives are computed for the complete set of the Rubin basis(i.e., free vibration modes and attachment modes). This allows to accurately capture the geometric nonlinear elastic behavior of the deformable body. When compared with a previous contribution (Wu & Tiso, 2016), where a modal derivatives-enhanced Craig-Bampton substructuring method is applied in the nodal-fixed floating frame, the presented approach offers a better representation of the nonlinearity at the interface, since the coupling between attachment modes and free-interface modes is considered.

For the reduced-order model, the modal derivatives essentially represent second-order terms of the Taylor expansion of the displacements from the undeformed configuration. As such, it is essential to minimize the relative displacements and rotations with respect to the reference frame when using a reduction basis. The mean-axis formulation indeed provides generally smaller relative displacements and rotations than their counterpart in the nodal-fixed frame, thus improving the accuracy of the reduced-order model, as shown in the numerical examples.

The method provides significant computational gains when tested on the simulation of a flexible wind turbine blade featuring about 24000 relative degrees of freedom. The necessary offline cost for the computation of reduction basis is higher than the one proposed in (Wu & Tiso, 2016), since the projected matrices are no longer sparse due to the embedding of the mean-axis constraints. However, the online speed-up is more advanced for the chosen test as compared to the one in (Wu & Tiso, 2016) for a reduced-order model of equal size. This is due to the fewer iterations within a time step required for convergence, as the relative displacements with respect to the reference frame are smaller. This technique is particularly useful when several load conditions need to be simulated so that neglecting offline cost can be justified.

6

CONCLUSIONS AND RECOMMENDATIONS

The previous four chapters discussed the nonlinear model order reduction and substructuring techniques for nonlinear multibody dynamics with several scientific contributions. In this section, we summarize the overall conclusions and provide the recommendations for further study.

6.1. CONCLUSIONS

In this thesis, nonlinear model order reduction techniques have been investigated step-by-step, from substructuring dynamic analysis to multibody system featuring rigid body and non-infinitesimal flexible motion. By doing so, the objective of this thesis, as defined in Section 1:

"How can the computational cost for the dynamic analysis of a complex structure, which features both nonlinear effects and large rigid body motions, be reduced efficiently?"

has been attained.

The study of different interface reduction techniques for linear systems suggests that the existing Craig-Bampton substructuring technique with system-level interface reduction could be extended to a more generalized framework, namely the multilevel Craig-Bampton substructuring method. By doing so, both offline cost (i.e. the computational time for construction of the reduction basis) and the online cost (i.e. the computational time for the time integration) can be reduced. While the system level interface reduction is preferred when high accuracy is required and significant offline cost can be accepted, the multilevel interface reduction method provides a promising alternative for large-scale problems when both accuracy and computational efficiency are of concern.

For many multi-component structures featuring geometric nonlinear behavior, the computational burden of the dynamic simulations could be a critical issue. We further proposed a modal-derivatives enhanced Craig-Bampton substructuring technique for the reduction of geometric nonlinear dynamic analysis, which can deliver compact reduced order models featuring system-level interface reduction. The modal derivatives are capable of describing the most significant contributions to geometric nonlinear behavior, for both internal and interface degrees of freedom. The reduced nonlinear force vector, which is computationally expensive, is constructed at a substructure-level in parallel across substructures. The presented reduced order models show excellent accuracy, when compared to the full models. Meanwhile, significant computational savings are obtained. The proposed enhanced Craig-Bampton substructuring technique allows highly efficient modeling of complex structures with geometric nonlinearities, and offers the flexibility to consider nonlinearities only for selected substructures undergoing moderate displacements and rotations.

In flexible multibody systems, each substructure may feature both large rigid body motion and nonlinear flexible behavior. For this case, we have embedded the enhanced Craig-Bampton technique within the floating frame of reference approach. The reduced order models are first discussed for planar nonlinear von-Kármán beam systems. The nodal-fixed formulation, where the reference frame is rigidly attached to one or more nodes of the flexible body, is applied. In the case of beam components, interface reduction methods are unnecessary since a single node connects the adjacent bodies. The computational saving is obtained by a substantial reduction in the size of the governing equations of motion. The proposed procedure allows for a very compact reduction basis and thus yields significant simulation time savings, provided that the internal force vectors are expressed directly in modal coordinates via reduced high-order tensors. We show that this method is superior, in terms of accuracy and efficiency, than the reduction using a large number of fixed interface modes. Moreover, the proposed enhanced Craig-Bampton method does not pose additional conceptual difficulties for the extension into three-dimensional discretization.

Because of the non-unique definition of the nodal-fixed frame, it might yield large relative displacements and rotations and therefore adversely impact the accuracy of a reduced order basis that attempts to capture the flexible motion. Moreover, in geometric complex three dimensional systems, the nonlinear behavior at the interface needs to be properly accounted. In order to tackle these difficulties, we combined the modal derivatives enhanced Rubin substructuring method with the mean-axis floating frame. When compared to the enhanced Craig-Bampton method, the enhanced Rubin substructuring approach better models the geometrical nonlinearities occurring at the interface, since the reduction basis comprises vibration modes and modal derivatives featuring free motion of the interface. Moreover, the mean-axis frame guarantees better accuracy when an approximate kinematic model (in this case, von-Kármán moderate rotations model) is adopted because the relative displacements and rotations with respect to the mean-axis frame are much smaller than their counterpart with respect to the nodal-fixed frame. The application of this method to a 61.5m blade of a reference 5MW wind turbine model has been discussed. The reduced order model can accurately describe the nonlinear dynamic behavior of the full system (less than 2×10^{-4} in terms of root mean square error) with a reduction of degrees of freedom. It can be observed that the proposed formulation provides better accuracy and significant computational savings (speeding up factor $\mathcal{S}_1 = 2157$) when compared to its counterpart featuring enhanced Craig-Bampton method and nodal-fixed frame (speeding up factor $\mathcal{S}_1 = 394$). Therefore, it can be concluded that the enhanced Rubin substructuring approach in combination with the mean-axis floating frame provides a powerful way of obtaining compact reduced order models.

6.2. RECOMMENDATIONS

Although several modal-derivatives enhanced model order reduction methods have been proposed in this thesis, there are always open topics for further study. The recommendations for potentially interesting future work, based on the author's opinion, are listed here:

- In this work, the linear projection based model order reduction techniques are the area of interest. We neglect the quadratic relationship between the modal amplitudes of the linear modes (not limited to truncated vibration modes) and the corresponding modal derivatives, and add the modal derivatives in the reduction basis as extra modes, paying for the price of additional degrees of freedom. However, the number of modal derivatives grows quadratically with the number of linear modes. Therefore, the interface reduction techniques have to be combined with substructuring methods to avoid the overwhelming number of interface modes. The quadratic manifold approach (Jain *et al.*, 2017) is an alternative model order reduction option that aims at constructing a configuration dependent projection subspace. This approach can yield a more compact reduced order model, as the modal derivatives amplitudes are enslaved to the linear modes. By doing so, the need for interface reduction, which inevitably degrades the accuracy, might vanish. However, the reliability of the quadratic manifold approach is not yet fully demonstrated, especially when membrane effects are not the dominating source of nonlinearity (Rutzmoser *et al.*, 2017). An interesting extension of this work would be to test the quadratic manifolds when applied to substructured problems.

- The proposed enhanced Craig-Bampton substructuring method is combined with system-level interface reduction. An accurate approximation has been achieved. However, the system-level interface modes, as well as the corresponding modal derivatives, are calculated after the substructures are assembled together. By doing so, in case of a local design change, all the interface modes and modal derivatives have to be recomputed. The cost of reduction basis reconstruction could be reduced if the enhanced Craig-Bampton substructuring method is combined with the local-level or multilevel interface reduction methods. However, the problem of interface incompatibility, introduced by the local-level interface reduction, has to be solved before the local-level method is applied to the nonlinear problems.

- In this work, we rank the model derivatives by a simple heuristic modes selection criterion, where the modal interaction between different modes based on a linear modal solution with the same load condition is utilized to determine the relative significance of the modal derivatives. This modal derivatives selection criterion is based on a modal linear solution. However, this selection criterion cannot be directly applied in the floating frame of reference owing to the following two reasons: i) the linear solution in the floating frame of reference is still very time-consuming, since the mass matrices and quadratic velocity vectors are configuration dependent, and therefore need to be updated at every iteration during each time step; ii) for many multibody system dynamic applications involving large elastic deflection and large centrifugal forces, neglecting the geometrical nonlinearities may lead to diverging solutions. A robust and comprehensive mode selection criterion should be studied for the flexible multibody system when the floating frame of reference is applied.

A

THE MASS MATRIX AND QUADRATIC VELOCITY VECTOR

This Appendix contains a detailed formulation of the mass matrix and quadratic velocity vector. Appendix A.1 gives all the quantities in full model in equation (4.6), while appendix A.2 refers to the reduced model (i.e., modal) formulation in equation (4.38).

A.1. PRECOMPUTED OFFLINE QUANTITIES IN NODAL COORDINATES

To obtain the detailed expression of the mass matrix $\mathbf{M}^j$, we first rewrite Eq. (4.3) as

$$\begin{aligned}\dot{\mathbf{r}}^j &= \dot{\mathbf{R}} + \dot{\mathbf{A}}\mathbf{N}^j(\mathbf{e}_0^j + \mathbf{q}_f^j) + \mathbf{A}\mathbf{N}^j\dot{\mathbf{q}}_f^j \\ &= \begin{bmatrix}\mathbf{I} & \mathcal{B}^j\{\boldsymbol{\theta},\mathbf{q}_f^j\} & \mathbf{A}\mathbf{N}^j\end{bmatrix}\begin{bmatrix}\dot{\mathbf{R}} \\ \dot{\boldsymbol{\theta}} \\ \dot{\mathbf{q}}_f^j\end{bmatrix}.\end{aligned} \tag{A.1}$$

The second term in (A.1) is rewritten as

$$\dot{\mathbf{A}}\mathbf{N}^j(\mathbf{e}_0^j + \mathbf{q}_f^j) = \mathcal{B}^j\{\boldsymbol{\theta},\mathbf{q}_f^j\}\dot{\boldsymbol{\theta}}, \tag{A.2}$$

in order to isolate the velocity terms $\dot{\boldsymbol{\theta}}$.

By substituting (A.1) into (4.2), we can obtain

$$\begin{aligned}\mathcal{T}^j &= \frac{1}{2}\int_{V^j}\rho^j(\dot{\mathbf{r}}^j)^{\mathrm{T}}\dot{\mathbf{r}}^j\,dV^j \\ &= \frac{1}{2}(\dot{\mathbf{q}}^j)^{\mathrm{T}}\int_{V^j}\rho^j\left(\begin{bmatrix}\mathbf{I} & \mathcal{B}^j\{\boldsymbol{\theta},\mathbf{q}_f^j\} & \mathbf{A}\mathbf{N}^j\end{bmatrix}\right)^{\mathrm{T}}\left(\begin{bmatrix}\mathbf{I} & \mathcal{B}^j\{\boldsymbol{\theta},\mathbf{q}_f^j\} & \mathbf{A}\mathbf{N}^j\end{bmatrix}\right)dV^j\dot{\mathbf{q}}^j \\ &= \frac{1}{2}(\dot{\mathbf{q}}^j)^{\mathrm{T}}\mathbf{M}^j\dot{\mathbf{q}}^j.\end{aligned} \tag{A.3}$$

Accordingly, the mass matrix $\mathbf{M}^j$ of the j^{th} element can be write in a partitioned form as

$$\mathbf{M}^j = \int_{V^j} \rho^j \begin{bmatrix} \mathbf{I} & \mathcal{B}^j & \mathbf{A}\mathbf{N}^j \\ & (\mathcal{B}^j)^{\mathrm{T}}(\mathcal{B}^j) & (\mathcal{B}^j)^{\mathrm{T}}\mathbf{A}\mathbf{N}^j \\ \mathrm{sym} & & (\mathbf{N}^j)^{\mathrm{T}}\mathbf{N}^j \end{bmatrix} \mathrm{d}V^j = \begin{bmatrix} \mathbf{M}^j_{RR} & \mathbf{M}^j_{R\theta}\{\boldsymbol{\theta},\mathbf{q}^j_f\} & \mathbf{M}^j_{Rf}\{\boldsymbol{\theta}\} \\ & \mathbf{M}^j_{\theta\theta}\{\boldsymbol{\theta},\mathbf{q}^j_f\} & \mathbf{M}^j_{\theta f}\{\boldsymbol{\theta},\mathbf{q}^j_f\} \\ \mathrm{sym} & & \mathbf{M}^j_{ff} \end{bmatrix}. \tag{A.4}$$

It can be shown that $\mathbf{M}^j_{RR}$ and $\mathbf{M}^j_{ff}$ are constant matrices which can be calculated offline. The off-diagonal components and $\mathbf{M}^j_{\theta\theta}$ are configuration dependent.

We can define the quadratic velocity $\mathbf{Q}^j_v$ to be

$$\mathbf{Q}^j_v = -\dot{\mathbf{M}}^j\dot{\mathbf{q}}^j + \left[\frac{\partial}{\partial\mathbf{q}^j}\left(\frac{1}{2}(\dot{\mathbf{q}}^j)^T\mathbf{M}^j\dot{\mathbf{q}}^j\right)\right]^T, \tag{A.5}$$

where $\mathbf{Q}^j_v$ results from the differentiation of the kinetic energy with respect to time and with respect to the body coordinates, and contains the gyroscopic and Coriolis contributions. The configuration quadratic velocity vector $\mathbf{Q}^j_v$ can be written in a partitioned form

$$\mathbf{Q}^j_v = \begin{bmatrix} (\mathbf{Q}_v)^j_r \\ (\mathbf{Q}_v)^j_f \end{bmatrix} = \begin{bmatrix} (\mathbf{Q}_v)^j_R \\ (\mathbf{Q}_v)^j_\theta \\ (\mathbf{Q}_v)^j_f \end{bmatrix}. \tag{A.6}$$

In the following, we define the components of (A.4-A.6) at element level as

$$\mathbf{M}^j_{RR} = \begin{bmatrix} m^j & 0 \\ 0 & m^j \end{bmatrix}, \tag{A.7}$$

$$\mathbf{M}^j_{ff} = \overline{\mathbf{C}}^{jT}\mathbf{S}^j_{ff}\overline{\mathbf{C}}^j = \mathbf{D}^j_1, \tag{A.8}$$

$$\mathbf{M}^j_{R\theta} = \mathbf{A}_\theta\mathbf{C}^j\overline{\mathbf{S}}^j\overline{C}^j(\mathbf{e}^j_0 + \mathbf{q}^j_f) = \mathbf{A}_\theta\mathbf{D}^j_2\mathbf{e}^j_0 + \mathbf{A}_\theta\mathbf{D}^j_2\mathbf{q}^j_f, \tag{A.9}$$

$$\mathbf{M}^j_{\theta\theta} = (\mathbf{e}^j_0 + \mathbf{q}^j_f)^T\mathbf{M}^j_{ff}(\mathbf{e}^j_0 + \mathbf{q}^j_f) = \mathbf{e}^{jT}_0\mathbf{D}^j_1\mathbf{e}^j_0 + 2\mathbf{e}^{jT}_0\mathbf{D}^j_1\mathbf{q}^j_f + \mathbf{q}^{jT}_f\mathbf{D}^j_1\mathbf{q}^j_f, \tag{A.10}$$

$$\mathbf{M}^j_{Rf} = \mathbf{A}\mathbf{C}^j\overline{\mathbf{S}}^j\overline{\mathbf{C}}^j = \mathbf{A}\mathbf{D}^j_2, \tag{A.11}$$

$$\mathbf{M}^j_{\theta f} = (\mathbf{e}^j_0 + \mathbf{q}^j_f)^T\overline{\mathbf{C}}^{jT}\widetilde{\mathbf{S}}^j\overline{\mathbf{C}}^j = \mathbf{e}^{jT}_0\mathbf{D}^j_3 + \mathbf{q}^{jT}_f\mathbf{D}^j_3, \tag{A.12}$$

$$\begin{aligned} (\mathbf{Q}_v)^j_R &= \dot{\theta}^2\mathbf{A}\mathbf{C}^j\overline{\mathbf{S}}^j\overline{C}^j(\mathbf{e}^j_0 + \mathbf{q}^j_f) - 2\dot{\theta}\mathbf{A}_\theta\mathbf{C}^j\overline{\mathbf{S}}^j\overline{\mathbf{C}}^j\dot{\mathbf{q}}^j_f \\ &= \dot{\theta}^2\mathbf{A}\mathbf{D}^j_2(\mathbf{e}^j_0 + \mathbf{q}^j_f) - 2\dot{\theta}\mathbf{A}_\theta\mathbf{D}^j_2\dot{\mathbf{q}}^j_f \end{aligned}, \tag{A.13}$$

$$(\mathbf{Q}_v)^j_\theta = -2\dot{\theta}\dot{\mathbf{q}}^{jT}_f\mathbf{M}^j_{ff}(\mathbf{e}^j_0 + \mathbf{q}^j_f) = -2\dot{\theta}\dot{\mathbf{q}}^{jT}_f\mathbf{D}^j_1(\mathbf{e}^j_0 + \mathbf{q}^j_f), \tag{A.14}$$

$$(\mathbf{Q}_v)^j_f = 2\dot{\theta}\overline{\mathbf{C}}^{jT}\widetilde{\mathbf{S}}^j\overline{\mathbf{C}}^j\dot{\mathbf{q}}^j_f + \dot{\theta}^2\mathbf{M}^j_{ff}(\mathbf{e}^j_0 + \mathbf{q}^j_f) = 2\dot{\theta}\mathbf{D}^j_3\dot{\mathbf{q}}^j_f + \dot{\theta}^2\mathbf{D}^j_1(\mathbf{e}^j_0 + \mathbf{q}^j_f), \tag{A.15}$$

where the superscript j refers to the element number of the corresponding body. $\mathbf{S}_{ff}^{j} \in \mathbb{R}^{6\times6}, \overline{\mathbf{S}}^{j} \in \mathbb{R}^{2\times6}, \widetilde{\mathbf{S}}^{j} \in \mathbb{R}^{6\times6}$ are inertia shape integrals defined for each element, $\mathbf{C}^{j} \in \mathbb{R}^{2\times2}$, and $\overline{\mathbf{C}}^{j} \in \mathbb{R}^{6\times6}$ are the orthogonal transformation matrix. All these quantities are constant and can be calculated offline.The details can be found in (Shabana, 2005). To simplify the expression, three constant matrices $\mathbf{D}_1^{j} \in \mathbb{R}^{6\times6}, \mathbf{D}_2^{j} \in \mathbb{R}^{2\times6}, \mathbf{D}_3^{j} \in \mathbb{R}^{6\times6}$ are defined as

$$\mathbf{D}_1^{j} = \overline{\mathbf{C}}^{jT}\mathbf{S}_{ff}^{j}\overline{\mathbf{C}}^{j}, \quad \mathbf{D}_2^{j} = \mathbf{C}^{j}\overline{\mathbf{S}}^{j}\overline{C}^{j}, \quad \mathbf{D}_3^{j} = \overline{\mathbf{C}}^{jT}\widetilde{\mathbf{S}}^{j}\overline{\mathbf{C}}^{j}. \tag{A.16}$$

After element assembly, the components of mass matrix $\mathbf{M}$ and quadratic velocity vector $\mathbf{Q}_v$ for the substructure can be expressed as

$$\mathbf{M}_{RR} = \underline{\begin{bmatrix} m & 0 \\ 0 & m \end{bmatrix}}, \tag{A.17}$$

$$\mathbf{M}_{ff} = \underline{\mathbf{D}_1}, \tag{A.18}$$

$$\mathbf{M}_{R\theta} = \mathbf{A}_{\theta}\underline{\mathbf{D}_2\mathbf{e}_0} + \mathbf{A}_{\theta}\underline{\mathbf{D}_2}\mathbf{q}_f, \tag{A.19}$$

$$\mathbf{M}_{\theta\theta} = \underline{\mathbf{e}_0^T\mathbf{D}_1\mathbf{e}_0} + 2\underline{\mathbf{e}_0^T\mathbf{D}_1}\mathbf{q}_f + \mathbf{q}_f^T\underline{\mathbf{D}_1}\mathbf{q}_f, \tag{A.20}$$

$$\mathbf{M}_{Rf} = \mathbf{A}\underline{\mathbf{D}_2}, \tag{A.21}$$

$$\mathbf{M}_{\theta f} = \underline{\mathbf{e}_0^T\mathbf{D}_3} + \mathbf{q}_f^T\underline{\mathbf{D}_3}, \tag{A.22}$$

$$(\mathbf{Q}_v)_R = \dot{\theta}^2\mathbf{A}\underline{\mathbf{D}_2\mathbf{e}_0} + \dot{\theta}^2\mathbf{A}\underline{\mathbf{D}_2}\mathbf{q}_f - 2\dot{\theta}\mathbf{A}_{\theta}\underline{\mathbf{D}_2}\dot{\mathbf{q}}_f, \tag{A.23}$$

$$(\mathbf{Q}_v)_{\theta} = -2\dot{\theta}\dot{\mathbf{q}}_f^T\underline{\mathbf{D}_1\mathbf{e}_0} - 2\dot{\theta}\dot{\mathbf{q}}_f^T\underline{\mathbf{D}_1}\mathbf{q}_f, \tag{A.24}$$

$$(\mathbf{Q}_v)_f = 2\dot{\theta}\underline{\mathbf{D}_3}\dot{\mathbf{q}}_f + \dot{\theta}^2\underline{\mathbf{D}_1\mathbf{e}_0} + \dot{\theta}^2\underline{\mathbf{D}_1}\mathbf{q}_f. \tag{A.25}$$

All the underlined terms in equations (A.17-A.25) can be computed offline. The cost of their construction scales with the size of high-dimensional FE model.

A.2. PRECOMPUTED OFFLINE QUANTITIES IN GENERALIZED MODAL COORDINATES

Referring to the reduced equation of motion in (4.38), the reduced mass matrix and quadratic velocity vector is written as:

$$\overline{\mathbf{M}} = \begin{bmatrix} \mathbf{M}_{rr} & \overline{\mathbf{M}}_{rf} \\ \overline{\mathbf{M}}_{rf} & \overline{\mathbf{M}}_{ff} \end{bmatrix} = \begin{bmatrix} \mathbf{M}_{RR} & \mathbf{M}_{R\theta} & \overline{\mathbf{M}}_{Rf} \\ & \mathbf{M}_{\theta\theta} & \overline{\mathbf{M}}_{\theta f} \\ sym & & \overline{\mathbf{M}}_{ff} \end{bmatrix}, \tag{A.26}$$

$$\overline{\mathbf{Q}}_v = \begin{bmatrix} (\mathbf{Q}_v)_r \\ (\overline{\mathbf{Q}}_v)_f \end{bmatrix} = \begin{bmatrix} (\mathbf{Q}_v)_R \\ (\mathbf{Q}_v)_{\theta} \\ (\overline{\mathbf{Q}}_v)_f \end{bmatrix}, \tag{A.27}$$

where all the quantities can be directly expressed as:

$$\mathbf{M}_{R\theta} = \mathbf{A}_\theta \mathbf{D}_2 \mathbf{e}_0 + \mathbf{A}_\theta \mathbf{D}_2 \mathbf{q}_f = \mathbf{A}_\theta \underline{\mathbf{D}_2 \mathbf{e}_0} + \mathbf{A}_\theta \underline{\mathbf{D}_2 \mathbf{V}} \boldsymbol{\gamma}, \tag{A.28}$$

$$\mathbf{M}_{\theta\theta} = \mathbf{e}_0^T \mathbf{D}_1 \mathbf{e}_0 + 2\mathbf{e}_0^T \mathbf{D}_1 \mathbf{q}_f + \mathbf{q}_f^T \mathbf{D}_1 \mathbf{q}_f = \underline{\mathbf{e}_0^T \mathbf{D}_1 \mathbf{e}_0} + 2\underline{\mathbf{e}_0^T \mathbf{D}_1 \mathbf{V}} \boldsymbol{\gamma} + \boldsymbol{\gamma}^T \underline{\mathbf{V}^T \mathbf{D}_1 \mathbf{V}} \boldsymbol{\gamma}, \tag{A.29}$$

$$\overline{\mathbf{M}}_{Rf} = \mathbf{M}_{Rf} \mathbf{V} = \mathbf{A} \underline{\mathbf{D}_2 \mathbf{V}}, \tag{A.30}$$

$$\overline{\mathbf{M}}_{\theta f} = \mathbf{M}_{\theta f} \mathbf{V} = \underline{\mathbf{e}_0^T \mathbf{D}_3 \mathbf{V}} + \boldsymbol{\gamma}^T \underline{\mathbf{V}^T \mathbf{D}_3 \mathbf{V}}, \tag{A.31}$$

$$\overline{\mathbf{M}}_{ff} = \mathbf{V}^T \mathbf{M}_{ff} \mathbf{V} = \underline{\mathbf{V}^T \mathbf{D}_1 \mathbf{V}}, \tag{A.32}$$

$$(\mathbf{Q}_v)_R = \dot{\theta}^2 \mathbf{A} \underline{\mathbf{D}_2 \mathbf{e}_0} + \dot{\theta}^2 \mathbf{A} \underline{\mathbf{D}_2 \mathbf{V}} \boldsymbol{\gamma} - 2\dot{\theta} \mathbf{A}_\theta \underline{\mathbf{D}_2 \mathbf{V}} \dot{\boldsymbol{\gamma}}, \tag{A.33}$$

$$(\mathbf{Q}_v)_\theta = -2\dot{\theta} \dot{\boldsymbol{\gamma}}^T \underline{\mathbf{V}^T \mathbf{D}_1 \mathbf{e}_0} - 2\dot{\theta} \dot{\boldsymbol{\gamma}}^T \underline{\mathbf{V}^T \mathbf{D}_1 \mathbf{V}} \boldsymbol{\gamma}, \tag{A.34}$$

$$(\overline{\mathbf{Q}}_v)_f = \mathbf{V}^T (\mathbf{Q}_v)_f = 2\dot{\theta} \underline{\mathbf{V}^T \mathbf{D}_3 \mathbf{V}} \dot{\boldsymbol{\gamma}} + \dot{\theta}^2 \underline{\mathbf{V}^T \mathbf{D}_1 \mathbf{e}_0} + \dot{\theta}^2 \underline{\mathbf{V}^T \mathbf{D}_1 \mathbf{V}} \boldsymbol{\gamma}. \tag{A.35}$$

Therefore all the underlined terms in (A.28-A.35) can be computed offline during the modal analysis. Note that all the quantities can be expressed directly in reduced coordinates (i.e., not evaluated with respect to nodal coordinates and then projected) and lead therefore to a computationally efficient reduced order model.

B

RIGID BODY CONSTRAINTS AT THE INTERFACE SETS

The matrix $\mathbf{L}_v$, as introduced in (5.10) to rigidize the interface DoFs, is calculated according to the relative position of each interface node with respect to the corresponding virtual node. To offer a clear view, the transformation matrix $\widehat{\mathbf{L}}_{v_p}$ from the DoFs $\widehat{\mathbf{q}}_{b_p}$ of an arbitrary node in the p^{th} interface set to the DoFs $\mathbf{q}_{v_p}$ of the corresponding virtual node has been written here

$$\underbrace{\begin{bmatrix} \widehat{q}_{X,b_p} \\ \widehat{q}_{Y,b_p} \\ \widehat{q}_{Z,b_p} \\ \widehat{q}_{\theta_x,b_p} \\ \widehat{q}_{\theta_y,b_p} \\ \widehat{q}_{\theta_z,b_p} \end{bmatrix}}_{\widehat{\mathbf{q}}_{bp}} = \underbrace{\begin{bmatrix} 1 & 0 & 0 & 0 & \Delta z & -\Delta y \\ 0 & 1 & 0 & -\Delta z & 0 & \Delta x \\ 0 & 0 & 1 & \Delta y & -\Delta x & 0 \\ 0 & 0 & 0 & 1 & 0 & 0 \\ 0 & 0 & 0 & 0 & 1 & 0 \\ 0 & 0 & 0 & 0 & 0 & 1 \end{bmatrix}}_{\widehat{\mathbf{L}}_{vp}} \underbrace{\begin{bmatrix} q_{X,v_p} \\ q_{Y,v_p} \\ q_{Z,v_p} \\ q_{\theta_x,v_p} \\ q_{\theta_y,v_p} \\ q_{\theta_z,v_p} \end{bmatrix}}_{\mathbf{q}_{vp}}, \tag{B.1}$$

where

$$\Delta x = x_{b_p} - x_{v_p}, \quad \Delta y = y_{b_p} - y_{v_p}, \quad \Delta z = z_{b_p} - z_{v_p},$$

and $x_{b_p}, y_{b_p}, z_{b_p}$ and $x_{v_p}, y_{v_p}, z_{v_p}$ are the nodal coordinates of the interface nodes and virtual nodes in all three directions, respectively. The vectors $\widehat{\mathbf{q}}_{b_p}$ and $\mathbf{q}_{v_p}$ have been split into 3 translation component $(\star_X, \star_Y, \star_Z)$ and 3 rotational components $(\star_{\theta_x}, \star_{\theta_y}, \star_{\theta_z})$, as in the subscripts. The transformation matrix $\mathbf{L}_v$ for the entire set of interface DoFs can then be obtained by concatenating the transformation matrices from each interface nodes in an analogous way.

C

THE CONSTRAINT EQUATIONS FOR THE MEAN-AXIS FRAME

In this appendix, we will derive the constrained equations for the mean-axis frame with proper assumptions, as first proposed in (Agrawal & Shabana, 1986). Substituting (5.14) into (5.16), we can obtain

$$\frac{\partial \mathcal{T}_r}{\partial \dot{\mathbf{R}}} = -\sum_j \int_{V^j} \rho^j \left[\dot{\mathbf{r}}^j - \dot{\mathbf{R}} - \dot{\mathbf{A}}\mathbf{N}^j(\mathbf{q}_0^j + \mathbf{q}_f^j)\right] \mathrm{d}V^j = \mathbf{0} \tag{C.1}$$

and

$$\frac{\partial \mathcal{T}_r}{\partial \boldsymbol{\omega}} = -\sum_j \int_{V^j} \rho^j \frac{\partial}{\partial \boldsymbol{\omega}} \left[\dot{\mathbf{A}}\mathbf{N}^j(\mathbf{q}_0^j + \mathbf{q}_f^j)\right]^{\mathrm{T}} \left[\dot{\mathbf{r}}^j - \dot{\mathbf{R}} - \dot{\mathbf{A}}\mathbf{N}^j(\mathbf{q}_0^j + \mathbf{q}_f^j)\right] \mathrm{d}V^j = 0. \tag{C.2}$$

Substituting (5.3) into (C.1) and (C.2), then noticing that **A** is not space dependent, we can further obtain that

$$\frac{\partial \mathcal{T}_r}{\partial \dot{\mathbf{R}}} = \mathbf{0} \;\Leftrightarrow\; \sum_j \int_{V^j} \rho^j \mathbf{N}^j \dot{\mathbf{q}}_f^j \mathrm{d}V^j = \mathbf{0} \tag{C.3}$$

and

$$\frac{\partial \mathcal{T}_r}{\partial \boldsymbol{\omega}} = \mathbf{0} \;\Leftrightarrow\; \sum_j \int_{V^j} \rho^j (\mathbf{q}_0^j + \mathbf{q}_f^j)^{\mathrm{T}} (\mathbf{N}^j)^{\mathrm{T}} \frac{\partial}{\partial \boldsymbol{\omega}} \left(\dot{\mathbf{A}}^{\mathrm{T}}\mathbf{A}\right) \mathbf{N}^j \dot{\mathbf{q}}_f^j \mathrm{d}V^j = \mathbf{0}, \tag{C.4}$$

where we can further utilize the identity (Shabana, 2005)

$$\dot{\mathbf{A}}^{\mathrm{T}}\mathbf{A} = -\begin{bmatrix} 0 & -\omega_3 & \omega_2 \\ \omega_3 & 0 & -\omega_1 \\ -\omega_2 & \omega_1 & 0 \end{bmatrix} = -\widetilde{\boldsymbol{\omega}}, \tag{C.5}$$

where $\widetilde{\star}$ indicates the skew symmetric matrix of the corresponding vector. Substituting (C.5) into (C.4), we can obtain

$$\sum_j \int_{V^j} \rho^j (\mathbf{q}_0^j + \mathbf{q}_f^j)^{\mathrm{T}} (\mathbf{N}^j)^{\mathrm{T}} \frac{\partial}{\partial \boldsymbol{\omega}} \widetilde{\boldsymbol{\omega}} \mathbf{N}^j \dot{\mathbf{q}}_f^j \mathrm{d}V^j = \mathbf{0}, \tag{C.6}$$

which can be further derived as

$$\begin{bmatrix} (\mathbf{q}_0^j+\mathbf{q}_f^j)^{\mathrm{T}}\widetilde{\mathbf{N}}_{23}^j \\ (\mathbf{q}_0^j+\mathbf{q}_f^j)^{\mathrm{T}}\widetilde{\mathbf{N}}_{31}^j \\ (\mathbf{q}_0^j+\mathbf{q}_f^j)^{\mathrm{T}}\widetilde{\mathbf{N}}_{12}^j \end{bmatrix} \dot{\mathbf{q}}_f = \mathbf{0}, \text{ with } \widetilde{\mathbf{N}}_{kl}^j = \int_{V^j} \rho^j \left[(\mathbf{N}_k^j)^{\mathrm{T}}\mathbf{N}_l^j - (\mathbf{N}_l^j)^{\mathrm{T}}\mathbf{N}_k^j \right] \mathrm{d}V^j, \tag{C.7}$$

where $\mathbf{N}_k^j$ and $\mathbf{N}_l^j$ are the k^{th} and l^{th} rows of the shape function $\mathbf{N}^j$. In order to linearise the mean-axis condition, the simplification in the reference (Agrawal & Shabana, 1986) aims to neglecting the higher order terms in (C.4) by stating

$$\begin{bmatrix} (\mathbf{q}_f^j)^{\mathrm{T}}\widetilde{\mathbf{N}}_{23}^j \\ (\mathbf{q}_f^j)^{\mathrm{T}}\widetilde{\mathbf{N}}_{31}^j \\ (\mathbf{q}_f^j)^{\mathrm{T}}\widetilde{\mathbf{N}}_{12}^j \end{bmatrix} \dot{\mathbf{q}}_f = \mathbf{0}. \tag{C.8}$$

Notice that $\widetilde{\mathbf{N}}_{kl}^j$ is a skew symmetric matrix. Therefore, assumption (C.8) can be justified on the basis that velocity $\dot{\mathbf{q}}_f^j$ occur approximately collinear with displacement $\mathbf{q}_f^j$, and hence the cross product vanishes.

With this assumption, the mean-axis condition can be linearized as

$$\frac{\partial \mathcal{T}_r}{\partial \dot{\mathbf{R}}} = \mathbf{0} \;\Rightarrow\; \mathbf{S}_1^j \dot{\mathbf{q}}_f^j = \mathbf{0} \quad \text{with} \quad \mathbf{S}_1^j = \sum_j \int_{V^j} \rho^j \mathbf{N}^j \mathrm{d}V^j \tag{C.9}$$

and

$$\frac{\partial \mathcal{T}_r}{\partial \boldsymbol{\omega}} = \mathbf{0} \;\Rightarrow\; \mathbf{S}_2 \dot{\mathbf{q}}_f = \mathbf{0}, \quad \text{with} \quad \mathbf{S}_2^j = \begin{bmatrix} (\mathbf{q}_0^j)^{\mathrm{T}}\widetilde{\mathbf{N}}_{23}^j \\ (\mathbf{q}_0^j)^{\mathrm{T}}\widetilde{\mathbf{N}}_{31}^j \\ (\mathbf{q}_0^j)^{\mathrm{T}}\widetilde{\mathbf{N}}_{12}^j \end{bmatrix} \tag{C.10}$$

Equation (C.9) and (C.10) can be further expressed, with a classic FE assembly, as

$$\begin{bmatrix} \mathbf{S}_1 \\ \mathbf{S}_2 \end{bmatrix} \dot{\mathbf{q}}_f = \mathbf{0}, \quad \Leftrightarrow \quad \mathbf{S}\dot{\mathbf{q}}_f = \mathbf{0}, \tag{C.11}$$

where $\mathbf{S}_1 \in \mathbb{R}^{3\times n}$ and $\mathbf{S}_2 \in \mathbb{R}^{3\times n}$ are the precomputed inertia integrals, which can be assembled over the elementary component $\mathbf{S}_1^j \in \mathbb{R}^{3\times n_e}$ and $\mathbf{S}_2^j \in \mathbb{R}^{3\times n_e}$. The mean-axis condition in (C.11) implies that the mean-axis condition can be written in terms of only $\dot{\mathbf{q}}_f$ that have been defined locally w.r.t. the body axis.

REFERENCES

AGRAWAL, O. P. & SHABANA, A. A. 1986 Application of deformable-body mean axis to flexible multibody system dynamics. *Computer Methods in Applied Mechanics and Engineering* **56** (2), 217–245.

ALLEMANG, R. J. & BROWN, D. L 1982 A correlation coefficient for modal vector analysis. In *Proceedings of the 1st international modal analysis conference*, , vol. 1, pp. 110–116. SEM, Orlando.

ALLMAN, D. J. 1976 A simple cubic displacement element for plate bending. *International Journal for Numerical Methods in Engineering* **10** (2), 263–281.

ALLMAN, D. J. 1988 Evaluation of the constant strain triangle with drilling rotations. *International Journal for Numerical Methods in Engineering* **26** (12), 2645–2655.

AOYAMA, Y. & YAGAWA, G. 2001 Component mode synthesis for large-scale structural eigenanalysis. *Computers & Structures* **79** (6), 605–615.

BAKR, E. M. & SHABANA, A. A. 1986 Geometrically nonlinear analysis of multibody systems. *Computers & Structures* **23** (6), 739–751.

BALMÈS, E. 1996 Use of generalized interface degrees of freedom in component mode synthesis. In *Proceedings of IMAC XIV Conference*, pp. 204–210.

BAMPTON, M. C. C. & CRAIG, JR R. R. 1968 Coupling of substructures for dynamic analyses. *AIAA Journal* **6** (7), 1313–1319.

BARBIC, J. & JAMES, D. L. 2005 Real-time subspace integration for st. venant-kirchhoff deformable models. *ACM Trans. Graph.* **24** (3), 982–990.

BARBIC, J. & ZHAO, Y. 2011 Real-time large-deformation substructuring. *ACM Trans. Graph.* **30** (4), 1–8.

BATHE, K. J., RAMM, E. & WILSON, E. L. 1975 Finite element formulations for large deformation dynamic analysis. *International Journal for Numerical Methods in Engineering* **9** (2), 353–386.

BELYTSCHKO, T. & HSIEH, B. J. 1973 Non-linear transient finite element analysis with convected co-ordinates. *International Journal for Numerical Methods in Engineering* **7** (3), 255–271.

BENNIGHOF, J. K. & LEHOUCQ, R. B. 2004 An automated multilevel substructuring method for eigenspace computation in linear elastodynamics. *SIAM Journal on Scientific Computing* **25** (6), 2084–2106.

BERKOOZ, G., HOLMES, P, & LUMLEY, J. L. 1993 The proper orthogonal decomposition in the analysis of turbulent flows. *Annual Review of Fluid Mechanics* **25** (1), 539–575.

BESSELINK, B., TABAK, U., LUTOWSKA, A., VAN DE WOUW, N., NIJMEIJER, H., RIXEN, D. J., HOCHSTENBACH, M. E. & SCHILDERS, W. H. A. 2013 A comparison of model reduction techniques from structural dynamics, numerical mathematics and systems and control. *Journal of Sound and Vibration* **332** (19), 4403–4422.

BESSET, S. & JÉZÉQUEL, L. 2007 Dynamic substructuring based on a double modal analysis. *Journal of Vibration and Acoustics* **130** (1), 011008–011008.

BILLAH, K. Y. & SCANLAN, R. H. 1991 Resonance, tacoma narrows bridge failure, and undergraduate physics textbooks. *American Journal of Physics* **59** (2), 118–124.

BOURQUIN, F. 1992 Component mode synthesis and eigenvalues of second order operators: discretization and algorithm. *ESAIM: Mathematical Modelling and Numerical Analysis - Modélisation Mathématique et Analyse Numérique* **26** (3), 385–423.

BRÜLS, O., DUYSINX, P. & GOLINVAL, J. C. 2007 The global modal parameterization for non-linear model-order reduction in flexible multibody dynamics. *International Journal for Numerical Methods in Engineering* **69** (5), 948–977.

CARDONA, A. 2000 Superelements modelling in flexible multibody dynamics. *Multibody System Dynamics* **4** (2-3), 245–266.

CASTANIER, M. P., TAN, Y. C. & PIERRE, C. 2001 Characteristic constraint modes for component mode synthesis. *AIAA journal* **39** (6), 1182–1187.

CAVIN, I. R. K. & DUSTO, A. R. 1977 Hamilton's principle - finite-element methods and flexible body dynamics. *AIAA Journal* **15** (12), 1684–1690.

CLOUGH, R. W. 1960 The finite element method in plane stress analysis. *In Proceedings of 2nd ASCE Conference on Electronic Computation* .

COPPERSMITH, DON & WINOGRAD, SHMUEL 1990 Matrix multiplication via arithmetic progressions. *Journal of Symbolic Computation* **9** (3), 251–280.

CORNWELL, R., CRAIG, R. R. & JOHNSON, C. P. 1983 On the application of the mode-acceleration method to structural engineering problems. *Earthquake engineering & structural dynamics* **11** (5), 679–688.

CRAIG, R. R. 2000 Coupling of substructures for dynamic analyses: an overview. In *Proceedings of AIAA/ASME/ASCE/AHS/ASC structures, structural dynamics, and materials conference and exhibit*, pp. 1573–1584.

CRAIG JR, ROY R. & CHANG, C. J. 1977 Substructure coupling for dynamic analysis and testing. Report. National Aeronautics and Space Administration.

CRISFIELD, M. A. 1991 *Non-Linear Finite Element Analysis of Solids and Structures*, , vol. 1. England: John Wiley & Sons.

DAVID, S. & THOMAS, C. 2005 *Selection of Characteristic Constraint Modes for Component Mode Synthesis Using a Modification of Effective Interface Mass*. American Institute of Aeronautics and Astronautics.

DICKENS, J. M., NAKAGAWA, J. M. & WITTBRODT, M. J. 1997 A critique of mode acceleration and modal truncation augmentation methods for modal response analysis. *Computers & Structures* **62** (6), 985–998.

FARHAT, C., AVERY, P., CHAPMAN, T. & CORTIAL, J. 2014 Dimensional reduction of nonlinear finite element dynamic models with finite rotations and energy-based mesh sampling and weighting for computational efficiency. *International Journal for Numerical Methods in Engineering* **98** (9), 625–662.

FARHAT, C., CHAPMAN, T. & AVERY, P. 2015 Structure-preserving, stability, and accuracy properties of the energy-conserving sampling and weighting method for the hyper reduction of nonlinear finite element dynamic models. *International Journal for Numerical Methods in Engineering* **102** (5), 1077–1110.

FEHR, J. & EBERHARD, P. 2011 Simulation process of flexible multibody systems with non-modal model order reduction techniques. *Multibody System Dynamics* **25** (3), 313–334.

FISCHER, M. & EBERHARD, P. 2014 Linear model reduction of large scale industrial models in elastic multibody dynamics. *Multibody System Dynamics* **31** (1), 27–46.

GALVANETTO, U. & CRISFIELD, M. A. 1996 An energy-conserving co-rotational procedure for the dynamics of planar beam structures. *International Journal for Numerical Methods in Engineering* **39** (13), 2265–2282.

GERADIN, M. & RIXEN, D. 1997 *Mechanical Vibrations: Theory and Application to Structural Dynamics*. England: John Wiley & Sons.

GOLUB, G. H. & REINSCH, C. 1970 Singular value decomposition and least squares solutions. *Numerische mathematik* **14** (5), 403–420.

GOLUB, G. H. & VAN L., CHARLES F. 2012 *Matrix computations*, 3rd edn., , vol. 3. Baltimore: Johns Hopkins University Press.

GRAF, P. A., STEWART, G., LACKNER, M., DYKES, K. & VEERS, P. 2016 High-throughput computation and the applicability of monte carlo integration in fatigue load estimation of floating offshore wind turbines. *Wind Energy* **19** (5), 861–872.

GRUBER, F. M. & RIXEN, D. J. 2016 Evaluation of substructure reduction techniques with fixed and free interfaces. *Journal of Mechanical Engineering* **62** (7-8).

GUYAN, R. J. 1965 Reduction of stiffness and mass matrices. *AIAA journal* **3** (2), 380–380.

HALLER, G. & PONSIOEN, S. 2017 Exact model reduction by a slow–fast decomposition of nonlinear mechanical systems. *Nonlinear Dynamics* **90** (1), 617–647.

HANSEN, M. H., THOMSEN, K., NATARAJAN, A. & BARLAS, A. 2015 Design load basis for onshore turbines-revision 00. *Tech. Rep.*. DTU Wind Energy.

HANSEN, M. O. L. 2015 *Aerodynamics of Wind Turbines*. London: Taylor & Francis.

HERRMANN, J., MAESS, M. & GAUL, L. 2010 Substructuring including interface reduction for the efficient vibro-acoustic simulation of fluid-filled piping systems. *Mechanical Systems and Signal Processing* **24** (1), 153–163.

HOLM-JØRGENSEN, K. & NIELSEN, S. R. K. 2009 System reduction in multibody dynamics of wind turbines. *Multibody System Dynamics* **21** (2), 147–165.

HOLMES, M., GRAY, A. & ISBELL, C. 2007 Fast svd for large-scale matrices. In *Workshop on Efficient Machine Learning at NIPS*, , vol. 58, pp. 249–252.

HOLZWARTH, P. & EBERHARD, P. 2015 Svd-based improvements for component mode synthesis in elastic multibody systems. *European Journal of Mechanics - A/Solids* **49** (0), 408–418.

HONG, S. K., EPUREANU, B. I. & CASTANIER, M. P. 2013 Next-generation parametric reduced-order models. *Mechanical Systems and Signal Processing* **37** (1–2), 403–421.

HSIAO, K. M., YANG, R. T. & LEE, A. C. 1994 A consistent finite element formulation for non-linear dynamic analysis of planar beam. *International Journal for Numerical Methods in Engineering* **37** (1), 75–89.

HURTY, W. C 1960 Vibrations of structural systems by component mode synthesis. *Journal of the Engineering Mechanics Division* **86** (4), 51–70.

HURTY, W. C. 1965 Dynamic analysis of structural systems using component modes. *AIAA Journal* **3** (4), 678–685.

IDELSOHN, S. R. & CARDONA, A. 1985*a* A load-dependent basis for reduced nonlinear structural dynamics. *Computers* & *Structures* **20** (1–3), 203–210.

IDELSOHN, S. R. & CARDONA, A. 1985*b* A reduction method for nonlinear structural dynamic analysis. *Computer Methods in Applied Mechanics and Engineering* **49** (3), 253–279.

JAIN, S., TISO, P., RUTZMOSER, J. B. & RIXEN, D. 2017 A quadratic manifold for model order reduction of nonlinear structural dynamics. *Computers & Structures* pp. 1–28 (resubmitted after major revision).

JEZEQUEL, L. & SEITO, H. D. 1994 Component modal synthesis methods based on hybrid models, part i: Theory of hybrid models and modal truncation methods. *Journal of Applied Mechanics* **61** (1), 100–108.

KAMMER, D. C. & TRILLER, M. J. 1996 Selection of component modes for craig-bampton substructure representations. *Journal of Vibration and Acoustics, Transactions of the ASME* **118** (2), 264–270.

KIM, C. W. 2006 Analysis of vibration levels of large structural system with recursive component mode synthesis method: theory and convergence. *Proceedings of the Institution of Mechanical Engineers, Part C: Journal of Mechanical Engineering Science* **220** (9), 1339–1345.

KIM, J. G. & LEE, P. S. 2015 An enhanced craig–bampton method. *International Journal for Numerical Methods in Engineering* **103** (2), 79–93.

KIM, T., HANSEN, A. M. & BRANNER, K. 2013 Development of an anisotropic beam finite element for composite wind turbine blades in multibody system. *Renewable Energy* **59** (0), 172–183.

KLERK, D. DE, RIXEN, D. J. & VOORMEEREN, S. N. 2008 General framework for dynamic substructuring: History, review and classification of techniques. *AIAA Journal* **46** (5), 1169–1181.

KUETHER, R. J., ALLEN, M. S. & HOLLKAMP, J. J. 2016 Modal substructuring of geometrically nonlinear finite-element models. *AIAA Journal* **54** (2), 691–702.

KUETHER, R. J., ALLEN, M. S. & HOLLKAMP, J. J. 2017 Modal substructuring of geometrically nonlinear finite element models with interface reduction. *AIAA Journal* **55** (5), 1695–1706.

LANG, H., LINN, J. & ARNOLD, M. 2011 Multi-body dynamics simulation of geometrically exact cosserat rods. *Multibody System Dynamics* **25** (3), 285–312.

LE, T. N., BATTINI, J. M. & HJIAJ, M. 2011 Efficient formulation for dynamics of corotational 2d beams. *Computational Mechanics* **48** (2), 153–161.

LE, T. N., BATTINI, J. M. & HJIAJ, M. 2014 A consistent 3d corotational beam element for nonlinear dynamic analysis of flexible structures. *Computer Methods in Applied Mechanics and Engineering* **269** (0), 538–565.

LEE, S., MOK, H. & KIM, C. W. 2011 On a component mode synthesis on multi-level and its application to dynamics analysis of vehicle system supported with spring-stiffness damper system. *Journal of mechanical science and technology* **25** (12), 3115–3121.

LI, Q., WANG, T. & MA, X. 2009 Geometric nonlinear effects on the planar dynamics of a pivoted flexible beam encountering a point-surface impact. *Multibody System Dynamics* **21** (3), 249–260.

LIEW, K. M., LEEK, S. E. & LIU, A. Q. 1996 Mixed-interface substructures for dynamic analysis of flexible multibody systems. *Engineering Structures* **18** (7), 495–503.

LINDBERG, E., HÖRLIN, N. E. & GÖRANSSON, P. 2013 Component mode synthesis using undeformed interface coupling modes to connect soft and stiff substructures. *Shock and Vibration* **20** (1), 157–170.

MACNEAL, R. H. 1971 Special issue on structural dynamics a hybrid method of component mode synthesis. *Computers & Structures* **1** (4), 581–601.

MAYO, J. & DOMÍNGUEZ, J. 1996 Geometrically non-linear formulation of flexible multibody systems in terms of beam elements: Geometric stiffness. *Computers & Structures* **59** (6), 1039–1050.

MAYO, J., SHABANA, A. A. & DOMINGUEZ, J. 1995 Geometrically nonlinear formulations of beams in flexible multibody dynamics. *Journal of Vibration and Acoustics* **117** (4), 501–509.

MEEK, J. L. & LIU, H. 1995 Nonlinear dynamics analysis of flexible beams under large overall motions and the flexible manipulator simulation. *Computers & Structures* **56** (1), 1–14.

MONTEIL, M., BESSET, S. & SINOU, J. J. 2016 A double modal synthesis approach for brake squeal prediction. *Mechanical Systems and Signal Processing* **70** (Supplement C), 1073–1084.

MULLIS, C. & ROBERTS, R. A. 1976 Synthesis of minimum roundoff noise fixed point digital filters. *IEEE Transactions on Circuits and Systems* **23** (9), 551–562.

NADA, A. A., HUSSEIN, B. A., MEGAHED, S. M. & SHABANA, A. A. 2010 Use of the floating frame of reference formulation in large deformation analysis: experimental and numerical validation. *Proceedings of the Institution of Mechanical Engineers, Part K: Journal of Multi-body Dynamics* **224** (1), 45–58.

NIKRAVESH, P. 2005 *Understanding Mean-Axis Conditions as Floating Reference Frames, Computational Methods in Applied Sciences*, vol. 2, book section 8, pp. 185–203. Springer Netherlands.

PEREIRA, M. S. & PROENCA, P. L. 1991 Dynamic analysis of spatial flexible multibody systems using joint co-ordinates. *International Journal for Numerical Methods in Engineering* **32** (8), 1799–1812.

PILLAGE, L. T. & ROHRER, R. A. 1990 Asymptotic waveform evaluation for timing analysis. *IEEE Transactions on Computer-Aided Design of Integrated Circuits and Systems* **9** (4), 352–366.

RAYLEIGH, J. W. S. 1945 *The Theory of Sound*. New York: Dover Publications.

REDDY, J. N. 2004 *Nonlinear finite element analysis*. Oxford University Press, New York.

RESOR, B. R. 2013 Definition of a 5mw/61.5 m wind turbine blade reference model. Report. Sandia National Laboratories.

RIXEN, D. J. 2002 Force modes for reducing the interface between substructures. In *Proceedings of IMAC-XX: A Conference on Structural Dynamics, Society for Experimental Mechanics, Bethel, CT*.

RIXEN, D. J. 2004 A dual craig–bampton method for dynamic substructuring. *Journal of Computational and Applied Mathematics* **168** (1–2), 383–391.

RIZZI, S. A. & PRZEKOP, A. 2008 System identification-guided basis selection for reduced-order nonlinear response analysis. *Journal of Sound and Vibration* **315** (3), 467–485.

DES ROCHES, G. V., BIANCHI, J. P., BALMES, E., LEMAIRE, R. & PASQUET, T. 2011 *Using component modes in a system design process*, pp. 617–625. New York, NY: Springer New York.

RUBIN, S. 1975 Improved component-mode representation for structural dynamic analysis. *AIAA Journal* **13** (8), 995–1006.

RUTZMOSER, J. B., RIXEN, D. J., TISO, P. & JAIN, S. 2017 Generalization of quadratic manifolds for reduced order modeling of nonlinear structural dynamics. *Computers & Structures* **192** (Supplement C), 196–209.

SCHULZE, M., DIETZ, S., BURGERMEISTER, B., TUGANOV, A., LANG, H., LINN, J. & ARNOLD, M. 2013 Integration of nonlinear models of flexible body deformation in multibody system dynamics. *Journal of Computational and Nonlinear Dynamics* **9** (1), 011012–011012.

SCHWERTASSEK, R., DOMBROWSKI, S. & WALLRAPP, O. 1999*a* Modal representation of stress in flexible multibody simulation. *Nonlinear Dynamics* **20** (4), 381–399.

SCHWERTASSEK, R., WALLRAPP, O. & SHABANA, A. 1999*b* Flexible multibody simulation and choice of shape functions. *Nonlinear Dynamics* **20** (4), 361–380.

SHABANA, A. A. 1986 Transient analysis of flexible multi-body systems. part i: Dynamics of flexible bodies. *Computer Methods in Applied Mechanics and Engineering* **54** (1), 75–91.

SHABANA, A. A. 1997 Flexible multibody dynamics: review of past and recent developments. *Multibody system dynamics* **1** (2), 189–222.

SHABANA, A. A. 2005 *Dynamics of Multibody Systems*. Cambridge: Cambridge University Press.

SHARF, I. 1996 Geometrically non-linear beam element for dynamics simulation of multibody systems. *International Journal for Numerical Methods in Engineering* **39** (5), 763–786.

SHARF, I. 1999 Nonlinear strain measures, shape functions and beam elements for dynamics of flexible beams. *Multibody System Dynamics* **3** (2), 189–205.

SIMO, J. C. & V. Q., L. 1986 On the dynamics of flexible beams under large overall motions—the plane case: Part i. *Journal of Applied Mechanics* **53**, 849.

SINOU, J. J. & BESSET, S. 2017 Simulation of transient nonlinear friction-induced vibrations using complex interface modes: Application to the prediction of squeal events. *Shock and Vibration* **2017**, 10.

SLAATS, P. M. A., DE JONGH, J. & SAUREN, A. A. H. J. 1995 Model reduction tools for nonlinear structural dynamics. *Computers & Structures* **54** (6), 1155–1171.

TC88-MT, IEC 2005 Iec 61400-3: Wind turbines–part 1: Design requirements. *International Electrotechnical Commission, Geneva* .

TISO, P. 2006 Finite element based reduction methods for static and dynamic analysis of thin-walled structures. Dissertation.

TISO, P. 2011 *Optimal second order reduction basis selection for nonlinear transient analysis*, book section 3, pp. 27–39. Springer New York.

TISO, P., JANSEN, E. & ABDALLA, M. 2011 Reduction method for finite element nonlinear dynamic analysis of shells. *AIAA journal* **49** (10), 2295–2304.

TRAN, D. M. 2001 Component mode synthesis methods using interface modes. application to structures with cyclic symmetry. *Computers* & *Structures* **79** (2), 209–222.

TRAN, D. M. 2009 Component mode synthesis methods using partial interface modes: Application to tuned and mistuned structures with cyclic symmetry. *Computers & Structures* **87** (17–18), 1141–1153.

VOORMEEREN, S. N 2012 Dynamic substructuring methodologies for integrated dynamic analysis of wind turbines. Thesis.

WALLRAPP, O. & WIEDEMANN, S. 2002 Simulation of deployment of a flexible solar array. *Multibody System Dynamics* **7** (1), 101–125.

WASFY, T. M. & NOOR, A. K. 2003 Computational strategies for flexible multibody systems. *Applied Mechanics Reviews* **56** (6), 553–613.

WEEGER, O. 2015 Isogeometric finite element analysis of nonlinear structural vibrations. Thesis.

WEEGER, O., WEVER, U. & SIMEON, B. 2014 Nonlinear frequency response analysis of structural vibrations. *Computational Mechanics* **54** (6), 1477–1495.

WEEGER, O., WEVER, U. & SIMEON, B. 2016 On the use of modal derivatives for nonlinear model order reduction. *International Journal for Numerical Methods in Engineering* .

WENNEKER, F. & TISO, P. 2014 *A Substructuring Method for Geometrically Nonlinear Structures*, , vol. 1, pp. 157–165. Springer.

WU, L. & TISO, P. 2016 Nonlinear model order reduction for flexible multibody dynamics: a modal derivatives approach. *Multibody System Dynamics* **36** (4), 405–425.

ZHAO, R. & YU, K. 2015 An efficient transient analysis method for linear time-varying structures based on multi-level substructuring method. *Computers & Structures* **146** (Supplement C), 76–90.

CURRICULUM VITÆ

Long WU

1988.02.25	Born in Shaanxi Province, China.

EDUCATION

2018.05– current	Postdoc in Dept. of Marine and Transport Technology Delft University of Technology, Delft, The Netherlands
2017.10–2017.12	Scientific assistant in Inst. of Mechanical System Eidgenössische Technische Hochschule (ETH) Zürich, Switzerland
2013.09–2017.09	Ph. D. in Dept. of Precision and Microsystems Engineering Delft University of Technology, Delft, The Netherlands
2010.09–2013.06	Postgraduate in the major of Power Machinery and Engineering Xi'an Jiaotong University, Xi'an, China
2006.08–2010.07	Undergraduate in the major of Energy and Power Engineering Xi'an Jiaotong University, Xi'an, China
2003.09–2006.07	Yaozhou Middle School Tongchuan, Shaanxi Province, China

MORE INFO

LIST OF PUBLICATIONS

JOURNAL PAPERS

5. **Wu, L.**, Tiso, P., & van Keulen, F., A Modal Derivatives Enhanced Craig-Bampton Method for Geometrically Nonlinear Structures. (submitted to Computers & Structures).

4. **Wu, L.**, Tatsis, K. , Chatzi, E., van Keulen, F., & Tiso, P. , A modal derivatives enhanced Rubin substructuring method for geometrically nonlinear multibody systems. (submitted to Multibody System Dynamics, minor revision).

3. Krattiger, D., **Wu, L.**, Zacharczuk, M., Buck, M., Kuether, R.J., Allen, M.S., Tiso, P., Brake, M.R.W.: Interface reduction for Hurty/Craig-Bampton substructured models: Review and improvements. Mechanical Systems and Signal Processing 114, 579-603 (2019). doi:https://doi.org/10.1016/j.ymssp.2018.05.031

2. **Wu, L.**, Tiso, P., van Keulen, F., Interface Reduction with Multilevel Craig-Bampton Substructuring for Component Mode Synthesis. AIAA journal. 56(5), 2030-2044 (2018).

1. **Wu, L.**, Tiso, P., Nonlinear model order reduction for flexible multibody dynamics: a modal derivatives approach. Multibody System Dynamics. 36(4), 405-425 (2016).

CONFERENCE PAPERS

4. **Wu, L.**, Tiso, P.: Modal derivatives based reduction method for finite deflections in floating frame. In: 11th World Congress on Computational Mechanics, WCCM 2014, 5th European Conference on Computational Mechanics, ECCM 2014 and 6th European Conference on Computational Fluid Dynamics, ECFD 2014 2014, pp. 3125-3135.

3. **Wu, L.**, Tiso, P.: Accuracy of the floating frame with nonlinear elastic expression: A comparative study. In: Proceedings of ISMA 2014 - International Conference on Noise and Vibration Engineering and USD 2014 - International Conference on Uncertainty in Structural Dynamics 2014, pp. 2943-2950.

2. **Wu, L.**, Tiso, P., Jain, S., Van Keulen, F.: Quadratic manifolds for reduced-order modelling of highly flexible multibody systems. In: Proceedings of the ECCOMAS Thematic Conference on Multibody Dynamics 2015, Multibody Dynamics 2015 2015, pp. 422-430.

1. **Wu, L.**, Tiso, P., Van Keulen, F.: A modal derivatives enhanced Craig-Bampton method for geometrically nonlinear structural dynamics. In: Proceedings of ISMA

2016 - International Conference on Noise and Vibration Engineering and USD2016 - International Conference on Uncertainty in Structural Dynamics 2016, pp. 3615-3624.

ACKNOWLEDGEMENTS

This dissertation is a collection of my Ph.D. research at Delft University of Technology, accompanied with both joy and sorrow during the last five years. While writing this acknowledgment, I can still recall the frustration and nervousness when I first came to the Netherlands, at one chilly morning in September of 2013. I would like to give my great appreciations to my families, colleagues, and friends, who brought numerous happiness and warmness during my Ph.D. journey.

I would like to express my most profound gratitude to my promoter Prof. *Fred van Keulen* and my supervisor Dr. *Paolo Tiso*. During my PhD journey, I learned valuable lessons from them. I appreciated the efforts of *Paolo* in continually supervising me, especially after he moved to Zürich. *Paolo*, we suffered the poor internet connection during the Skype meeting in the last four years, your patient guidance and inspiring discussion are essential for me to continue this PhD work. *Fred*, I received many support and encouragement from you to get rid of my sad moments, especially in those days when I doubt whether I should continue my PhD study when Paolo left Delft. Your help is not limited to the academic activities, motivating me to sharpen my mind in all aspects of life.

Besides my promoter and supervisor in Delft, I would also like to show my thanks to my master's supervisor, Prof. *Qi Yuan*, who supported me a lot during my PhD application. I appreciated the nice and warm experience as a member of his research group.

I would like to express my particular appreciation to Prof. *Daniel Rixen* for his inspiration. Prof. *Rixen* knows well about my research topic and offered many helpful suggestions during my PhD study. I would like to thank him for his support.

I am also particularly grateful to Prof. *Eleni Chatzi* and *Konstantinos Tatsis* for their contributions to my research when I was an assistant scientific in ETH Zürich. *Eleni* and *Konstantinos* provided me the finite element model of the NREL 5 MW reference wind turbine blade, and we had intensive and inspiring discussions during my stay in Zürich.

Meanwhile, I would like to thank the thesis committee, Prof. *H. Nijmeijer*, Prof. *P. G. Steeneken*, Prof. *J.W. van Wingerden*, Prof. *Daniel Rixen* and Prof. *Eleni Chatzi* for spending a large amount of time reading the thesis and offering me valuable feedback.

Then I want to thank my colleagues at the department of Precision and Microsystems Engineering (PME). It is of great pleasure to work with all my colleagues. Please be ready for the upcoming list of my kind colleagues: *Abhilash*, *Alejandro*, *Alex*, *Arnoud*, *Andre*, *Banafsheh*, *Can*, *Cristina*, *Davood*, *Deepak*, *Dirk*, *Evert*, *Eleonoor*, *Elena*, *Floris*, *Freek*, *Farbod*, *Giuseppe*, *Gijs*, *Guishan*, *Hans*, *Hassan*, *Ivan*, *Jian Zhang*, *Kai Wu*, *Laura*, *Luigi*, *Marco, Matthijs, Maarten, Max, Michael, Niranjan, Paola, Paul van der Valk, Paul van Woerkom, Prabat, Pierpaolo, Qi Wang, Rajit, Renato, Rob Dedden, Rob Eling, Roy, Selman, Samee, Sanne, Sasan, Stefan, Tomas, Yabin, Yexian, Yi, Yong, Marcel, Minchang, Murali, Ruijun Deng, Stijn, Urs*. Also, I am thankful for all the support from our secretaries, including *Birgit, Corinne, Eveline, Gaby, Harry, Lisette, Jos, Marianne, Marli, Patrick* and *Rob Luttjeboer*. Thank you all for your help in the last five years.

I also appreciate the stay in ETH Zürich, so that I can work with the friendly and brilliant colleagues: *Beate, Thomas, Mattia, Stergios, Florian, Sten*. I would like to give my special appreciation to Prof. dr. *George Haller* for offering me the opportunities to work in his group, and to *Shobhit* for many helpful discussions and valuable collaborations in my work. I also want to thank my landlord *Georgiana* and her son *Lars*, who make my life in Switzerland colorful.

Life is not easy when living abroad. I would like to extend my gratitude to my friends who accompanied and supported me during the last four years. I want to show my special and everlasting appreciation to my friends *Yueting Liu* and *Jie Zhou*. Without your support and help, I could not experience such a pleasant life in Delft. *Yueting*, we know each other since the first working day I am in the Netherlands. We are colleagues for four years, roommates for two years, and friends forever. You are THE most helpful people I have ever meet, and you bind all the friends in Delft together as a big brother. *Jie*, I sincerely enjoyed all the moments with you. We spent most of the weekends together for drinking, poker games, and outdoor running. It is my precious memory. I would also like to thank my two beautiful roommates: *Peiyao* and *Yixiao*, who bring endless happiness in the last years. I enjoyed all the moments with my Chinese friends: creative *Yu* and *Zhijie*, passionate *Fei*, facetious *Anqi*, enthusiastic *SIxin*, *Daijie* and *Jiahuan*, sportive *Yageng*, as well as *Chuang Yu*, *Mingjuan*, *Lian Liu*, *Xu Huang*, and *Zhen Yang*. I want to give special thanks to my friends *Yingbiao Zhao* (应标) and *Qilin Hao* (麒麟) in China, who are always willing to listen to my endless complaint. I would also like to thank *Pradeep* and *Pavlo*, who introduced the meditation to me. It is really helpful.

写在最后的话：

感谢我的父母对我的支持与付出。身在海外，我从未停止过对你们的爱与思念。无论我身在何处，你们都将是我前进的动力。谢谢关心我，支持我的亲人，也谢谢坚持到此刻的我自己。